2009

Numerical heat transfer during partially-confined, confined, and free liquid jet impingement with rotation and chemical mechanical planarization process modeling

Jorge C. Lallave-Cortes
University of South Florida

Numerical Heat Transfer During Partially–confined, Confined, and Free Liquid Jet Impingement with Rotation and Chemical Mechanical Planarization Process Modeling

by

Jorge C. Lallave Cortes

A dissertation submitted in partial fulfillment of
the requirements for the degree of
Doctor of Philosophy
Department of Mechanical Engineering
College of Engineering
University of South Florida

Co–Major Professor: Muhammad M. Rahman, Ph.D.
Co–Major Professor: Ashok Kumar, Ph.D.
Aydin K. Sunol, Ph.D.
Craig P. Lusk, Ph.D.
Garrett Matthews, Ph.D.

Date of Approval:
March 17, 2009

Keywords: steady–state, transient analysis, conjugate heat transfer with spinning boundaries, slurry abrasive particles, and CMP temperature distributions

Note to Reader

The original of this document contains color that is necessary for understanding the data.

The original dissertation is on file with the USF library in Tampa, Florida.

Dedication

To my wife Milda, and my children Lyann and Christian for their unconditional love. To my parents Jorge Lallave, Sr. and Carmen Cortes and sister Lynnette Lallave for encouraging me to pursue a professional career with high standards and always run the extra mile. To my mother–in–law Providencia and father–in–law Luciano, for their support during all these years. I'm thankful and blessed for having a family that believes in me.

Acknowledgements

Firstly, I would like to thank my major professor, Dr. Muhammad Mustafizur Rahman, for giving me an opportunity to pursue this work under his guidance and support throughout my doctoral studies. I will like to thank Dr. Tapas Das, Dr. Ashok Kumar, Dr. Geoffrey Okogbaa, and Dr. Griselle Centeno for their guidance and professional encouragement as part of the STARS Program. I am grateful for the financial assistance of the National Science Foundation through the GK–12 STARS Fellowship (Grant # 0139348). I thank Dr. Ashok Kumar, Dr. Aydin K. Sunol, Dr. Amy L. Stuart and Dr. Craig Lusk, for being members of my dissertation committee and for their valuable suggestions to improve this work.

Many thanks also to my USF mentors, Dr. Abdul–Lateef Gari and Cesar Hernandez, for their inspiration and achievements as part of Dr. Muhammad M. Rahman's research group. I would like to thank Dr. Son Hong Ho, whose guidance in the areas of FEM and software modeling were crucial for completion of this dissertation. Special thanks go to all my friends of the STARS program for their support and encouragement which helped me to fulfill this work. I am extremely grateful to God for all the opportunities He provides throughout my life.

Table of Contents

List of Tables

List of Figures

List of Symbols

b	Disk thickness, [m]
C_p	Specific heat [J/kg–K]
d_n	Diameter of the nozzle [m]
d_w	Diameter of the wafer [m]
g	Acceleration due to gravity [m/s^2]
Ek	Ekman number, $\nu_f/(4\cdot\Omega\cdot r_d^2)$
Ek_1	Ekman number of impingement disk, $\nu_f/(4\cdot\Omega_1\cdot r_d^2)$
Ek_2	Ekman number of confinement disk, $\nu_f/(4\cdot\Omega_2\cdot r_d^2)$
F_o	Fourier number, $\alpha_f\, t/d_n^2$
h	Heat transfer coefficient [W/m^2K], $q_{int}/(T_{int}-T_j)$
h_{av}	Average heat transfer coefficient [W/m^2K], defined by equation 3.1.16.
$h_{av_{p,w}}$	Average pad and wafer heat transfer convection coefficients [W/m^2K]
H_n	Height of the nozzle from the plate [cm]
k	Thermal conductivity [W/m K]
nr	Number of elements in radial direction
nz	Number of elements in axial direction
Nu	Nusselt number, $(h\cdot d_n)/k_f$
Nu_{av}	Average Nusselt number for the entire surface, $(h_{av}\cdot d_n)/k_f$
p	Pressure [Pa]
Pr	Prandtl number, $(\mu_f\cdot Cp_f)/\ k_f$

q Heat flux [W/m^2]

Q Volumetric flow rate (m^3/s) or cc/min

r Radial coordinate [m]

r_{0-1} Pad to wafer center distance, [m]

$r_{1,2}$ CMP model radial coordinate system of reference, [m]

r_d Disk radius [m]

r_p Plate radius [m]

r_p/r_d Confinement plate to disk radius ratio, (Confinement ratio)

Re Reynolds number, $(V_j \cdot d_n)/\nu_f$

t Time [s]

T Temperature [K]

T_1 Solid disk sub layer temperature [K]

$\overline{T}_{int}$ Average interface temperature [K], $\frac{2}{r_d^2}\int_0^{r_d} T_{int} r dr$

V_j Jet velocity [m/s]

$V_{r,\,z,\,\theta}$ Velocity component in the r, z and θ–direction [m/s]

$V\theta_{pc}$ Co–tangential relative velocity, [m/s], defined by equation 3.4.10.

z Axial coordinate [m]

$z_{1,2}$ CMP model axial coordinate system of reference, [m]

Greek Symbols:

α Thermal diffusivity [m^2/s]

β Dimensionless nozzle–to–plate spacing, H_n/d_n

δ Free surface height [m]

δ_{sl} Slurry film thickness [m]

Γ Disk radius to nozzle diameter ratio, r_d/d_n

ε Thermal conductivity ratio, k_s/k_f

μ Dynamic viscosity [kg/m–s]

μ_{fr} Pad coefficient of friction

ν Kinematic viscosity [m^2/s]

θ Angular coordinate [rad]

$\theta_{1,2}$ CMP model axial coordinate system of reference, [m]

Θ Dimensionless temperature, $2 \cdot k_f \cdot (T_{int} - T_j) / (q \cdot d_n)$

ρ Density [kg/m^3]

σ Surface tension coefficient [N/m]

Ω Angular velocity [rad/s]

Ω_1 Angular velocity of the impingement disk [rad/s]

Ω_2 Angular velocity of the confinement disk [rad/s]

$\Omega_{p,c}$ Pad and carrier angular velocity [rad/s]

Subscripts:

atm Ambient

av Average

c Carrier

f Fluid

i Initial condition

in Inlet

int Solid–fluid interface

j Jet or inlet

max	Maximum
n	Nozzle
p	Plate or pad
pw	Polishing pad center to wafer edge distance, [m]
s	Solid disk
sl	Slurry
SS	Steady state
w	Bottom surface of the impingement disk or wafer

Numerical Heat Transfer During Partially–confined, Confined, and Free Liquid Jet Impingement with Rotation and Chemical Mechanical Planarization Process Modeling

Jorge C. Lallave Cortes

ABSTRACT

This work presents the use of numerical modeling for the analysis of transient and steady state liquid jet impingement for cooling application of electronics, and energy dissipation during a CMP process under the influence of a series of parameters that controls the transport phenomena mechanism. Seven thorough studies were done to explore how the flow structure and conjugated heat transfer in both the solid and fluid regions was affected by adding a secondary rotational flow during the jet impingement process. Axis–symmetrical numerical models of round jets with a spinning or static nozzle were developed using the following configurations: confined, partially–confined, and free liquid jet impingement on a rotating or stationary uniformly heated disk of finite thickness and radius. Calculations were done for various materials, namely copper, silver, Constantan, and silicon with a solid to fluid thermal conductivity ratio covering a range of 36.91–2222, at different laminar Reynolds numbers ranging from 220 to 2,000, under a broad rotational rate range of 0 to 1,000 RPM (Ekman number=∞–3.31×10^{-5}), nozzle–to–plate spacing (β=0.25–5.0), dimensionless disk thicknesses (b/d_n=0.167–1.67), confinement ratio (r_p/r_d=0.2–0.75), and Prandtl number (1.29–124.44) using NH_3, H_2O,

FC–77 and MIL–7808 as working fluids. An engineering correlation relating the average Nusselt number with the above parameters was developed for the prediction of system performance. The simulation results compared reasonably well with previous experimental studies.

The second major contribution of this research was the development of a three dimensional CMP model that shows the temperature distributions profile as an index of energy dissipation at the wafer and pad surfaces, and slurry interface. A finite element analysis was done with FIDAP 8.7.4 package under the influence of physical parameters, such as slurry flow rates (0.5–1.42 cc/s), polishing pressures (17.24–41.37 kPa), pad spinning rates (100–250 RPM), carrier spinning rates (15–75 RPM), and slurry film thicknesses (40–200 μm). Results in this study provide further insight of how the above parameters influence the thermal aspects of pad and wafer temperature and heat transfer coefficients distributions across the control volume under study. Numerical results support the interpretation of the experimental data.

Chapter 1 Introduction

The impinging jet can be defined as a high velocity mass flow ejected from a nozzle or slot that impinges on the heat transfer surface. The principal virtues of this method of cooling are the large rate of heat transfer and the relative ease with which both the heat transfer rate and distribution can be controlled. Impinging jets and sprays have been demonstrated to be an effective means of providing high heat/mass transfer rates in industrial processes where rapid heating, cooling, or drying is necessary. Processes like annealing of metal and plastic sheets, tempering glass, chemical vapor deposition, avionics cooling, cooling of turbine blades, and drying of textiles are some examples where we use this technique. In confined regions of airfoils such as the leading edge or trailing edge, span wise lines of impingement jets are sometimes used to focus cooling on a primary location of high external heat load, like the airfoil's stagnation region. Nowadays, many of these processes have become more complex and electronic products are becoming smaller in size, opening the doors to new techniques where conventional methods are inadequate or ineffective.

The second part of the investigation involved a three dimensional model of the chemical mechanical polishing process using a finite element method (FEM) to examine further the outcome of a series of experimental set up characteristics as part of the overall process. During the last twenty years, CMP process has been generally used in the microelectronics industry due to its versatility, simplicity, and cost effectiveness to

achieve global planarization, pattering of metals, and dielectric layers in fewer steps than other conventional methods. Nowadays, the modeling of the material removal process during CMP seems to have taken two distinctive types of approaches based on two extremes in dealing with the interactions between the pad and the wafer. The first is purely a fluid mechanical approach, in which the wafer and the pad are assumed to be separated by a continuous fluid layer of slurry and the material removal is viewed as a consequence of erosion, chemical removal and particles abrasion of the slurry. These are called wafer–scale macroscopic analyses or hydrodynamic contact modes, which may provide useful information about the influence of the shear and normal stress on the removal rate. The second approach is based on solid to solid contact mechanics in CMP and the assumptions of plastic contact over the wafer, abrasive particles, and pad interface in which the material removal is attributed to abrasive wear of the wafer surface in direct contact of the slurry particles and the pad. The solid to solid contact mode is referred to the mode where the down pressure is relatively large and the velocity is relatively small. This is considered the most frequent mode in CMP process, in which the two–body abrasion dominates and the fluid flow effects are immaterial. Many researchers extensively acknowledged that this approach seems to be physically more reasonable in describing experimental results.

On the contrary, there has been experimental evidence that various chemical effects observed like oxidizing and change in concentration of the slurry are responsible for the material removal rate (MRR) and the quality of the surface finish. Such observations cannot be explained by changes in the surface charge because its effect is irrelevant. Indeed, significant changes in the wafer surface exposed to the chemicals in

the slurry will play a significant role in the CMP process. As a result of the previous findings, an intermediate approach for the actual material removal mechanism is introduced as a semi–direct contact approach that is analogous to the transition region of the boundary layer approach of Prandtl. This approach presents the removal mechanism as a function of various factors that includes mechanical and chemical effects. In a non–direct contact mode, the CMP process occurs by the two body and three body abrasions occurring simultaneously at the interface. As the roughness of the pad is in the order of microns, and the size of the abrasive particles is in the order of nanometers, the two body abrasions mainly occur across the wafer surface and the pad surface asperities. Conversely, the process of CMP is more complicated at times when the wafer, abrasive particles in slurry and pad surfaces come in contact constituting a three body abrasion at the interface. In this model, it is assumed that the abrasive particles are fully embedded across the wafer surface under the applied pressure using the polishing pad, in which ploughing and cutting processes occur simultaneously, resulting in the material removal from the wafer surface. This model does not cover factors such as chemical effects, thermal effects, pad wear, and so on. The model is based on the assumptions of the abrasive wear theory, in which the abrasive indents and causes plastic deformation in the wafer.

Due to the friction between the particles of the slurry, pad asperity and wafer surface under a given pressure yield to high temperatures. The changes in friction and wear, especially during the run–in period, are strongly correlated to the blockage of energy dissipation paths within the sliding materials. As such, the preservation of the tribological integrity of a rubbing material depends mainly on the efficiency of

dissipation of the friction–induced thermal energy. Wafer, being more thermally conductive than the polymeric polishing pad, absorbs a major part of the heat. Thermal effects are important in the CMP process, as the chemical reactions and pad properties are affected to a considerable extent.

1.1 Configuration of Impinging Jets

Jets can be configured in different ways. The two main qualitatively flow configurations are free surface impinging jet and confined submerged impinging jet. A third physical configuration of partially–confined impinging jet has been studied as part of this investigation. The fluid dynamics of all cases are different.

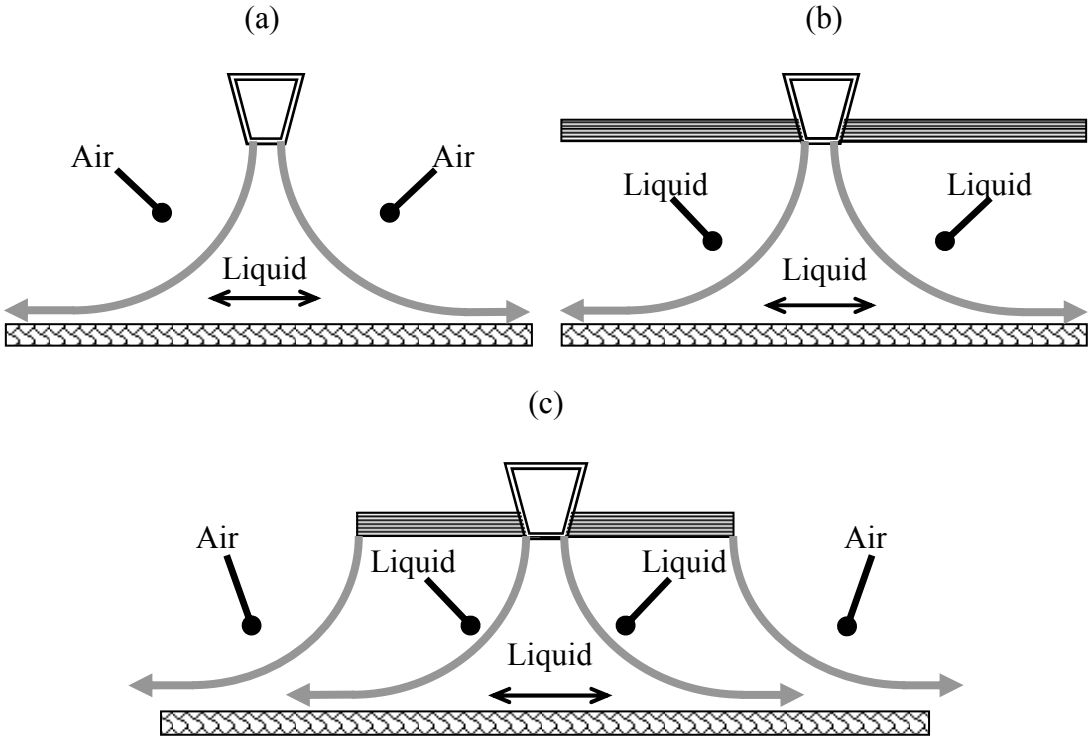

Figure 1.1 (a) Free liquid jet impingement, (b) Confined liquid jet impingement, and (c) Partially–confined liquid jet impingement.

Figure 1.1 shows the two dimensional representation of all previous cases. In terms of geometry, there two main cases a planar case with the jet issuing from a slot, and an axis–symmetric case with a round nozzle. Additional geometries such as jet issuing from square, rectangular or elliptical nozzles, or oblique jets are also possible.

1.2 Impinging Jet Characteristics and Zones

1.2.1 Free Surface Jets

A free surface jet is formed when a liquid discharges from a nozzle or orifice into the ambient air or other gaseous environment. The free surface develops instantly at the nozzle exit and remains throughout the impingement process. When an axial free surface jet impinges on a circular disk, the fluid forms a boundary layer, which grows along the disk radius. The flow can be divided into two regions, the impingement or stagnation zone and the wall jet region. The jet flow is undeveloped up to six or seven times the nozzle diameter measured from the lip. The stagnation zone is characterized by pressure gradient, which stops the flow in the axial direction and turns radially outward.

The boundary layer around the stagnation point is laminar due to a favorable pressure gradient effect. The increase of the velocity along the wall keeps a thin boundary layer thickness. The wall jet zone is free of gradients of the mean pressure; the flow decelerates and spreads radially. At the end, the structure of the jet free surface depends on surface tension, and gravitational and pressure forces. The liquid jet size, speed, and orientation determine the magnitude of these forces. The interaction of free liquid jet impingement and target rotation results in a complex and powerful flow capable of improving the heat transfer processes considerably. This method of cooling or heating can be used for processes involving a rapid heat dissipation rate or high heat flux.

1.2.2 Confined Submerged Jets

If the fluid is discharged from a nozzle or orifice attached to a confinement plate into a body of surrounding fluid that is the same as the jet itself, then it is called confined submerged. Confined submerged liquid jets find use in both axis–symmetric and planar configuration. Both configurations share the common feature of a small stagnation zone at the impingement surface whose size is of the order of the nozzle diameter or slot dimension, with the subsequent formation of a wall jet region.

The model covers the entire fluid region (impinging jet and flow spreading out under a stationary or spinning confined surface) and stationary or spinning solid disk as a conjugate problem. The liquid jet considered in this study is axis–symmetric and submerged, with the jet issuing into a region containing the same liquid. In most applications, the nozzle–to–plate distance is too small to enable the development of a jet flow condition. A thicker shear layer forms under laminar conditions around the nozzle, with a similar behavior as a plane shear layer. The shear layer thickness becomes comparable with the jet diameter downstream, and the behavior of the layer changes considerably. The interaction of rotation and impingement creates a complex and powerful flow capable of improving heat transfer processes considerably. This arrangement is suitable for microgravity applications where centrifugal force due to disk rotation can be used to force the fluid over the heated surface.

1.2.3 Partially–confined Jets

In a partially–confined jet the nozzle or slot is attached to a confinement plate parallel to the impingement surface with a separation distance of H_n. The diameter or length of the confinement region is smaller than the impingement target, and therefore the

fluid comes out of confinement spreading downstream as a free surface flow exposed to the ambient environment. To achieve a reliable cooling system design with impinging jet one has to choose an appropriate jet configuration and surrounding geometry. It is necessary to understand that the heat transfer rate from an impinging jet onto a surface is a complex function of many parameters, such as flow rate, working fluid properties, nozzle structure and orientation, nozzle to target spacing, confinement ratio and displacement from the stagnation point. The liquid jet considered in this study is axis–symmetric. Heat transfer capabilities of jets impinging on a rotating body are of importance in the thermal analysis of various types of machineries and in a wide variety of applications in the area of thermal heating and cooling. Processes like microgravity flow delivery, annealing of metal, chemical vapor deposition, and electronics packaging can use this technique.

Nowadays, many of these processes have become more complex and electronic products are becoming smaller in size, opening the doors to new techniques where conventional methods are inadequate or ineffective. The principal virtues of this method of cooling are the large heat transfer rate attainable relative to nonimpinging flows and the relative ease with which both the heat transfer rate and distribution can be controlled.

1.3 Chemical Mechanical Polishing Process Set–up

A standard CMP process consists of three main components. The first component includes a polishing pad fastened to a circular polishing platform. The second component is a wafer carrier (polishing head) that holds the substrate with a retaining ring that is adjusted to generate a uniform pressure profile across the entire wafer to help offset excessive material removal at the edges. Currently the wafer pressure versus retaining

ring pressure adjustment is done by trial and error. This wafer is rotated about its axis while being pressed down against a rotating polymeric polishing pad commonly made of polyurethane, since the chemistry of this polymer allows the pad characteristics (such as hardness and porosity) to be tailored to meet specific material property needs in CMP Jairath et al. [1]. Both previous components of the process are circular and typically rotate at similar speed and in the same direction but eccentrically oriented, despite the fact that pressing the wafer against the pad surface by applying a load or force which can be varied. The third component of the process is carried by the polishing pad and is the slurry, a liquid that contains a colloidal suspension of abrasive particles such as alumina (Al_2O_3) or silica SiO_2 as well as specific chemicals chosen for polishing. Finally, the surface layer of the polished material is removed progressively as a result of the chemical and mechanical interactions provided by the polishing slurry.

The slurry chemistry, including chemical reagents and its concentration, modifies the properties of the surface to be polished. The mechanical interactions, on the other hand, vary depending on solid loading, the slurry particle size, and distribution, in view of the fact that these factors create a disparity in the load applied per particle. Other empirical variables can be recognized, such as the applied normal force (or down pressure), relative velocity of the wafer to the pad, and pad properties (Young's Modulus, hardness and porosity, etc.). However, due to the complexity of CMP by concurrent polishing of multiple materials and lumped parameter conditions, the fundamental polishing mechanism underlying the process are not yet well understood [2]. Figure 1.2 shows a schematic side view of a CMP process.

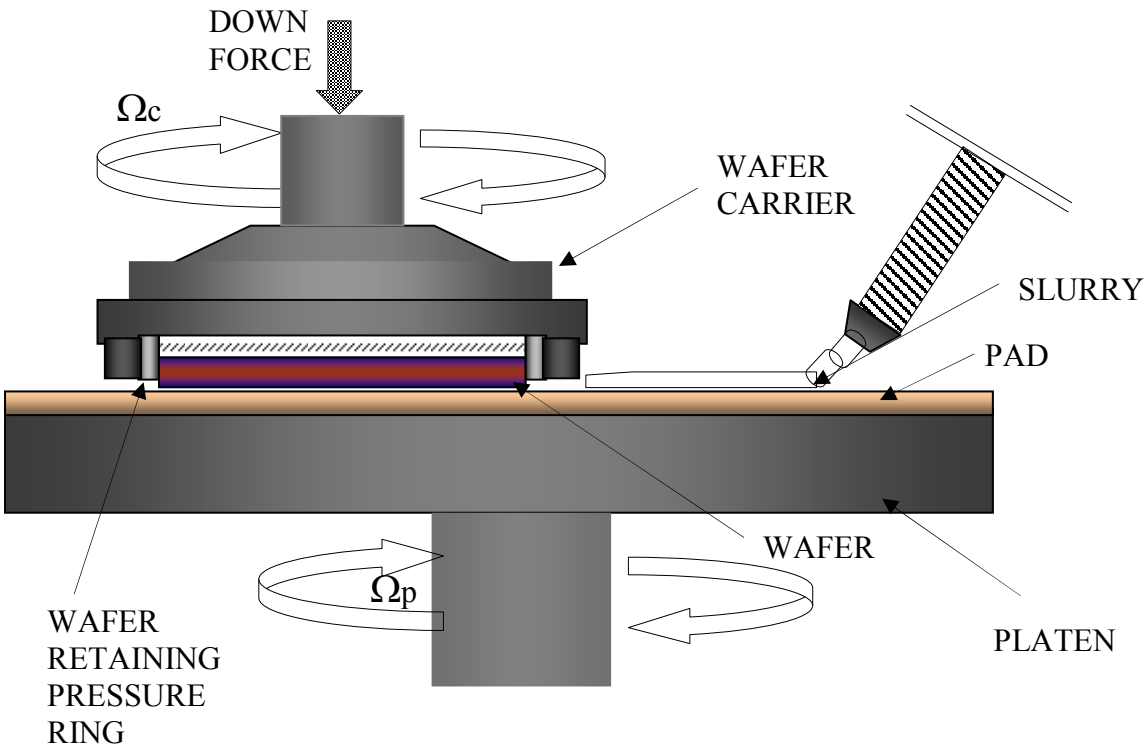

Figure 1.2 Schematic side view representation of a CMP process.

1.3.1 Experimental Testing Set Up

The universal tribological tester (UTT) technique is done with a bench top Center for Tribology Research (CETR) universal tribometer to examine the nature of polish (acoustic emission versus time) and the surface roughness of the sample. The real–time measurements of the data, along with other measurements, are used to calculate the wear and material removal rate (MRR) of the sample. In addition, it helps to quantify the wear resistance of the material at different pressure and rotational velocity. Table 1.1 provides the basic specifications of an experimental universal tribometer. The UTT tester provides real–time measurements of the following tribological parameters of the polishing: carrier and platen speed ranging, minimum and maximum load, and contact pressure load resolution and coefficient of friction as results of acoustic frequency as function of time.

Table 1.1 CETR universal tribometer specifications.

Specifications	Measurement or Description
Specimens dimensions	0.25 inch to 4 inches
Pad dimensions	1 inch to 9 inches
Speed ranging	0.1 micron/s (0.001 RPM) up to 50 m/s (10,000 RPM)
Minimum load	0.1 mN (10 mg)
Maximum load (w/high load system)	0.5 kN (50 Kg)
Contact Pressure	0.05 to 500 psi
Load resolution (w/high load system)	50 nN (yes, the same as without the high load system!
Total sampling rate	20 kHz

1.4 Problem Under Study

The detailed information about conjugate heat transfers from a rotating target (Prob. #1) or spinning confinement disk (Prob. #2) cooled by a confined liquid jet is currently not available in open literature. Table 1.2 summarized the nine problems under study as part of this work. Past studies are restricted to either cooling of a stationary disk by jet impingement or by pure rotation. Additionally, most of these works deal with average heat transfer measurements rather than local distributions. The intent of the following research is to study the conjugate heat transfer effect with a steady flow over a rotating solid wafer under confinement with constant fluid properties (Prob. #1) and to study the conjugate heat transfer effect of a spinning confinement disk over a solid stationary disk under temperature dependent properties (Prob. #2). Numerical results were done for various flow rates or jet Reynolds numbers, spinning rates or Ekman numbers, different disk thicknesses and nozzle to target spacing ratios. A broad range of Prandtl numbers was covered with the use of four working fluids, namely water,

ammonia, FC–77, and MIL–7808. The thermal conductivity effect was studied with the implementation of four different disk materials: copper, silicon, silver, and Constantan. The results offer a better understanding of the fluid mechanics and heat transfer behavior of liquid jet impingement under an insulated spinning or stationary wall condition on a stationary or rotating target. In addition, the enhancements of heat transfer during liquid jet impingement over a rotating disk could be done by triggering the turbulence in the flow field by increasing the flow rate or rotational speed but it was not examine as part of this study. The following studies were limit to laminar flow conditions during the present investigation. Even though no new numerical technique has been developed, results obtained in the present investigation are entirely new. The quantitative effects of different parameters as well as the correlation for average Nusselt numbers will be practical guides for enhancement of heat or mass transfer under microgravity.

There have been only a few studies on transient heat transfer and most of them are experimental work on free jet impingement. None of these studies considered transient heat transfer during partially–confined liquid jet impingement. Prob. #3 and #7 considered only laminar flow conditions to address the enhancement of heat transfer removal that is critical in space borne applications and accomplish the job with lower fluid inventory and hence lower the mass of the cooling system by adding rotation to the process. A higher rate of rotation is expected to enhance heat transfer at the impingement region, but may result in flow separation from the heat transfer surface further downstream, which is not desirable. Therefore, present studies are significant in addressing the heat transfer enhancement under steady state (Prob. #3) and transient conditions (Prob. #7) for a partially–confined liquid jet impingement over a spinning

target. The variation of disk temperature as well as local and average heat transfer coefficients during steady state (Prob. #3) and transient heating process (Prob. #7) are explored for different combinations of flow rate, spin rate of the target disk, nozzle to target spacings, confinement ratio, disk thickness and disk materials. The numerical results as well as the correlation for average Nusselt number are expected to be valuable towards the design of cooling or heating systems for engineering applications.

A wealth of information exists on heat transfer effects on the basic cases of individual and array set up of free and confined jet impingement. However, newer and more specific cases of cooling design require additional information to account for the heat transfer effects of partially–confined jet impingement. Prob. #4 considered the simultaneous spinning of a confinement disk and target surface under laminar partially–confined jet impingement. In addition, none of the studies have considered the steady state rotation of the nozzle cover plate and target disk to further induce fluid motion at microgravity. Therefore, the present study is significant in addressing heat transfer enhancement under certain conditions. Calculations were done under five different flow rates or jet Reynolds numbers, six spinning rates or Ekman numbers, five different disk thicknesses and four nozzle to target spacings. A broad range of Prandtl numbers was covered with the use of four working fluids, namely water (H_2O), ammonia (NH_3), flouroinert (FC–77) and MIL–7808 lubricating oil. The thermal conductivity effect was studied with the implementation of five different disk materials: aluminum, Constantan, copper, silicon, and silver. Even though jet impingement heat transfer from a stationary surface has been thoroughly investigated, only a few attempted to produce local heat transfer distribution for a rotating disk in combination with a free liquid jet impingement.

In addition, none of the studies have attempted to explore conjugate heat transfer effect in a rotating target during axial free jet impingement. The present study attempts to carry out a comprehensive investigation of a steady state (Prob. #5) and (Prob. #6) transient conjugate heat transfer analysis for a free liquid jet impingement over a spinning solid disk. Computations using water (H_2O), ammonia (NH_3), flouroinert (FC–77), and oil (MIL–7808) as working fluids were carried out for different combinations of geometric and flow parameters and five different disk materials. The numerical model along with the results for steady state and transient heat transfer for different Reynolds numbers, Ekman numbers, disk thicknesses and solid material properties is expected to be valuable towards the design of liquid jet impingement cooling or heating systems for various engineering applications.

Most publications primarily focus on other aspects of the CMP process like film stress, pattern dependencies, pad roughness, material removal rate, abrasive particles size, slurry film and pressure distributions, and chemicals effects. Only a few examine the thermal aspects during the planarization process over the wafer surface. However, in these research works, the reported temperature rise is either the average temperature on the pad surface, a predicted average temperature on the wafer surface, or temperature rise at different isolated locations on the wafer. These works report the overall temperature rise but do not provide the information about the temperature distribution on the wafer surface. The temperature profile on the wafer surface as a function of the radius under the influence of the above parameters will provide valuable insight into the extent of temperature rise at different locations on the wafer. For example, since the material removal rate during copper CMP is sensitive to temperature, the temperature distribution

over the entire wafer will significantly affect the uniformity of material removal over the entire wafer. Understanding the temperature profile of the substrate will decrease the with–in–wafer non–uniformity and thus improves yield by minimizing the number of faulty dies. The physical representation of a three dimensional CMP schematic is shown in figure 1.3.

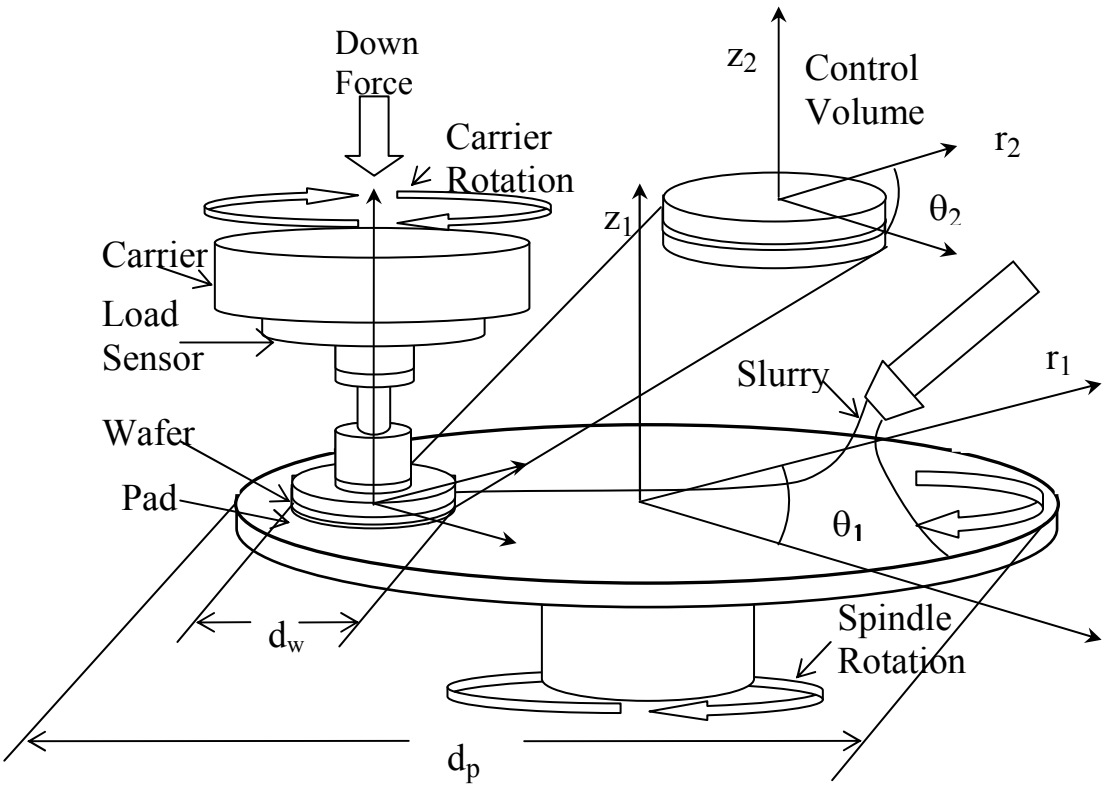

Figure 1.3 Three dimensional (3–D) CMP schematic.

Prob. #8 and #9 characterized the steady state and transient temperature distributions or profile as the index of energy dissipation at the wafer surface, slurry and pad interface. By solving the numerical problems, we present the temperature profiles and heat transfer convection coefficients on the pad and wafer surfaces under the influence of different physical parameters, such as slurry flow rate, slurry film thickness, wafer spinning rate, pad spinning rate, and polishing pressure.

The numerical modeling efforts are supported with a finite element analysis using the computer fluid dynamics of the FIDAP 8.7.4 package. The coefficient of friction values (μ_{fr}= 0.2–0.5) at different pressures and velocities required to calculate the heat dissipation at the interface are obtained from copper polishing experiments conducted on a CETR universal tribometer bench top tester. To gain greater insight into this behavior, the thermal dynamics associated with energy are further discussed in the results by figures and parameters. Finally, temperature distribution and heat transfer convection coefficients results are compared with experimental data under the same process conditions, which were found to be consistent. The main characteristics of the nine problems reported in this work are summarized in Table 1.2. They are presented in an order such that the difficulty from a computational point of view increases gradually.

Table 1.2 Summary of problems under study.

Problem #	Fluid	Model	BC's and Fluid Properties	Analysis	Body force
1	water, ammonia flouroinert and oil (MIL–7808)	Axis–symmetric, Confined submerged jet	Target rotation and constant	Steady–State	Gravity
2	water, ammonia flouroinert and oil (MIL–7808)	Axis–symmetric, Confined submerged jet	Confined disk rotation and Temperature dependent	Steady State	Gravity
3	water, ammonia flouroinert and oil (MIL–7808)	Axis–symmetric, Partially–confined submerged jet	Target rotation and Temperature dependent	Steady State	Gravity
4	water, ammonia flouroinert and oil (MIL–7808)	Axis–symmetric, Partially–confined submerged jet	Target and confined disk rotation, Temperature dependent	Steady State	Gravity
5	water, ammonia flouroinert and oil (MIL–7808)	Axis–symmetric, Free surface jet	Target rotation and Temperature dependent	Steady State	Gravity
6	water, ammonia flouroinert and oil (MIL–7808)	Axis–symmetric, Free surface jet	Target rotation and Temperature dependent	Transient	Gravity
7	water	Axis–symmetric, Partially–confined submerged jet	Target rotation and Temperature dependent	Transient	Gravity
8	Alumina	3–D	Carrier and pad spinning, and constant	Steady State	Gravity
9	Alumina	3–D	Carrier and pad spinning, and constant	Transient	Gravity

The level of difficulty includes model set up, time, and the computing resources required as part of the simulation process. The computational difficulty for each problem appears in different aspects that can be simplified into the following rules:

1. 3–D models (prob. #8 and #9) are more difficult than axis–symmetric (prob. #1 through #7).
2. Transient analysis with fixed time steps (probs. #6, #7, and #9) are more difficult than steady state analyses (prob. #1 through #5).
3. Free surface jet (prob. #5 and #6) are more sensitive and difficult than confined and partially–confined jet impingement (prob. #1 through #4).

1.5 Objectives

The main objective of the first part of the present investigation is to understand the relationship between fluid and solid as conjugated heat transfer phenomena during a process of free, confined, and partially–confined jet impingement under steady state and transient cooling conditions. Most of the above simulations consider temperature dependent properties of the fluid region in order to predict more precise results currently not available in the literature. In addition, this research examines the thermal boundary layer behaviors that control the steady state and transient convective heat transfer under the influence of a secondary rotational flow.

The present research focuses on addressing the effects of the following parameters on the steady state and transient heat transfer process.

1. Jet Reynolds number.
2. Ekman numbers of target and confined wall at different spinning rates.
3. Disk thicknesses.

4. Nozzle to target spacings.
5. Confinement ratio (r_p/r_d).
6. Prandtl number of different fluids.
7. Thermal conductivity of various materials.
8. Free, confined and partially–confined jet impingement configurations.

Additionally, a set of correlations for average Nusselt numbers results have been developed as a function of the above parameters to characterize the above heat transfer processes. The quantitative effects of different parameters are attached to the exponent that correlates with actual numerical results. These correlations are expected to be valuable and practical towards the design of cooling or heating systems under jet impingement or microgravity engineering applications.

The second part of this research includes the development of a three dimensional heat transfer model to estimate the steady state and transient temperature distributions at the wafer surface, slurry and pad interface during the CMP process. The model examines the index of energy dissipation at the slurry interface, wafer and pad surfaces as a differentiation technique of the CMP mechanism.

These numerical studies capture the effects of the following parameters on the steady state and transient chemical mechanical polishing process.

1. Slurry flow rates.
2. Different polishing pressures.
3. Variable heat flux at the polishing surface.
4. Polishing pad and carrier spinning rates.
5. Slurry film thickness.

Chapter 2 Literature Review

2.1 Free Surface Jet Impingement

Heat transfer from a stationary surface by free jet impingement has been well documented in the literature. One of the first theoretical analyses of a circular laminar impinging jet spreading into a thin film was done by Glauert [3]. Solutions to the boundary layer equations were sought for a laminar flow using similarity transformation. Watson [4] considered the flow due to jet spreading out over a plane surface, either radially or in two dimensions. Chaudhury [5] presented the heat transfer aspect of Watson's problem. Heat and mass transfer characteristics of an impinging axis–symmetric jet issuing from a circular nozzle has been studied by Scholtz and Trass [6]. The theoretical and experimental findings are well correlated in the stagnation–flow and in the wall jet regions. Metzger et al. [7] experimentally studied the effects of Prandtl numbers on heat transfer by liquid jets on a uniform temperature boundary condition at the test surface. They presented only surface average values of the Stanton number, determined from the measurement of the total heat flux, test surface temperature, and the adiabatic jet wall temperature. The correlations are based on the data for oil and water, and their correlations represent 95% of the data for disk radii up to 6.6 jet diameters to within ± 25%. Jiji and Dagan [8] carried out experimental studies for single jet and arrays of jets using water and FC–77 coolant for various heat source configurations. Theoretical flow solutions for laminar axis–symmetric liquid jet impingement over a

stationary surface were discussed by Adachi [9]. Liu and Lienhard [10] investigated circular sub–cooled liquid jet impinging on a surface maintained at uniform heat flux. They used an integral method to obtain analytical predictions of temperature distribution in the liquid film and the local Nusselt number. They carried out experiments to test the predictions of the theory.

A review of both analytical and experimental studies on jet impinging on a flat surface has been presented by Polat et al. [11]. Wang et al. [12, 13] presented an analytical study of heat transfer between an axis–symmetric free impinging jet and a solid flat surface with a non–uniform wall temperature or wall heat flux. The results obtained showed that the non–uniformity of the wall temperature or heat flux has a considerable effect on the Nusselt number. Wolf et al. [14] performed experiments on a planar, free surface jet of water to investigate the effects of non–uniform velocity profile on the local convective heat transfer coefficient for a uniform heat flux surface. The heat transfer coefficient was measured for different heat fluxes and Reynolds numbers. Vader et al. [15] measured temperature and heat flux distributions on a flat, upward facing, and constant heat flux surface cooled by a planar, impinging water jet. The jet velocity, the fluid temperature, and heat flux were varied. They found that the stagnation convection coefficient exceeded those predicted by laminar flow analysis and this was caused by the existence of free stream turbulence.

Stevens and Webb [16] considered an axis–symmetric free liquid jet impinging on a flat uniformly heated surface. Their experimental study presented the effects of Reynolds number, nozzle–to–plate spacing, and jet diameter. Liu et al. [17] presented an analytical and experimental investigation for jet impingement cooling of uniformly

heated surfaces to determine local Nusselt number from the stagnation point to radii up to 40 diameters. Womac et al. [18] presented correlating equations for heat transfer coefficient for the cooling of discrete heat sources by liquid jet impingement. Leland and Pais [19] performed an experimental investigation to determine the heat transfer rate for an impinging free surface axis–symmetric jet of lubricating oil for a wide range of Prandtl numbers, and for conditions varying inside the fluid film. They concluded that the heat transfer surface configuration has an important effect on Nusselt number. Rahman et al. [20] performed a numerical simulation of a free jet of high Prandtl number fluid impinging perpendicularly on a solid substrate of finite thickness containing electronics on the opposite surface. Computed results were validated with available experimental data. Chattopadhyay and Saha [21] performed a numerical study of turbulent flow and heat transfer from an array of impinging horizontal knife jets on a moving surface using large eddy simulation with a dynamic sub grid stress model. Roy et al. [22] reported surface temperature measurements for rectangular jet impingement heat transfer on a vehicle windshield using liquid crystals. Chan et al. [23] reported experimental results on heat transfer characteristics of a heated slot jet impinging on a semi–circular convex surface. Aldabbagh and Sezai [24] carried out a numerical investigation of the flow and heat transfer characteristics of a laminar three dimensional, square twin jet impingement on a flat plate under steady state condition. Their results showed that the flow structure is strongly affected by jet–to–plate distance.

Chatterjee et al. [25] studied laminar impinging flow heat transfer for a purely viscous inelastic fluid. Their study demonstrated that a small departure from Newtonian rheology leads to qualitative changes in the Nusselt number distribution along the

impinging surface. Yilbas et al. [26] numerically examined the jet impingement onto a hole with a constant wall temperature using a control–volume approach. Tong [27] numerically studied convective heat transfer of a circular liquid jet impinging onto a substrate to understand the hydrodynamics and heat transfer of the impingement process using the volume–of–fluid method to track the free surface of the jet. The effects of several key parameters on the hydrodynamics and heat transfer of an impinging liquid jet were examined. Silverman and Nagler [28] reported experimental data on the application of jet impingement for the cooling of accelerator targets using water as the coolant. Sezai and Aldabbagh [29] investigated the structure of the flow field and its effect on the heat transfer characteristics of a jet array system in steady state for Reynolds numbers between 100 and 400. Yang and Hwang [30] presented the numerical simulations of flow characteristics of a turbulent slot jet impinging on a semi–cylindrical convex surface.

2.2 Jet Impingement with Spinning Boundaries

The applications of liquid jet impingement over a rotating surface are growing in various processes encountered in mechanical, manufacturing, electrical and chemical engineering. The high heat transfer rate, along with the simplicity of hardware requirements makes this cooling process an attractive option in a variety of applications. In addition, rotation is used in metal etching, rinsing operations to dissolve species, surface preparation or coating, and microgravity fluid handling. The interaction of liquid jet impingement and rotation generates a powerful flow capable of improving thermal diffusion and mass transfer considerably in the absence of gravity.

On all rotating disks, whether smooth or roughened, there is an inherent pumping of fluid radially outward along the disk surface. Early research work on rotational flow

confined between two infinite parallel disks, one at rest and the other rotating was performed by Batchelor [31]. His analysis showed that three flow regions develop at high rotational rate, having the structure of two shear layers bounding an inviscid core rotating at constant angular velocity. An additional study on heat transfer rate from a rotating disk was carried out by Kreith et al. [32]. Their research covered a wide range of rotational Reynolds numbers (400 to 10,000) including laminar, turbulent and transitional regimes. This type of flow is found in parallel disk viscometers, rotary disk in a stationary housing of a rotor, and the chemical mechanical polishing process where the abrasive polishing slurry interacts with the pad and the wafer. The presence of rotation adds more complexity to the flow field. Experimental studies of a single round jet impinging on a rotating disk were conducted by Metzger and Grochowsky [33]. Tests were conducted for a range of flow rates and disk rotational speeds with various combinations of jet and disk sizes. Flow visualization using smoke addition to the jet flow revealed the presence of a transition regime. They concluded that higher rotational speeds, larger impingement radii, and smaller jet flow rate favor a rotationally dominated flow whereas the opposite trends favor an impingement dominated flow. Heat transfer rate was essentially independent of jet flow rate in the rotationally dominated regime but increased strongly with increasing flow rate in the impingement dominated regime. Carper and Deffenbaugh [34] conducted experiments to determine the average convective heat transfer coefficient for the rotating solid–fluid interface at uniform temperature, cooled by a single liquid jet of oil impinging normal to the rotating disk. Tests were conducted for a range of Reynolds numbers from 230 to 1,800 and for various disk rotational speeds. Carper et al. [35] conducted further experiments to consider the Prandtl number effects on the average heat transfer

coefficient at the rotating disk. They documented the effects of rotational Reynolds number on the average Nusselt number for various liquid jet Reynolds numbers.

Popiel and Boguslawski [36] reported measurements of heat transfer rate for a range of rotational and jet Reynolds numbers. Metzger et al. [37] employed liquid crystal for mapping local heat transfer distributions on a rotating disk with jet impingement. Brodersen et al. [38] experimentally studied the flow field interaction between an impinging liquid jet and a rotating disk. Their experiments covered separate measurements of the disk–wall flow, the jet flow and interaction between the two. Saniei et al. [39] investigated the heat transfer coefficients from a rotating disk with jet impingement at its geometric center. The air jet was placed perpendicular to the disk surface at four different distances from the center of the disk. Saniei and Yan [40] presented local heat transfer measurements for a rotating disk cooled with an impinging air jet. Several important factors, such as rotational Reynolds numbers, jet Reynolds numbers, jet–to–disk spacing, and the location of the jet center relative to the disk center, were examined.

Hung and Shieh [41] reported experimental measurements of heat transfer characteristics of jet impingement onto a horizontally rotating ceramic–based multichip disk. The chip temperature distributions along with local and average Nusselt numbers were presented. Kang and Yoo [42] carried out an experimental study using hotwire anemometry to investigate the turbulence characteristics of the three dimensional boundary layer on a rotating disk with liquid jet impingement at its center. Shevchuk et al. [43] presented an approximate analytical solution using integral method for jet impingement heat transfer over a rotating disk. The characterization of a thin film of

water from an axis–symmetric controlled impinging jet over stationary and rotating disk surfaces were experimentally studied by Ozar et al. [44, 45]. The authors measured the thickness of the liquid film on the disk surface by an optical method, including the characterization of the hydraulic jump. They concluded that the effect of rotation on heat transfer was larger for a lower liquid flow rate and gradually decreases with the increment of liquid flow rate. Semi–empirical correlations for both local and average Nusselt numbers were proposed based on their experimental results.

In a later study, Rice et al. [46] presented an analysis of the liquid film and heat transfer characteristics of a free surface controlled liquid jet impingement onto a rotating disk. Computations were run for a two dimensional axis–symmetric Eulerian mesh while the free surface was calculated with the volume of fluid method. Iacovides et al. [47] reported an experimental study of impingement cooling in a rotating passage of semi–cylindrical cross section. Cooling fluid was injected from a row of five jet holes along the centerline of the flat surface of the passage and impinged the concave surface. An integral analysis of hydrodynamics and heat transfer in a thin liquid film flowing over a rotating disk surface was presented by Basu and Cetegen [48]. The model considered constant temperature and constant heat flux boundary conditions over a range of Reynolds and Rossby numbers covering both inertia and rotation dominated regimes. Rahman and Lallave [49] numerically studied the convective heat transfer performance of a free liquid jet impinging on a rotating and uniformly heated solid disk of finite thickness and radius. A generalized average Nusselt number correlation was developed from numerical results.

2.3 Transient Jet Impingement

Transient heat transfer during jet impingement has been the subject matter in only a few past studies. Moallemi and Naraghi [50] performed a series of transient experiments to study the freezing of water impinging vertically on a subzero disk through a circular jet. Their experiments characterized the ice layer profiles at different times for different values of jet Reynolds number and Stefan number of the surface. Van Treuren et al. [51] measured the local heat transfer under an array of impinging jets employing a transient method. They used a temperature–sensitive coating consisting of three encapsulated thermo chromic liquid crystal materials to determine the local adiabatic wall temperature and the local heat transfer coefficient over the complete surface of a target plate for various Reynolds numbers. Steady state and transient methods were used by Owens and Liburdy [52] in order to study jet impingement cooling of surfaces. Thermo chromic liquid crystals were employed to measure the surface temperature which could be used to study the local heat transfer coefficient distribution. Kumagai et al. [53] investigated transient boiling heat transfer rate of a two dimensional impinging water jet on a rectangular surface for jet sub cooling from 14 K to 50 K. They discovered that boiling occurs at the moment of jet impingement and generates vapor at that region.

Lachefski et al. [54] numerically analyzed the velocity field and heat transfer in rows of rectangular impinging jets in transient state. Axial and radial jets coming out of rectangular nozzles were considered. Sazhin et al. [55] investigated the thermal characteristics of jet impingement drying of a moist porous solid using a one dimensional transient model. Fujimoto et al. [56] presented a numerical simulation of transient cooling of a hot solid by an impinging circular free surface liquid jet. The flow and thermal fields

in the liquid as well as the temperature distribution in the hot solid were predicted numerically by a finite difference method. Rahman et al. [57] presented the transient analysis of a free jet of high Prandtl number fluid impinging on a stationary solid disk of finite thickness. Computed results included the velocity, temperature, and pressure distributions in the fluid and the local and average heat transfer coefficients at the solid–fluid interface. Bula–Silvera et al. [58] presented information on transient heat transfer process of a free slot jet of high Prandtl number fluid impinging perpendicularly on a solid flat substrate of finite thickness containing discrete electronics sources on the opposite surface. The geometry of the free surface was determined iteratively. The influences of different operating parameters, such as jet velocity, heat flux, plate thickness, plate material, and the location of the heat generating electronics, were investigated.

Liu et al. [59] presented a numerical simulation of transient convective heat transfer during air jet impingement cooling of a confined multichip module disk. They found that a large rate of decrease of chip temperature and average Nusselt number happens in the earlier part of the transient. Sarghini and Ruocco [60] presented a transient numerical analysis of a planar jet impingement on a finite thickness substrate at low volumetric flow rate, including the effects of buoyancy. They found that conduction plays a significant role at the initial part of the transient. Fang et al. [61] reported experimental transient mixed convection measurements of heat transfer characteristics of jet impingement onto a horizontally rotating ceramic–based multichip disk. Their results were presented in terms of transient dimensionless temperature distribution on the chip, transient heat flux distribution of input power, and local and average Nusselt numbers.

2.4 Confined Submerged Jet Impingement

In the literature a reasonable amount of heat transfer information is available for circular disks. These data are typically restricted to either cooling of a stationary disk by jet impingement or cooling by pure rotation. The effect of the combination of rotation and jet impingement has been considered in only a small number of investigations. Additionally, most of these works deal with average heat transfer measurements rather than local distributions. As in all convective heat transfer situations, the flow field of an impinging liquid jet controls the heat transfer characteristics. In support of this statement, much work has been done on submerged confined liquid jets. The following provides a sample of some of the previous research related to this study.

McMurray et al. [62] studied the convective heat transfer of an impinging plane jet over a uniform heat flux boundary condition at the wall. To fit their data, they based heat transfer correlations on the stagnation flow in the impingement zone and on the flat plate boundary layer thickness in the uniform parallel flow zone. Impinging slot jet techniques under confinement with a plate parallel to the impingement surface were studied by Korger and Krizek [63], Kumada and Mabuchi [64], Miyazaki and Silberman [65], and Sparrow and Wong [66], and many of them are in practice in various industrial operations. Heat transfer from a stationary surface by liquid jet impingement has been reported by Saad et al. [67]. They investigated the effects of Reynolds number, distance between nozzle and impingement surface, diameters of impingement and confinement surfaces, and the shape of the velocity profile at the nozzle exit. Nakoryakov et al. [68] studied, both theoretically and experimentally, the hydrodynamics and mass transfer of a radial submerged liquid jet impinging onto a horizontal plate. Their studies measured the

wall shear stress, local and mean mass transfer coefficients within the entire flow region by an electro–diffusion method in a wide range of liquid flow rates. In addition, simple formulas were developed for the calculation of friction factor, liquid layer thickness, surface velocity, and convection heat transfer coefficient at stagnation point as a function of discharge parameters. Ma et al. [69] reported experimental measurements for local heat transfer coefficient during impingement of a circular jet perpendicular to a target plate. Both confined and free jet configurations were used. Ethylene glycol and transformer oil were used as working fluids.

Polat et al. [70, 71] measured local and average heat transfer coefficient for a confined turbulent slot jet impinging on a permeable surface and moving surface considering through flow. Measurements were carried out for a wide range of jet Reynolds and through flow velocity. Moreno et al. [72] investigated the mass transfer behavior of a confined impinging jet applied to wet chemical processes such as water rinsing and metal etching or platting, and the potential applicability to printed wiring board's fabrication. Chang et al. [73] examined the local heat transfer distributions of submerged liquid jet under confinement. Their investigation confirmed the local heat transfer coefficients trend of a half bell–shaped distribution with respect to radial distance from the stagnation point. Hung and Lin [74] proposed an axis–symmetric sub–channel model for evaluating local surface heat flux for confined and unconfined cases. Their models reveal that no significant deviation occurs for stagnation Nusselt numbers at nozzle–to–plate spacing ($H_n/d_n \geq 2$) while significant deviation exists when $H_n/d_n<2$. Experimental results for the distribution of local heat transfer coefficient during confined

submerged liquid jet impingement with FC–77 as the working fluid were presented by Garimella and Rice [75].

In addition, Webb and Ma [76] presented a comprehensive review of studies on jet impingement heat transfer. They concluded that heat transfer in submerged jets is more sensitive to nozzle–to–plate spacing than in free jets, especially when the heat transfer surface is beyond the potential core of the jet. Garimella and Nenaydykh [77], Fitzgerald and Garimella [78, 79], and Li et al. [80] all considered a confining top plate such as the one used at the present study for a submerged liquid jet using FC–77 as the working fluid at different volumetric flow rates. However, no rotation was used. Their experiments were done to determine the effects of the nozzle geometry on the local heat transfer coefficients from a small heat source to a normally impinging, axis–symmetric, submerged and confined liquid jet at different nozzle–to–plate spacing and Reynolds numbers. They concluded that the effect of the aspect ratio becomes less pronounced as the nozzle–to–plate spacing is increased. Ma et al. [81] investigated the radial distribution of the recovery factor for a confined impinging jet of high Prandtl number liquid by a numerical approach, with emphasis on its physical mechanism. They found that the recovery factor is strongly dependent on the Prandtl number, nozzle–to–plate spacing, and the velocity profile at the nozzle exit, but basically independent of the Reynolds number.

Abou–Ziyan and Hassan [82] made an experimental study on forced convection due to impingement of confined submerged and fully turbulent jets in relation to the cooling of engine cylinder heads by water. They concluded that jet impingement can save between 50 and 92 percent of the required cooling water compared to simple forced

convection. Morris and Garimella [83] computationally investigated the flow fields in the orifice and the confinement regions of a normally impinging, axis–symmetric, confined and submerged liquid jet. Tzeng et al. [84] numerically studied a series of confined impinging turbulent slot jet models. Eight turbulence models, including one standard and seven low Reynolds number k–ε models were employed and tested to predict the heat transfer performance of multiple impinging jets. Chatterjee and Deviprasath [85] numerically investigated the heat transfer to a laminar impinging jet at small nozzle–to–plate distances. Li and Garimella [86] studied the effects of fluid thermo–physical properties on heat transfer from a confined and submerged impinging jet. Local heat transfer coefficients were obtained experimentally from a discrete heat source. Generalized correlations for heat transfer were reported for the Prandtl number range of 0.7–25.2.

Rahman et al. [87] numerically evaluated the conjugate heat transfer of a confined jet impingement over a stationary disk using liquid ammonia as the coolant. Ichimiya and Yamada [88] presented the heat transfer and fluid flow characteristics of a single circular laminar impinging jet, including buoyancy effect in a comparatively narrow space with a confining wall. They identified the presence of forced, mixed, and natural convection modes of heat transfer as the flow moved downstream in the radial direction. Temperature distribution and velocity vectors in the space were obtained numerically. The flow and heat transfer characteristics in the cooling of a heated surface by impinging slot jets were investigated numerically by Sahoo and Sharif [89]. Computations were done for vertically downward–directed two dimensional slot jets impinging on a hot isothermal surface at the bottom and confined by a parallel adiabatic surface on top. The

local and average Nusselt numbers and skin friction coefficients at the hot surface for various conditions were presented. Qing–Guang et al. [90] studied the flow characteristics associated with a three dimensional laminar impinging jet issuing from a square pipe nozzle. The authors discussed the flow–field characteristics for different nozzle–to–plate spacing and Reynolds numbers. El–Gabry and Kaminski [91] presented experimental measurements of local heat transfer distribution on smooth and roughened surfaces under an array of angled impinging jets. Liquid crystal video thermography was used to capture surface temperature data at five different jet Reynolds numbers ranging from 15,000 to 35,000. Heat transfer from a row of turbulent jets impinging on a stationary surface was investigated by Salamah and Kaminski [92]. The geometric parameters of the jet array and the effects of Reynolds number were examined as part of this study. Rahman and Mukka [93] developed a numerical model for the conjugate heat transfer during vertical impingement of a two dimensional (slot) submerged confined liquid jet using liquid ammonia as the working fluid. Lin et al. [94] carried out a series of experimental investigations on transient and steady state cooling performance of heat sinks with a confined slot jet impingement.

2.5 Partially–confined Jet Impingement

Thomas et al. [95] measured the film thickness across a stationary and rotating horizontal disk using the capacitance technique, where the liquid was delivered to the disk by a controlled semi–confined impinging jet. The aim was to provide an understanding of the fundamental hydrodynamics processes which occur in the flow. Rahman and Faghri [96] presented the results of a numerical simulation of the flow field and associated heat transfer coefficient for the free surface flow of a thin liquid film

adjacent to a horizontal rotating disk. The computation was performed for different flow rates and rotational velocities using a three dimensional boundary–fitted coordinate system. Al–Sanea [97] presented a numerical model that studied three cases: free jet, semi–confined jet and semi–confined jet impingement through a crossflow for laminar slot–jet impinging on an isothermal flat surface. Rahman and Faghri [98] analyzed the processes of heating and evaporation in a thin liquid film adjacent to a horizontal disk rotating about a vertical axis at a constant angular velocity. The fluid emanated axis–symmetrically from a source at the center of the disk and was carried downstream by inertial and centrifugal forces.

Faghri et al. [99] experimentally, analytically, and numerically studied the heat transfer effect from a heated stationary or rotating horizontal disk to a liquid film from a controlled impinging jet under a partially–confined condition for different volumetric flow rates and inlet temperatures for both supercritical and subcritical regions. Rahman [100] presented a theoretical analysis of the gas absorption process of a thin liquid film formed by the impingement of a partially–confined liquid jet at the center of the disk and the subsequent radial spreading of the liquid along the surface of a horizontal rotating disk. Shi et al. [101] presented a numerical study to examine the effects of thermo–physical properties for semi–confined laminar slot jet. The fluid Prandtl number ranged from 0.7 to 71. Local, stagnation, and average values of the impingement Nusselt number were reported. Dano et al. [102] investigated the flow and heat transfer characteristics of confined jet array impingement with crossflow. Digital particle image velocimetry and flow visualization were used to determine the flow characteristics. Lallave and Rahman

[103] numerically studied the conjugate heat transfer for a partially–confined liquid jet impinging on a rotating and uniformly heated solid disk of finite thickness and radius.

2.6 Chemical Mechanical Polishing Process

The CMP process was applied primarily on silica (SiO_2) and tungsten layers. The ever increasing demand in the semiconductor industry for high performance microelectronics has resulted in the fabrication of increasingly complex, dense and miniaturized devices and circuits [104]. This event has unlocked the doors to a large variety of polishing materials such as Al, Cu, Ti, TiN, Ta, W, and their alloys, and insulators such as Si_3N_4, polysilicon and polymeric low–κ materials that are currently used as part of the CMP process development. CMP has been adopted in the following three areas of integrated circuits (IC) fabrications: The first areas includes the interlayer dielectric (ILD) and inter metal dielectric (IMD) planarization to form interconnections between devices during multilevel metallization (MLM). The second area covers the copper damascene process and the third area involves the process of shallow trench isolation (STI).

In fact, the CMP process in the current semiconductor device manufacturing industry needs to be optimized in all the aspects of polishing. Specifically, defects induced during the polishing process such as non–uniformity, dishing and erosion, need to be reduced in order to get good yields and thus lower operational costs. Improving wafer–scale uniformity would at the least reduce many defects during polishing. A critical step of the CMP process optimization requires the proper understanding of how different parameters influence the complex function of planarization.

The characterization of chemical mechanical polishing (CMP) process in recent years has traditionally focused on the use of Preston's equation to model the mechanics of the polishing process. Fu and Chandra [105] presented an analytical expression for the pressure distributions at the wafer and pad interface during the CMP process. Their profiles were used to determine the MRR using Preston's Equations. Their analytical model was compared with the FEM simulations and experimental data observations. The volume removal rate properties for a floating polishing process under different lubricating conditions were investigated by Su [106]. These lubricating conditions are those that make the pad in non–contact with the work surface. Su's paper tries to confirm the lubricating hypothesis and the two possible roles of the abrasive particles on the volume removal rate (VRR) of the film surface. Su [106] study result suggests that the high removal rate occurs at the lubrication near the boundary between the iso–viscous–elastic (IE) and iso–viscous rigid (IR) regimes. Zhou et al. [107] experimentally investigated the interfacial fluid pressure and friction effects during the polishing process. An analytical model was developed to predict the magnitude and the distribution of this fluid pressure. The effects of process variables such as normal load, relative velocity, pad surface roughness and modulus, fluid viscosity, and target surface curvature, were studied by comparing the 1D fluid pressure distributions. The effects of the sub–ambient fluid pressure on the material removal rate and the profile with thermally grown SiO_2 on single crystal silicon wafers were shown as part of their results.

Luo and Dornfeld [108] numerically investigated the abrasion mechanism in solid to solid contact mode for CMP process. Based on assumptions of plastic contact over wafer–abrasive and pad–abrasive interfaces, the proposed model integrates process

parameters like velocity and pressure. In addition, it integrates input parameters, such as wafer and pad hardness, pad roughness, abrasive size and abrasive geometry into the same formulation to predict the material removal rate ($MRR=\rho_w N Vol_{removed}$). The experimental results of the material removal rate were compared with the suggested model, showing how accurately it predicts the material removal rate. Much work has been done to incorporate the roughness effect into lubrication. Previous studies that quantify the surface roughness effect [109, 110] of large systems with small topographies proved to be computationally exhaustive, even though getting the topography intricate details of the system experimentally could be difficult and impractical. Hence, some work [111–115] has been done to employ stochastic concepts to solve the problem. Most of these models are limited to one dimensional ridges oriented either transversely or longitudinally. It is difficult to extend to three dimensional or anisotropic roughness using the stochastic approach. There is also a perturbation method [116, 117] to model roughness in lubrication.

Fu et al. [118] presented the behavior of the hydroxylated layer by a perfectly plastic material and mechanistic model for the material removal rate (MRR) during a CMP process. The plasticity model was utilized to explore the effects of various design parameters (e.g., abrasive shape, size and concentration, and pad rigidity) on the MRR. Their model took into account the dependence of pressure and relative velocity, plus delineated the effects of pad and slurry properties. Thakurta et al. [119] presented a three dimensional chemical planarization slurry model based upon the lubrication theory, using the generalized Reynolds equation that includes pad porosity and bending. Their model calculated the slurry film thickness and slurry velocity distribution between the wafer and

pad, with the minimum slurry film thickness determining the degree of contact between the wafer and pad. In addition, the minimum slurry film thickness was examined over a range of input variables, namely, applied pressure, carrier and pad velocity, wafer radius and curvature, slurry viscosity, and pad porosity and compressibility. Yang [120] developed a model for the CMP of copper dual damascene based on the multi–step, multi–slurry process platform. His model predicted copper dishing and ILD erosion for three steps copper CMP. The first step involved fast copper removal slurry, the second, a low pressure step for copper clearing, and a final step for diffusion barrier removal.

Even though a number of publications have been considered, most of them primarily focus on other aspects of the CMP process such as film stress, pattern dependencies, pad roughness, material removal rate, abrasive particles, slurry film taxonomy, chemicals effects, and pressure and velocity distributions. Only a few examine the thermal effects during the planarization process over the wafer surface. The first attempt to measure the temperature on the silicon–copper wafer was done by Sampurno et al. [121]. A direct temperature measurement set up was developed wherein a novel wafer carrier was designed such that the temperature on the back side of the wafer was measurable using a thermal imaging infra red (IR) camera. However, in all these research works, the reported temperature rise is either the average temperature on the pad surface, a predicted average temperature on the wafer surface, or the temperature rise at different isolated locations on the wafer. These works reported the overall temperature rise but did not provide information about the temperature distributions or contour plots along the substrate and pad surfaces. Since the material removal rate during copper CMP is so sensitive to temperature, temperature distributions over the entire wafer will significantly

affect the uniformity of material removal at the substrate surface. Understanding the temperature profile will decrease the with–in–wafer non–uniformity and therefore improving the yield by minimizing the number of faulty dies.

The activation energy of the copper oxidation reaction in the slurry is very low [122, 123]. Heat dissipation due to friction can result in a temperature rise at the interface and a rise of about 10 K at the polishing interface; it is high enough to double the removal rate during copper polishing [124, 125]. Also, it has been noted that a change of 1 K can affect the process removal rate during polishing by 7% [124]. Fractions of heat generated at the interface are either conducted to the wafer and pad, or convected away by the slurry, which acts as a coolant at the interface. The thermal aspect of CMP even though it is a significant factor that affects the process output, has not been researched as extensively as other parameters like pressure, velocity, slurry flow rate, and chemical aspects.

Research work on polishing pads during the interlayer dielectric (ILD) and metal polishing processes that includes the removal rate dependence on temperature and the effect of slurry flow rate on wafer and pad temperature rise, etc., has been carried out in the recent past to understand the role of temperature at the interface on CMP performance [124, 126–129]. Borucki et al. [127, 128] developed a thermal model for ILD polishing and then modified it slightly to get a model for copper CMP, which was validated by comparing with temperature measurements on the pad during metal CMP. They developed a theoretical understanding of the thermal aspects in their research and predicted the temperature on the pad for the initial stages (first 60 seconds) of polishing by evaluating the model based on transient heat transfer mechanism. White et al., [129]

have modeled the dynamic thermal behavior, which explains the energy exchange between the pad and slurry. Heat accumulation in the pad and the convection of heat to the slurry were explained in their research work. In addition, a transient thermal model was proposed to explain the initial behavior observed during CMP. Sorooshian et al. [130] investigated the effect of heat generation and thermal inputs on the frictional characteristics of interlayer dielectric (ILD) and copper CMP processes. Their coefficient of friction results indicated an increasing trend for ILD and copper polishing temperature. The dynamic mechanical analysis of the polishing pads revealed links between the softening effects of the pad, with rising temperatures, and the increment of shear forces resulting from the contact of the pad and wafer during polishing. Additional research works on thermal aspects that used the temperature change as an end–point detection, and experimental works that involved the temperature rise on polishing pad [131–133], can also be found in the literature.

However, infrared red (IR) experiments and the presented numerical results showed that thermal behavior of the slurry around the carrier and across the pad wafer interface is still a complex and dynamic process. The temperature profiles on the pad and wafer surfaces as a function of radius under the influence parameters like slurry flow rate, pad and carrier spinning rates, slurry film thickness, and polishing pressure will provide valuable insight into the extent of temperature rise at different locations on the wafer.

Chapter 3 Mathematical Models and Computation

3.1 Free Liquid Jet Impingement Model

The physical problem corresponds to an axis–symmetric liquid jet that impinges on a solid spinning disk, as shown in figure 3.1. The free jet discharges from the nozzle and impinges perpendicularly at the center of the top surface of the disk while the bottom surface is subjected to a constant heat flux. The present study considered an incompressible, Newtonian, and axis–symmetric flow under a steady state condition.

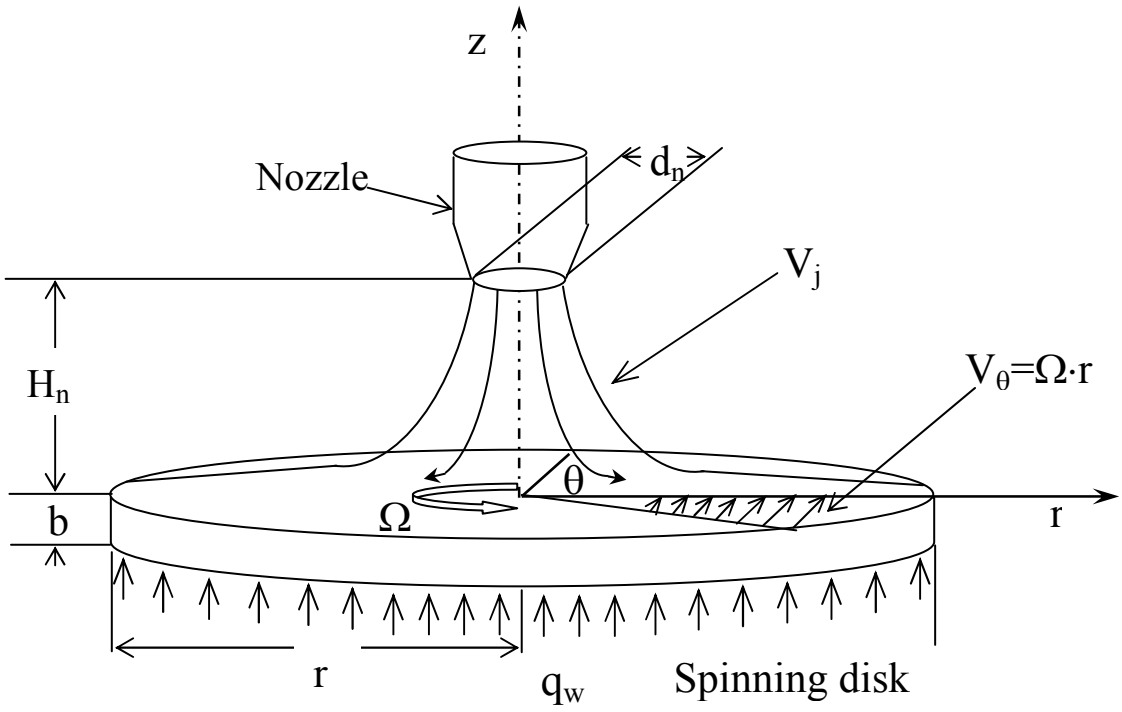

Figure 3.1 Three dimensional schematic of axis–symmetric free liquid jet impingement on a uniformly heated spinning disk.

Fluid properties for H_2O, NH_3, MIL–7808, and FC–77 were obtained from Bejan [134], Brady vendor, and 3M Specialty Fluids respectively. The fluid properties such as density, viscosity, thermal conductivity, and specific are assumed to be constant for the temperature range encountered in the system. The initial jet flow temperature condition of Ammonia was set to a lower value due to the feasibility of the fluid to remains in the liquid state during the process at normal atmospheric pressure conditions. In terms of MIL–7808 the initial temperature value or jet flow conditions was set to a hotter temperature to reduce the viscosity effect of the fluid and prevent any clogging issues on such small jets or nozzle to target spacing ratios. The thermo–physical properties of the solid materials used for the numerical analysis are assumed to remain constant over the working temperature range, as shown in Table 3.1.

Table 3.1 Constant thermo–physical properties used for computational analysis.

Material	Reference Temperature T(K)	Density $\rho(kg/m^3)$	Dynamic viscosity μ (kg/m s)	Pr	Conductivity k(W/mK)	Specific Heat C_p (J/kgK)
Constantan	303	8,922	—	—	22.7	410
Copper	303	8,954	—	—	386	383.1
Silicon	303	2,330	—	—	140	712
Aluminum	303	2700	—	—	202.4	900
Silver	300	10,500	—	—	429	235
Water	310	996	$798x10^{-6}$	5.49	0.615	4,179
Ammonia	273	500	$87x10^{-6}$	1.29	0.3682	5,460
MIL–7808	375	915	0.0082	124.44	0.1423	2,159
FC–77	310	1,780	0.001424	23.66	0.063	1,047

3.1.1 Governing Equations and Boundary Conditions: Steady State Cooling of Spinning Target

Due to rotational symmetry of the problem the $\partial/\partial\theta$ terms could be omitted. The equations describing the conservation of mass, momentum (r,θ and z directions respectively), and energy can be written as Schlichting [135]:

$$\frac{\partial V_r}{\partial r}+\frac{V_r}{r}+\frac{\partial V_z}{\partial z}=0 \tag{3.1.1}$$

$$V_r\frac{\partial V_r}{\partial r}-\frac{V_\theta^2}{r}+V_z\frac{\partial V_r}{\partial z}=-\frac{1}{\rho_f}\frac{\partial p}{\partial r}+\nu_f\left[\frac{\partial^2 V_r}{\partial r^2}+\frac{1}{r}\frac{\partial V_r}{\partial r}+\frac{\partial^2 V_r}{\partial z^2}-\frac{V_r}{r^2}\right] \tag{3.1.2}$$

$$V_r\frac{\partial V_\theta}{\partial r}+\frac{V_r V_\theta}{r}+V_z\frac{\partial V_\theta}{\partial z}=\nu_f\left[\frac{\partial^2 V_\theta}{\partial r^2}+\frac{1}{r}\frac{\partial V_\theta}{\partial r}+\frac{\partial^2 V_\theta}{\partial z^2}-\frac{V_\theta}{r^2}\right] \tag{3.1.3}$$

$$V_r\frac{\partial V_z}{\partial r}+V_z\frac{\partial V_z}{\partial z}=-g-\frac{1}{\rho_f}\frac{\partial p}{\partial z}+\nu_f\left[\frac{\partial^2 V_z}{\partial r^2}+\frac{1}{r}\frac{\partial V_z}{\partial r}+\frac{\partial^2 V_z}{\partial z^2}\right] \tag{3.1.4}$$

$$V_r\frac{\partial T_f}{\partial r}+V_z\frac{\partial T_f}{\partial z}=\alpha_f\left(\frac{1}{r}\frac{\partial}{\partial r}\left(r\frac{\partial T_f}{\partial r}\right)+\frac{\partial^2 T_f}{\partial z^2}\right) \tag{3.1.5}$$

The variation of thermal conductivity of solids with temperature encountered in the problem was not significant. Therefore, the conservation of energy inside the solid can be characterized by the following equation:

$$\frac{\partial^2 T_s}{\partial r^2}+\frac{1}{r}\left(\frac{\partial T_s}{\partial r}\right)+\frac{\partial^2 T_s}{\partial z^2}=0 \tag{3.1.6}$$

The following boundary conditions were used to complete the physical problem formulation.

$$\text{At}\quad r=0,\ -b\le z\le 0:\frac{\partial T_s}{\partial r}=0 \tag{3.1.7}$$

$$\text{At } r = 0,\ 0 \le z \le H_n : V_\theta = V_r = 0, \frac{\partial V_z}{\partial r} = 0, \frac{\partial T_f}{\partial r} = 0 \tag{3.1.8}$$

$$\text{At } r = r_d,\ -b \le z \le 0 : \frac{\partial T_s}{\partial r} = 0 \tag{3.1.9}$$

$$\text{At } r = r_d,\ 0 \le z \le \delta :\ p = p_{atm} \tag{3.1.10}$$

$$\text{At } z = -b,\ 0 \le r \le r_d : -k_s \frac{\partial T_s}{\partial z} = q_w \tag{3.1.11}$$

$$\text{At } z = 0,\ 0 \le r \le r_d : V_\theta = \Omega \cdot r, V_r = V_z = 0, T_s = T_f, k_s \frac{\partial T_s}{\partial z} = k_f \frac{\partial T_f}{\partial z} \tag{3.1.12}$$

$$\text{At } z = H_n,\ 0 \le r \le d_n/2 : V_z = -V_j, V_r = V_\theta = 0, T_f = T_j \tag{3.1.13}$$

The boundary condition at the free surface can be expressed as:

$$\text{At } z = \delta,\ d_n/2 \le r \le r_d$$

$$\frac{d\delta}{dr} = \frac{V_z}{V_r}, p = p_{atm} - \frac{\sigma \frac{d^2\delta}{dr^2}}{\left[1 + \left(\frac{d\delta}{dr}\right)^2\right]^{3/2}}, \frac{\partial V_s}{\partial n} = 0, \frac{\partial T_f}{\partial n} = 0 \tag{3.1.14}$$

where V_s is the fluid velocity component along the free surface and n is the coordinate normal to the free surface. The boundary conditions at the free surface $d_n/2 \le r \le r_d$ include the kinematic condition and balance of normal and shear stresses. The kinematic condition relates the velocity components to local slope of the free surface. The normal stress balance takes into account the effects of surface tension. In the absence of any significant resistance from the ambient air, the shear stress encountered at the free surface is essentially zero. Similarly, a negligible heat transfer results in zero temperature gradient at the free surface. The local and average heat transfer coefficients can be defined as:

$$h = -\frac{k_s}{z_{int} - z_1} \cdot \left(\frac{T_{int} - T_1}{T_{int} - T_j} \right) \tag{3.1.15}$$

$$h_{av} = \frac{2}{r_d{}^2 \cdot \left(\overline{T}_{int} - T_j \right)} \int_0^{r_d} hr \left(T_{int} - T_j \right) dr \tag{3.1.16}$$

where $\overline{T}_{int}$ is the average temperature at the solid–liquid interface. The local and average Nusselt numbers are calculated according to the following expressions:

$$Nu = \frac{h \cdot d_n}{k_f} \tag{3.1.17}$$

$$Nu_{av} = \frac{h_{av} \cdot d_n}{k_f} \tag{3.1.18}$$

3.1.2 Governing Equations and Boundary Conditions: Transient Cooling of Spinning Target

At t=0, the power supply is turned on and the heat is supplied to the bottom surface of the disk starting with an isothermal solid disk and fluid flow that has been established on the disk due to jet impingement. The present study considered an incompressible, Newtonian, and axis–symmetric fluid flow. The fluid properties were dependent on temperature only. The properties of the above fluids in section 3.1 were correlated according to the following equations. For water between 300 K<T<411 K; $Cp_f = 9.5x10^{-3} \cdot T^2 - 5.93 \cdot T + 5098.1$; $k_f = -7.0x10^{-6} \cdot T^2 + 5.8x10^{-3} \cdot T - 0.4765$; $\rho_f = -2.7x10^{-3} \cdot T^2 + 1.3104 \cdot T + 848.07$; and $\ln(\mu_f) = -3.27017 - 0.0131 \cdot T$. For ammonia between 273.15 K<T<370 K; $Cp_f = 0.083 \cdot T^2 - 40.489 \cdot T + 9468$; $k_f = 1.159 - 2.30x10^{-3} \cdot T$; $\rho_f = 579.81 + 1.6858 \cdot T - 0.0054 \cdot T^2$; and $\ln(\mu_f) = -5.33914 - 0.0115 \cdot T$. For MIL–7808 between 303 K<T<470 K; $Cp_f = 903.8 + 3.332 \cdot T$; $k_f = 0.18 - 1x10^{-4} \cdot T$; $\rho_f = 1181 - 0.708 \cdot T$; and $\ln(\mu_f) = 3.2436 - 0.0229 \cdot T$.

For FC–77 between 273 K<T<380 K; Cp_f=589.2+1.554·T; k_f=0.0869–8x10^{-5}·T; ρ_f=2,507.2–2.45·T; and ln (μ_f) = –2.38271–0.0145·T. The initial jet flow temperature condition of Ammonia was set to a lower value due to the feasibility of the fluid to remains in the liquid state during the process at normal atmospheric pressure conditions. In terms of MIL–7808 the inlet jet flow temperature value was set to a hotter temperature to reduce the viscosity effect of the fluid and prevent any clogging issues on such small jets or nozzle to target spacing ratios. In these correlations, the absolute temperature T was used in K.

Due to rotational symmetry of the problem the $\partial/\partial\theta$ terms could be omitted. The equations describing the conservation of mass, momentum (r,θ and z directions respectively), and energy can be written as Burmeister [136]:

$$\frac{\partial \rho_f}{\partial t}+\frac{1}{r}\frac{\partial}{\partial r}\left(\rho_f r V_r\right)+\frac{\partial}{\partial z}\left(\rho_f V_z\right)=0 \tag{3.1.19}$$

$$\rho_f\left(\frac{\partial V_r}{\partial t}+V_r\frac{\partial V_r}{\partial r}+V_z\frac{\partial V_r}{\partial z}-\frac{V_\theta^2}{r}\right)=-\frac{\partial p}{\partial r}+$$
$$\frac{1}{r}\frac{\partial}{\partial r}\left[\frac{2}{3}\cdot\mu_f r\left(2\frac{\partial V_r}{\partial r}-\frac{V_r}{r}-\frac{\partial V_z}{\partial z}\right)\right]+\frac{\partial}{\partial z}\left[\mu_f\left(\frac{\partial V_r}{\partial z}+\frac{\partial V_z}{\partial r}\right)\right]+\frac{2}{3}\cdot\frac{\mu_f}{r}\left(\frac{\partial V_r}{\partial r}+\frac{\partial V_z}{\partial z}-\frac{2\cdot V_r}{r}\right) \tag{3.1.20}$$

$$\rho_f\left(\frac{\partial V_\theta}{\partial t}+V_r\frac{\partial V_\theta}{\partial r}+V_z\frac{\partial V_\theta}{\partial z}+\frac{V_r V_\theta}{r}\right)=\frac{1}{r^2}\frac{\partial}{\partial r}\left[r^2\mu_f\left[r\frac{\partial}{\partial r}\left(\frac{V_\theta}{r}\right)\right]\right]+\frac{\partial}{\partial z}\left[\mu_f\left(\frac{\partial V_\theta}{\partial z}\right)\right] \tag{3.1.21}$$

$$\rho_f\left(\frac{\partial V_z}{\partial t}+V_r\frac{\partial V_z}{\partial r}+V_z\frac{\partial V_z}{\partial z}\right)=-\rho_f g-\frac{\partial p}{\partial z}+\frac{1}{r}\frac{\partial}{\partial r}\left[r\mu_f\left(\frac{\partial V_r}{\partial z}+\frac{\partial V_z}{\partial r}\right)\right]+\frac{\partial}{\partial z}\left[\frac{2}{3}\mu_f\left(2\frac{\partial V_z}{\partial z}-\frac{V_r}{r}-\frac{\partial V_r}{\partial r}\right)\right] \tag{3.1.22}$$

$$\rho_f\left(\frac{\partial T_f}{\partial t}+V_r\frac{\partial\left(Cp_f T_f\right)}{\partial r}+V_z\frac{\partial\left(Cp_f T_f\right)}{\partial z}\right)=\frac{1}{r}\frac{\partial}{\partial r}\left(k_f r\frac{\partial T_f}{\partial r}\right)+\frac{\partial}{\partial z}\left(k_f\frac{\partial T_f}{\partial z}\right)+$$
$$2\cdot\mu_f\left[\left(\frac{\partial V_r}{\partial r}\right)^2+\left(\frac{V_r}{r}\right)^2+\left(\frac{\partial V_z}{\partial z}\right)^2+\frac{1}{2}\left(\frac{\partial V_\theta}{\partial r}-\frac{V_\theta}{r}\right)^2+\frac{1}{2}\left(\frac{\partial V_\theta}{\partial z}\right)^2+\frac{1}{2}\left(\frac{\partial V_r}{\partial z}+\frac{\partial V_z}{\partial r}\right)^2-\frac{1}{3}\left(\frac{\partial V_r}{\partial r}+\frac{V_r}{r}+\frac{\partial V_z}{\partial z}\right)^2\right] \tag{3.1.23}$$

The conservation of energy inside the solid can be defined as:

$$\frac{\partial T_S}{\partial t} = \alpha_S \left[\frac{\partial^2 T_S}{\partial r^2} + \frac{1}{r}\left(\frac{\partial T_S}{\partial r}\right) + \frac{\partial^2 T_S}{\partial z^2} \right] \tag{3.1.24}$$

Equations (3.1.19–3.1.24) were subjected to the boundary conditions described by equations (3.1.7–3.1.14). The solid disk was assumed to be at thermal equilibrium with jet fluid before the transient heating of the plate was turned on. The velocity field at this condition was determined by solving only the continuity and momentum equations (3.1.19–3.1.22) in the fluid region. Thus,

$$\text{At } t=0: \; T_f = T_s = T_j, \; \vec{V}_i = \vec{V}(\text{isothermal}) \tag{3.1.25}$$

To complete the mathematical formulation it is necessary to define different relevant parameters, such as local and average heat transfer coefficients, and local and average Nusselt numbers. The local and average heat transfer coefficients and Nusselt numbers can be defined according to equations (3.1.15–3.1.18).

3.2 Confined Liquid Jet Impingement Model

A three dimensional representation of the confined axial jet impinging perpendicularly on a uniformly heated spinning solid wafer corresponds to two parallel disks, as shown in figure 3.2. The liquid jet is discharged through an orifice at the center of the top disk. The remainder of the top disk acts as an insulated stationary confinement plate. The bottom disk (wafer) is subjected to a uniform rotational velocity. Heat sources are located at the bottom of the wafer producing a constant heat flux along the surface. Heat is conducted through the wafer and convected out to the fluid adjacent to the top surface of the wafer, as shown in figure 3.2. The present study considered an incompressible, Newtonian, and axis–symmetric flow under a steady state condition.

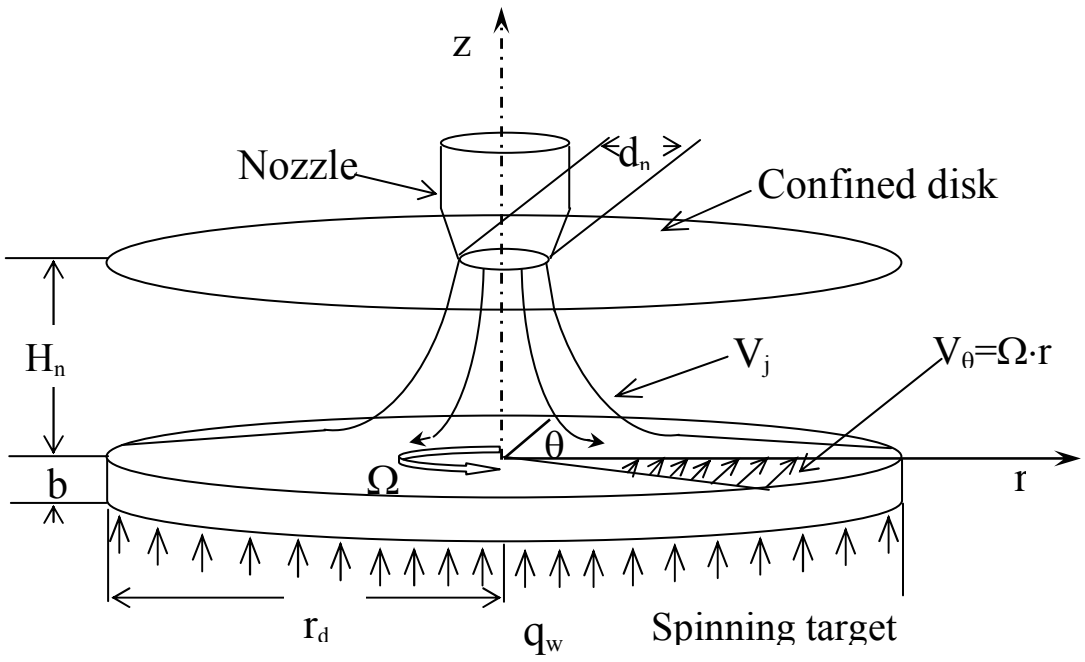

Figure 3.2 Three dimensional schematic of a confined axial jet impinging on a uniformly heated and spinning disk.

Fluid properties for H_2O, NH_3, MIL–7808, and FC–77 were obtained from Bejan (1995) [134], Brady vendor, and 3M Specialty Fluids respectively. The fluid properties were assumed to be constant for the temperature range encountered in the system, as shown in Table 3.1.

3.2.1 Governing Equations and Boundary Conditions: Steady State Cooling of Spinning Target

Due to rotational symmetry of the problem the $\partial/\partial\theta$ terms could be omitted. The equations describing the conservation of mass, momentum (r,θ and z directions respectively), and energy can be written as [135]:

$$\frac{\partial V_r}{\partial r}+\frac{V_r}{r}+\frac{\partial V_z}{\partial z}=0 \qquad (3.2.1)$$

$$V_r \frac{\partial V_r}{\partial r} - \frac{V_\theta^2}{r} + V_z \frac{\partial V_r}{\partial z} = -\frac{1}{\rho_f}\frac{\partial p}{\partial r} + \nu_f \left[\frac{\partial^2 V_r}{\partial r^2} + \frac{1}{r}\frac{\partial V_r}{\partial r} + \frac{\partial^2 V_r}{\partial z^2} - \frac{V_r}{r^2} \right] \tag{3.2.2}$$

$$V_r \frac{\partial V_\theta}{\partial r} + \frac{V_r V_\theta}{r} + V_z \frac{\partial V_\theta}{\partial z} = \nu_f \left[\frac{\partial^2 V_\theta}{\partial r^2} + \frac{1}{r}\frac{\partial V_\theta}{\partial r} + \frac{\partial^2 V_\theta}{\partial z^2} - \frac{V_\theta}{r^2} \right] \tag{3.2.3}$$

$$V_r \frac{\partial V_z}{\partial r} + V_z \frac{\partial V_z}{\partial z} = -g - \frac{1}{\rho_f}\frac{\partial p}{\partial z} + \nu_f \left[\frac{\partial^2 V_z}{\partial r^2} + \frac{1}{r}\frac{\partial V_z}{\partial r} + \frac{\partial^2 V_z}{\partial z^2} \right] \tag{3.2.4}$$

$$V_r \frac{\partial T_f}{\partial r} + V_z \frac{\partial T_f}{\partial z} = \alpha_f \left(\frac{1}{r}\frac{\partial}{\partial r}\left(r \frac{\partial T_f}{\partial r} \right) + \frac{\partial^2 T_f}{\partial z^2} \right) \tag{3.2.5}$$

The variation of thermal conductivity of solids with temperature encountered in the problem was not significant. Therefore, the conservation of energy inside the solid can be characterized by the following equation:

$$\frac{\partial^2 T_s}{\partial r^2} + \frac{1}{r}\left(\frac{\partial T_s}{\partial r} \right) + \frac{\partial^2 T_s}{\partial z^2} = 0 \tag{3.2.6}$$

To complete the set of equations to be solved, equations (3.2.1–3.2.6) were subjected to the following boundary conditions:

$$\text{At } \; r = 0, \; -b \le z \le 0 : \frac{\partial T_s}{\partial r} = 0 \tag{3.2.7}$$

$$\text{At } \; r = 0, \; 0 \le z \le H_n : V_\theta = V_r = 0, \frac{\partial V_z}{\partial r} = 0, \frac{\partial T_f}{\partial r} = 0 \tag{3.2.8}$$

$$\text{At } \; r = r_d, \; -b \le z \le 0 : \frac{\partial T_s}{\partial r} = 0 \tag{3.2.9}$$

$$\text{At } \; r = r_d, \; 0 \le z \le H_n : \; p = 0 \tag{3.2.10}$$

$$\text{At } \; z = -b, \; 0 \le r \le r_d : -k_s \frac{\partial T_s}{\partial z} = q_w \tag{3.2.11}$$

$$\text{At} \quad z = H_n, \quad 0 \le r \le d_n/2 : V_z = -V_j, V_r = V_\theta = 0, T_f = T_j \tag{3.2.12}$$

$$\text{At} \quad z = H_n, \quad d_n/2 \le r \le r_d : V_r = V_z = V_\theta = 0, \frac{\partial T_f}{\partial z} = 0 \tag{3.2.13}$$

$$\text{At} \quad z = 0, \quad 0 \le r \le r_d : V_\theta = \Omega \cdot r, V_r = V_z = 0, T_s = T_f, k_s \frac{\partial T_s}{\partial z} = k_f \frac{\partial T_f}{\partial z} \tag{3.2.14}$$

The local and average heat transfer coefficients can be defined as:

$$h = \frac{q_w}{T_{int} - T_j} \tag{3.2.15}$$

$$h_{av} = \frac{2}{r_d^2 \cdot \left(\overline{T}_{int} - T_j\right)} \int_0^{r_d} hr\left(T_{int} - T_j\right) dr \tag{3.2.16}$$

where $\overline{T}_{int}$ is the average temperature at the solid–liquid interface. The local and average Nusselt numbers are calculated according to the following expressions:

$$Nu = \frac{h \cdot d_n}{k_f} \tag{3.2.17}$$

$$Nu_{av} = \frac{h_{av} \cdot d_n}{k_f} \tag{3.2.18}$$

3.2.2 Governing Equations and Boundary Conditions: Steady State Cooling of Spinning Wall

A schematic of the physical problem is shown in figure 3.3. An axis–symmetric liquid jet is discharged through a nozzle and impinges at the center of a stationary solid disk subjected to a uniform heat flux. The top plate acts as an insulated confinement surface spinning at constant angular velocity. Heat is conducted through the disk and convected out to the fluid adjacent to the top surface of the stationary disk, as shown in

figure 3.3. The present study considered an incompressible, Newtonian, and axis–symmetric flow under a steady state condition. The variation of fluid properties with local temperature was taken into account. Due to rotational symmetry of the problem the $\partial/\partial\theta$ terms could be omitted.

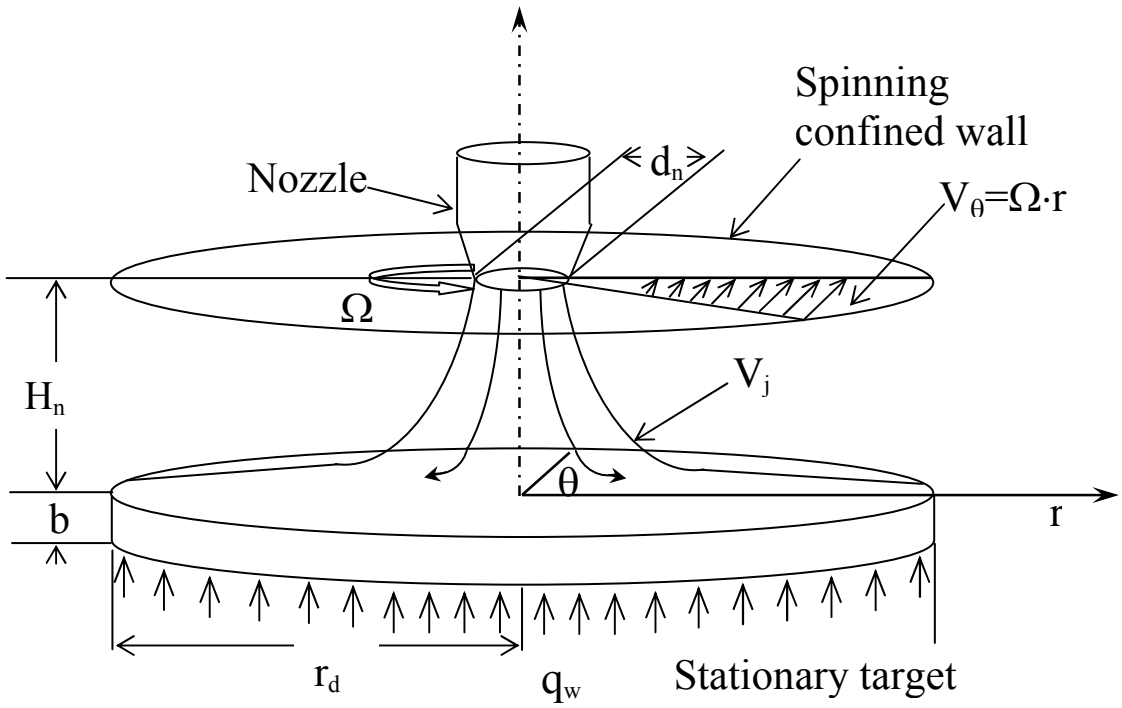

Figure 3.3 Three dimensional schematic of axis–symmetric confined spinning disk liquid jet impingement on a uniformly heated disk.

The equations describing the conservation of mass, momentum (r,θ and z directions respectively), and energy can be written as seen in [136]:

$$\frac{1}{r}\frac{\partial}{\partial r}\left(\rho_f r V_r\right)+\frac{\partial}{\partial z}\left(\rho_f V_z\right)=0 \tag{3.2.19}$$

$$\rho_f\left(V_r\frac{\partial V_r}{\partial r}+V_z\frac{\partial V_r}{\partial z}-\frac{V_\theta^2}{r}\right)=-\frac{\partial p}{\partial r}+\frac{1}{r}\frac{\partial}{\partial r}\left[\frac{2}{3}\cdot\mu_f r\left(2\frac{\partial V_r}{\partial r}-\frac{V_r}{r}-\frac{\partial V_z}{\partial z}\right)\right]$$
$$+\frac{\partial}{\partial z}\left[\mu_f\left(\frac{\partial V_r}{\partial z}+\frac{\partial V_z}{\partial r}\right)\right]+\frac{2}{3}\cdot\frac{\mu_f}{r}\left(\frac{\partial V_r}{\partial r}+\frac{\partial V_z}{\partial z}-\frac{2\cdot V_r}{r}\right) \tag{3.2.20}$$

$$\rho_f\left(V_r\frac{\partial V_\theta}{\partial r}+V_z\frac{\partial V_\theta}{\partial z}+\frac{V_r V_\theta}{r}\right)=\frac{1}{r^2}\frac{\partial}{\partial r}\left[r^2\mu_f\left[r\frac{\partial}{\partial r}\left(\frac{V_\theta}{r}\right)\right]\right]+\frac{\partial}{\partial z}\left[\mu_f\left(\frac{\partial V_\theta}{\partial z}\right)\right] \quad (3.2.21)$$

$$\rho_f\left(V_r\frac{\partial V_z}{\partial r}+V_z\frac{\partial V_z}{\partial z}\right)=-\rho_f g-\frac{\partial p}{\partial z}+\frac{1}{r}\frac{\partial}{\partial r}\left[r\mu_f\left(\frac{\partial V_r}{\partial z}+\frac{\partial V_z}{\partial r}\right)\right]+\frac{\partial}{\partial z}\left[\frac{2}{3}\mu_f\left(2\frac{\partial V_z}{\partial z}-\frac{V_r}{r}-\frac{\partial V_r}{\partial r}\right)\right] \quad (3.2.22)$$

$$\rho_f\left(V_r\frac{\partial\left(Cp_f T_f\right)}{\partial r}+V_z\frac{\partial\left(Cp_f T_f\right)}{\partial z}\right)=\frac{1}{r}\frac{\partial}{\partial r}\left(k_f r\frac{\partial T_f}{\partial r}\right)+\frac{\partial}{\partial z}\left(k_f\frac{\partial T_f}{\partial z}\right)+$$
$$2\cdot\mu_f\left[\left(\frac{\partial V_r}{\partial r}\right)^2+\left(\frac{V_r}{r}\right)^2+\left(\frac{\partial V_z}{\partial z}\right)^2+\frac{1}{2}\left(\frac{\partial V_\theta}{\partial r}-\frac{V_\theta}{r}\right)^2+\frac{1}{2}\left(\frac{\partial V_\theta}{\partial z}\right)^2+\frac{1}{2}\left(\frac{\partial V_r}{\partial z}+\frac{\partial V_z}{\partial r}\right)^2-\frac{1}{3}\left(\frac{\partial V_r}{\partial r}+\frac{V_r}{r}+\frac{\partial V_z}{\partial z}\right)^2\right] \quad (3.2.23)$$

The variation of thermal conductivity of solids with temperature is not significant. Therefore, the conservation of energy inside the solid can be characterized by the following equation:

$$\alpha_s\left[\frac{\partial^2 T_s}{\partial r^2}+\frac{1}{r}\left(\frac{\partial T_s}{\partial r}\right)+\frac{\partial^2 T_s}{\partial z^2}\right]=0 \quad (3.2.24)$$

To fulfill the physical formulation of equations (3.2.19–3.2.24) it is necessary to use the boundary conditions described by equations (3.2.7–3.2.12) and update the boundary conditions of the target and confined wall currently defined by equations (3.2.25–3.2.26).

$$\text{At}\quad z=H_n,\quad d_n/2\le r\le r_d: V_\theta=\Omega\cdot r, V_r=V_z=0,\frac{\partial T_f}{\partial z}=0 \quad (3.2.25)$$

$$\text{At}\quad z=0,\quad 0\le r\le r_d: V_r=V_z=V_\theta=0, T_s=T_f, k_s\frac{\partial T_s}{\partial z}=k_f\frac{\partial T_f}{\partial z} \quad (3.2.26)$$

The mathematical formulation was completed with the definition of relevant parameters, such as local and average heat transfer coefficients, and local and average Nusselt numbers according to equations (3.2.15–3.2.18).

3.3 Partially–confined Liquid Jet Impingement Model

An axis–symmetric liquid jet is discharged through a nozzle and impinges at the center of the top surface of a solid circular disk or wafer spinning with a uniform angular velocity about the z–axis.

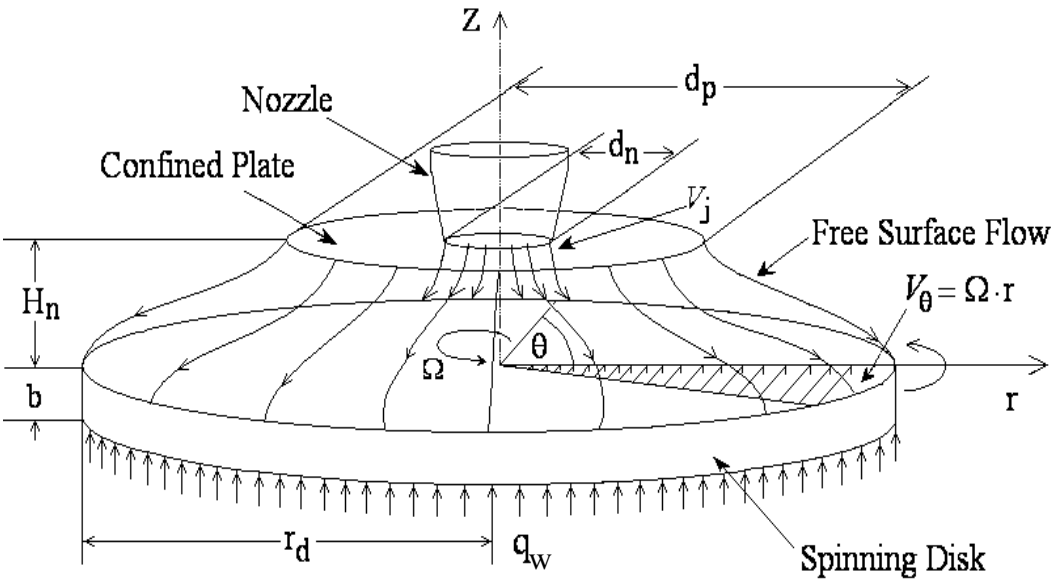

Figure 3.4 Three dimensional schematic of axis–symmetric partially–confined liquid jet impingement on a uniformly heated spinning disk.

The insulated confinement plate attached to the nozzle is smaller in diameter than the disk which allows the formation of free surface flow when the fluid exits the confined region, as shown in figure 3.4. The present study considered an incompressible, Newtonian, and axis–symmetric laminar flow under a steady state condition. The variation of fluid properties with local temperature was taken into account.

3.3.1 Governing Equations and Boundary Conditions: Steady State Cooling of Spinning Target

Due to rotational symmetry of the problem the $\partial/\partial\theta$ terms could be omitted. The equations describing the conservation of mass, momentum (r,θ and z directions respectively), and energy can be written as [136]:

$$\frac{1}{r}\frac{\partial}{\partial r}\left(\rho_f r V_r\right)+\frac{\partial}{\partial z}\left(\rho_f V_z\right)=0 \tag{3.3.1}$$

$$\rho_f\left(V_r\frac{\partial V_r}{\partial r}+V_z\frac{\partial V_r}{\partial z}-\frac{V_\theta^2}{r}\right)=-\frac{\partial p}{\partial r}+\frac{1}{r}\frac{\partial}{\partial r}\left[\frac{2}{3}\cdot\mu_f r\left(2\frac{\partial V_r}{\partial r}-\frac{V_r}{r}-\frac{\partial V_z}{\partial z}\right)\right]$$
$$+\frac{\partial}{\partial z}\left[\mu_f\left(\frac{\partial V_r}{\partial z}+\frac{\partial V_z}{\partial r}\right)\right]+\frac{2}{3}\cdot\frac{\mu_f}{r}\left(\frac{\partial V_r}{\partial r}+\frac{\partial V_z}{\partial z}-\frac{2\cdot V_r}{r}\right) \tag{3.3.2}$$

$$\rho_f\left(V_r\frac{\partial V_\theta}{\partial r}+V_z\frac{\partial V_\theta}{\partial z}+\frac{V_r V_\theta}{r}\right)=\frac{1}{r^2}\frac{\partial}{\partial r}\left[r^2\mu_f\left[r\frac{\partial}{\partial r}\left(\frac{V_\theta}{r}\right)\right]\right]+\frac{\partial}{\partial z}\left[\mu_f\left(\frac{\partial V_\theta}{\partial z}\right)\right] \tag{3.3.3}$$

$$\rho_f\left(V_r\frac{\partial V_z}{\partial r}+V_z\frac{\partial V_z}{\partial z}\right)=-\rho_f g-\frac{\partial p}{\partial z}+\frac{1}{r}\frac{\partial}{\partial r}\left[r\mu_f\left(\frac{\partial V_r}{\partial z}+\frac{\partial V_z}{\partial r}\right)\right]+\frac{\partial}{\partial z}\left[\frac{2}{3}\mu_f\left(2\frac{\partial V_z}{\partial z}-\frac{V_r}{r}-\frac{\partial V_r}{\partial r}\right)\right] \tag{3.3.4}$$

$$\rho_f\left(V_r\frac{\partial\left(Cp_f T_f\right)}{\partial r}+V_z\frac{\partial\left(Cp_f T_f\right)}{\partial z}\right)=\frac{1}{r}\frac{\partial}{\partial r}\left(k_f r\frac{\partial T_f}{\partial r}\right)+\frac{\partial}{\partial z}\left(k_f\frac{\partial T_f}{\partial z}\right)+$$
$$2\cdot\mu_f\left[\left(\frac{\partial V_r}{\partial r}\right)^2+\left(\frac{V_r}{r}\right)^2+\left(\frac{\partial V_z}{\partial z}\right)^2+\frac{1}{2}\left(\frac{\partial V_\theta}{\partial r}-\frac{V_\theta}{r}\right)^2+\frac{1}{2}\left(\frac{\partial V_\theta}{\partial z}\right)^2+\frac{1}{2}\left(\frac{\partial V_r}{\partial z}+\frac{\partial V_z}{\partial r}\right)^2-\frac{1}{3}\left(\frac{\partial V_r}{\partial r}+\frac{V_r}{r}+\frac{\partial V_z}{\partial z}\right)^2\right] \tag{3.3.5}$$

The conservation of energy inside the solid can be defined as:

$$\alpha_s\left[\frac{\partial^2 T_s}{\partial r^2}+\frac{1}{r}\left(\frac{\partial T_s}{\partial r}\right)+\frac{\partial^2 T_s}{\partial z^2}\right]=0 \tag{3.3.6}$$

The following boundary conditions were used.

$$\text{At}\quad r=0,\ -b\le z\le 0:\frac{\partial T_s}{\partial r}=0 \tag{3.3.7}$$

$$\text{At } r = 0,\ 0 \le z \le H_n : V_\theta = V_r = 0, \frac{\partial V_z}{\partial r} = 0, \frac{\partial T_f}{\partial r} = 0 \tag{3.3.8}$$

$$\text{At } r = r_d,\ -b \le z \le 0 : \frac{\partial T_s}{\partial r} = 0 \tag{3.3.9}$$

$$\text{At } r = r_d,\ 0 \le z \le \delta :\ p = p_{atm} \tag{3.3.10}$$

$$\text{At } z = -b,\ 0 \le r \le r_d : -k_s \frac{\partial T_s}{\partial z} = q_w \tag{3.3.11}$$

$$\text{At } z = H_n,\ 0 \le r \le d_n/2 : V_z = -V_j, V_r = V_\theta = 0, T_f = T_j \tag{3.3.12}$$

$$\text{At } z = H_n,\ d_n/2 \le r \le r_p : V_r = V_z = V_\theta = 0, \frac{\partial T_f}{\partial z} = 0 \tag{3.3.13}$$

$$\text{At } z = 0,\ 0 \le r \le r_d : V_\theta = \Omega \cdot r, V_r = V_z = 0, T_s = T_f, k_s \frac{\partial T_s}{\partial z} = k_f \frac{\partial T_f}{\partial z} \tag{3.3.14}$$

The boundary condition at the free surface can be expressed as:

$$\text{At } z = \delta,\ r_p \le r \le r_d :$$

$$\frac{d\delta}{dr} = \frac{V_z}{V_r}, p = p_{atm} - \frac{\sigma \frac{d^2\delta}{dr^2}}{\left[1 + \left(\frac{d\delta}{dr}\right)^2\right]^{3/2}}, \frac{\partial V_s}{\partial n} = 0, \frac{\partial T_f}{\partial n} = 0 \tag{3.3.15}$$

where V_S is the fluid velocity component along the free surface and n is the coordinate normal to the free surface. The boundary conditions at the free surface were obtained by satisfying the kinematic condition relating the slope of the free surface with velocity components as well as from the balance of normal and shear stresses at the free surface. For steady flow of a Newtonian fluid normal stress balance essentially reduces to an

equation relating the pressure and surface tension as shown by White [137]. The shear stress encountered from the ambient gaseous medium is expected to be negligible. Similarly, the heat transfer from the free surface to the ambient gas is also assumed to be negligible. Relevant parameters, such as local and average heat transfer coefficients and local and average Nusselt numbers are defined according to equations (3.2.15–3.2.18) to complete the mathematical formulation.

3.3.2 Governing Equations and Boundary Conditions: Steady State Cooling of Co–Rotating Target and Confined Wall

An axis–symmetric liquid jet is discharged through a nozzle and impinges at the center of a solid uniformly heated circular disk that spins at constant angular velocity about the z–axis, as shown in figure 3.5. The insulated top plate acts as a confined spinning wall that ends allowing the exposure of the fluid to a free surface boundary condition.

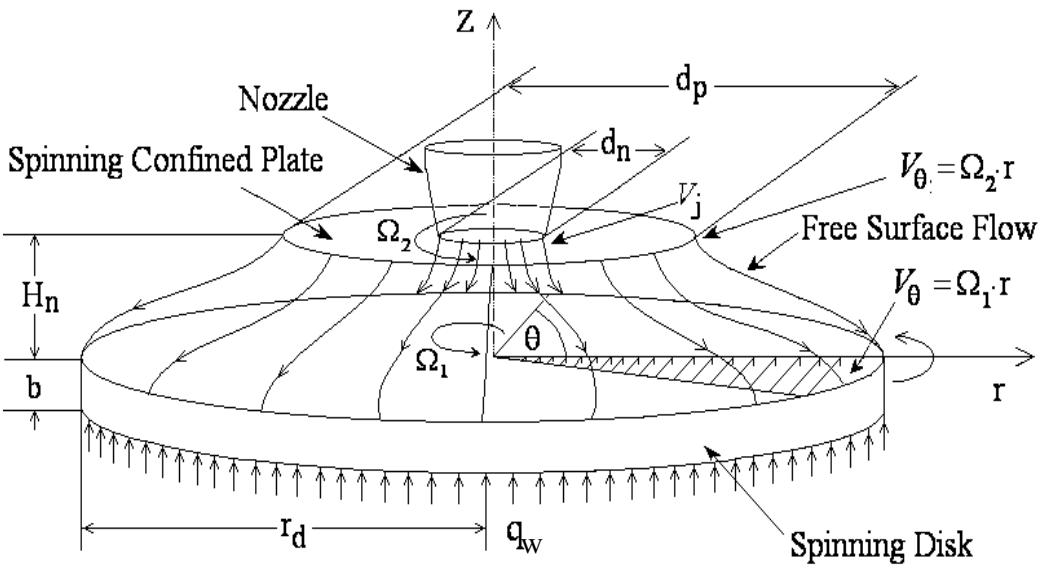

Figure 3.5 Three dimensional schematic of axis–symmetric partially–confined liquid jet impingement on a uniformly heated disk with two spinning boundaries.

The present study considered an incompressible, Newtonian, and axis–symmetric flow under a steady state condition. The variation of fluid properties with local temperature was taken into account. Fluid properties for H_2O, NH_3, MIL–7808, and FC–77 were obtained from Bejan [134] and Bula [138]. The physical formulation of the above problem is defined in section 3.3.1. The equations that described the conservation of mass, momentum (3.3.1–3.3.6) and boundary conditions (3.3.7 through 3.3.12, and 3.3.15) remain the same. The new boundary conditions at the target and confined wall were defined by the following equations:

$$\text{At} \quad z = H_n, \quad d_n/2 \le r \le r_p : V_r = V_z = 0, V_\theta = \Omega_2 \cdot r, \quad \frac{\partial T_f}{\partial z} = 0 \tag{3.3.16}$$

$$\text{At} \quad z = 0, \quad 0 \le r \le r_d : V_r = V_z = 0, V_\theta = \Omega_1 \cdot r, T_s = T_f, \quad k_s \frac{\partial T_s}{\partial z} = k_f \frac{\partial T_f}{\partial z} \tag{3.3.17}$$

The mathematical formulation was completed by the definition of relevant parameters, such as local and average heat transfer coefficients, and local and average Nusselt numbers. In addition, the local and average heat transfer coefficients and Nusselt numbers are defined according to equations (3.2.15–3.2.18).

3.3.3 Governing Equations and Boundary Conditions: Transient Cooling of Spinning Target

The transient conjugate heat transfer of both solid and fluid regions of a partially–confined liquid jet impinging on a rotating and uniformly heated solid disk of finite thickness and radius are examined as part of this study. A constant heat flux was imposed at the bottom surface of the solid disk at t=0 and heat transfer was monitored for the entire duration of the transient until the steady state condition was reached.

After an isothermal fluid flow has been established on the disk, at t=0, the power source is turned on to deliver a uniform heat flux at the bottom surface of the disk while the confinement plate is kept insulated. Due to symmetry of the problem about the axis of rotation, all $\partial/\partial\theta$ terms can be dropped out. The equations for the conservation of mass, momentum (r,θ and z directions respectively), and energy for incompressible flow of a Newtonian fluid with temperature dependent properties can be written as [136]:

$$\frac{\partial \rho_f}{\partial t}+\frac{1}{r}\frac{\partial}{\partial r}\left(\rho_f r V_r\right)+\frac{\partial}{\partial z}\left(\rho_f V_z\right)=0 \tag{3.3.18}$$

$$\rho_f\left(\frac{\partial V_r}{\partial t}+V_r\frac{\partial V_r}{\partial r}+V_z\frac{\partial V_r}{\partial z}-\frac{V_\theta^2}{r}\right)=-\frac{\partial p}{\partial r}+$$
$$\frac{1}{r}\frac{\partial}{\partial r}\left[\frac{2}{3}\cdot\mu_f r\left(2\frac{\partial V_r}{\partial r}-\frac{V_r}{r}-\frac{\partial V_z}{\partial z}\right)\right]+\frac{\partial}{\partial z}\left[\mu_f\left(\frac{\partial V_r}{\partial z}+\frac{\partial V_z}{\partial r}\right)\right]+\frac{2}{3}\cdot\frac{\mu_f}{r}\left(\frac{\partial V_r}{\partial r}+\frac{\partial V_z}{\partial z}-\frac{2\cdot V_r}{r}\right) \tag{3.3.19}$$

$$\rho_f\left(\frac{\partial V_\theta}{\partial t}+V_r\frac{\partial V_\theta}{\partial r}+V_z\frac{\partial V_\theta}{\partial z}+\frac{V_r V_\theta}{r}\right)=\frac{1}{r^2}\frac{\partial}{\partial r}\left[r^2\mu_f\left[r\frac{\partial}{\partial r}\left(\frac{V_\theta}{r}\right)\right]\right]+\frac{\partial}{\partial z}\left[\mu_f\left(\frac{\partial V_\theta}{\partial z}\right)\right] \tag{3.3.20}$$

$$\rho_f\left(\frac{\partial V_z}{\partial t}+V_r\frac{\partial V_z}{\partial r}+V_z\frac{\partial V_z}{\partial z}\right)=-\rho_f g-\frac{\partial p}{\partial z}+\frac{1}{r}\frac{\partial}{\partial r}\left[r\mu_f\left(\frac{\partial V_r}{\partial z}+\frac{\partial V_z}{\partial r}\right)\right]+\frac{\partial}{\partial z}\left[\frac{2}{3}\mu_f\left(2\frac{\partial V_z}{\partial z}-\frac{V_r}{r}-\frac{\partial V_r}{\partial r}\right)\right] \tag{3.3.21}$$

$$\rho_f\left(\frac{\partial T_f}{\partial t}+V_r\frac{\partial\left(Cp_f T_f\right)}{\partial r}+V_z\frac{\partial\left(Cp_f T_f\right)}{\partial z}\right)=\frac{1}{r}\frac{\partial}{\partial r}\left(k_f r\frac{\partial T_f}{\partial r}\right)+\frac{\partial}{\partial z}\left(k_f\frac{\partial T_f}{\partial z}\right)+$$
$$2\cdot\mu_f\left[\left(\frac{\partial V_r}{\partial r}\right)^2+\left(\frac{V_r}{r}\right)^2+\left(\frac{\partial V_z}{\partial z}\right)^2+\frac{1}{2}\left(\frac{\partial V_\theta}{\partial r}-\frac{V_\theta}{r}\right)^2+\frac{1}{2}\left(\frac{\partial V_\theta}{\partial z}\right)^2+\frac{1}{2}\left(\frac{\partial V_r}{\partial z}+\frac{\partial V_z}{\partial r}\right)^2-\frac{1}{3}\left(\frac{\partial V_r}{\partial r}+\frac{V_r}{r}+\frac{\partial V_z}{\partial z}\right)^2\right] \tag{3.3.22}$$

The conservation of energy inside the solid can be defined as:

$$\frac{\partial T_s}{\partial t}=\alpha_s\left[\frac{\partial^2 T_s}{\partial r^2}+\frac{1}{r}\left(\frac{\partial T_s}{\partial r}\right)+\frac{\partial^2 T_s}{\partial z^2}\right] \tag{3.3.23}$$

Equations (3.3.18–3.3.23) are subjected to the boundary conditions described by equations (3.3.7–3.3.15). The solid disk was assumed to be at thermal equilibrium with

jet fluid before the transient heating of the plate was turned on. The velocity field at this condition was determined by solving only the continuity and momentum equations (3.3.18–3.3.21) in the fluid region. Thus,

$$\text{At } t=0:\ T_f=T_s=T_j,\ \bar{V}_i=\vec{V}(\text{isothermal}) \tag{3.3.24}$$

To complete the mathematical formulation it is necessary to define different relevant parameters, such as local and average heat transfer coefficients, and local and average Nusselt numbers. In addition, the local and average heat transfer coefficients and Nusselt numbers are defined according to equations (3.2.15–3.2.18).

3.4 Three Dimensional Chemical Mechanical Polishing Model

The controlled volume under study of the CMP process, sketched in figure 3.6, consists of the wafer surface, slurry interface and polishing pad subjected to a variable heat flux boundary condition at its polished surface. The variable heat flux is driven by the pad coefficient of friction, the down force pressure, the radial distance measure from the pad center and the relative spinning rate of the pad and carrier ($q_w=\mu_{fr}\cdot P\cdot V\theta_{pc}$).

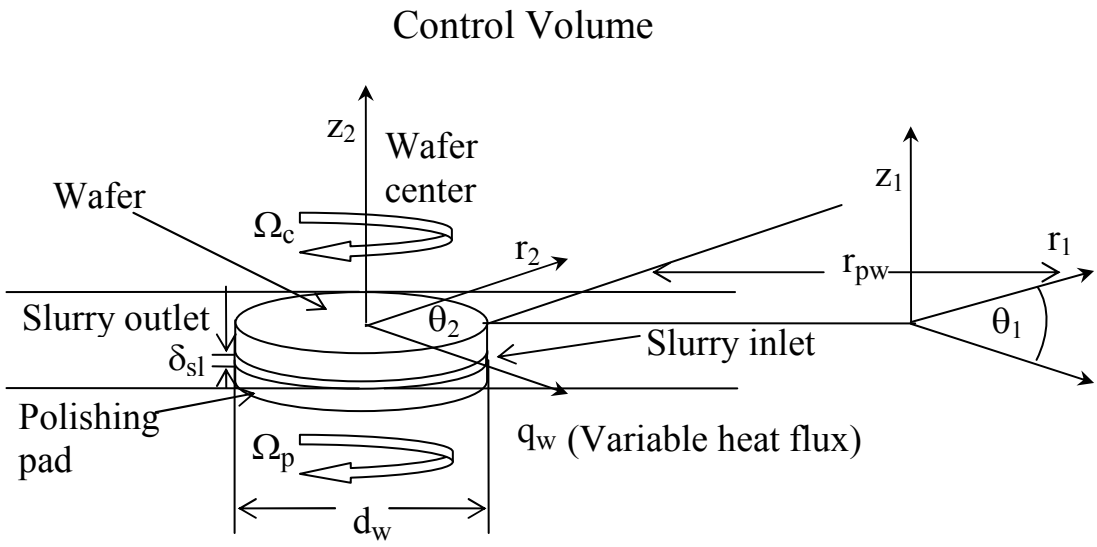

Figure 3.6 Three dimensional CMP control volume outline.

Figure 3.6 shows that the inlet of the slurry (alumina) covers half of the wafer circumference, and the other half is considered as being the flow outlet. The slurry flow is driven to the inlet by the spinning rate of the platen that holds the polishing pad. The centrifugal motion assumption of the slurry is valid for the closeness of the boundary layer thickness of the flow that is going to pass through a confined area with a magnitude of the micrometer scale size. This observation is in agreement with work done by Lallave and Rahman [103], and Brodersen et al. [38] that studied the characteristics of a predominant rotational driven flow versus a jet impingement momentum flow. A contact area of a flat pad surface was used as part of the control volume on this model. The gravity and surface tension effects and angular acceleration of the platen was taken into account as part of the slurry film thickness description.

The present model ignores the non–uniformity of the slurry particles and their height distribution, including the heat transfer effect during conditioning and all losses of heat along the wafer retaining ring. The offset thickness between the ring and wafer is not taken into account as part of the CMP model set up. As part of the numerical analysis and experimental set up, this model starts with an isothermal slurry–to–substrate boundary condition and a thin layer of slurry that has been established on the pad as part of the polishing process. In addition, a variable heat flux is input into the numerical problem as the product of the mechanical abrasion of the pad, and chemical interactions of the slurry at the substrate surface.

3.4.1 Governing Equations and Boundary Conditions: Steady State

The Navier–Stokes equations were used to simulate the fluid mechanics of an incompressible (constant–density and viscosity) Newtonian flow that reaches the steady

state condition throughout the CMP process. The fluid properties used for the numerical simulation such as density, viscosity, thermal conductivity, and specific heat are assumed to remain constant over the working temperature range. Detailed explanations on the formulation of the governing equations describing the conservation of mass, momentum (r,θ, and z directions respectively), and energy using cylindrical coordinate system can be found in [136]:

$$\frac{\partial V_r}{\partial r}+\frac{V_r}{r}+\frac{1}{r}\frac{\partial V_\theta}{\partial \theta}+\frac{\partial V_z}{\partial z}=0 \tag{3.4.1}$$

$$V_r\frac{\partial V_r}{\partial r}+\frac{V_\theta}{r}\frac{\partial V_r}{\partial \theta}+V_z\frac{\partial V_r}{\partial z}-\frac{V_\theta^2}{r}=-\frac{1}{\rho_{sl}}\frac{\partial p}{\partial r}+\nu_{sl}\left[\frac{\partial^2 V_r}{\partial r^2}+\frac{1}{r}\frac{\partial V_r}{\partial r}+\frac{1}{r^2}\frac{\partial^2 V_r}{\partial \theta^2}+\frac{\partial^2 V_r}{\partial z^2}-\frac{V_r}{r^2}-\frac{2}{r^2}\frac{\partial V_\theta}{\partial \theta}\right] \tag{3.4.2}$$

$$V_r\frac{\partial V_\theta}{\partial r}+\frac{V_r V_\theta}{r}+\frac{V_\theta}{r}\frac{\partial V_\theta}{\partial \theta}+V_z\frac{\partial V_\theta}{\partial z}=-\frac{1}{\rho_{sl}}\frac{\partial p}{\partial \theta}+\nu_{sl}\left[\frac{\partial^2 V_\theta}{\partial r^2}+\frac{1}{r}\frac{\partial V_\theta}{\partial r}+\frac{1}{r^2}\frac{\partial^2 V_\theta}{\partial \theta^2}+\frac{\partial^2 V_\theta}{\partial z^2}+\frac{2}{r^2}\frac{\partial V_r}{\partial \theta}-\frac{V_\theta}{r^2}\right] \tag{3.4.3}$$

$$V_r\frac{\partial V_z}{\partial r}+\frac{V_\theta}{r}\frac{\partial V_z}{\partial \theta}+V_z\frac{\partial V_z}{\partial z}=-g-\frac{1}{\rho_{sl}}\frac{\partial p}{\partial z}+\nu_{sl}\left[\frac{\partial^2 V_z}{\partial r^2}+\frac{1}{r}\frac{\partial V_z}{\partial r}+\frac{1}{r^2}\frac{\partial^2 V_z}{\partial \theta^2}+\frac{\partial^2 V_z}{\partial z^2}\right] \tag{3.4.4}$$

The Navier–Stokes equations (3.4.2–3.4.4) are useful for the hydrodynamic regime where the combined roughness (s), of the two opposing surfaces is smaller than the film thickness, h_{sl}, and there is little or no contact between the asperities of the surfaces. For the slurry film and roughness ratio (h_{sl}/s) >> 3, the roughness effects are not important and the smooth film Navier–Stokes equations are sufficiently accurate. When the slurry film and roughness ratio (h_{sl}/s) are equal to 3, the roughness effects become important. When h_{sl}/s < 3, contacts between asperities from the opposing surfaces can occur and the system goes into the mixed lubrication regime. In CMP, the surfaces involved are a relatively flat and rigid wafer beneath a rough and soft pad. Another sign

of intimate wafer and pad contact is when pad glazing is observed. Thus, a mixed lubrication approach has to be taken [139].

The energy equation for incompressible slurry properties and negligible viscous dissipation can be written as:

$$V_r \frac{\partial T_{sl}}{\partial r} + \frac{V_\theta}{r} \frac{\partial T_{sl}}{\partial \theta} + V_z \frac{\partial T_{sl}}{\partial z} = \alpha_{sl} \left(\frac{1}{r} \frac{\partial}{\partial r} \left(r \frac{\partial T_{sl}}{\partial r} \right) + \frac{1}{r^2} \frac{\partial^2 T_{sl}}{\partial \theta^2} + \frac{\partial^2 T_{sl}}{\partial z^2} \right) \tag{3.4.5}$$

The energy transferred in the controlled volume is due to mechanical abrasion of the pad and slurry particles on the wafer surface, and chemical energy associated with slurry chemistry and enthalpy. For neutral slurries, the major chemical energy source is the enthalpy. In a good number of thermal systems, there exist heat loss mechanisms that can be neglected as part of the analysis. The thermal losses from the rubber and plastic bladder between the wafer and steel polishing carrier were neglected due to their lower thermal conductivity and insulator properties. As we know, most of the pads used for experimentation, like IC–1,000 and FX–9, are made of polyurethane, a material considered to be a thermal insulator as such. Therefore, we neglect any loss from conduction through the pad as part of our numerical analysis.

The above analysis concentrates on the heat loss mechanisms associated with download pressure, slurry flow rate, relative spinning velocity of pad and wafer, and slurry film thickness under different coefficients of friction. To define the problem completely, appropriate boundary conditions were required on all boundaries of the computational domain. The boundary conditions at the inlet, outlet, wafer surface, and pad surface respectively have the following form:

$$\text{At } -(r_w + r_{pw}) \le r_1 \le -r_{pw},\ -h_{sl} \le z \le 0, -\frac{\pi}{2} \le \theta \le \frac{\pi}{2} : V_r = \Omega_p \cdot r_1, V_z = V_\theta = 0, T_{sl} = T_j \tag{3.4.6}$$

$$\text{At } -r_w \le r_2 \le 0,\ -h_{sl} \le z \le 0, -\frac{\pi}{2} \le \theta \le \frac{\pi}{2} : p = p_{atm} \tag{3.4.7}$$

$$\text{At } z=0, -r_w \le r_2 \le r_w, 0 \le \theta \le 2\pi : V_{\theta c} = \Omega_c \cdot r_2, V_r = V_z = 0, k_{sl}\frac{\partial T_{sl}}{\partial z} = \mu_{fr} \cdot P \cdot V_{\theta pc} = k_w \frac{\partial T_w}{\partial z} \tag{3.4.8}$$

$$\text{At } z=-h_{sl}, -(r_{pw}+d_w) \le r_1 \le -r_{pw}, 0 \le \theta \le 2\pi : V_{\theta p} = \Omega_p \cdot r_1, V_r = V_z = 0, \frac{\partial T_p}{\partial z} = 0 \tag{3.4.9}$$

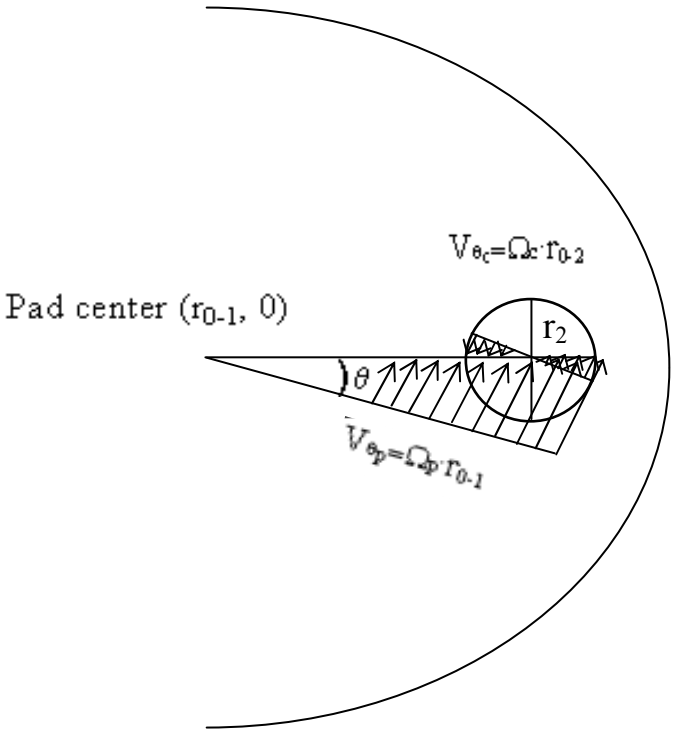

Figure 3.7 Wafer–pad relative velocity profile.

The relative co–tangential velocity effect of both surfaces along the two axes of rotation is shown in figure 3.7. The co–tangential velocity effect ($V_{\theta pc}$) was used to determine the magnitude of the variable heat flux input into the system. The carrier pad relative velocity in cylindrical coordinates system with the origin at the pad center can be derived as:

$$V_{\theta pc} = \sqrt{(\Omega_p - \Omega_c)^2 \cdot r_2^2 \sin^2\theta + \left[(\Omega_p - \Omega_c) \cdot r_2 \cos\theta + \Omega_p \cdot r_{0-1}\right]^2} \tag{3.4.10}$$

The numerical equations (3.4.1–3.4.5) were subjected to the boundary conditions described by equations (3.4.6–3.4.10) as part of the mathematical formulation of present model. Subsequently, the steady state temperature contours or profile as the index of energy dissipation along the center of wafer surface, and pad interface are plotted as part of the CMP model solution. In addition, the local heat transfer coefficients for wafer and pad are calculated according to the following expressions:

$$h_w = \frac{\mu_{fr} \cdot P \cdot V_{\theta pc}}{(T_w - T_{sl})} \tag{3.4.11}$$

$$h_p = \frac{\mu_{fr} \cdot P \cdot V_{\theta pc}}{(T_p - T_{sl})} \tag{3.4.12}$$

3.4.2 Governing Equations and Boundary Conditions: Transient

The current three dimensional CMP model of substrate surface, fluid region (slurry) and pad surface as a control volume were studied under the exposure of a variable heat flux at t=0, due to the mechanical abrasion of the pad and slurry particles. The chemical interactions of the slurry acts and supplies the heat onto the surface of the wafer, starting with an isothermal solid–fluid boundary condition and a thin film of slurry that has been established on the wafer as part of polishing process. The model description, including geometry, model set up, and assumptions are described in section 3.4.1.

The Navier–Stokes equations were used to simulate the fluid mechanics during the transient stage of the CMP process. The slurry properties (water plus alumina) were assumed to be constant for the temperature range encountered in the system. Detailed explanations on the formulation of the governing equations describing the conservation

of mass, momentum (r,θ, and z directions respectively), and energy using cylindrical coordinate system can be found in [136]:

The conservation of mass of the slurry can be written in the most general form as:

$$\frac{\partial \rho_{sl}}{\partial t}+\frac{1}{r}\frac{\partial (r\rho_{sl}V_r)}{\partial r}+\frac{1}{r}\frac{\partial (\rho_{sl}V_\theta)}{\partial \theta}+\frac{\partial (\rho_{sl}V_z)}{\partial z}=0 \tag{3.4.13}$$

The conservation of momentum (Navier–Stokes equations) for constant density and viscosity liquid or incompressible slurry properties can be written as:

$$\frac{\partial V_r}{\partial t}+V_r\frac{\partial V_r}{\partial r}+\frac{V_\theta}{r}\frac{\partial V_r}{\partial \theta}+V_z\frac{\partial V_r}{\partial z}-\frac{V_\theta^2}{r}=-\frac{1}{\rho_{sl}}\frac{\partial p}{\partial r}+\nu_{sl}\left[\frac{\partial^2 V_r}{\partial r^2}+\frac{1}{r}\frac{\partial V_r}{\partial r}+\frac{1}{r^2}\frac{\partial^2 V_r}{\partial \theta^2}+\frac{\partial^2 V_r}{\partial z^2}-\frac{V_r}{r^2}-\frac{2}{r^2}\frac{\partial V_\theta}{\partial \theta}\right] \tag{3.4.14}$$

$$\frac{\partial V_\theta}{\partial t}+V_r\frac{\partial V_\theta}{\partial r}+\frac{V_rV_\theta}{r}+\frac{V_\theta}{r}\frac{\partial V_\theta}{\partial \theta}+V_z\frac{\partial V_\theta}{\partial z}=-\frac{1}{\rho_{sl}}\frac{\partial p}{\partial \theta}+\nu_{sl}\left[\frac{\partial^2 V_\theta}{\partial r^2}+\frac{1}{r}\frac{\partial V_\theta}{\partial r}+\frac{1}{r^2}\frac{\partial^2 V_\theta}{\partial \theta^2}+\frac{\partial^2 V_\theta}{\partial z^2}+\frac{2}{r^2}\frac{\partial V_r}{\partial \theta}-\frac{V_\theta}{r^2}\right] \tag{3.4.15}$$

$$\frac{\partial V_z}{\partial t}+V_r\frac{\partial V_z}{\partial r}+\frac{V_\theta}{r}\frac{\partial V_z}{\partial \theta}+V_z\frac{\partial V_z}{\partial z}=-g-\frac{1}{\rho_{sl}}\frac{\partial p}{\partial z}+\nu_{sl}\left[\frac{\partial^2 V_z}{\partial r^2}+\frac{1}{r}\frac{\partial V_z}{\partial r}+\frac{1}{r^2}\frac{\partial^2 V_z}{\partial \theta^2}+\frac{\partial^2 V_z}{\partial z^2}\right] \tag{3.4.16}$$

The energy equation for incompressible slurry properties and negligible viscous dissipation can be written as:

$$\frac{\partial T_{sl}}{\partial t}+V_r\frac{\partial T_{sl}}{\partial r}+\frac{V_\theta}{r}\frac{\partial T_{sl}}{\partial \theta}+V_z\frac{\partial T_{sl}}{\partial z}=\alpha_{sl}\left(\frac{1}{r}\frac{\partial}{\partial r}\left(r\frac{\partial T_{sl}}{\partial r}\right)+\frac{1}{r^2}\frac{\partial^2 T_{sl}}{\partial \theta^2}+\frac{\partial^2 T_{sl}}{\partial z^2}\right) \tag{3.4.17}$$

Equations (3.4.13–3.4.17) were subjected to the boundary conditions described by equations (3.4.6–3.4.10). The wafer surface is assumed to be at thermal equilibrium with the alumina (Al_2O_3) slurry before the transient heating of the polishing takes place. The velocity field at this condition is determined by solving only the continuity and momentum equations (3.4.13–3.4.16) in the fluid region. Thus,

$$\text{At } t=0:\ T_{sl}=T_p=T_w,\ \vec{V}_i=\vec{V}(\text{isothermal}) \tag{3.4.18}$$

By solving the numerical problem, the transient temperature contours or profile as the index of energy dissipation of the wafer surface, the slurry and pad interface, were shown as part of the results. In addition, as part of this study, temperature distributions as function of time on isolated nodes were examined for the entire transient process. This was done under a different set of physical parameters, such as slurry flow rates, polishing pressures, carrier and pad spinning rates, and slurry film thicknesses. To complete the mathematical formulation the local heat transfer coefficients for wafer and pad surfaces are defined according to equations (3.4.12–13).

3.5 Numerical Computation

3.5.1 Free Surface Liquid Jet Impingement Steady State and Transient Process

The governing equations (3.1.1–3.1.6) of Prob. #5 and (3.1.19–3.1.24) of Prob. #6 and the boundary conditions (3.1.7–3.1.14) and (3.1.25) just for the transient conditions described in the preceding sections (3.1.1 and 3.1.2), were solved using the Galerkin finite element method [140]. Four node quadrilateral elements were used. A scaled dense grid distribution was used to adequately capture large variations near the solid–fluid interface of the meshed domain, as shown in figure 3.8.

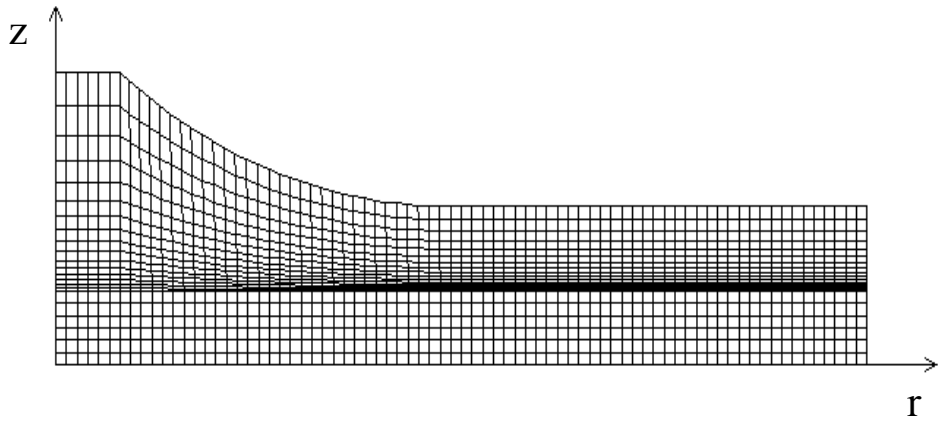

Figure 3.8 Axis–symmetric free surface liquid jet impingement mesh plot.

In each element, the velocity, pressure, and temperature fields were approximated which led to a set of equations that defined the continuum. The solution of the resulting non–linear equations was carried out using the Newton–Raphson method. The approach used to solve the free surface problem described here was to introduce a new degree of freedom representing the position of the free surface. This degree of freedom was introduced as a new unknown into the global system of equations.

Due to non–linear nature of the governing transport equations, an iterative procedure was used to arrive at the solution for the velocity and temperature fields. In order to determine the initial velocity field (V_i), the equations for the conservation of mass and momentum were solved. Since the solution of the momentum equation required only two out of the three boundary conditions at the free surface, the third condition that relates the slope of the free surface to local velocity components at the free surface was used to upgrade the position of the free surface at the end of each iteration step. The Newton–Raphson solver used spines to track the free surface and re–arranged grid distribution with the movement of the free surface. These spines are straight lines passing through the free surface nodes and connecting the nodes underneath the free surface. The free surface movement affected only nodes along the spine.

Once the final free surface height distribution and the flow–field for the isothermal equilibrium condition were reached, the power of the heat source was turned on and heat began to flow. Then the computation domain included both solid and fluid regions. The continuity, momentum, and energy were solved simultaneously as a conjugate problem taking into account the variation of fluid properties with temperature. The computation covered the entire transient period all the way to the steady state

condition. Because of large changes at the outset of the transient and very small changes when the solution approached the steady state condition, a fixed time step was used to cover the earlier part of the transient up to 25 seconds, and a variable time step was used for the rest of the computation. At each time step, the solution was considered converged when relative change in field values from a particular iteration to the next, and the sums of the residuals for each variable became less than 10^{-6}.

The characteristics of the flow are controlled by three major physical parameters: the Reynolds number, $Re_j=V_j\ d_n\ /\nu_f$, the dimensionless nozzle–to–plate spacing ratio, $\beta=H_n/d_n$, and the Ekman number, $Ek=\nu_f\ /4\Omega\ r_d^2$. The values of Reynolds number was limited to a maximum of 1,800 to stay within the laminar region. The materials properties used for the numerical simulation such as density, viscosity, thermal conductivity, and specific heat are assumed to remain constant over the working temperature range. The properties of the following solid materials: Constantan, copper, aluminum, silicon, and silver were obtained from Özisik [141].

The nozzle diameter opening was varied over the range of 1.20 to 3.60 mm. The disk radius was kept at a constant value of 7.6 mm and the heat flux (q_w) was also kept constant at 250 kW/m^2 for steady state conditions (Prob. #5) and 125 kW/m^2 transient state conditions (Prob. #6). The incoming fluid jet temperature (T_j) was 310 K for water and FC–77, 303 K for ammonia (at a pressure of 20 bars), and 375 K for MIL–7808. The thickness of the disk was varied over the following values: 0.20, 0.40, 0.60, 0.90, 1.2, 1.5 and 2.0 mm. The jet impingement height or the distance between the nozzle and disk was set at the following values: $6.6\text{x}10^{-4}$, $9.0\text{x}10^{-4}$, $1.5\text{x}10^{-3}$, $2.4\text{x}10^{-3}$, $3.6\text{x}10^{-3}$, $4.8\text{x}10^{-3}$, and $6.0\text{x}10^{-3}$ m at (Prob. #5), conversely the jet impingement height was kept at a constant

value of 3.2 mm for Prob. #6. However, for comparison with other numerical and experimental results the impingement heights were set to: 2.4, 1.5, 0.9, and 0.66 mm respectively. The spinning rate (Ω), and flow rate (Q) were varied from 13.10 to 157.08 rad/s or 125 to 1,500 RPM and 3.360×10^{-7} to 1.133×10^{-6} m^3/s; respectively at Prob. #5. The range for Reynolds number and Ekman number were set at: Re=445 to 1,800 and Ek=2.21×10^{-5} to 2.65×10^{-4}. On Prob. #6 the spinning rate (Ω) was varied from 0 to 52.36 rad/s or 0 to 500 RPM, that correspond to the range of Ekman number from ∞ to 6.62×10^{-5}. In addition, the flow rate was varied from 3.775×10^{-7} to 1.057×10^{-6} m^3/s, for a range of Reynolds number from 500 to 1,400. The possibility of getting into turbulent flow due to disk rotation was checked using the laminar–turbulent transition criterion of Popiel and Boguslawski [36] and Vanyo [142]. All runs used in the study checked out to be laminar.

3.5.2 Confined Submerged Liquid Jet Impingement Steady State Process

The governing equations along with the boundary conditions were solved using the Galerkin finite element method as demonstrated by Fletcher [140]. Four node quadrilateral elements were used. For each element, the velocity, pressure, and temperature fields were approximated which led to a set of equations that defined the continuum. Due to non–linear nature of the governing transport equations, an iterative procedure was used to arrive at the solution for the velocity and temperature fields. The solution of the resulting non–linear differential equations was carried out using the Newton–Raphson method. The solution was considered converged when the field value did not change from one iteration to the next and the sum of the residuals for all the dependent variables was less than a predefined tolerance value; in this case, 10^{-6}.

The number of elements required for accurate results was determined from a grid independence study. Figure 3.9 shows an unstructured grid of the confined region in which the size of the elements near the solid–fluid interface was made smaller to adequately capture the large variations in velocity and temperature near wall.

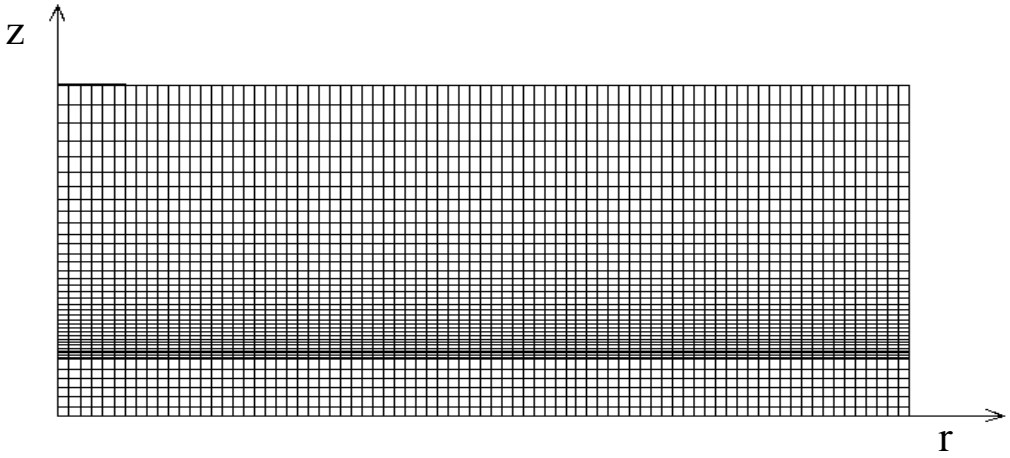

Figure 3.9 Axis–symmetric confined liquid jet impingement mesh plot.

3.5.2.1 Stationary Confined Wall with Spinning Target

The top disk remains stationary while the bottom disk rotates at a uniform angular velocity (Ω) of 5.236 to 104.72 radians/sec or 50 to 1,000 RPM to cover different scenarios. The values of Reynolds number was limited over 750 to avoid any fluid boiling condition up to a maximum of 2,000 to stay within the laminar region. The orifice nozzle and the solid wafer disk have radii of 0.3 and 7.6 mm respectively; additionally the solid wafer thickness was kept at a value of 0.3 mm. The jet impingement height was varied from: $7x10^{-4}$ to $3.2x10^{-3}$ m. The heat flux (q_w) and jet temperature were kept constant at 250 kW/m^2 and 310 K respectively. The fluid and solid material properties are assumed to be constant for the temperature range encountered in the system, as shown in Table 3.1.

3.5.2.2 Spinning Confined Wall with Stationary Target

The bottom disk remains stationary while the top disk rotates at a uniform angular velocity. The values of Reynolds number was limited to a maximum of 1,500 to stay within the laminar region. The nozzle opening and the solid wafer disk have radii of 0.6 and 6.0 mm respectively. The heat flux (q_w) was kept constant at a value of 250 kW/m^2. The incoming fluid jet temperature (T_j) was 310 K for water and FC–77, 303 K for ammonia (at a pressure of 20 bars), and 375 K for MIL–7808. The thickness of the disk was varied over the following values: 0.3, 0.6, 0.9, 1.2, 1.5 and 2.0 mm. The jet impingement height or the distance between the nozzle and disk was set at the following values: $3x10^{-4}$, $6x10^{-4}$, $9.0x10^{-4}$, $1.2x10^{-3}$, $2.4x10^{-3}$, $3.6x10^{-3}$, $4.8x10^{-3}$, and $6x10^{-3}$ m. The spinning rate (Ω) was varied from 0 to 78.54 rad/s or 0 to 750 RPM. The flow rate was varied from $3.78x10^{-7}$ to $1.13x10^{-6}$ m^3/s. The range for Reynolds number and Ekman number ranged from: Re=500 to 1,500 and Ek=$7.08x10^{-5}$ to ∞ respectively. Using the laminar–turbulent transition criterion used by Popiel and Boguslawski [36] and Vanyo [142], all runs used in the paper checked out to be laminar.

The simulation was carried out for a number of disk materials, namely Constantan, copper, silicon, and silver. The properties of solid materials were obtained from Özisik [141]. Fluid properties for H_2O, NH_3, MIL–7808, and FC–77 were obtained from Bejan [134], the Brady vendor, and 3M Specialty Fluids respectively. The properties of the above fluids were correlated according to the equations shown in section 3.1.2. In these correlations, the absolute temperature T was used in K.

3.5.3 Partially–confined Submerged Liquid Jet Impingement Steady State and Transient Process

The purpose of a finite element method is to break down the continuum problem, of essentially an infinite number of degrees of freedom, to a finite number of degrees by discrete sizing the continuum into a number of simple shaped elements. The governing equations along with the boundary conditions of section (3.3.1 to 3.3.3) were solved using the Galerkin finite element method [140]. Four node quadrilateral elements were used. For each element, the velocity, pressure, and temperature fields were approximated which led to a set of discretized equations that defined the continuum.

In order to determine the initial velocity field (V_i), the equations for the conservation of mass and momentum were solved. The number of elements required for accurate results was determined from a grid independence study. The size of the elements near the solid–fluid interface was made smaller to adequately capture large variations in velocity and temperature in that region, as shown in figure 3.10.

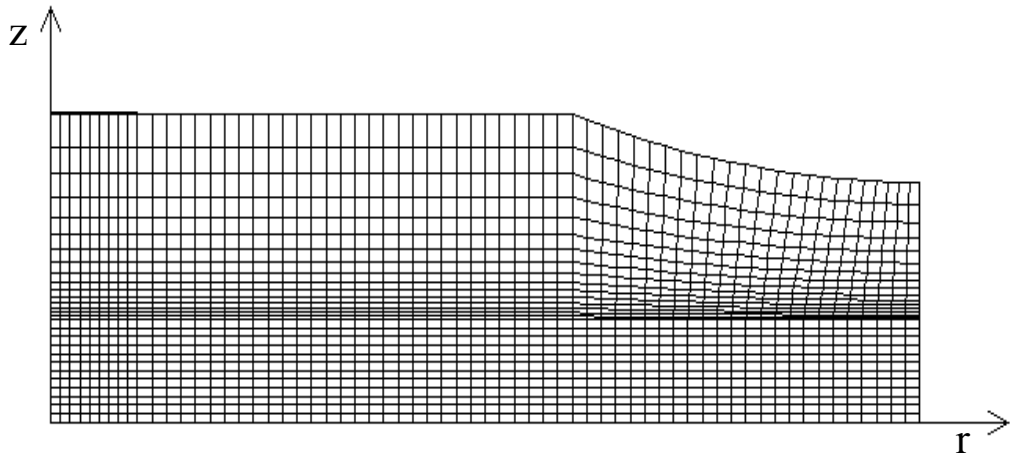

Figure 3.10 Axis–symmetric partially–confined jet impingement mesh plot.

Due to non–linear nature of the governing differential equations the Newton–Raphson method was used to arrive at the solution for the velocity and temperature fields. The solver used spines to track the free surface and re–arranged grid distribution with the movement along the free surface. The movement of the free surface affected only the nodes along the spine. The approach used to solve the free surface problem described here was to introduce a new unknown δ representing the position of the free surface in the global system of equations. In order to start the computation, initial values of δ were assigned to all nodes at the free surface. A linear distribution with $\delta=H_n$ at $r=r_p$ to $\delta\approx H_n/2$ at $r=r_d$ was used as the initial guess. Since the solution of the momentum equation required only two out of the three boundary conditions at the free surface, the third condition in equation (3.3.15) was used to upgrade the position of the free surface at the end of each iteration step. Then the velocity components at the free surface were used to check the fulfillment of the kinematic condition (the first condition in equation 3.3.15). The value of the free surface height (δ) was upgraded by applying a correction obtained from the required slope of the free surface at each free surface node. In order to preserve the numerical stability during this iterative solution for δ a relaxation factor of 0.1 was used. Once a new location for the free surface node has been determined, the location of all fluid nodes underneath the free surface extending to the solid–fluid interface were adjusted keeping the same grid ratio. It may be noted that the adjustment was done only in the vertical direction (along the z axis) and only in the region of $r_p < r < r_d$ and $0 < z < \delta$. The iterative solution for the determination of the free surface height distribution was continued by solving the conservation of mass and momentum equations and upgrading the grid structure underneath the free surface.

Once the final free surface height distribution was obtained no further change in δ was needed and the flow–field for the isothermal equilibrium condition was reached, the power source was turned on and the heat began to flow. Then the energy equation (3.3.5) was solved simultaneously, along with the conservation of mass and momentum equations (3.3.1–3.3.4) as a conjugate problem taking into account the variation of fluid properties with temperature to determine the final distribution of velocity, pressure, and temperature. The computation covered the entire transient period all the way to the steady state condition. Because of large changes at the outset of the transient and very small changes when the solution approached the steady state condition, a fixed time step was used to cover the earlier part of the transient up to 25 seconds, and a variable time step was used for the rest of the computation. The solution was considered converged when relative change in field values from a particular iteration to the next, and the sums of the residuals for each variable became less than 10^{-6}. The conservation of mass was independently checked by calculating the flow rate at the outlet ($r=r_d$) from computed velocity field and comparing that with fluid intake at the nozzle ($z=H_n$). The difference was essentially zero.

The characteristics of the flow are controlled by three major physical parameters: the Reynolds number, $Re_j=V_j\ d_n\ /\nu_f$, the dimensionless nozzle–to–plate spacing ratio, $\beta=H_n/d_n$, and the Ekman number, $Ek_{1,2}=\nu_f/4\Omega_{1,2}r_d^2$. The values of Reynolds number was limited to a maximum of 900 to stay within the laminar region. The nozzle opening and the heated target disk have radii of 0.6 and 6.0 mm respectively. The heat flux (q_w) was kept constant at 125 kW/m^2. The incoming fluid jet temperature (T_j) was 310 K for water and FC–77, 303K for ammonia (at a pressure of 20 bars), and 375 K for MIL–7808. The

thickness of the disk (b) was varied over the values of: 0.30, 0.60, 1.0, 1.5 and 2.0 mm. The jet impingement height or the distance between the nozzle and disk was set at the following values: $3x10^{-4}$, $6x10^{-4}$, $9.0x10^{-4}$, and $1.2x10^{-3}$ m. The spinning rate (Ω) was varied from 0 to 78.54 rad/s or 0 to 750 RPM. The flow rate was varied from $6.65x10^{-7}$ to $2.72x10^{-6}$ m^3/s. These values covers the range of Ekman numbers of $Ek_{1,2}=7.08x10^{-5}$ to ∞ and Reynolds numbers of 220 to 900 respectively. The laminar–turbulent transition criterion of Popiel and Boguslawski [36] and Vanyo [142] confirms that all runs in this study were laminar.

The solid and fluid properties were obtained from Özisik [141], Bejan [134], and Bula [138].The fluid properties are correlated according to the following equations. For water between 300 K<T<411 K; $Cp_f=9.5x10^{-3}T^2-5.9299T+5098.1$; $k_f= -7.0x10^{-6}T^2+5.8x10^{-3}T-0.4765$; $\rho_f= -2.7x10^{-3}T^2+1.3104T+848.07$; and $\ln(\mu_f) = -3.27017-0.0131T$. For ammonia between 273.15 K<T<370 K; $Cp_f=0.083T^2-40.489T+9468$; $k_f=1.159-2.30x10^{-3}T$; $\rho_f=579.81+1.6858T-0.0054T^2$; and $\ln(\mu_f) = -5.33914-0.0115T$. For MIL–7808 between 303 K<T<470 K; $Cp_f=903.8+3.332T$; $k_f=0.18-1x10^{-4}T$; $\rho_f=1181-0.708T$; and $\ln(\mu_f) =3.2436-0.0229T$. For FC–77 between 273 K<T<380 K; $Cp_f=589.2+1.554T$; $k_f=0.0869-8x10^{-5}T$; $\rho_f=2{,}507.2-2.45T$; and $\ln(\mu_f) = -2.38271-0.0145T$. In these correlations, the absolute temperature T is in K.

3.5.4 Chemical Mechanical Polishing Steady State and Transient Process

For a problem under study, the governing equations and the boundary conditions were solved using the finite element method (FEM). The FI–GEN module of FIDAP (Fluent, 2005) and the software GAMBIT (Fluent, 2006) were used for geometric modeling and mesh generation. In FEM, the computational domain is discretized into

elements. Four node quadrilateral elements were used. In each element, velocity components, pressure, and temperature fields, if any, were approximated by using the Galerkin FEM procedure [140] that leads to a set of algebraic equations that defines the discretized continuum.

For 3–D models, the number of elements and nodal points are usually so large that the use of a fully coupled algorithm may require computing resources that exceed those available. To avoid that type of problem, the solution of the resulting non–linear equations was carried out using the segregated method.

The segregated solution algorithm avoids the direct formation of a global system matrix. Instead, in each iteration, only one unknown is solved for, while the others keep their previous values. The next iteration is used to solve for the next unknown. Due to its sequential and uncoupled nature, the segregated approach requires less disk storage but more iterations than the fully coupled approach. The formulation of the segregated algorithm is quite involved and can be found in FIDAP Documentation (Fluent, 2005).

The present CMP model solution was considered converged when the relative change in field values from a particular iteration to the next, and the sums of the residuals for each variable became less than 10^{-4}. The technical computing program Matlab (The MathWorks, 2007) was used to compute and generate 3–D visualizations contour plots for the numerical solutions from FIDAP imported into MATLAB through the neutral files (*.FPNEUT).

The polishing pad and heated wafer of present investigation had a radius of 7.65 cm and 1.9 cm respectively. The source of heat flux (q_{sl}) in the model was from the non–uniform shear friction and it was varied over a range of 3.75 to 23.12 (kW/m^2). The

incoming slurry temperature (T_{sl}) was set to 297 K for alumina (Al_2O_3). The slurry film thickness was varied from 40 to 200μm. The pad and carrier spinning rate ($\Omega_{p,c}$) was varied from 8.38 to 25.13 rad/s and 1.57 to 7.85 rad/s respectively. The flow rate was varied from 0.5–1.42 cc/s. The possibility of getting into a turbulent flow due to disk rotation was checked using the laminar–turbulent transition criterion of Popiel and Boguslawski [36] and Vanyo [142]. All runs used in the study checked out to be laminar.

3.6 Mesh Independence and Time Step Study

3.6.1 Free Liquid Jet Impingement Model

The examination of the spatial convergence of a simulation is a straight–forward method that determines the ordered of the discretization error in a CFD simulation. The method involves performing the simulation on two or more successively finer grids. As part of this study, a quantitative difference of grid independence was calculated by the accuracy of code using the asymptotic range of convergence of Roache's methodology [143]. The Grid Convergence Index (GCI) was used to measure the numerical results percentage of accuracy in terms of the asymptotic numerical value of the exact solution. The GCI indicates an error band and how far the solution is from the asymptotic value. It indicates how much the solution would change with a further refinement of the grid. A small value of GCI indicates that the computation is within the asymptotic range. The GCI can be computed using two levels of grid; however, three levels are recommended to determine the order of convergence and to check if the solutions are within the asymptotic range of convergence. The GCI on the grid is defined as:

$$GCI = \frac{F_S \left| \frac{T2 - T1}{T1} \right|}{(r^p - 1)} \cdot 100 \qquad (3.6.1)$$

where F_S is a factor of safety. The refinement may be spatial or in time. The safety factor of F_S=3.0 is recommended for two grids. On the other hand, a safety factor of F_S=1.25 is recommend for three or more grids. It is important that each grid level yield to a solution that is in the asymptotic range of convergence of the mesh. This can be checked by observing two of the GCI values as computed over three grids,

$$GCI_{23}=r^{p}\, GCI_{12} \tag{3.6.2}$$

As the grid spacing reduces, the temperature values at the interface approach to the asymptotic zero grid spacing value. We can determine the local order of convergence from these results, that direct evaluation of p can be obtained from a three grid solution using the grid refinement ratio r, equal to the number of elements of the fine grid (M_{n+1}) divided by the number of elements of the coarse grid (M_n) .

$$p=\frac{\ln\left(\frac{T3-T2}{T2-T1}\right)}{\ln\left(\frac{N3}{N1}\right)} \tag{3.6.3}$$

The local order of accuracy is the order of the stencil representing the discretization of the equation at one location (r/r_d) in the grid. The global order of accuracy considers the propagation and accumulation of errors outside the stencil. This propagation causes the global order of accuracy to be, in general, one degree less than the local order of accuracy. To fulfill the analysis of the Grid Convergence Index (GCI), it was necessary to use Richardson's extrapolation method for higher–order. The Richardson's extrapolation method was used to estimate the continuum value at zero grid spacing from a series of lower–order discrete values. The continuum value at zero grid spacing and the percentage error can be generalized for a p–th order methods and r–value of grid ratio (which does not have to be an integer) defined by the following expressions:

$$T_{h=0} = T1 + \left[\frac{T1 - T2}{r^p - 1}\right] \tag{3.6.4}$$

$$\left|\frac{T_{int} - T_{h=0}}{T_{h=0}}\right| x100 \tag{3.6.5}$$

Additionally, to determine the number of elements for accurate numerical solution, computation was performed for several grids or combinations of number of elements in the horizontal and vertical directions covering the solid and fluid regions, as shown in figure 3.11.

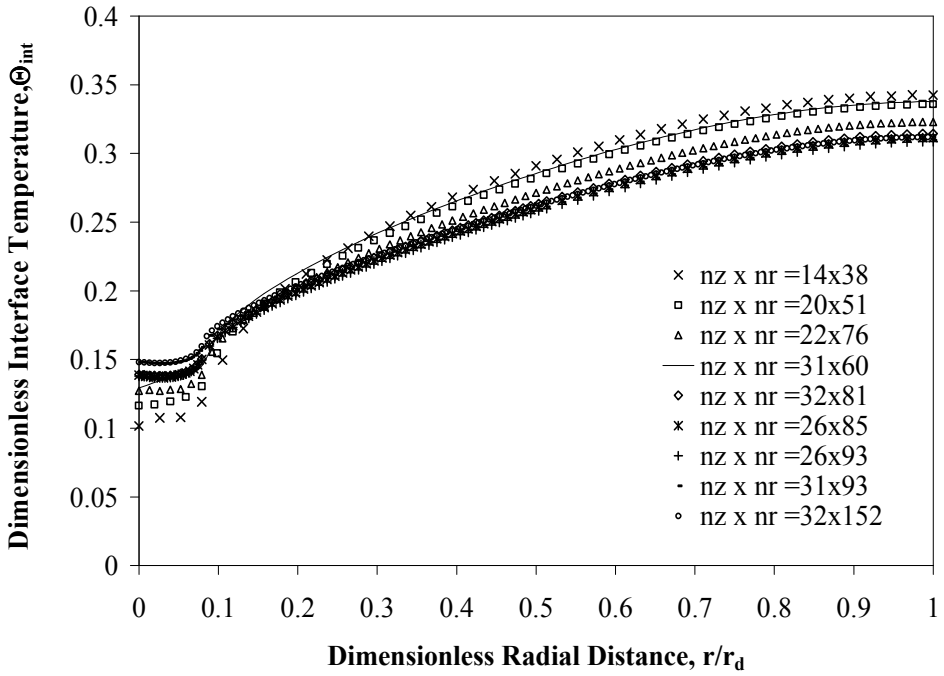

Figure 3.11 Solid–fluid interface temperature for different number of elements in r and z directions (Re=1,500, b=0, d_n=1.2 mm, Ek=2.65x10^{-4}, β=2.67).

The numerical solution becomes grid independent when the number of divisions equal to 26x85 in the axial (z) and radial (r) directions respectively is used. Numerical results for a 26x85 grid gave almost identical results compared to those using 22x76 and

32x152 grids. The average difference was 0.69%. Therefore, further computations were carried out using a 26x85 grid.

Subsequently, the GCI method was used to confirm the accuracy of the chosen mesh. The GCI's values, the percent error, and $T_{h=0}$ at r/r_d=0.75 are shown in Table 3.2. Thus, the above set of equations (3.6.1 to 3.6.4) was solved to determine the local accuracy of convergence or GCI's values for the following three grids. The last column of Table 3.2 shows that a grid of 26x85 is the most accurate with a percent error of $3.36x10^{-3}$ from its asymptotic numerical exact solution. The purpose of the GCI method is to point out an error band and how far the local solution of the mesh is from its asymptotic value.

Table 3.2 Grid convergence study of figure 3.11.

Run #	MSH	GCI (%)	T_{int} at r/r_d= 0.75 (K)	$T_{h=0}$ at r/r_d= 0.75 (K)	Eq.3.6.5 (%error)
1	22x76	GCI_{12} = 0.497	340.85069	339.496	0.399
2	26x85	GCI_{23} = 0.046	339.50792		$3.36x10^{-3}$
3	32x152	GCI_{31} = 0.453	339.37213		0.037

Computations were also performed to calculate a suitable fixed time step to determine its sensitivity on the transient solution. Figure 3.12 plots the variation of maximum dimensionless solid–fluid interface temperature for different time increments as a function of Fourier number (F_o) as a dimensionless number to represent the time. It may be noted that the solution is not susceptible to the size of the time step or increment when an increment of 0.075 seconds or less is chosen. A time increment of 0.05 seconds was selected to ensure a smooth variation. Notice how the maximum dimensionless temperature increases rapidly all the way to the steady state condition.

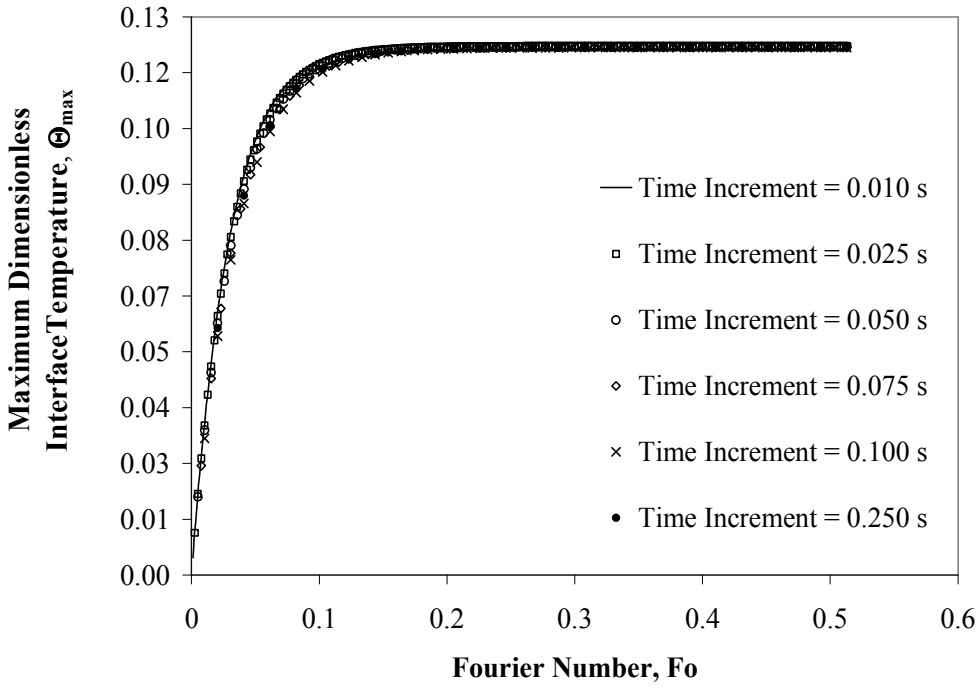

Figure 3.12 Time step independence study for maximum dimensionless interface temperature variation at different time steps (Re=550, silicon disk, water, b/d_n=0.5, Ek=2.65x10^{-4}, q_w=125 kW/m^2, β=2.67).

3.6.2 Confined Liquid Jet Impingement Model

3.6.2.1 Stationary Confined Wall with Spinning Target

The solid–fluid dimensionless interface temperatures for different number of grids are plotted in figure 3.13. Several grids were used to determine the number of elements needed for accurate numerical solution. It was observed that the numerical solution becomes grid independent when the grids reach a number of divisions equal to 35x79 in the axial (z) and radial (r) directions respectively. Numerical results for a 35x79 grid gave almost identical results compared to a 64x76 grid for an impingement height (H_n) equal to 0.32 cm. Therefore, the chosen grid was 35x79 that carried an average error margin of 0.243% compared to 64x76 grids.

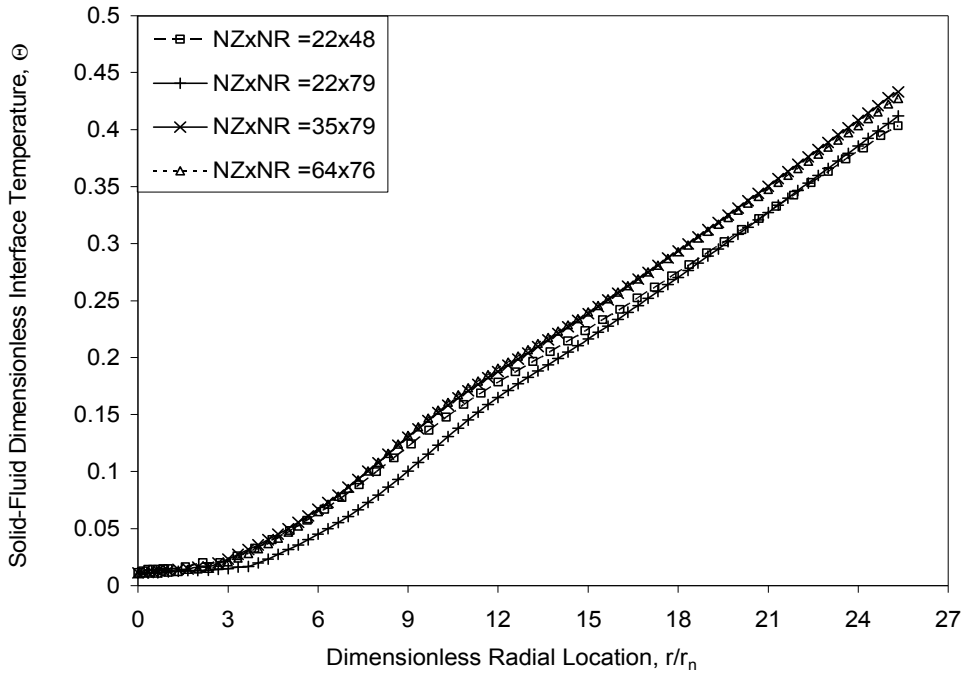

Figure 3.13 Local dimensionless interface temperature for different number of elements in r and z directions at constant flow rate (Re=1,500, Q=7.08x10^{-2} m^3/s, b=0, Ek=2.65x10^{-4}, q_w =250 kW/m^2, H_n/d_n= 5.33, Ω=125 RPM, H_n=0.32 cm).

The GCI's values, the percent error, and $T_{h=0}$ at r/r_n=8 are shown in Table 3.3. Thus, the above set of equations (3.6.1–3.6.5) was solved to determine the local accuracy of convergence or GCI for each of the following mesh domains.

Table 3.3 Grid convergence study of figure 3.13.

Run #	MSH	GCI (%)	T_{int} at r/r_n= 8 (K)	$T_{h=0}$ at r/r_n= 8 (K)	Eq.3.6.5 (%error)
1	22x79	GCI_{12} = 3.2x10^{-3}	323.16375	323.143	6.45x10^{-3}
2	35x79	GCI_{23} = 8.1x10^{-3}	323.15114		2.55x10^{-3}
3	64x76	GCI_{31} = 0.011	323.19566		0.016

The last column of Table 3.3 shows that a grid of 35x79 is the most accurate with a percent error of 2.55x10^{-3} from its asymptotic numerical exact solution. The purpose of

the GCI method is to point out an error band and how far the local solution of each particular grid is from its asymptotic value.

3.6.2.2 Spinning Confined Wall with Stationary Target

For the spinning confined wall with stationary target, several grids or combinations of a number of elements were used to determine the accuracy of the numerical solution. Dimensionless solid–fluid or interface temperatures at the heated plate for several grids are plotted in figure 3.14.

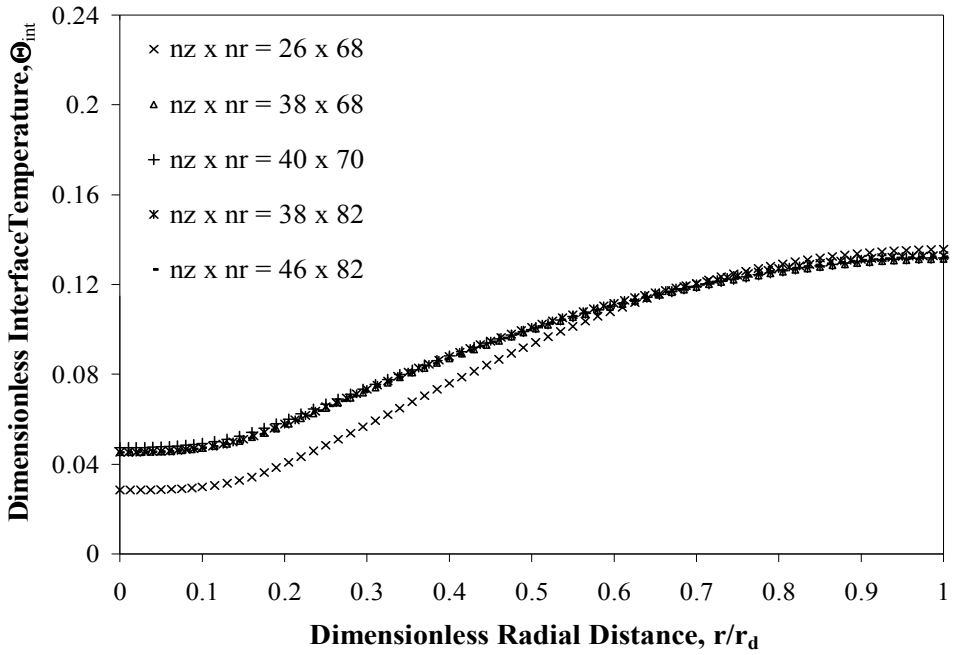

Figure 3.14 Dimensionless interface temperature distributions for different number of elements in r and z directions (Re=1,000, b=0.3 mm, d_n=0.12 mm, Ek=1.06x10^{-3}, β=2.0).

The numerical solution becomes grid independent when the number of divisions equal to 40x70 in the axial (z) and radial (r) directions respectively is used. Numerical results for a 40x70 grid gave almost identical results compared to 38x82 and 46x82 grids for an impingement height (H_n) equal to 0.24 cm. The average difference was equal to

0.22%. Therefore, further computations were carried out using 40x70 elements. The size of the elements varies with denser distribution at the solid–fluid interface and at the nozzle axis. Scaling ratios of 1.5 and 1.62 were used in radial and axial directions respectively.

Table 3.4 Grid convergence study of figure 3.14.

Run #	MSH	GCI (%)	T_{int} at r/r_d= 0.4 (K)	$T_{h=0}$ at r/r_d= 0.4 (K)	Eq.3.6.5 (%error)
1	38x82	$GCI_{12} = 2.4x10^{-3}$	331.62446	331.631	$1.97x10^{-3}$
2	46x82	$GCI_{23} = 2.5x10^{-3}$	331.80240		0.052
3	40x70	$GCI_{31} = 9.4x10^{-5}$	331.63125		$7.5x10^{-5}$

A quantitative difference in local grid convergence was calculated using equation (3.6.1 to 3.6.4) for the temperature at the solid–fluid interface T_{int} at a given r/r_d–location of the target disk for each grid. The GCI's values and the exact solution for a grid size of zero spacing at r/r_d=0.4, are shown in Table 3.4. In addition, the last column of Table 3.4 shows the calculated percent error obtained by equation 3.6.5 for a grid of 40x70. These results show that the chosen grid of 40x70 is the most accurate. The purpose of the GCI method is to point out an error band and how far the local solution of the mesh is from its asymptotic value. It can be found that the numerical solution becomes grid independent when the number of divisions equal to 28x63 in the axial (z) and radial (r) directions, as shown in figure 3.15. Comparing the numerical results for the 32x72 and 45x100 grids with a 28x63 grid shows an average difference of 0.72%. Therefore, further computations were carried out using a 28x63 grid.

3.6.3 Partially–confined Liquid Jet Impingement Model

3.6.3.1 Stationary Confined Wall with Spinning Target

The number of elements required for accurate numerical solution was determined from a systematic grid–independence study.

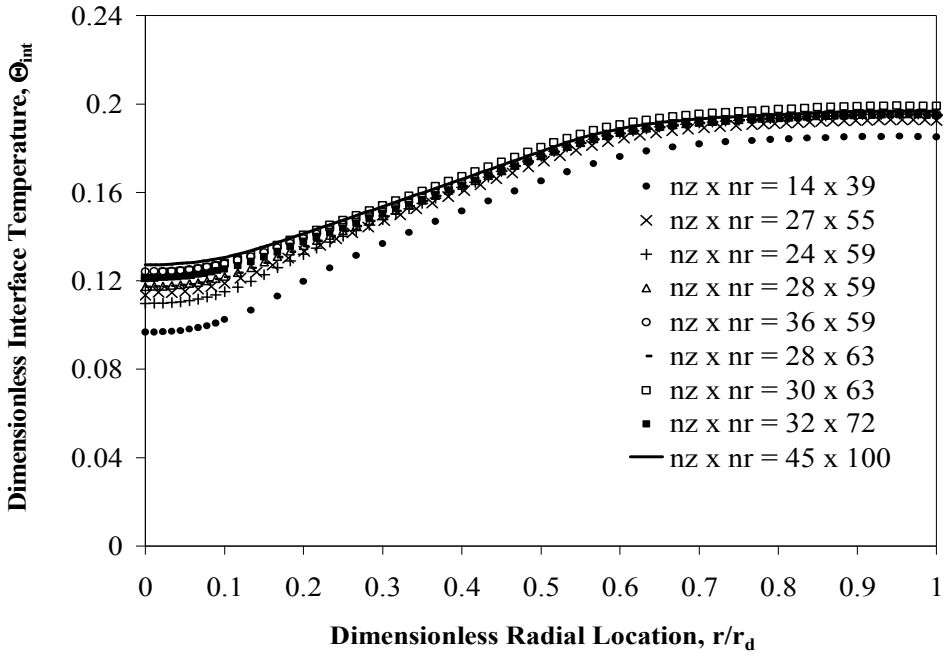

Figure 3.15 Dimensionless interface temperature distributions for different number of elements in r and z directions (Re=750, r_p/r_d=0.667, b/d_n=0.5, Ek=4.25x10^{-4}, β=0.5).

Table 3.5 Grid convergence study of figure 3.15.

Run #	MSH	GCI (%)	T_{int} at r/r_d= 0.5 (K)	$T_{h=0}$ at r/r_d= 0.5 (K)	Eq.3.6.5 (%error)
1	28x63	GCI_{12} = 6.7x10^{-5}	353.13354	353.133	5.4x10^{-5}
2	32x72	GCI_{23} = 3.6x10^{-3}	353.12285		3.0x10^{-3}
3	45x100	GCI_{31} = 3.7x10^{-3}	353.71234		0.164

The GCI's values, the percent error, and $T_{h=0}$ at r/r_d=0.5 are shown in Table 3.5. Thus, the above set of equations (3.6.1–3.6.5) was solved to determine the local accuracy

of the following grids 32x72 and 45x100 in comparison with a 28x63 grid. In addition, the last column of Table 3.5 shows the calculated percent error obtained by equation 3.6.5 for a grid of 28x63 is the most accurate in comparison with its asymptotic numerical exact solution. The purpose of the GCI method is to point out an error band and how far the local solution of the mesh is from its asymptotic value.

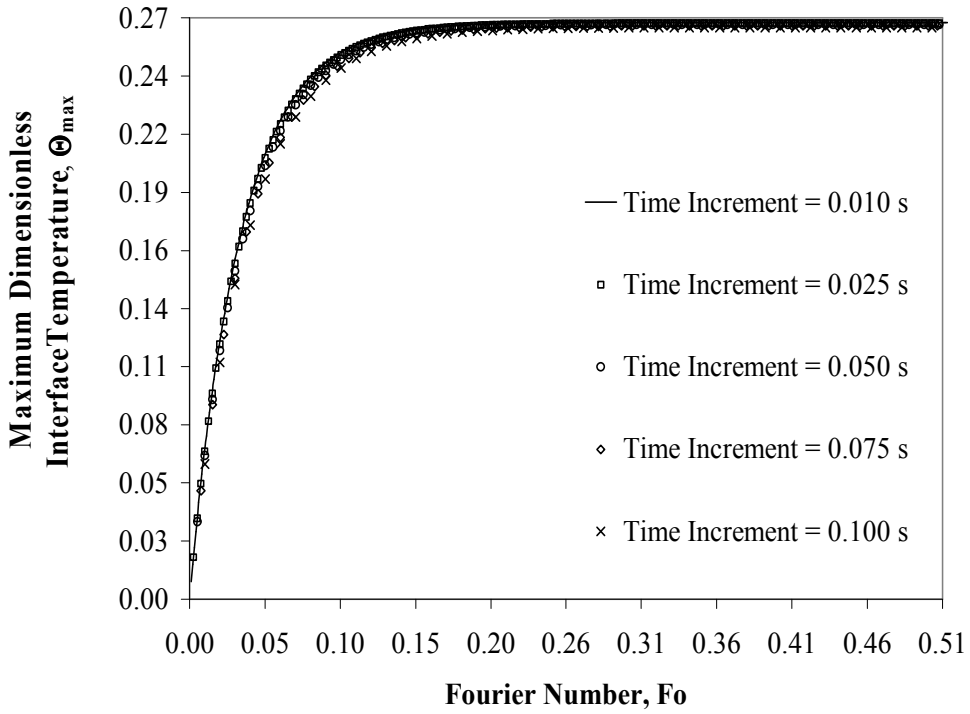

Figure 3.16 Maximum dimensionless interface temperature variation for different time steps with water as the cooling fluid (Re=225, Ek=2.13x10^{-4}, β=0.5, silicon disk, b/d_n=0.5, and r_p/r_d=0.667).

To determine the sensitivity of the transient solution further computations were performed to calculate a suitable fixed time step, as shown in figure 3.16. These transient computations showed that the variation of the temperature is not sensitive to time step size when an increment of 0.075 seconds or less is chosen. For this study, the time increment of 0.05 seconds was selected to ensure a smooth variation.

3.6.3.2 Co–Rotating Target and Confined Wall

For the co–rotating target and confined wall, several grids or combinations of number of elements were used to determine the accuracy of the numerical solution, as shown in figure 3.17. The numerical solution becomes grid independent when the numbers of divisions used were equal to 34x63 in the axial (z) and radial (r) directions respectively. Comparing the numerical results for the 34x59 and 36x64 grids with a 34x63 grid showed an average difference of 0.159%.

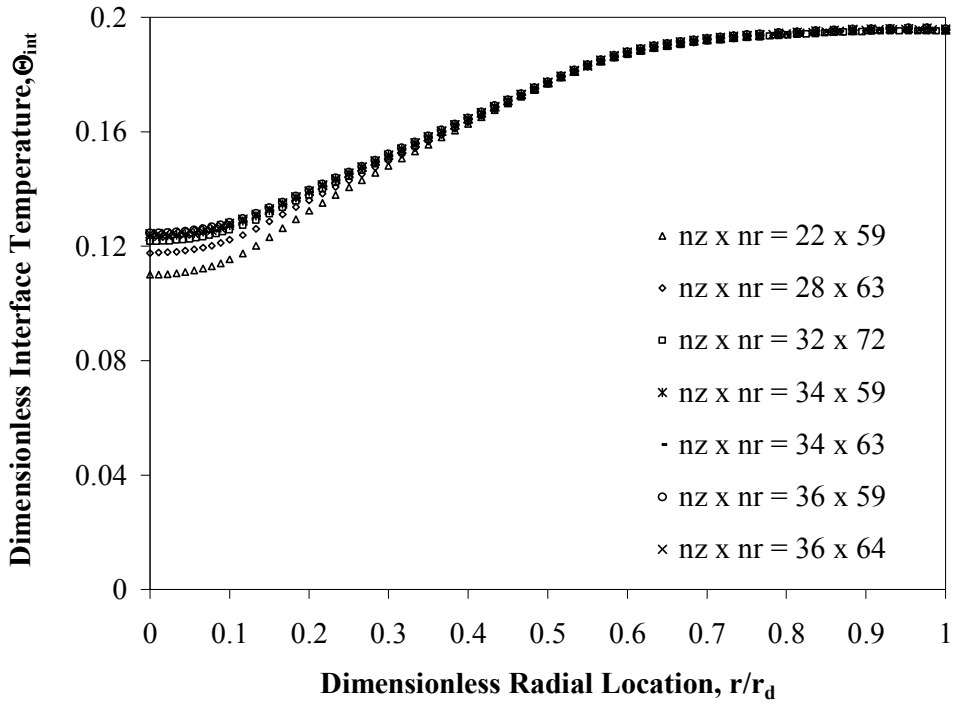

Figure 3.17 Dimensionless interface temperature distributions for different number of elements in r and z directions (Re=750, b/d_n=0.5, $Ek_{1,2}$=4.25x10^{-4}, r_p/r_d=0.667, β=0.5).

The GCI's values, the percent error, and $T_{h=0}$ at r/r_d=0.4 are shown in Table 3.6. The mesh convergence for different grids was calculated using the following equations (3.6.1 to 3.6.5). In addition, the last column of Table 3.6 shows that a grid of 34x63 is the most accurate with a percent error of 5.70x10^{-3} from its asymptotic numerical exact

solution. The purpose of the GCI method is to point out an error band and how far the local solution of each particular grid is from its asymptotic value.

Table 3.6 Grid convergence study of figure 3.17.

Run #	MSH	GCI (%)	T_{int} at r/r_d= 0.4 (K)	$T_{h=0}$ at r/r_d= 0.4 (K)	Eq.3.6.5 (%error)
1	34x59	$GCI_{12} = 8.8x10^{-3}$	333.06414	333.043	$6.3x10^{-3}$
2	34x63	$GCI_{23} = 8.8x10^{-4}$	333.024125		$5.7x10^{-3}$
3	36x64	$GCI_{31} = 7.9x10^{-3}$	333.019651		$7.0x10^{-3}$

3.6.4 Chemical Mechanical Polishing Model

The distribution of an element size in a computational domain is determined from a mesh independence study by systematically changing the element density in all space directions to obtain a mesh of acceptable accuracy. Several grids or combinations of number of elements were used to determine the flow field and wafer interface temperature distribution, as shown in figure 3.18. The numerical solution becomes grid independent for the number of elements equal to 1,344. Numerical results for 1,344 elements gave almost identical results compared to those using 780 and 1,600 elements. The average margin of error was 0.0244%. A set of temperature distributions across the slurry region just below the wafer surface along the film thickness was used to characterize the accuracy of the mesh model. Therefore, all further computations were carried out using a grid of 1,344 elements.

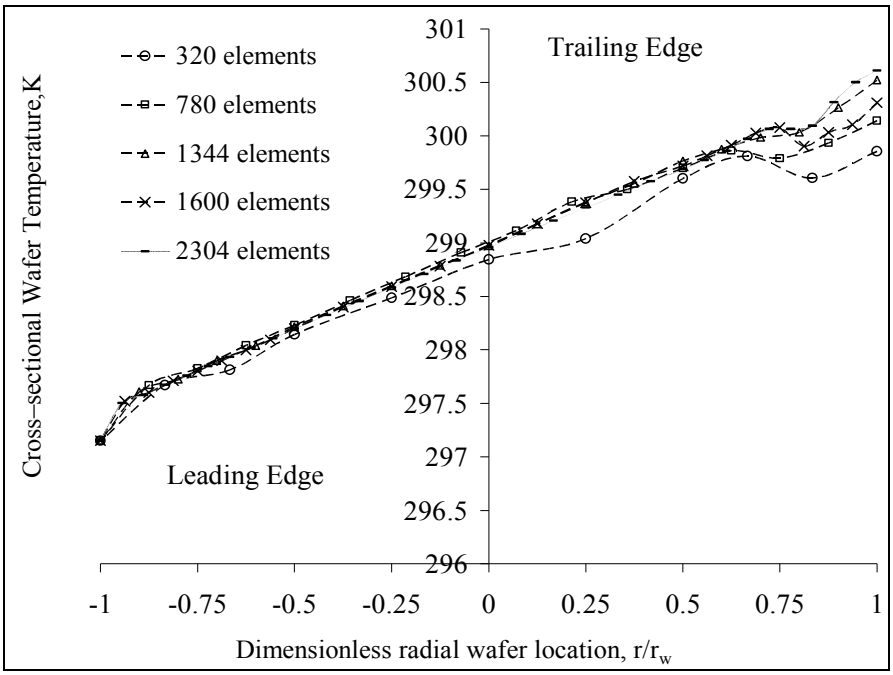

Figure 3.18 Temperature distribution across the slurry region beneath the substrate surface for various number of elements (Q_{sl}=65 cc/min, Ω_w=15 RPM, Ω_p=150 RPM, COF=0.4, δ_{sl}=50 μm, P=24.35 kPa, r_w=1.9 cm, q_{sl}=7.24 to 10.12 kW/m^2).

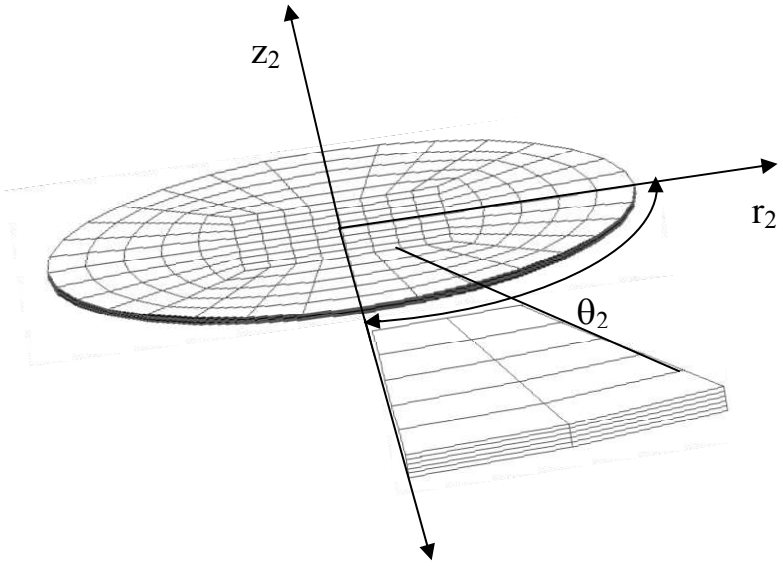

Figure 3.19 Grid topology of control volume that includes the wafer, alumina slurry, and polishing pad.

The mesh grid topology of a slurry film thickness of 50 μm is plotted at figure 3.19. A uniform and denser distribution of elements was used at the center of the control volume region to capture the thermal effect of the constrict alumina slurry, as shown in figure 3.19.

Chapter 4 Free Liquid Jet Impingement Model Results

4.1 Steady State Cooling of Spinning Target

A typical velocity vector distribution is shown in figure 4.1. It can be seen that the velocity remains almost uniform at the potential core region of the jet. The velocity decreases and the fluid jet diameter increases as the fluid gets closer to the plate during the impingement process.

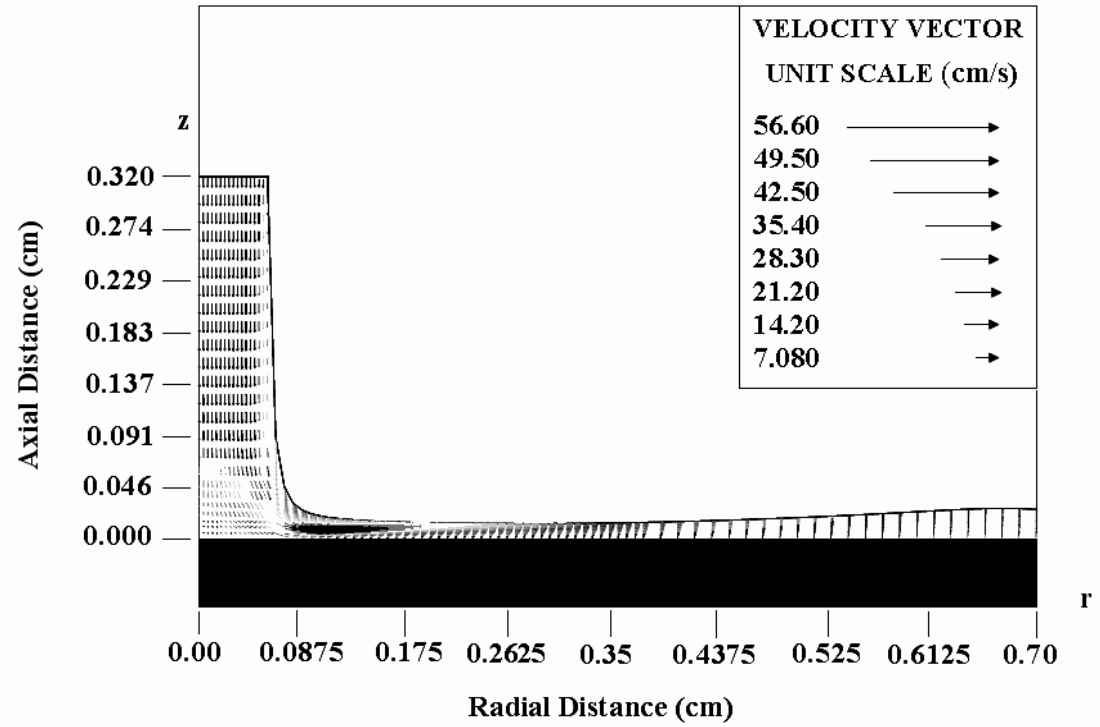

Figure 4.1 Velocity vector distribution for jet impingement on a silicon wafer with water as the cooling fluid (Re=900, Ek=2.65x10^{-4}, β=2.67, b/d_n=0.5).

The direction of motion of the fluid particles shifts by as much as 90°. After this, the fluid accelerates creating a region of minimum sheet thickness. This is the start of the

boundary layer zone. It can be noticed that as the boundary layer thickness increases with radius, the frictional resistance from the wall is eventually transmitted to the entire film thickness. This is called fully viscous zone. The three different regions observed in the present investigation are in agreement with the experiments of Liu et al. [17].

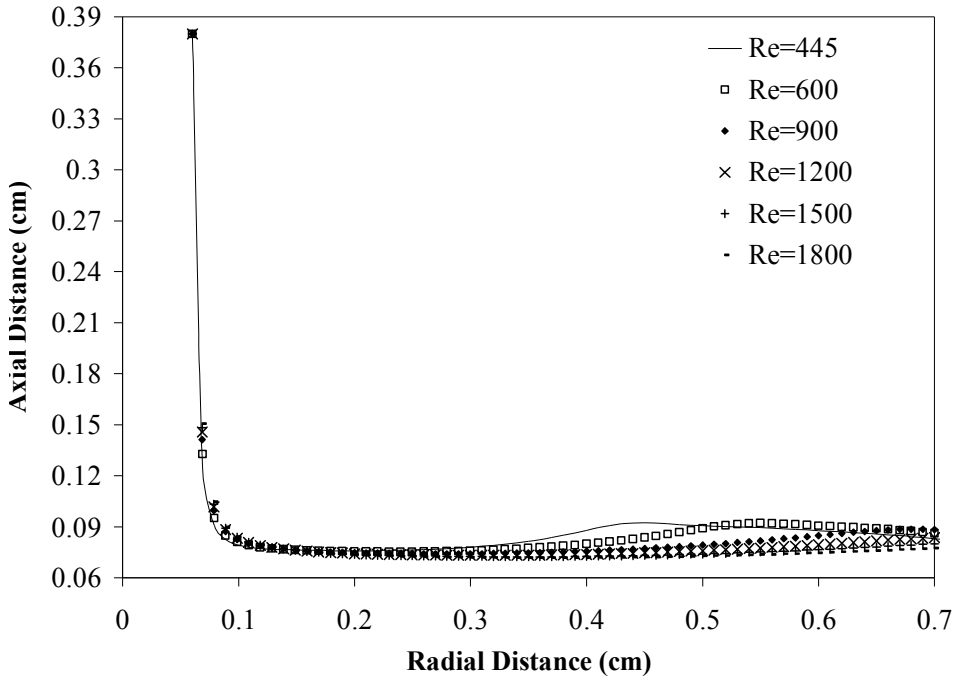

Figure 4.2 Free surface height distribution for different Reynolds numbers with water as the cooling fluid ($Ek=2.65x10^{-4}$, $\beta=2.67$, $b/d_n=0.5$).

Figure 4.2 presents the free surface height distribution for different Reynolds numbers when the jet strikes the center of the disk while it is spinning at a rate of 125 RPM. It can be seen that the fluid spreads out radially as a wavy thin film. As the Reynolds number increases the film diminishes in thickness under the same constant spinning rate due to a larger impingement velocity that translates to a higher fluid velocity in the film. For the conditions considered in the present investigation, the flow was supercritical and a hydraulic jump did not occur within the computation domain. These observations are in agreement with the experimental work of Metzger et al. [37].

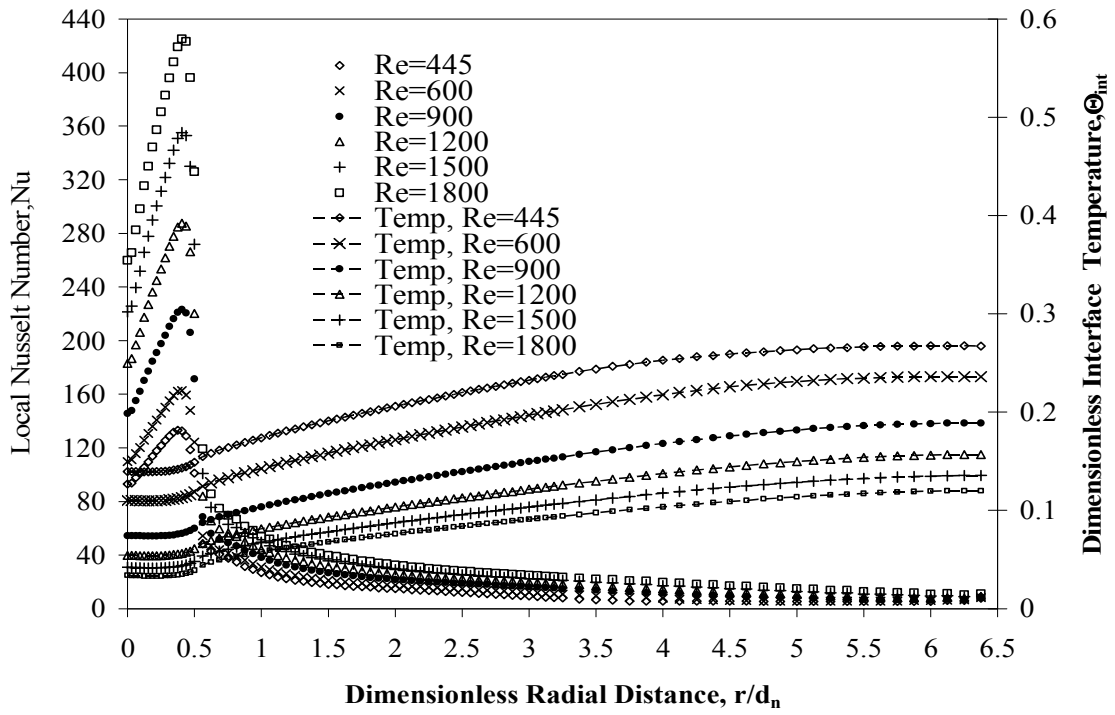

Figure 4.3 Dimensionless interface temperature and local Nusselt number distributions for a silicon wafer with water as the cooling fluid for different Reynolds numbers ($Ek=2.65x10^{-4}$, $\beta=2.67$, $b/d_n=0.5$).

Figure 4.3 shows the dimensionless interface temperature and local Nusselt number distributions as a function of dimensionless radial distance (r/d_n) along the solid–fluid interface at different Reynolds numbers for a rotational rate of 125 RPM. The curves in figure 4.3 reveal that the dimensionless interface temperature decreases with jet velocity (or Reynolds number). The dimensionless interface temperature has the lowest value at the stagnation point (underneath the center of the axial opening) and increases radially reaching the highest value at the end of the disk. The local Nusselt number distributions, as shown in figure 4.3 increases rapidly over a small distance (core region) measured from the stagnation point, reaching a maximum around $r/d_n=0.40$, and then decreases along the radial distance as the boundary layer develops further downstream. The location of the maximum Nusselt number can be associated with the transition of the

flow from the vertical impingement to horizontal displacement where the boundary layer starts to develop. Figure 4.3 confirms to us how an increasing Reynolds number contributes to a more effective cooling by the enhancement of the convective heat transfer coefficient.

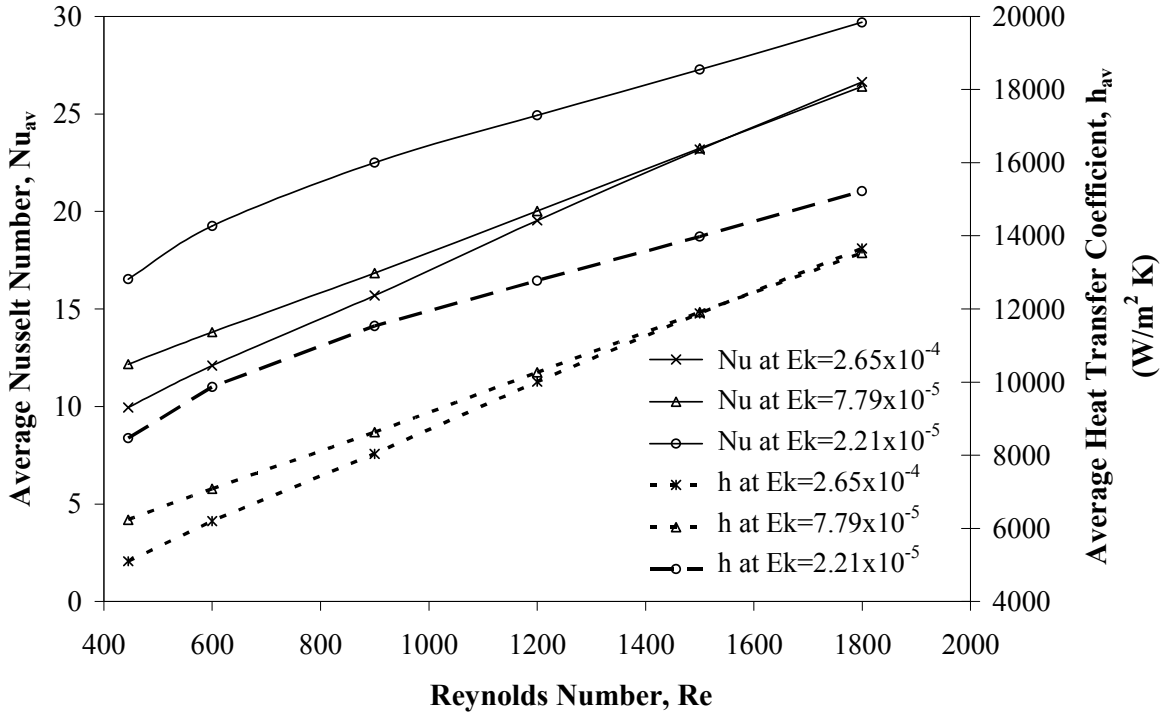

Figure 4.4 Average Nusselt number and heat transfer coefficient variations with Reynolds number for a silicon wafer with water as the cooling fluid (β=2.67, b/d_n=0.5).

Figure 4.4 plots the average Nusselt number and average heat transfer coefficient as a function of Reynolds numbers for low, intermediate, and high Ekman numbers or rotational rates. It may be noted that average Nusselt number increases with Reynolds number. As the flow rate (or Reynolds number) increases, the magnitude of fluid velocity near the solid–fluid interface that controls the convective heat transfer rate increases. Furthermore, at a particular Reynolds number the graphical values are shifted gradually upward due to an increment of the spinning rate. This behavior confirms the positive

influence of the rotational rate on the average Nusselt number and average heat transfer coefficient.

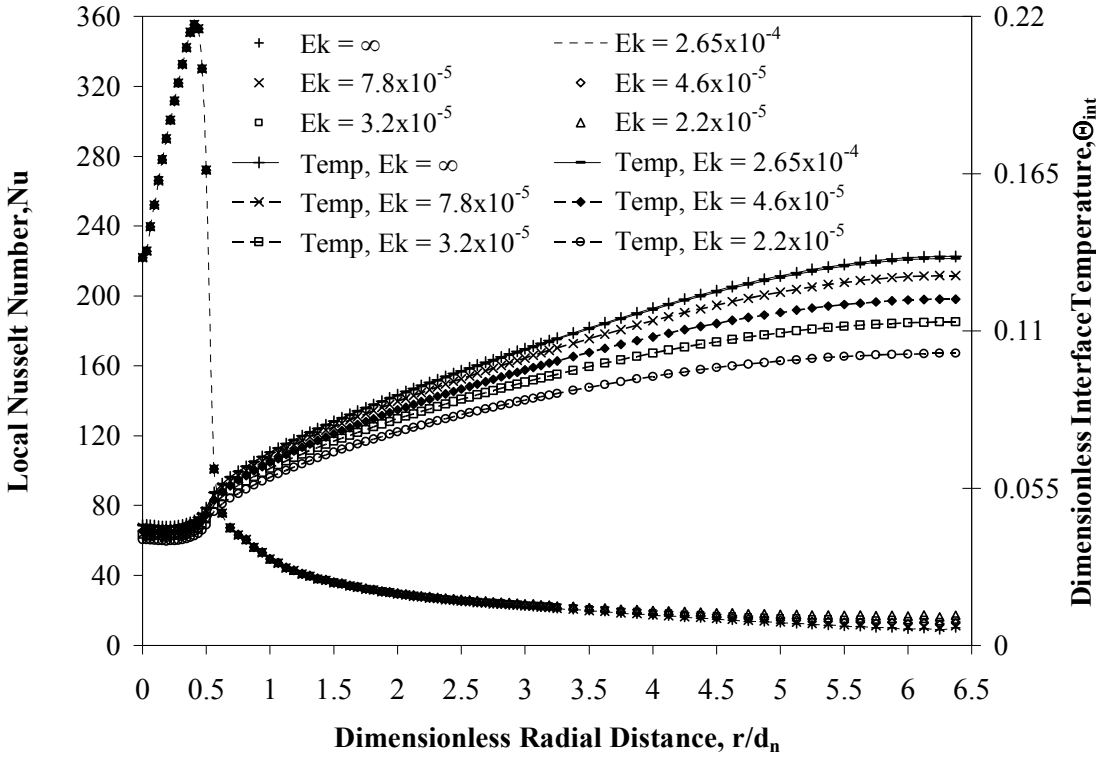

Figure 4.5 Dimensionless interface temperature and local Nusselt number distributions for a silicon wafer with water as the cooling fluid at different Ekman numbers (Re=1,500, β=2.67, b/d_n=0.5).

The rotational rate effects of the solid wafer on the dimensionless interface temperature and local Nusselt number are illustrated in figure 4.5. It can be noted that Nusselt number distribution does not change drastically with the variation of rotational rate or Ekman number in figure 4.5. Differences are seen only at large radial location of the disk where the magnitude of the centrifugal force encountered by the liquid film is higher. This clearly indicates that at Re=1,500 the flow field is dominated by the momentum of the impinging jet. However, the dimensionless interface temperature changes along the entire disk radius with the variation of Ekman number. It can be noted

that dimensionless interface temperature decreases with the increment of the rotational rate due to the enhancement of local fluid velocity adjacent to the wafer.

The average Nusselt number and heat transfer coefficient variations as a function of Ekman number at high, intermediate, and low Reynolds numbers are shown in figure 4.6. As the Ekman number decreases from 2.65×10^{-4} to 2.21×10^{-5} the average Nusselt number and heat transfer coefficient increases by an average 27.15% under high Reynolds number (Re=1,500) and 13.19% under low Reynolds number (Re=750) with an overall increment of 20.17% in general.

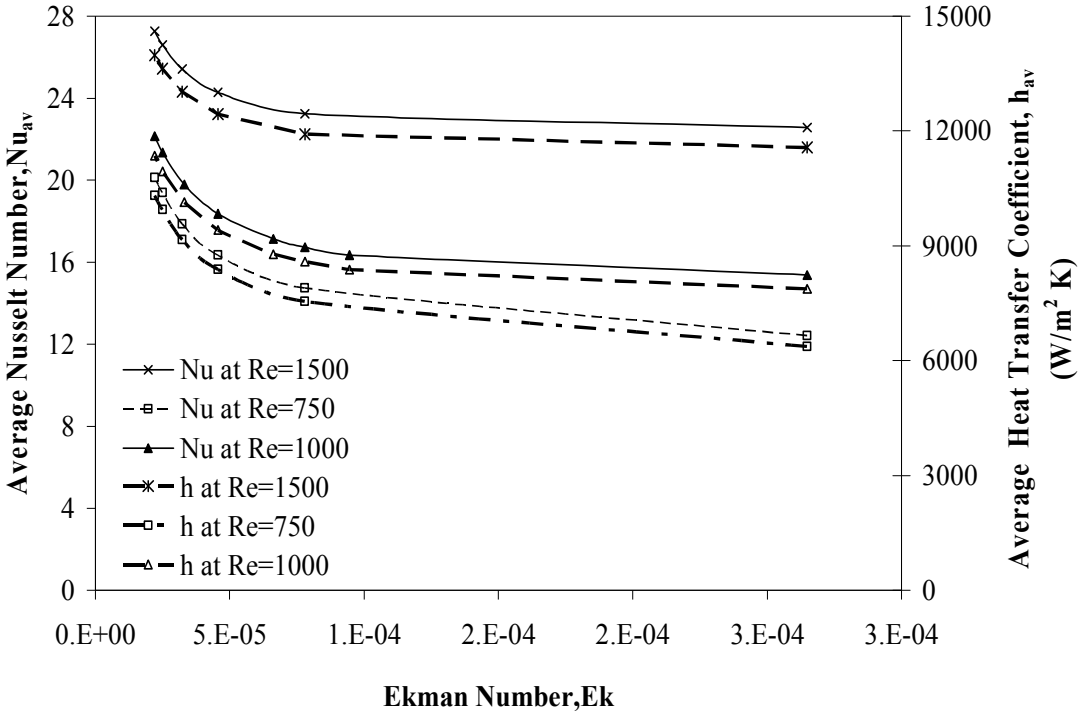

Figure 4.6 Average Nusselt number and heat transfer coefficient variations with Ekman number for a silicon wafer with water as the cooling fluid (β=2.67, b/d_n=0.5).

The effects of disk thickness variation on the solid–fluid dimensionless interface temperature and local Nusselt number are shown in figure 4.7.

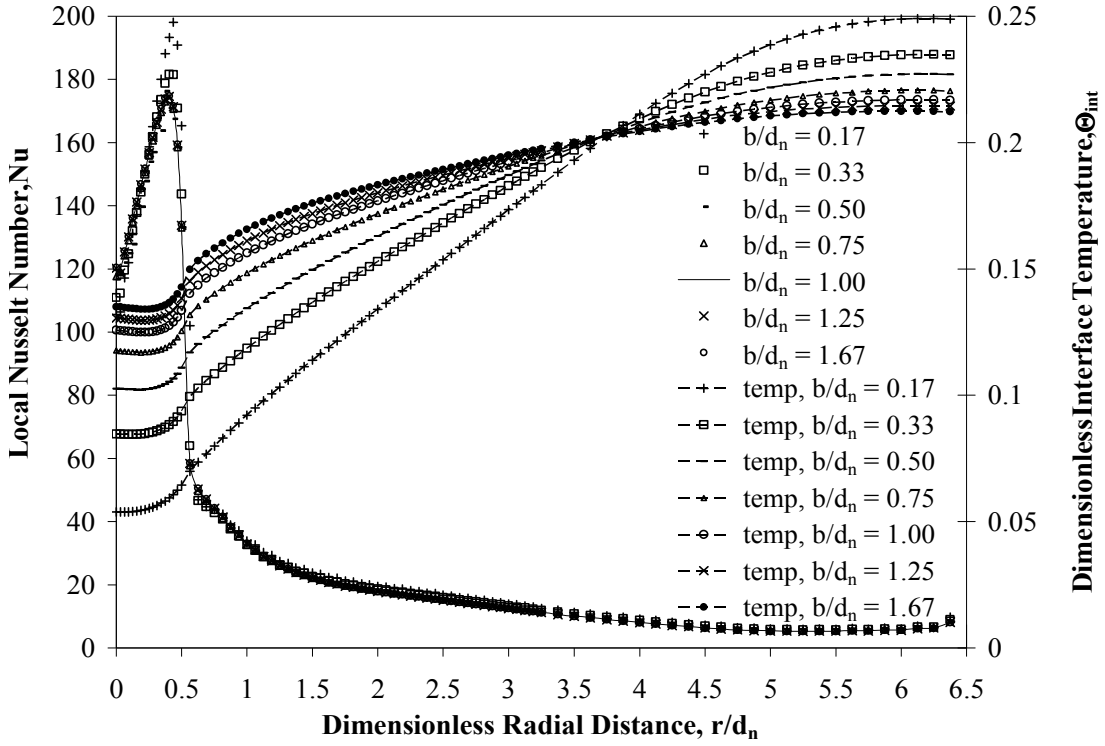

Figure 4.7 Dimensionless interface temperature and local Nusselt number distributions for different wafer thicknesses with water as the cooling fluid (Re=1,000, Ek=2.65x10^{-4}, β=2.67).

In these plots, silicon has been used as the disk material and water as the cooling fluid. The dimensionless solid–fluid interface temperature distribution in figure 4.7 increases from the impingement region all the way to the end of the disk. It may be also noted that the curves intersect with each other at a dimensionless radial distance of r/d_n=3.75. Thicker disks generate more uniform dimensionless interface temperature due to a larger radial conduction within the disk. In addition, the dimensionless solid–fluid interface temperature and local Nusselt number distributions did not change much beyond a disk thickness of 0.60 mm, or dimensionless thickness b/d_n=0.50 indicating that the overall heat transport reached a convection–conduction equilibrium condition at the solid–fluid interface. Local Nusselt number distributions do not change significantly with the

variation of disk thickness. Higher local Nusselt number values are observed at a dimensionless radial distance (r/d_n) of less than 0.5 for all curves. These steep Nusselt numbers values were generated by a higher rate of heat removal at the impingement zone.

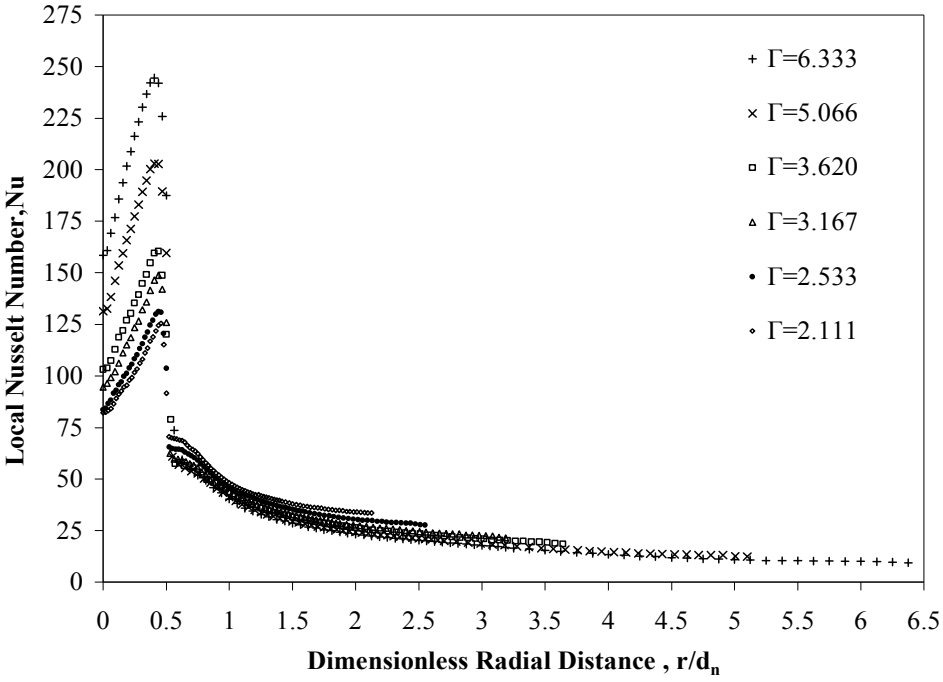

Figure 4.8 Local Nusselt number distribution for different nozzle diameters for a silicon wafer with water as the cooling fluid (Re=1,000, Ek=6.62×10^{-5}, β=2.67, b/d_n=0.5).

Figures 4.8 shows the local Nusselt number distributions as a function of dimensionless radial distance (r/d_n) along the solid–fluid interface for different disk radius to nozzle diameter ratio (Γ) from 2.11 to 6.33 under a Reynolds number of 1,000 and rotational rate of 500 RPM. Nusselt number increases rapidly over a small distance at the core region measured from the stagnation point, reaches a maximum around r/d_n=0.40, and then decreases along the radial distance as the boundary layer develops further downstream. The location of the maximum Nusselt number can be associated with the transition of the flow from the vertical impingement to horizontal displacement

where the boundary layer starts to develop. It can be noticed that local Nusselt number is greater for higher Γ in the impingement zone whereas it is somewhat lower at higher Γ in the boundary layer zone. For a constant Reynolds number and constant disk radius, a larger value of Γ is realized at higher jet velocity. Therefore it provides a higher rate of convective heat transfer in the stagnation region where the jet directly strikes the disk. Since higher Γ is also associated with lower jet diameter. The fluid has to travel over a longer path in the boundary layer region where it losses its momentum resulting in lower convective heat transfer rate by the time it exists the disk surface.

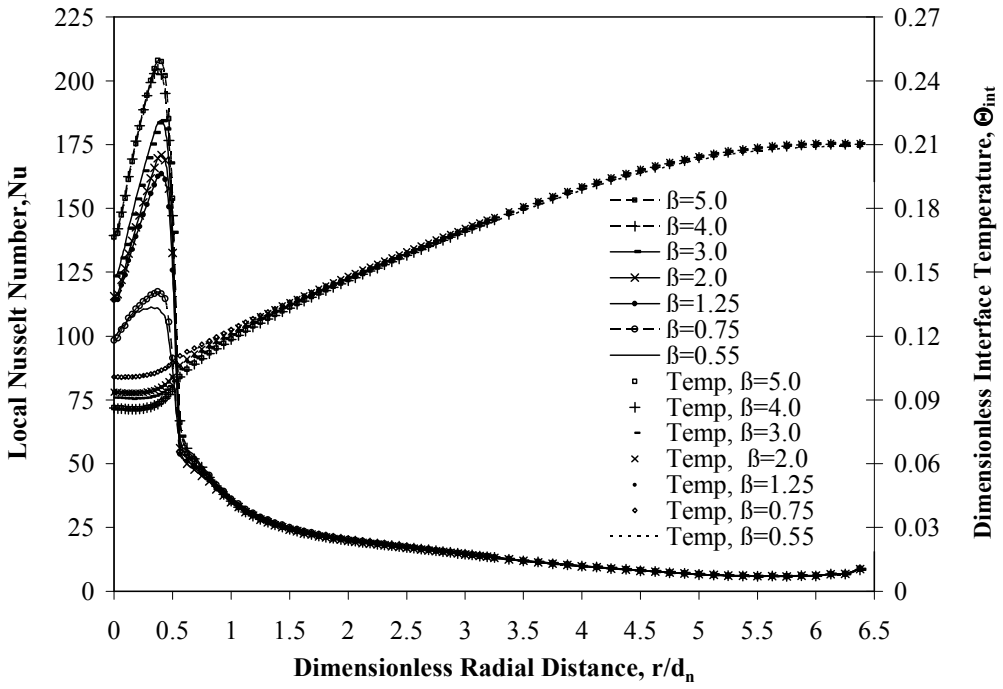

Figure 4.9 Dimensionless interface temperature and local Nusselt number distributions for a silicon disk with water as the cooling fluid for different nozzle to target spacing (Re=750, Ek=2.65x10^{-4}, b/d_n=0.5).

The solid–fluid dimensionless interface temperature and local Nusselt number distributions for seven different nozzle to target spacing for water as the coolant at a spinning rate of 125 RPM and Reynolds number of 750 are shown in figure 4.9. It may

be noticed that the impingement height quite significantly affects the dimensionless interface temperature as well as the Nusselt number only at the smaller radii that contain the stagnation region and the early part of the boundary layer region. At larger radii the values are identical for all impingement heights. It is quite expected since the impingement height essentially controls the change in velocity the fluid particles encounter during the free fall from nozzle exit to target disk surface and therefore affects areas controlled by direct impingement. This observation is somewhat similar to a previous study by Owosina [143] for free jet impingement over a stationary disk.

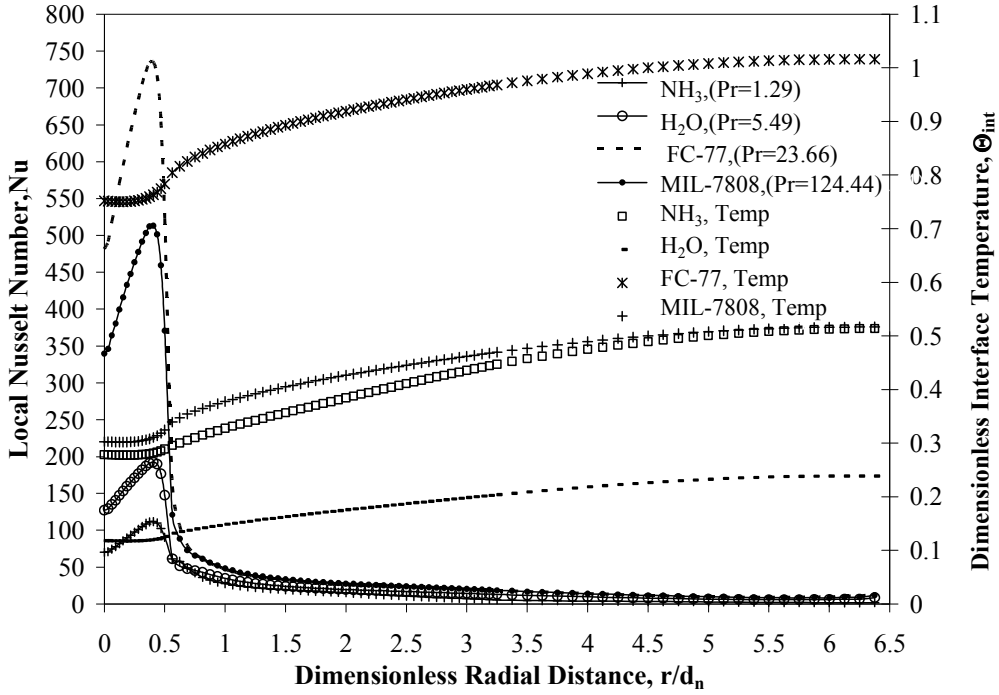

Figure 4.10 Local Nusselt number and dimensionless interface temperature variations for different cooling fluids for silicon as the disk material (Re=750, Ω=125 RPM, β=2.67, b/d_n=0.5).

Figures 4.10 compares the solid–fluid interface temperature and local Nusselt number distribution results of our primary working fluid (water) with three other coolants that have been considered in previous thermal management studies, namely ammonia

(NH_3), flouroinert (FC–77) and oil (MIL–7808). It may be noticed that water presents the lowest interface temperature and second lowest Nusselt number distribution in comparison with FC–77, NH_3 and MIL–7808. The highest Nusselt number is obtained when FC–77 is used as the working fluid. This is primarily because of its lower thermal conductivity compared to the other fluids. There results are for a constant Reynolds number of 750 while the disk is spinning at a rate of 125 RPM.

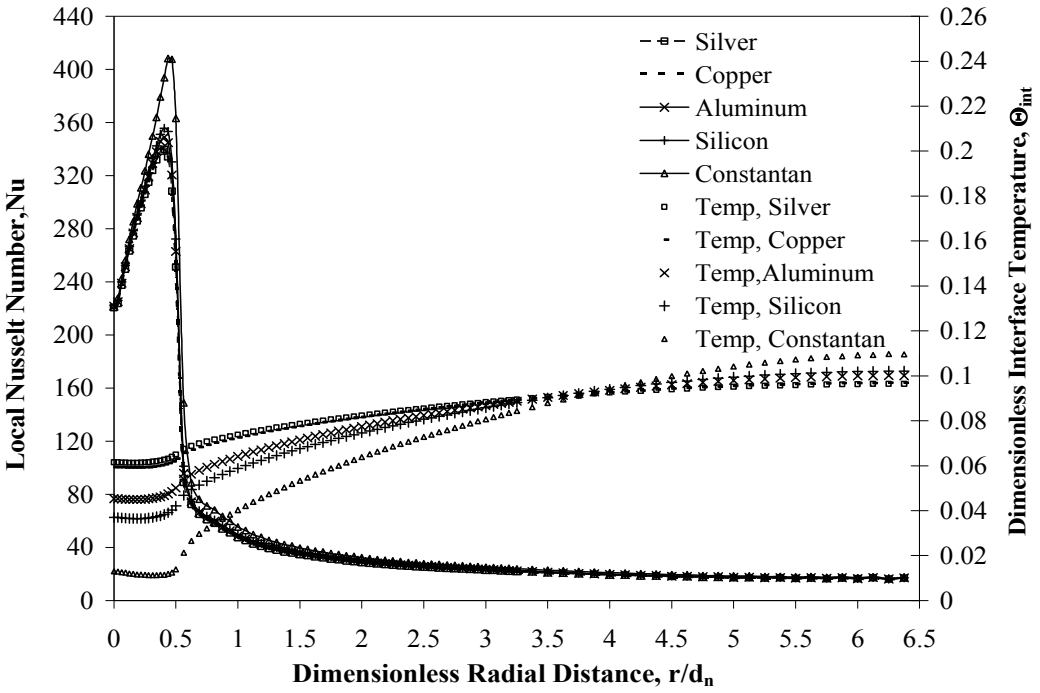

Figure 4.11 Local Nusselt number and dimensionless interface temperature variations for different solid materials with water as the cooling fluid (Re=1,500, Ek=2.21×10^{-5}, β=2.67, b/d_n=0.5).

Figure 4.11 shows the dimensionless interface temperature and local Nusselt number distribution plots as a function of a dimensionless radial distance (r/d_n) for different solid materials with water as the working fluid. The studied materials were silicon, silver, aluminum, copper, and Constantan, having different thermo–physical properties. Constantan shows the lowest dimensionless temperature at the impingement

zone and the highest at the outlet in comparison with other solid materials. Copper and silver show a more uniform distribution and higher temperature values at the impingement zone due to their higher thermal conductivity. The dimensionless temperature and local Nusselt number distributions of these two materials are almost identical due to their similar thermal conductivity values. The cross–over of curves for all five materials occurred due to a constant fluid flow and heat flux rate that reaches a thermal energy balance. Solid materials with lower thermal conductivity show higher maximum local Nusselt number.

Figure 4.12 presents the maximum temperature and maximum to minimum temperature difference at the interface for all five disk materials studied under different disk thicknesses with water as the working fluid. The temperature control is crucial in the design of electronic packages. The maximum temperature at the interface as well as the maximum solid disk temperature decreases as the disk thickness increases. It maybe noticed that effects are fairly large at smaller thicknesses indicating that it is a crucial parameter in maintaining the temperature uniformity. On the other hand increasing the disk thickness beyond certain limit, for each solid material, may not be useful. The choice of disk material is also crucial in determining the magnitudes of these temperatures. A material with larger thermal conductivity will facilitate a faster rate of heat transfer, and therefore will result in a lower maximum temperature at the solid–fluid interface and inside the solid. The temperature difference at the interface is an indication of the level of temperature non–uniformity at the impingement surface, while the maximum temperature inside the solid indicates the thermal resistance generated by the disk material. When the disk thickness is negligible, the interface temperature is controlled by the heat flux

condition at the heater. Adequate thickness provided a more uniform interface temperature due to radial heat spreading within the solid. The maximum to minimum temperature difference is strongly affected by thermal conductivity of the disk material decreasing it as the disk thermal conductivity increases. These findings are in agreement with Rahman et al. [20] who studied free liquid jet impingement over a stationary disk.

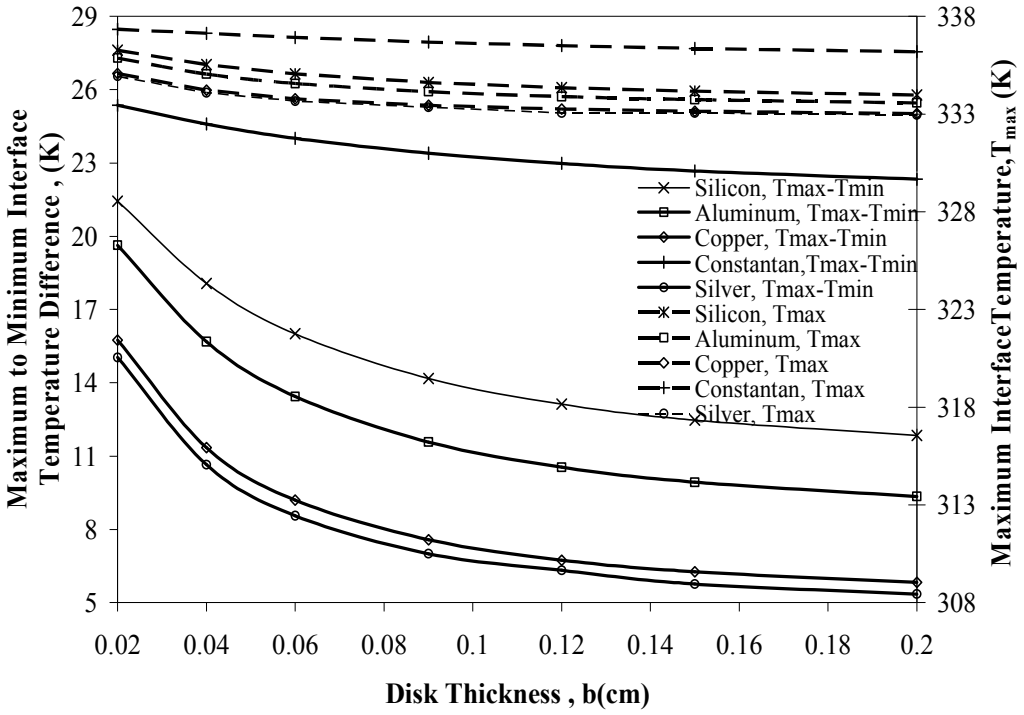

Figure 4.12 Maximum to minimum temperature difference and maximum solid–fluid interface temperature (Re=1,500, d_n=0.12 cm, β=2.67, Ek=2.21x10^{-5}).

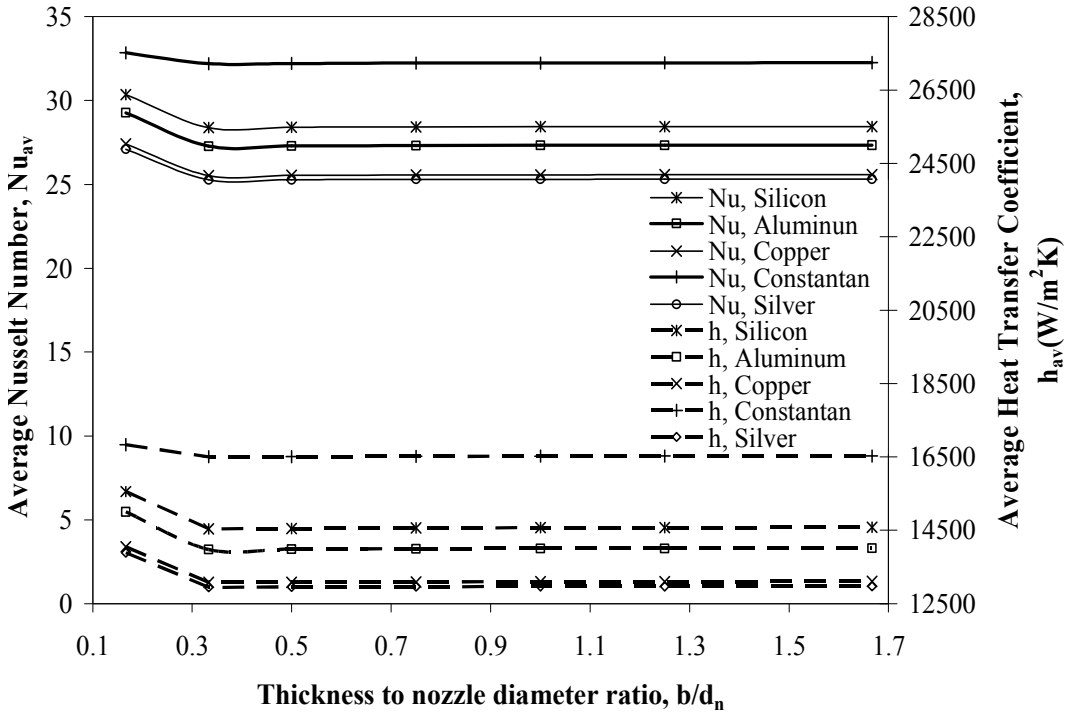

Figure 4.13 Average Nusselt number and heat transfer coefficient variations with disk thickness (Re=1,500, Ek=2.21x10^{-5}).

The effects of disk thickness on the average heat transfer coefficient and Nusselt number for all five materials can be observed in figure 4.13. It shows that the average heat transfer coefficient and average Nusselt number attain constant values at b/d_n greater than 0.50 for all the materials. Constantan has the highest average heat transfer coefficient value among these materials. This behavior is in agreement with the local Nusselt number distribution shown in figure 4.11. The radial conduction becomes stronger as the disk thickness increases generating a better heat distribution at the interface. However, the increment of solid thickness beyond certain limit creates more thermal resistance, which ends up crippling the heat transfer process.

Two of the papers used for the validation of this numerical study were the experimental work carried out by Stevens and Webb [16] and analytical studies by

Watson [4]. Computations were carried out for a water jet that impinges perpendicularly at the center of a stationary solid disk at various nozzle to target spacing ratios. Figure 4.14 compares the calculated local free surface height distributions with the profiles reported by the experimental studies of Stevens and Webb [3] and the analytical results of Watson [4] at different nozzle diameters (d_n=2.1 and 4.6 mm. The numerical values compare reasonably well with the measured free surface heights and Watson's analytical predictions.

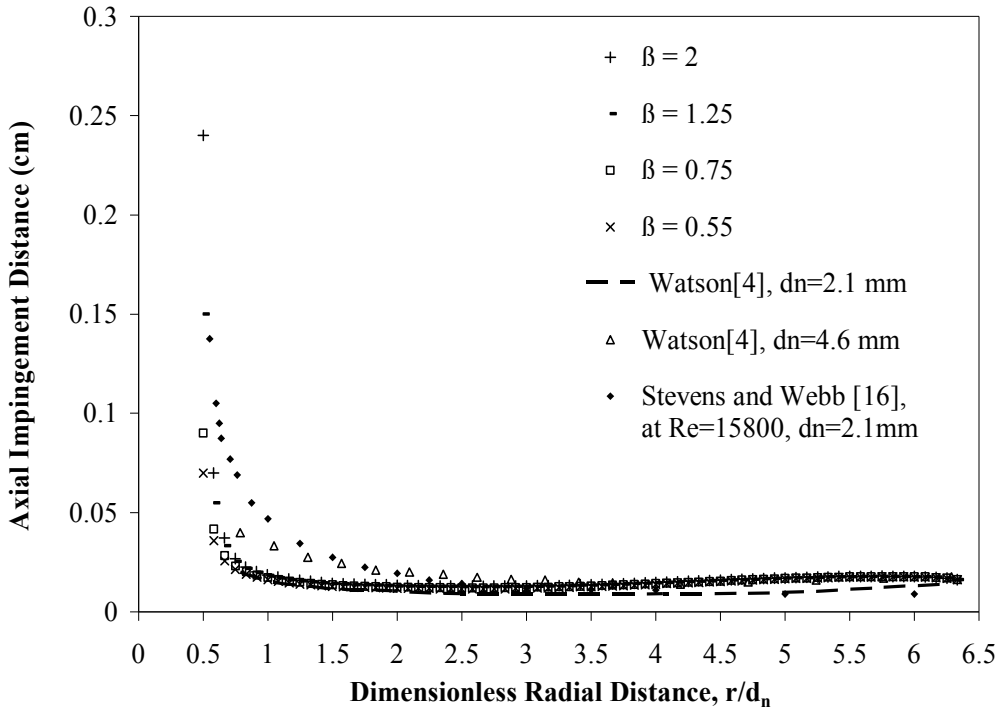

Figure 4.14 Comparison of height of the free surface with analytical predictions of Watson [4] and experimental data of Stevens and Webb [16] (Re=1,500, Ek=∞, b/d_n=0.5).

In addition, the present numerical simulation results at steady state were compared with the steady state test data acquired by Leland and Pais [19] for a disk with no rotation. The average heat transfer coefficient from the present numerical simulation using MIL–7808 as the working fluid for different combinations of Reynolds number and

input heat flux were compared with the experimental measurements of Leland and Pais [19]. The percent difference of present average heat transfer coefficient results was defined in the following form: % diff = $((h_{num} - h_{exp})/h_{exp})\times 100$. The percent difference was in the range of 0.41%–5.53%. Considering the uncertainty of experimental measurements and round off and discretization errors in numerical computation, the overall comparison between test data and numerical results can be considered quite satisfactory.

The third paper used for comparison of this numerical study was the analytical work carried out by Liu and Lienhard [10]. They obtained an integral solution for the heat transfer coefficient in the boundary layer and similarity regions for Prandtl number greater than the unity for a stationary disk.

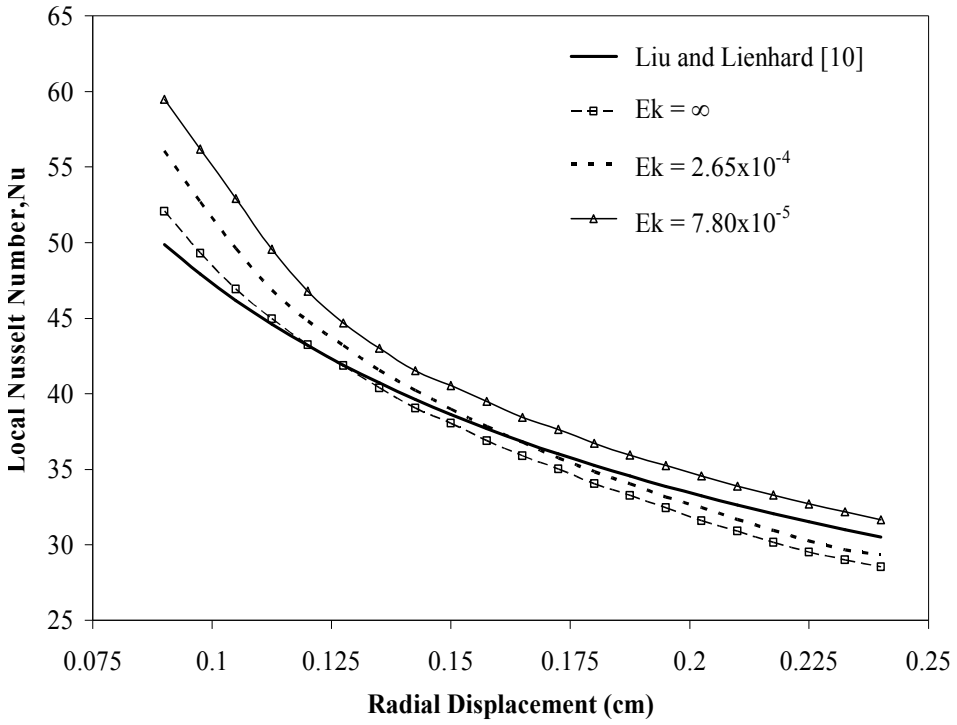

Figure 4.15 Local Nusselt number comparison with Liu and Lienhard [10] under different Ekman numbers (Re=1,500, β=2.67, b/d_n=0.5).

A graphical representation of the Nusselt number correlation from Liu and Lienhard [10] and present numerical results at different spinning rates with water as the working fluid are shown in figure 4.15. The percent difference of present local Nusselt number was defined in the form: % diff = $((Nu_{num} - Nu_{analy})/Nu_{analy}) \times 100$. The results shown for a stationary disk compare within an average difference of 3.25% with Liu and Lienhard correlation. The local Nusselt number under spinning rates at 125 and 425 RPM correlates with an average margin of 3.49% and 21.83% respectively. In general, the overall average difference of local Nusselt numbers was equal to 9.52%. A better comparison for stationary disk and higher deviation with higher spinning rate is expected, since the correlation in [10] was developed for a stationary disk.

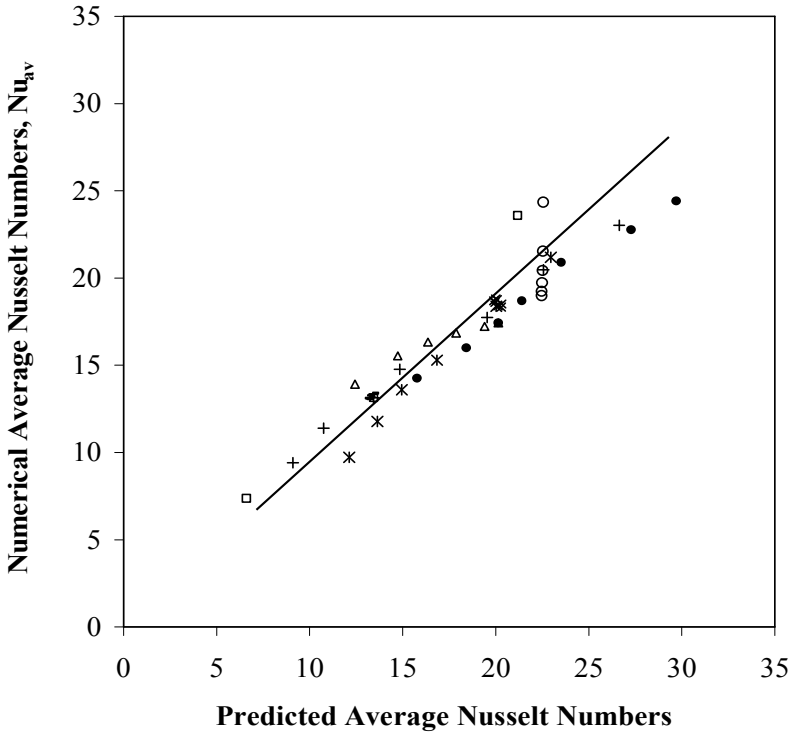

Figure 4.16 Comparison of predicted average Nusselt numbers of equation 4.1 with present numerical data.

One of the goals of this dissertation was to develop a predictive trend of the average heat transfer coefficient. A graphical comparison of the correlating equation and the numerical average Nusselt numbers obtained from this computational analysis is shown in figure 4.16. A correlation for the average Nusselt number was developed as a function of thermal conductivity ratio, nozzle–to–plate spacing, Prandtl number, Ekman number, and Reynolds number to accommodate most of the transport characteristics of a free liquid jet impingement cooling process. A correlation that best fitted the numerical data can be placed in the following form:

$$Nu_{av}=Re^{0.385} \cdot Ek^{-0.091} \cdot Pr^{0.4} \cdot \beta^{0.0114} \cdot \varepsilon^{-0.25} \quad (4.1)$$

The ranges of the dimensionless variables used are the following: $445 \leq Re \leq 1{,}800$, $2.65\text{x}10^{-4} \leq Ek \leq 2.21\text{x}10^{-5}$, $Pr=5.49$, $0.55 \leq \beta \leq 5.0$, $227.6 \leq \varepsilon \leq 697.5$. The Prandtl number exponent was taken from Martin's equation [144] for single round nozzle impinging jet. The Average Nusselt number data were then correlated in order to determine the other exponents of equation 4.1 using the least squares curve fitting method. The percent difference of the predicted average Nusselt number was defined as: $\%\ \text{diff} = ((Nuav_{pred} - Nuav_{num})/Nuav_{num}) \times 100$. The differences between numerical and predicted average Nusselt number values are in the range of +19.63% to –17.83%. It should be noted from figure 4.16 that a large number of data points are well correlated with equation 4.1 and only a few are near the limits.

4.2 Transient Cooling of Spinning Target

The following section presents the transient conjugate heat transfer of a free liquid jet impinging on a rotating solid disk of finite thickness and radius. Figure 4.17 illustrates the dimensionless interface temperature for different time instants. It can be observed that

at the early part of the transient heat transfer process, the solid–fluid interface maintains a more uniform temperature. The difference of dimensionless maximum and minimum temperature at the solid–fluid interface increases from 0.012 at Fo=0.005 to 0.128 when the steady state condition reached at Fo=0.339. This pattern is due to the thermal storage in the fluid that is necessary to develop the thermal boundary layer since an isothermal condition was present at the beginning of the transient heat transfer process. As time goes on, the thickness of the thermal boundary layer increases and therefore the temperature rises. The interface temperature responds to the boundary layer thickness that increases downstream. Therefore, the temperature becomes minimum at the impinging point and maximum at the outer edge of the disk.

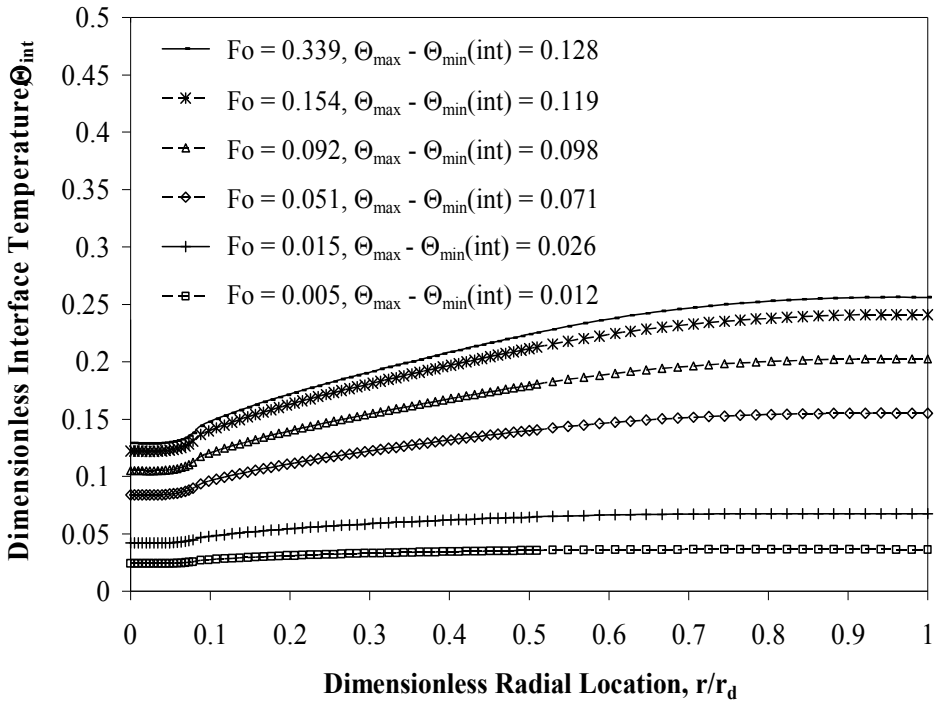

Figure 4.17 Dimensionless interface temperature distributions for different Fourier numbers (Re=500, Ek=2.65x10^{-4}, β=2.67, silicon disk, water, b/d_n=0.5, q_w=125 kW/m^2).

Figure 4.18 shows the variation of local Nusselt number along the solid–fluid interface at different time instants. The local Nusselt number decreases with time until it reaches the steady state equilibrium distribution. The local Nusselt number is controlled by local temperature and local heat flux at the solid–fluid interface. Both of these quantities increase with time. The local Nusselt number shows a higher value at early stages of the transient process due to smaller temperature difference between the liquid jet and disk solid–fluid interface. This essentially means that all heat reaching the solid–fluid interface via conduction through the solid is more efficiently convected out as the local fluid temperature is low everywhere at the interface. The local Nusselt number, as shown in figure 4.18 increases rapidly over a small distance (core region) measured from the stagnation point, reaching a maximum around r/d_n=0.04, and then decreases along the radial distance as the boundary layer develops further downstream.

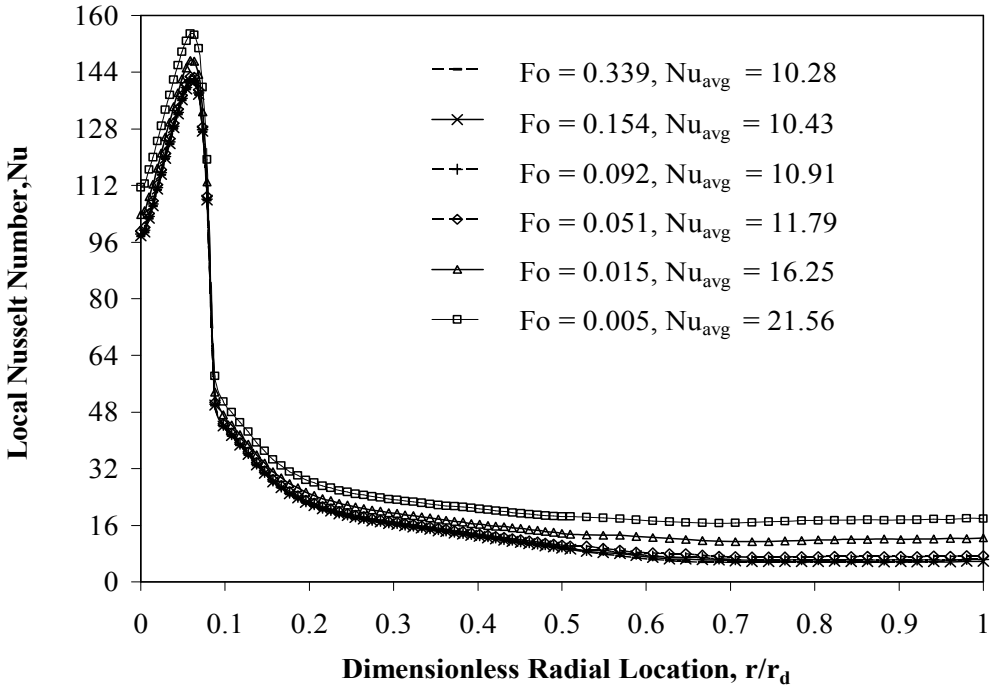

Figure 4.18 Local Nusselt number distributions for different Fourier numbers (Re=500, $Ek=2.65\times10^{-4}$, β=2.67, silicon disk, water, b/d_n=0.5, q_w=125 kW/m^2).

The location of the maximum Nusselt number can be associated with the transition of the flow from the vertical impingement to horizontal displacement where the boundary layer starts to develop. The variation of dimensionless maximum temperature at the interface, maximum temperature inside the solid, and maximum–to–minimum temperature difference at the interface for different Fourier numbers with water as the cooling fluid at different Reynolds numbers are shown in figure 4.19. The control of maximum temperature is important in many critical thermal management applications including electronic packaging. As expected, the temperature increases everywhere with time starting from the initial isothermal condition. A rapid increment is seen at the earlier part of the transient, and it levels off as the thermal storage capacity of the solid diminishes and become zero at the steady state condition.

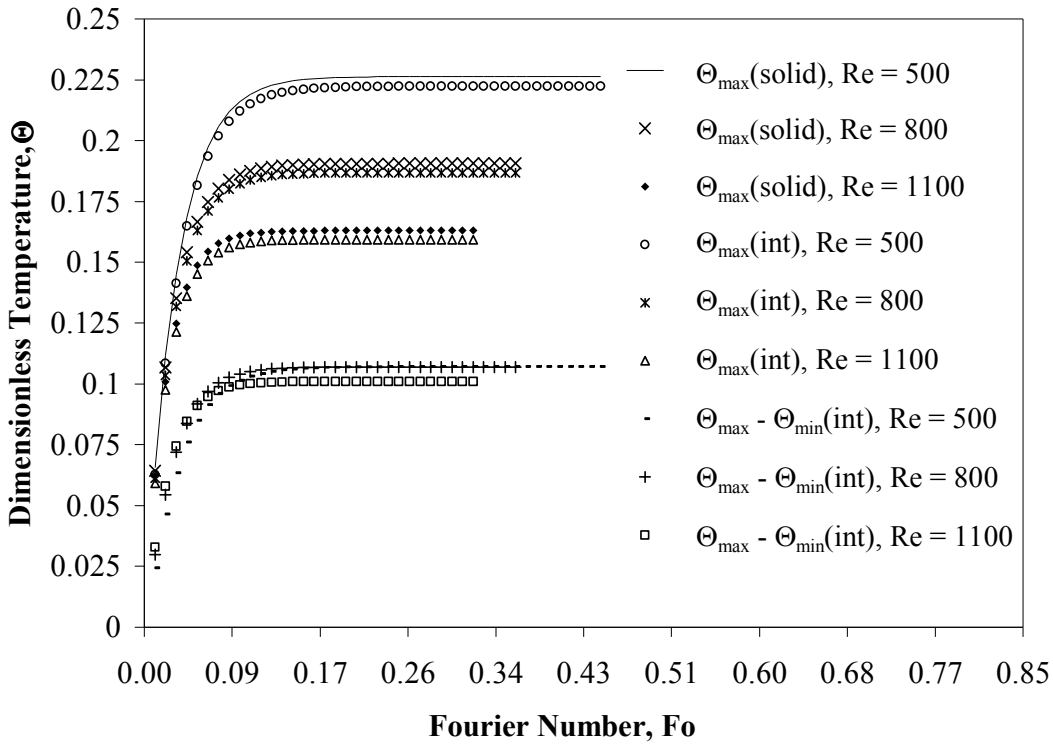

Figure 4.19 Dimensionless maximum temperature variations for different Reynolds numbers ($Ek=2.65x10^{-4}$, $\beta=2.67$, silicon disk, water, $b/d_n=0.5$, $q_w=125$ kW/m^2).

It maybe noted that the time required to reach the steady state condition is lower at a higher Reynolds number because the higher velocity of the fluid helps to enhance the convective heat transfer process. The maximum–to–minimum temperature difference at the interface increases with time as more heat flows throughout the solid disk and transmitted to the fluid.

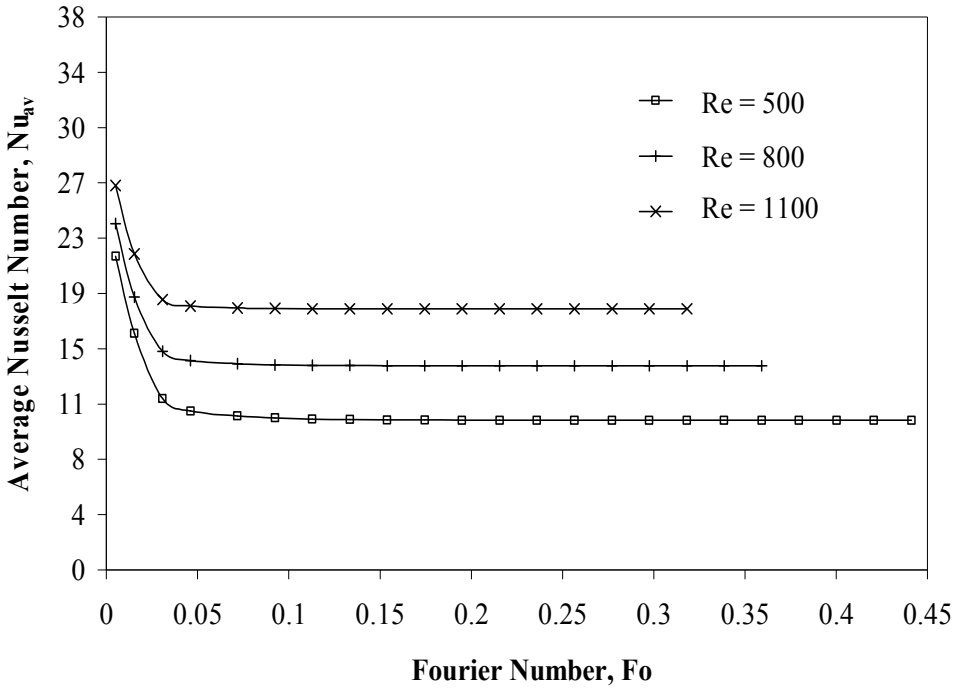

Figure 4.20 Average Nusselt number variations for different Reynolds numbers (Ek=2.65x10^{-4}, β=2.67, silicon disk, water, b/d_n=0.5, q_w=125 kW/m^2).

Figure 4.20 provides the integrated average Nusselt number variations for various Reynolds number with water as the cooling fluid at different time instants. As expected, the average Nusselt number is large at the early part of the transient and monotonically decreases with time ultimately reaching the value for the steady state condition. A higher Reynolds number increases the magnitude of fluid velocity near the solid–fluid interface that controls the convective heat transfer and therefore increases the average Nusselt

number. These observations are in–line with the previous studies by Rahman and Faghri [96, 98] and Saniei et al. [39].

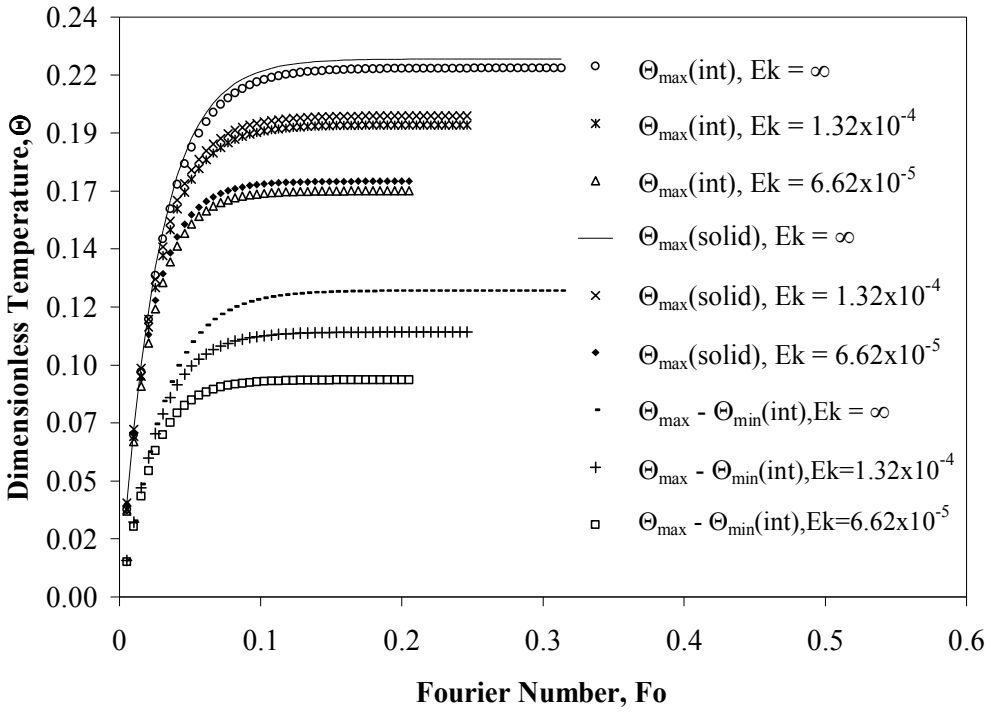

Figure 4.21 Dimensionless maximum temperature variations for different Ekman numbers (Re=750, β=2.67, silicon disk, water, b/d_n=0.5, q_w=125 kW/m^2).

Figure 4.21 shows the results for the dimensionless maximum temperature variation at the interface, maximum temperature inside the solid and maximum–to–minimum temperature difference at the interface for different time instants with water as the cooling fluid for various Ekman numbers. The maximum temperature within the solid was encountered at the outlet adjacent to the heated surface (z= –b, r=r_d). The temperatures rise with time as the solid disk and the fluid store heat showing a rapid response at the earlier part of the heating process until the thermal storage capacity reaches its limit at steady state. The maximum–to–minimum temperature difference at the interface increases with time as more heat flows through the solid disk and transmitted to

the fluid. It may be noted that the magnitude of the dimensionless temperature as well as the time required to reach the steady state condition becomes smaller as the Ekman number decreases. This is because the magnitude of fluid velocity nears the solid–fluid interface that controls the convective heat transfer rate increases with the increment of the rotational rate of the disk or the reduction of Ekman number.

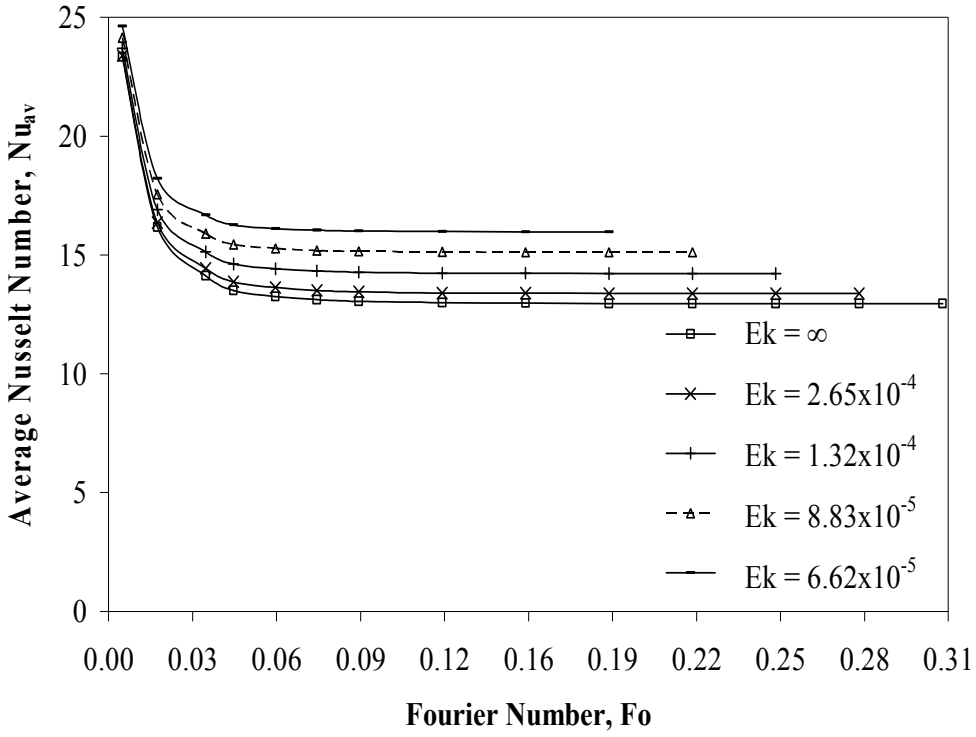

Figure 4.22 Average Nusselt number variations for different Ekman numbers (Re=750, β=2.67, silicon disk, water, b/d_n=0.5, q_w=125 kW/m^2).

The average Nusselt number variations with time for various Ekman numbers are shown in figure 4.22. As expected, the average Nusselt number is large at the early part of the transient and monotonically decreases with time ultimately reaching the value for the steady state condition. Throughout the transient heating process, the average Nusselt number is greater at larger spinning rate or smaller Ekman number. As the Ekman number decreases from ∞ to 6.62x10^{-5} the average Nusselt number increases by an

average of 20.81% when the Reynolds number is kept constant at 750. This observation is in agreement with Rice et al. [46].

Another important factor that controls the transient heat transfer process is the thickness of the disk. Its effect on the dimensionless maximum temperature variation at the interface, maximum temperature inside the solid and maximum–to–minimum temperature difference at the interface for different time instants with water as the cooling fluid is presented in figure 4.23. The plate thickness significantly affects the temperature distribution. It may be noted that as the thickness of the disk increases, the time needed to achieve the steady state condition increases. This is due to more storage capacity of heat within the solid.

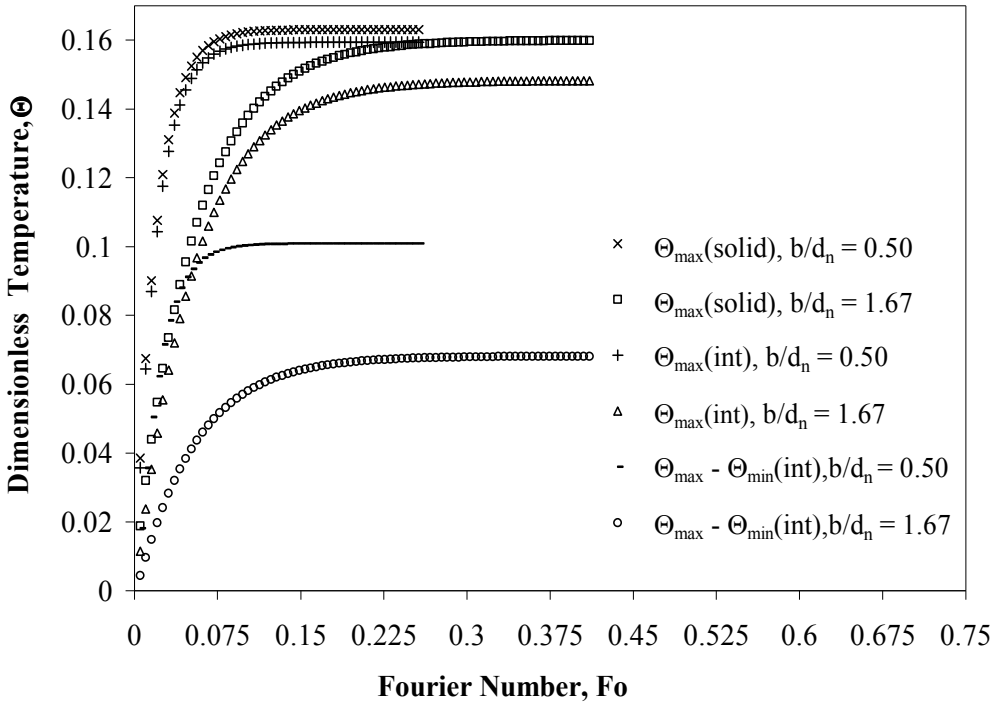

Figure 4.23 Dimensionless maximum temperature variations for different dimensionless disk thicknesses (Re=1,100, Ek=1.20x10^{-4}, β=2.67, silicon disk, water, and q_w=125 kW/m^2).

Also, the temperature at the solid–fluid interface remains lower and more uniform due to higher thermal resistance of the solid to the path of heat flow and higher opportunity for radial conduction within the disk.

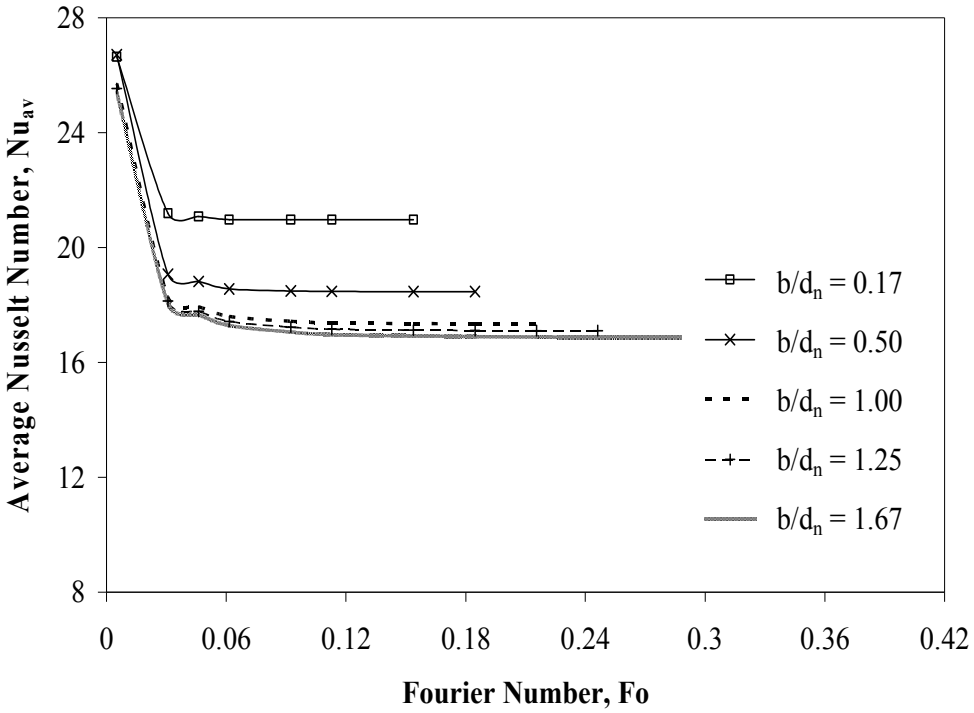

Figure 4.24 Average Nusselt number variations for different dimensionless disk thicknesses (Re=1,100, Ek=1.20x10^{-4}, β=2.67, silicon disk, water, and q_w=125 kW/m^2).

Figure 4.24 shows the average Nusselt number variation as a function of time for five distinct plate thicknesses using silicon as the solid material. The average Nusselt number is higher for a thinner disk. A thinner disk offers lower thermal resistance to the path of the heat flow. In addition, the local convective heat transfer coefficient at the impingement region turns out to be higher because of less smoothing out of interfacial transport due to lower opportunity for radial conduction within the disk. There result in higher average Nusselt number for a thinner disk.

The effect of solid material properties on transient heat transfer is presented in figure 4.25. The studied materials were aluminum, Constantan, copper, silicon, and silver having different thermo–physical properties. For all materials, the temperature changes occur faster at the earlier part of the heating process and the slope gradually decays when the steady state approaches. The change of slope shows the thermal energy balance response of the transient conduction–convection heat transfer at the solid–fluid interface. It can be observed that a material having a lower thermal conductivity such as Constantan maintains a higher temperature at the solid disk interface and within the solid as the thermal conductivity controls how effectively the heat flows and distributes through the material.

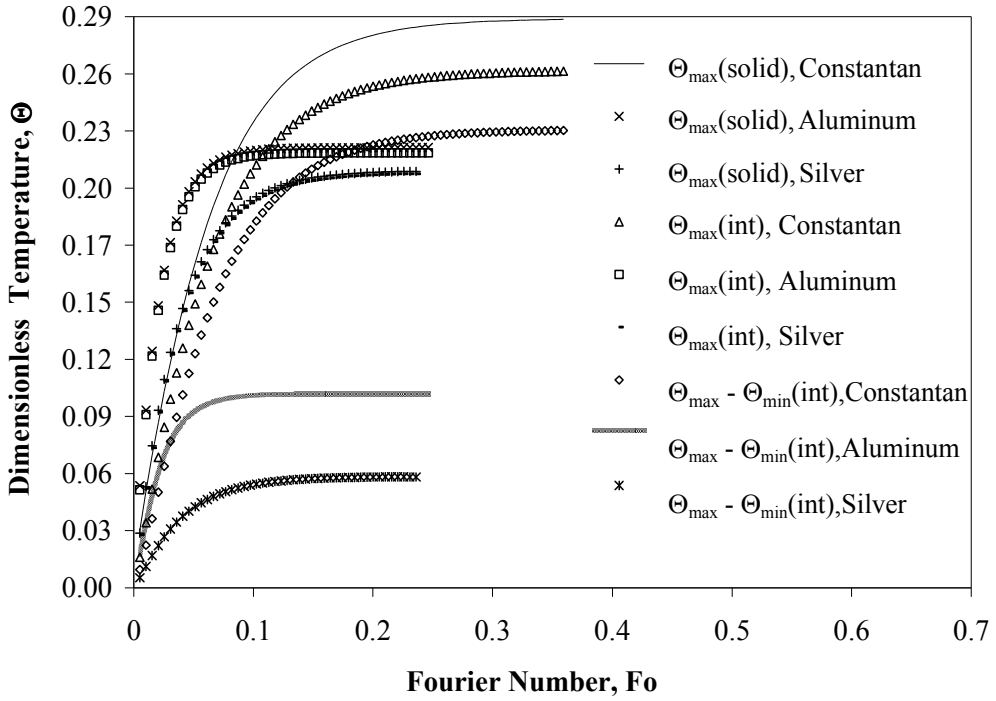

Figure 4.25 Dimensionless maximum temperature variations for different solid materials (Re=650, Ek=2.65x10^{-4}, b/d_n=0.5, β=2.67, water, and q_w=125 kW/m^2).

For the same reason, the maximum temperature within the solid and that at the interface are significantly different for Constantan, whereareas about the same for both silver and aluminum. The thermal diffusivity of the material also contributes to the transient heat transfer process. As noticed, silver and aluminum reach the steady state faster than Constantan due to their higher thermal diffusivity. The values of thermal diffusivity for the materials considered here at 303K are α_{silver}=1.74 x10 $^{-4}$ m^2/s, $\alpha_{aluminum}$ =8.33 x10 $^{-5}$ m^2/s, and $\alpha_{Constantan}$= 6.20 x10 $^{-6}$ m^2/s.The magnitude of the temperature non–uniformity at the interface at steady state is controlled by thermal conductivity of the material. It may be noted that the thermal conductivity of Constantan ($k_{Constantan}$=22.7 W/m·K) has an average maximum–to–minimum temperature difference of 23.39 K, whereareas the thermal conductivity of silver (k_{silver}= 429 W/m·K) has only an average 6.22 K temperature difference at the interface.

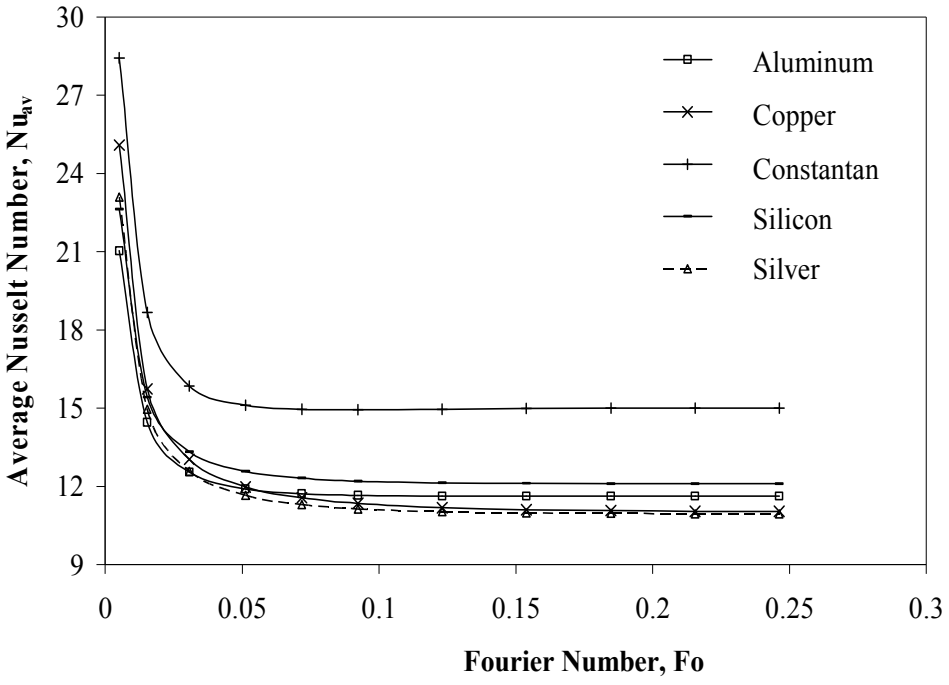

Figure 4.26 Average Nusselt number variations for different solid materials (Re=650, Ek=2.65x10^{-4}, b/d$_n$=0.5, β=2.67, water, and q_w=125 kW/m^2).

Figure 4.26 shows the distribution of average Nusselt number with time for the five materials used in this study. Constantan shows a higher average heat transfer coefficient compared to the other materials over the entire transient process due to its lower thermal conductivity. The average Nusselt number distributions of copper and silver are almost identical due to their similar thermal conductivity values.

It will be also important to know how the materials responded in reaching thermal equilibrium based on their thickness. Figure 4.27 presents the steady state Fourier number (Fo_{ss}) for these materials at different plate thicknesses. The steady state Fourier number (Fo_{ss}) was defined as the time needed to approach 99.99% of the steady state local Nusselt number over the entire solid–fluid interface. As the thickness increases in value, the time to reach steady state also increases. The radial conduction becomes stronger as the disk thickness increases generating a more uniform heat distribution at the interface.

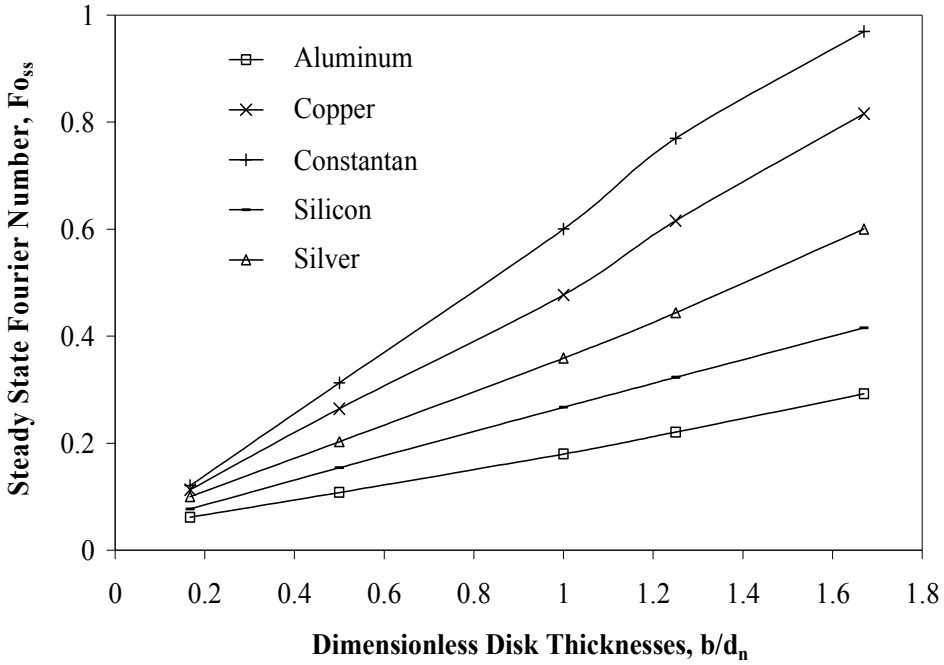

Figure 4.27 Time required to reach steady state under the effects of various material properties and disk thickness (Re=1,100, Ek=1.20x10^{-4}, β=2.67, water, and q_w=125 kW/m^2).

However, the increment of solid thickness creates more thermal resistance to the heat transfer process. The thermal diffusivity of the solid plays a significant role in determining the duration of the transient heat transfer process. Constantan takes longer in reaching steady state due to its lower thermal diffusivity compared to the other materials.

Figure 4.28 presents the time required to reach the steady state condition as a function of Reynolds number. The duration of the transient heat transfer decreases as the Reynolds number increases. This is due to quicker dissipation of heat with higher flow rate and lower thermal boundary layer thickness.

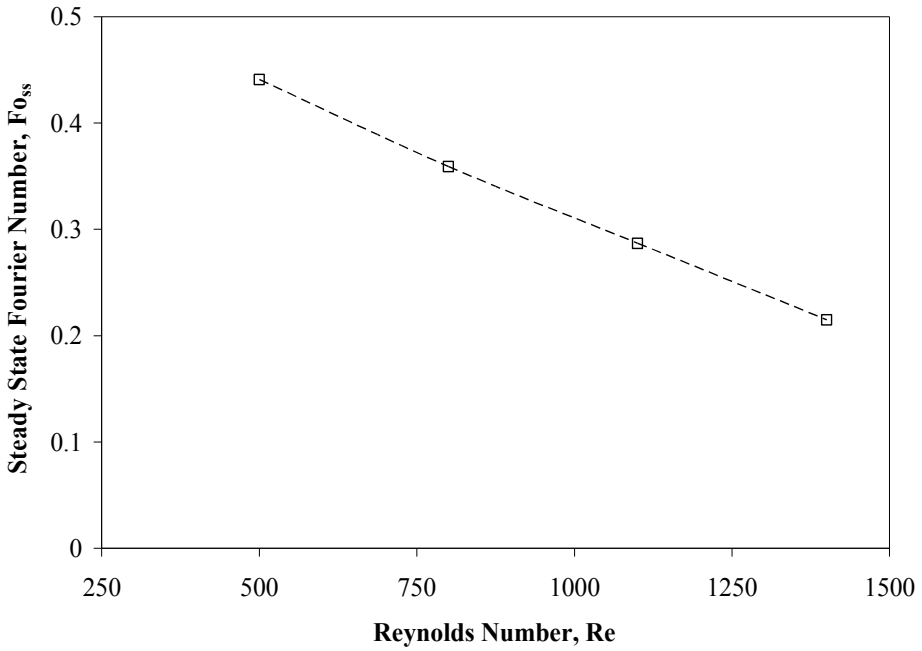

Figure 4.28 Time required to reach steady state under the effects of different Reynolds number (β=2.67, water, Ek=2.65x10^{-4}, silicon disk, b/d$_n$=0.5, and q_w=125 kW/m^2).

Figures 4.29 and 4.30 show the development of isothermal lines within the solid at different time instants. It is important to notice that at early stages of the transient heat transfer process, the isothermal lines grow parallel to the bottom heated surface of the solid disk.

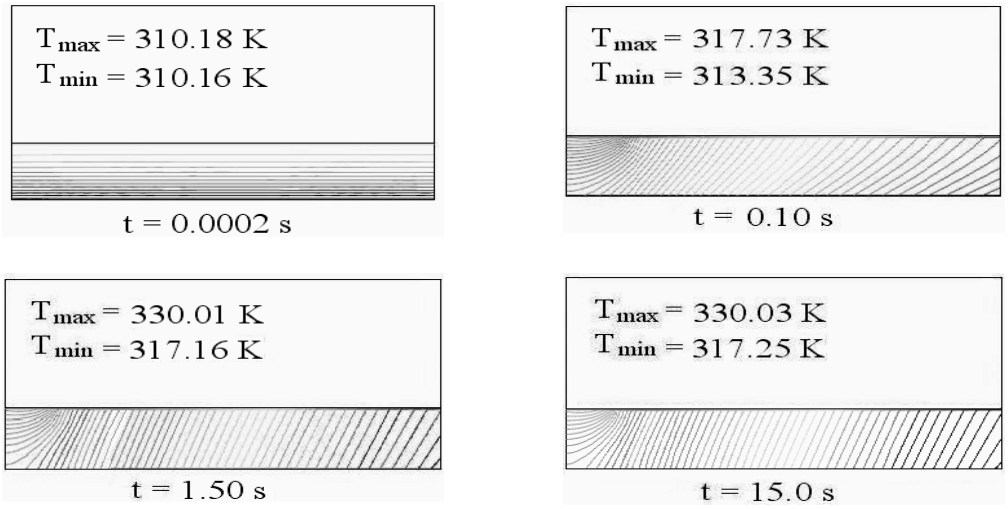

Figure 4.29 Isothermal lines at different instants (Re=1,100, Ek=1.20x10^{-4}, β=2.67, silicon disk, water, q_w=125 kW/m^2 , and b/d_n=0.5).

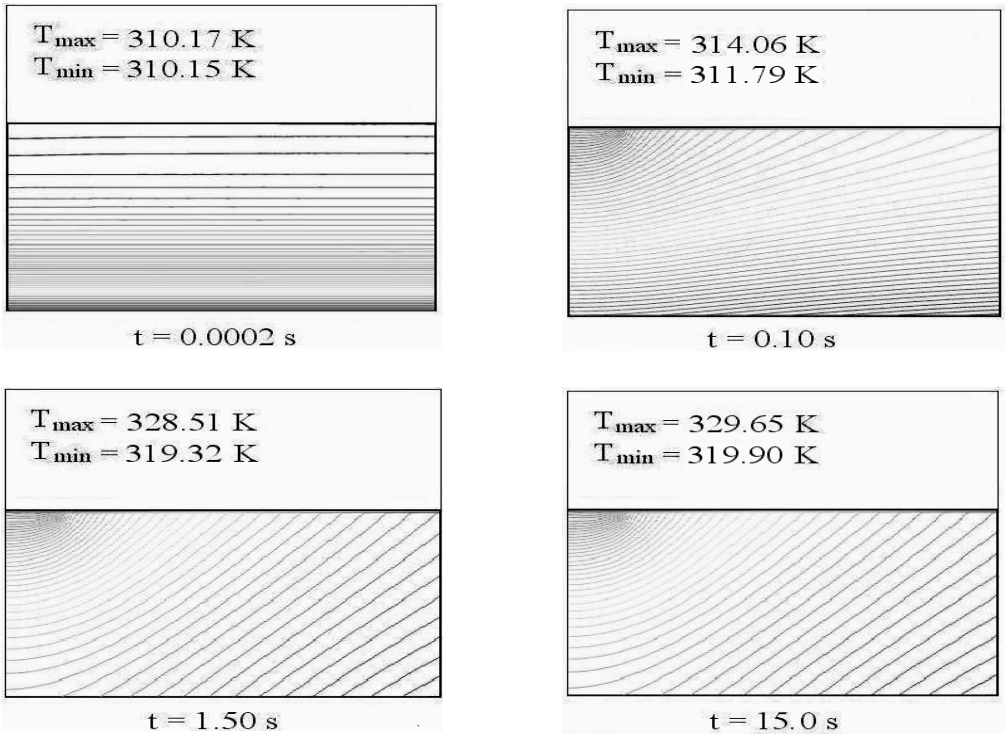

Figure 4.30 Isothermal lines at different instants (Re=1,100, Ek=1.20x10^{-4}, β=2.67, silicon disk, water, and q_w=125 kW/m^2 , and b/d_n=1.67).

As time goes on, the isothermal lines start moving upward toward lower temperature regions until they reach the solid–fluid interface. After that, they start to form concentric lines near the stagnation point and expand further down into the solid until a steady state condition is achieved. The temperatures inside the solid for figure 4.29 are lower compared to figure 4.30. Also, isothermal lines have larger slope in figure 4.29. The increment of solid thickness creates more thermal resistance and provides a more uniform interface temperature due to radial heat spreading within the solid.

Based on our numerical data, a correlation for the average Nusselt number was developed as a function of thermal conductivity ratio, Ekman number, Reynolds number, and Fourier number to accommodate most of the transport characteristics of the transient heat transfer during axial free liquid jet impingement on a thick solid disk spinning at a constant angular velocity.

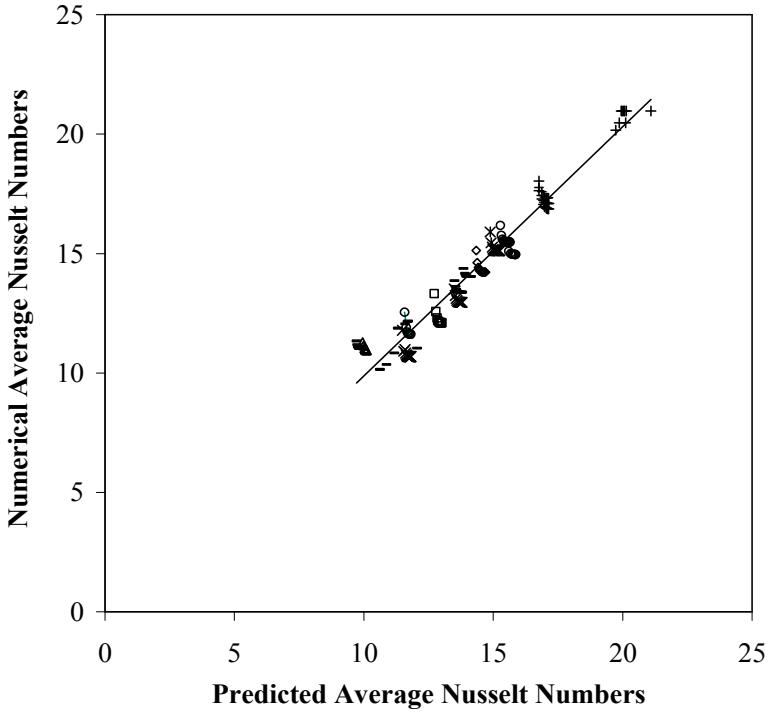

Figure 4.31 Comparison of predicted average Nusselt number of equation 4.2 with present numerical data.

Figure 4.31 gives a graphical comparison between the numerical average Nusselt numbers to the average Nusselt numbers predicted by equation 4.2. The correlation that best fitted the numerical data can be placed in the following form:

$$Nu_{av}=1.965\cdot Re^{0.3875}\cdot Ek^{-0.091}\cdot \varepsilon^{-0.25}\cdot Fo^{0.01} \quad (4.2)$$

In developing this correlation, all average Nusselt number data corresponding to the variation of different parameters were used. The least squares curve fitting method was used. The percent difference of the predicted average Nusselt number was defined as: $\%\ diff = ((Nuav_{pred} - Nuav_{num})/Nuav_{num}) \times 100$. The differences between numerical and predicted average Nusselt number values are in the range of +10.58% to –13.83%. In general, the overall average difference of average Nusselt numbers was equal to 6.59%. The values of the dimensionless variables used in this study are: $500 \leq Re \leq 1{,}100$, $6.62\text{x}10^{-5} \leq Ek \leq 2.65\text{x}10^{-4}$, $\beta=2.67$, $Pr=5.49$, $227.6 \leq \varepsilon \leq 697.5$ and $0.031 \leq Fo \leq 0.504$. It should be noted from figure 4.31 that a large number of data points are well correlated with equation 4.2. This correlation provides a convenient tool for the prediction of average heat transfer coefficient during the transient heat transfer process.

Chapter 5 Confined Liquid Jet Impingement Model Results

5.1 Steady State: Stationary Confined Wall with Spinning Target

The numerical results of a confined liquid jet impingement on top of a spinning target or wafer are presented in terms of dimensionless solid–fluid interface temperature distribution and local as well as average Nusselt number variation. A characteristic velocity vector distribution is shown in figure 5.1.

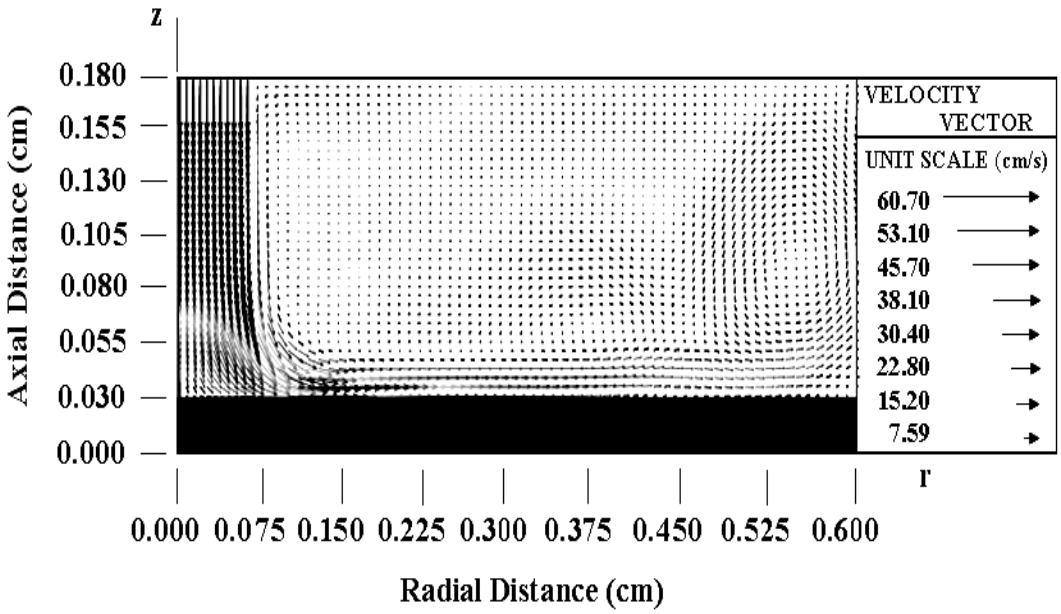

Figure 5.1 Velocity vector distribution for a confined jet impingement on a silicon wafer with water as the cooling fluid (Re=1,000, β=1.5, Ek=1.42x10^{-4}, b/d_n=0.25).

It can be seen that the velocity remains almost uniform at the potential core region of the jet. The velocity decreases and the jet diameter increases as the fluid gets closer to the plate during the impingement process. Thereafter, the fluid strikes the solid surface at

which point there is a rapid deceleration while the flow changes direction parallel to the solid disk. After this, there is a brief acceleration starting the development of boundary layer. It can be noticed that the boundary layer thickness increases along the radius. The fluid between the boundary layer zone and confined top plate remains quasi–stagnant with a flow velocity ten times less than the inlet velocity. The proximity of the spinning confined plate generates a recirculation pattern in this region.

Figure 5.1 shows the variation of local Nusselt number distributions and solid–fluid dimensionless interface temperature plots for different Reynolds number under a low rotational rate of 125 RPM. All local Nusselt number distributions are half–bell shaped with a peak at the stagnation point. It may be noted, however, that due to spinning streamlines are not aligned along the disk radius, rather the fluid moves at an angle based on the rate of rotation. The plots in figure 5.2 reveal that dimensionless interface temperature decreases with jet velocity (or Reynolds number). At any Reynolds number, the interface temperature has the lowest value at the stagnation point (underneath the center of the axial opening) and increases radially along the radius reaching the highest value at the end of the disk. This is due to the development of thermal boundary layer as the fluid moves downstream from the center of the disk. The thickness of the thermal boundary layer increases with radius and causes the interface temperature to increase. Figures 5.2 confirm to us how an increasing Reynolds number contributes with a more effective cooling.

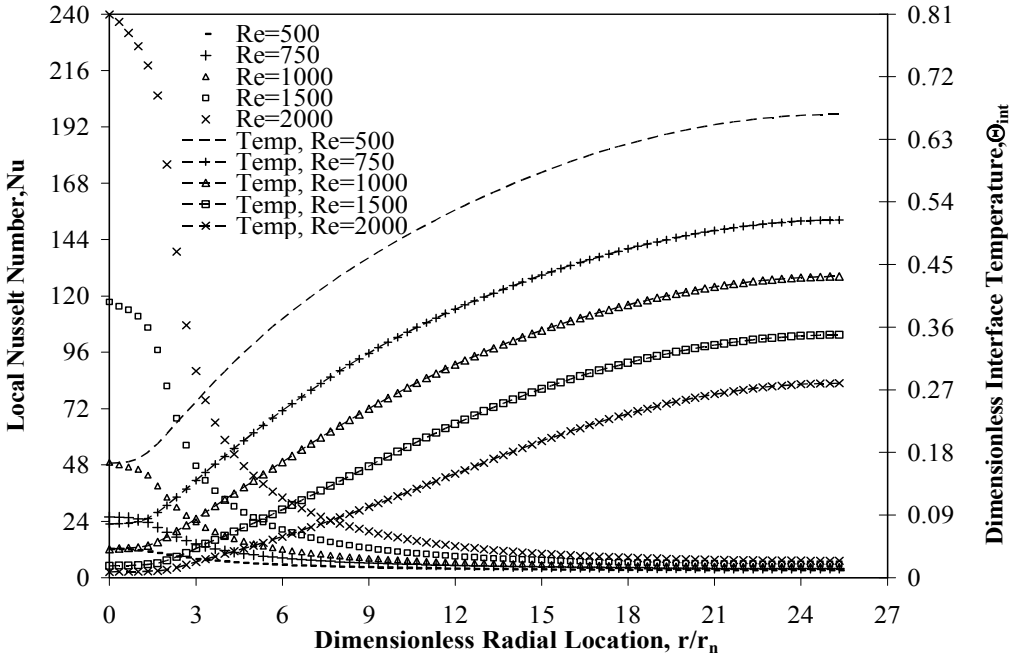

Figure 5.2 Local Nusselt number and dimensionless interface temperature distribution for a silicon wafer at different Re, and water as the cooling f1uid (b=0.3 mm , H_n=0.32 cm, Ek=2.65x10^{-4}, and q_w=250 kW/m^2).

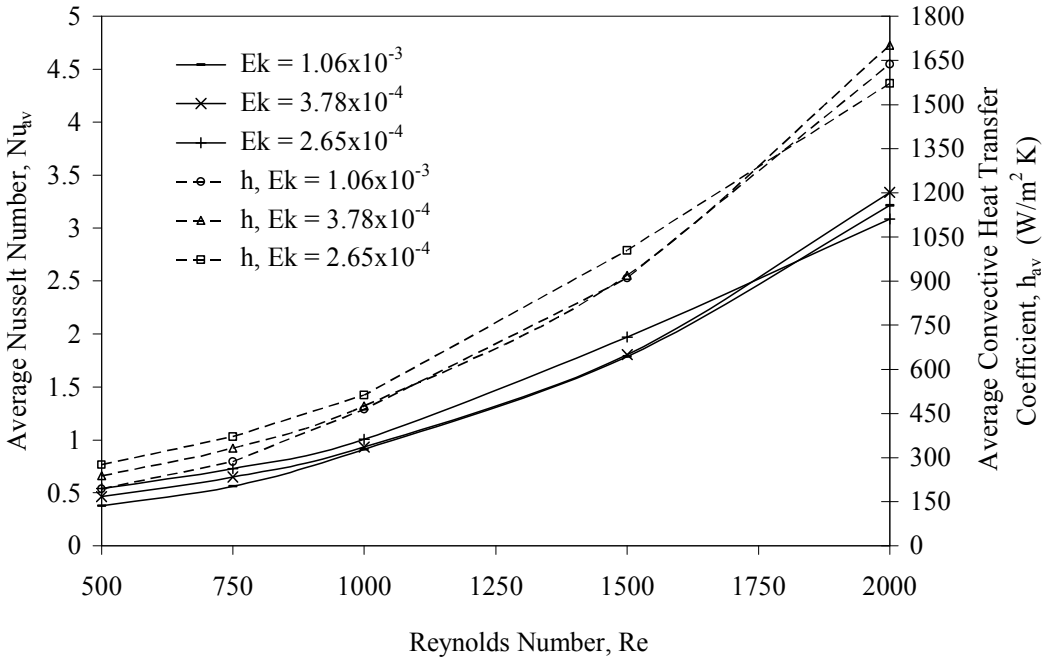

Figure 5.3 Average Nusselt number and heat transfer coefficient comparison for different Reynolds number at low, intermediate and high Ekman numbers (q_w=250 kW/m^2, H_n=0.32 cm).

Figure 5.3 plots the average Nusselt number and average heat transfer coefficient as a function of Reynolds number for low, intermediate, and high Ekman numbers or rotational rates. It may be noted that average Nusselt number increases with Reynolds number. As the flow rate (or Reynolds number) increases, the magnitude of fluid velocity near the solid–fluid interface that controls the convective heat transfer rate increases. It may be also noted that at lower Reynolds number (1,500–1,700) the average heat transfer coefficient (or average Nusselt number) decreases with Ekman number (or increases with disk spinning rate). Therefore, spinning provides a positive influence on convective heat transfer at this Reynolds number range. The graphs intersect around 1,750 and at higher Reynolds number (1,800–2,000) a higher Nusselt number is observed at a lower spinning rate. The intersection of all graphs indicates the presence of the liquid jet momentum dominated region at Reynolds numbers greater than 1,750.

The rotational rate effects on the local Nusselt number and solid–fluid dimensionless interface temperature are illustrated in figure 5.4. All curves on figure 5.4 portray a half–bell shaped profile with crest at the stagnation region. This trend matches with previous studies by Webb and Ma [76] and Chang et al. [73]. It may be noted that rotational effect increases local Nusselt number and generates lower temperature over the entire solid–fluid interface with somewhat less intensity in comparison with the Reynolds number effect. An exception is the case with $Ek=3.31x10^{-5}$ where the local Nusselt number distribution shows significantly higher values up to $r/r_n=6$ and afterward it becomes lower in comparison with other plots in figure 5.4. In this particular case the rotation generates a positive effect at smaller radial locations, whereas at higher radial locations the boundary layer separates from the wall and causes an ineffective cooling.

This type of behavior is consistent with the results of Popiel and Boguslawski [36] where in rotation dominated regime the impinging jet started being underscored by the fluid rejection of the rotating disk.

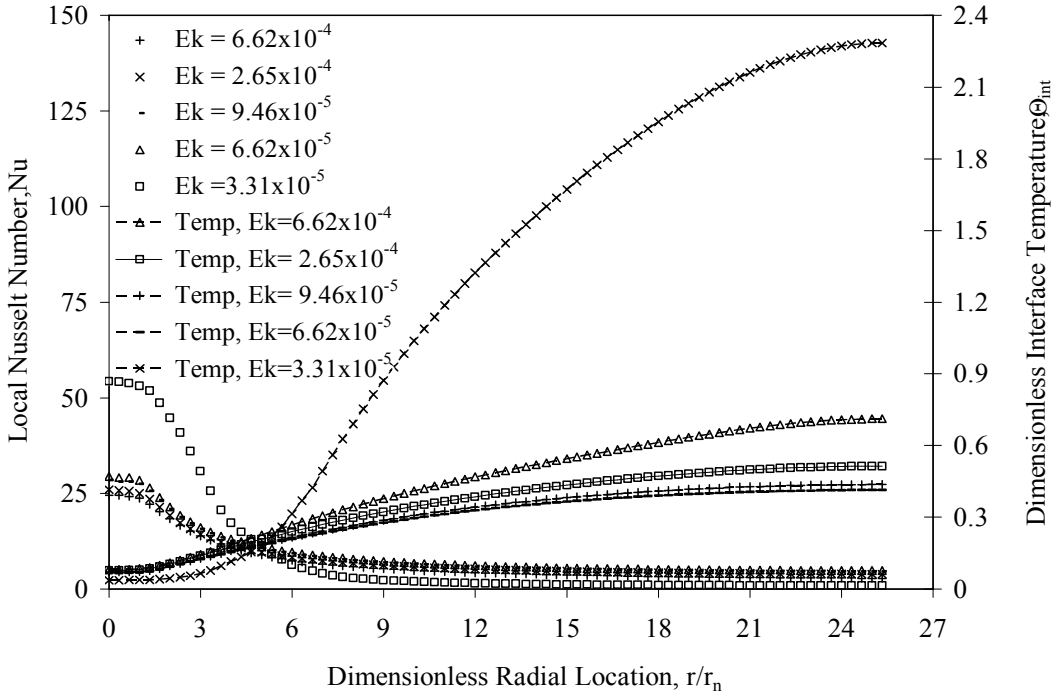

Figure 5.4 Local Nusselt number and dimensionless interface temperature plots for a silicon wafer at different Ekman numbers and water as the cooling f1uid (Re=750, Q=3.54x10^{-2} m^3/s, b=0.3 mm, H_n/d_n=5.333, and q_w=250 kW/m^2).

Figures 5.5 compares the solid–fluid interface temperature results of the present working fluid (water) with three other coolants that have been considered in previous thermal management studies, namely ammonia (NH_3), flouroinert (FC–77) and oil (MIL–7808). Figure 5.6 shows the corresponding Nusselt number distributions. It may be noticed that water presents lower interface temperature and Nusselt number distribution in comparison with FC–77, NH_3 and MIL–7808 at most locations. Ammonia on the other hand has the overall highest interface temperature.

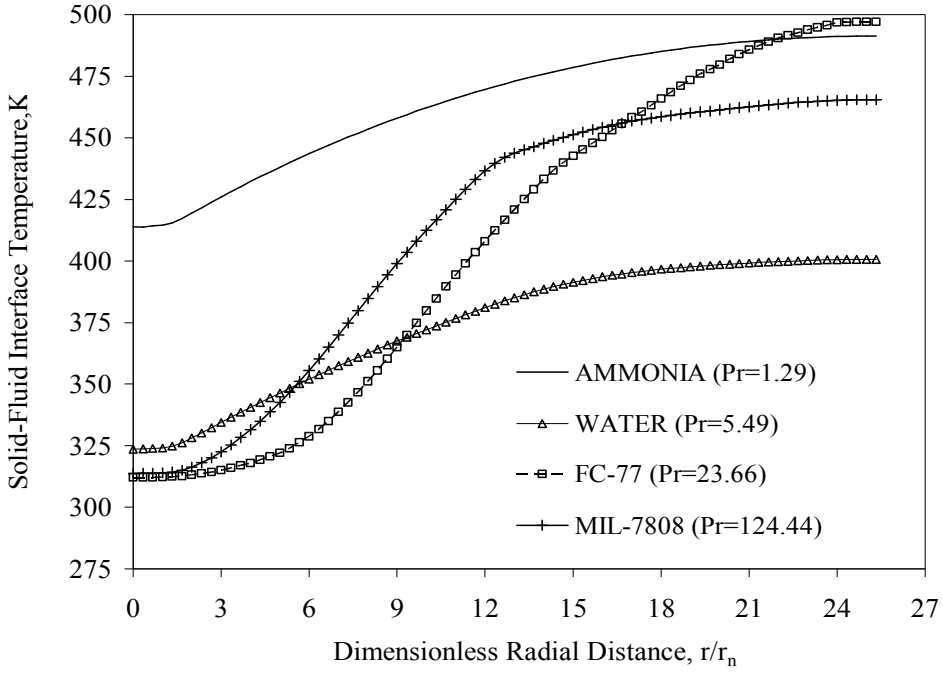

Figure 5.5 Interface temperature for different cooling fluids (Re=750, $Q=3.54x10^{-2}$ m^3/s, Ω=125 RPM, b=0.3 mm, $H_n/d_n=2.67$, and $q_w=250$ kW/m^2).

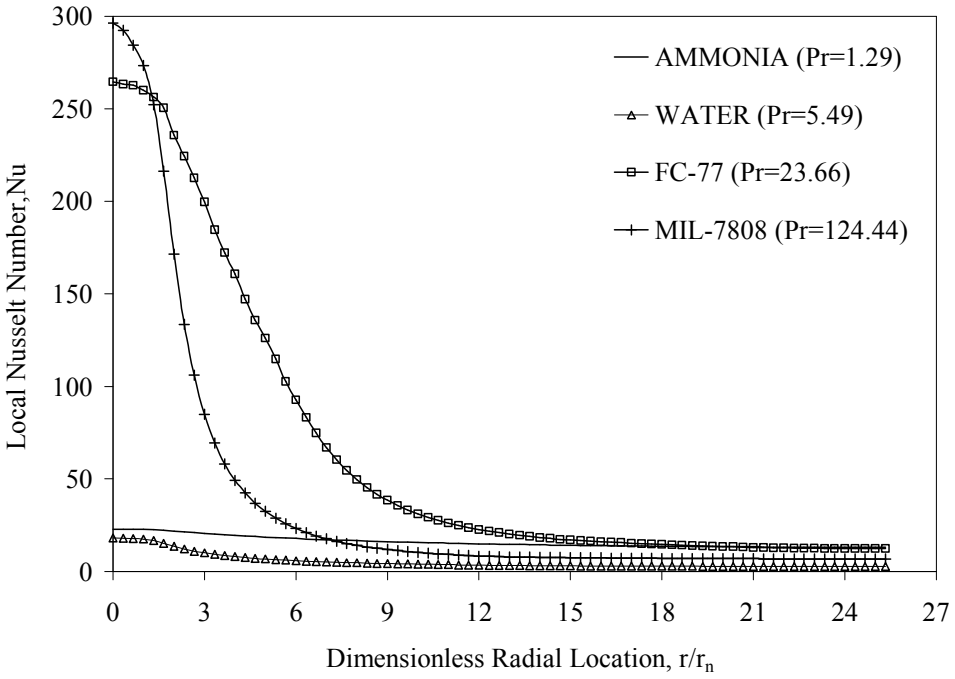

Figure 5.6 Local Nusselt number for different cooling fluids (Re=750, $Q=3.54x10^{-2}$ m^3/s, Ω =125 RPM, b=0.3 mm, $H_n/d_n=2.67$, and $q_w=250$ kW/m^2).

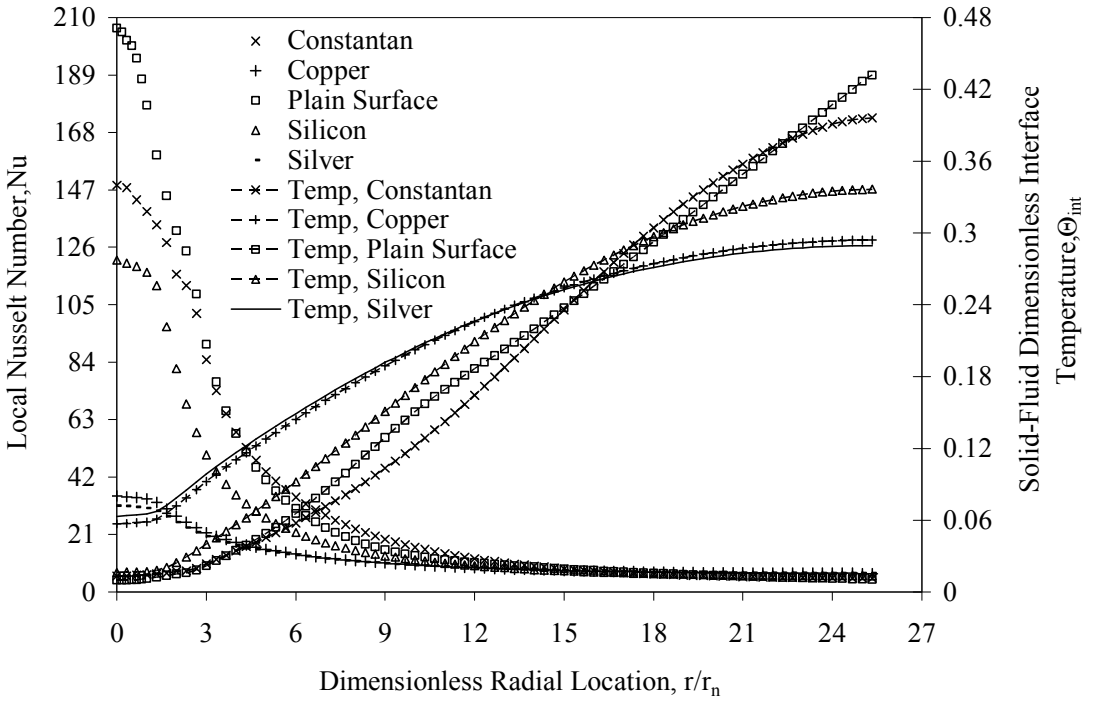

Figure 5.7 Local Nusselt number and dimensionless interface temperature distributions for different solid materials with water as the cooling fluid (Re=1,500, $Q=7.08x10^{-2}$ m^3/s, $q_w=250$ kW/m^2, $\Omega=125$ RPM, $H_n=0.32$ cm, $q_w=250$ kW/m^2).

Figure 5.7 shows the dimensionless solid–fluid interface temperature and local Nusselt number distribution plots respectively as a function of the dimensionless radial distance measured from the axis–symmetric impingement axis for different solid materials with water as the working fluid. The numerical simulation was carried for a set of materials, namely copper, silver, Constantan and silicon, having different thermo–physical properties. Results for plain surface (zero thickness of the disk) are also plotted to identify the extent of conjugate effects. The temperature distribution plots reveal how the thermal conductivity of the solids affects the heat flux distribution that controls the local interface temperature. It may be noted that Constantan has the lowest temperature at the impingement axis and the highest at the outer edge of the disk. This large interface

temperature variation is due to its lower thermal conductivity. As the thermal conductivity increases, the thermal resistance within the solid becomes lower and the interface temperature becomes more uniform as seen in the plots corresponding to copper and silicon. The cross–over of the curves of the four materials and plain surface occurred due to a constant fluid flow and heat flux rate that provides a constant thermal energy transfer for all circumstances. Narrow and elevated bell shape pattern is seen in figure 5.4 for all solid materials with low thermal conductivity. Conversely high thermal conductivity materials like copper and silver portray a more uniform Nusselt number distribution in general.

Considering the trends of heat transfer enhancement as functions of thermal conductivity ratio, nozzle–to–plate spacing, Prandtl number, Ekman number, and Reynolds number and by accommodating most of the transport characteristics of a confined liquid jet impingement cooling, a correlation was developed in the following form:

$$Nu_{av}=Re^{1.26}\cdot Ek^{-0.1111}\,Pr^{-2.58}\,\beta^{0.5}\,\varepsilon^{-0.65} \qquad (5.1)$$

Figure 5.8 gives the comparison between the numerical average Nusselt numbers to average Nusselt numbers predicted by equation 5.1. The percent difference of the predicted average Nusselt number was defined as: $\%\ \text{diff} = ((Nuav_{pred}–Nuav_{num})/Nuav_{num}) \times 100$. The differences between numerical and predicted average Nusselt number values are in the range –20.36% to +14.47%. The mean value of the error was 7.70%. The ranges of the dimensionless variables in this study are: $750 \leq Re \leq 2{,}000$, $6.62\text{x}10^{-5} \leq Ek \leq 2.65\text{x}10^{-4}$, $Pr=5.49$, $227.6 \leq \varepsilon \leq 697.5$. The Prandtl number exponent was derived from

Martin's equation [144] for single round nozzle impinging jet. It should be noted from figure 5.8 that a large number of data points are well correlated with equation 5.1.

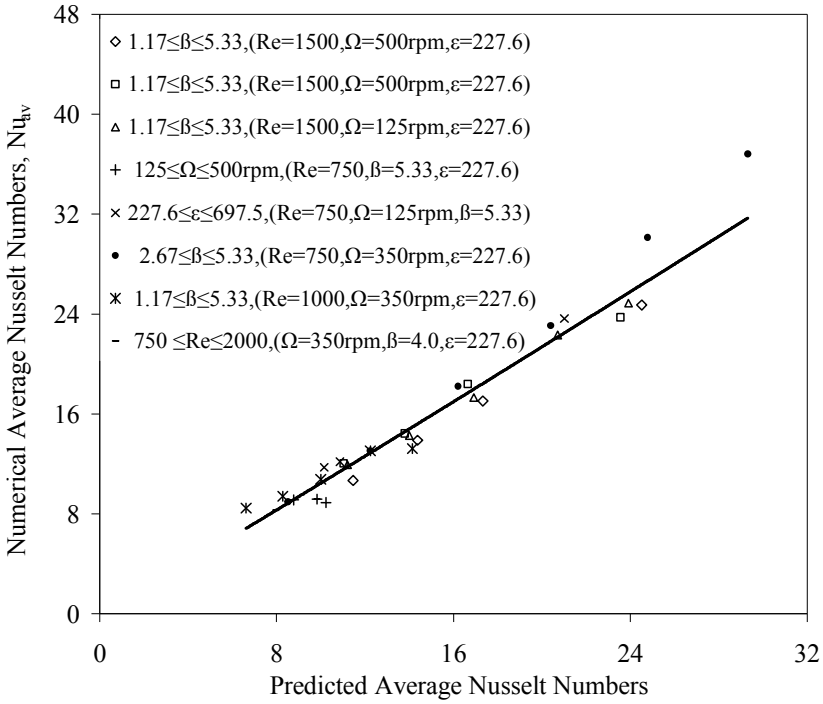

Figure 5.8 Average Nusselt number correlation results for various studied parameters.

The deviation is primarily in the core region where the heat transfer values are larger under large Reynolds number and different spinning rates. This correlation provides a convenient tool for the prediction of average heat transfer coefficient under confined liquid jet impingement on top of a spinning disk. The major difference between past studies and the present investigation is the accounting for conduction within the solid wafer and fluid for various materials, plus the nozzle–to–plate spacing ratio as a part of the correlation.

One of the papers used for the validation of this numerical study was the experimental work carried out by Garimella and Rice [75] using flouroinert (FC–77) as the coolant. This liquid was tested for heat removal under confined liquid jet

impingement on a stationary disk (Ek=∞). The simulation attempted to duplicate the exact conditions of that experiment. Figure 5.9 compares the variations of local Nusselt number distribution along the solid–fluid interface obtained from the simulation with the correlation developed from the experimental data. The percent difference of the predicted average Nusselt number was defined as: % diff = $((Nuav_{pred} - Nuav_{num})/Nuav_{num}) \times 100$. Considering the errors inherent in any experimental measurements (the reported uncertainty range from –2.46% to 3.32%) as well as discretization and round off errors in the simulation, the comparison is quite satisfactory. A similar profile has also been documented by Ma et al. [69].

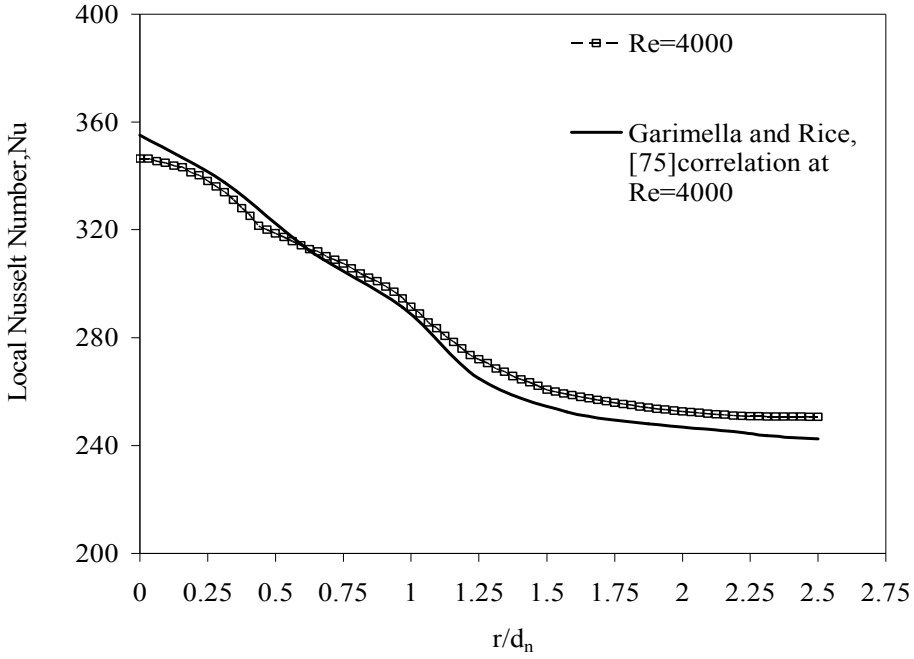

Figure 5.9 Local Nusselt number distribution for a silver disk with FC–77 as the cooling fluid (H_n/d_n=4, q_w=250 kW/m^2).

The experimental work carried out by Carper et al. [35] to determine the average heat transfer coefficient of a rotating disk, with an approximately uniform surface temperature, cooled by a single oil liquid jet impinging normal to the surface, was also

used for the validation of the numerical results. The authors presented correlations that related the average Nusselt number to rotational Reynolds number, jet Reynolds number, and Prandtl number.

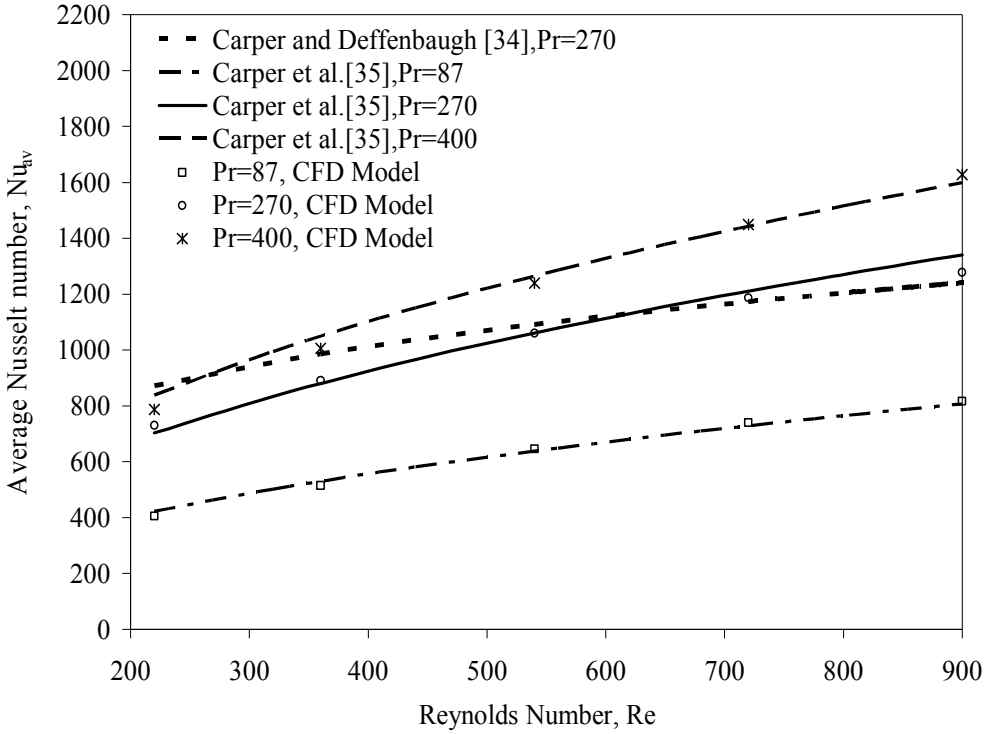

Figure 5.10 Average Nusselt number correlation for various Reynolds numbers and Ekman number and three different Pr values of liquid oil axis–symmetric jet impingement.

The simulation has attempted to duplicate numerically the exact conditions of that experiment. The computation was conducted for three nominal values of T_j of 375, 331 and 320 K resulting in values of Pr of 87, 270 and 400 respectively. The rotational Reynolds number was kept constant at a value equal to 26,000. As a result of these behavior three distinct angular velocities values (Ω) had to be used: 140, 480 and 730 RPM corresponding to the Prandtl numbers of 87, 270 and 400 respectively. The disk had a diameter of 10 cm and thickness of 2.54 cm and was made of 7075–T6 Aluminum, a

material with a relatively high thermal conductivity of 121.4 W/mK. As seen in figure 5.10, the agreement of the results from the average Nusselt number correlation of Carper et al. [35] with the present data is quite good. Three different plots based on this correlation have been included in order to make a qualitative and quantitative comparison. The percent difference of the experimental average Nusselt number was defined in the form: % diff = $((Nuav_{num} - Nuav_{exp})/Nuav_{exp}) \times 100$. The average Nusselt number uncertainties of Carper et al. [35] range from –6% to 3.96% for all Prandtl numbers. An additional average Nusselt number plot was included from Carper and Deffenbaugh [34] for Prandtl number of 270. The average Nusselt number uncertainties for Carper and Deffenbaugh [34] correlation range from –9.21% to 18.34%. This validation with available experimental data may provide good level of confidence on the numbers obtained during present numerical simulation.

5.2 Steady State: Spinning Confined Wall with Stationary Target

This section describes the heat transfer characteristics of a confined liquid jet impingement under a spinning confinement disk. Figure 5.11 shows the variation of local Nusselt number and solid–fluid dimensionless interface temperature distributions for different Reynolds number under a low rotational rate ($Ek=4.25 \times 10^{-4}$). All local Nusselt number distributions are half–bell shaped with a peak at the stagnation point. It may be noted, however, that due to spinning streamlines are not aligned along the disk radius, rather the fluid moves at an angle based on the rate of rotation. The positive influence of the spinning of the confinement disk can be observed particularly at Re=750, at which point the Nusselt number at $r/r_d > 0.6$ becomes higher in comparison with that of the

Reynolds number of 1,000. The plots in figure 5.11 reveal that dimensionless interface temperature decreases with jet velocity (or Reynolds number).

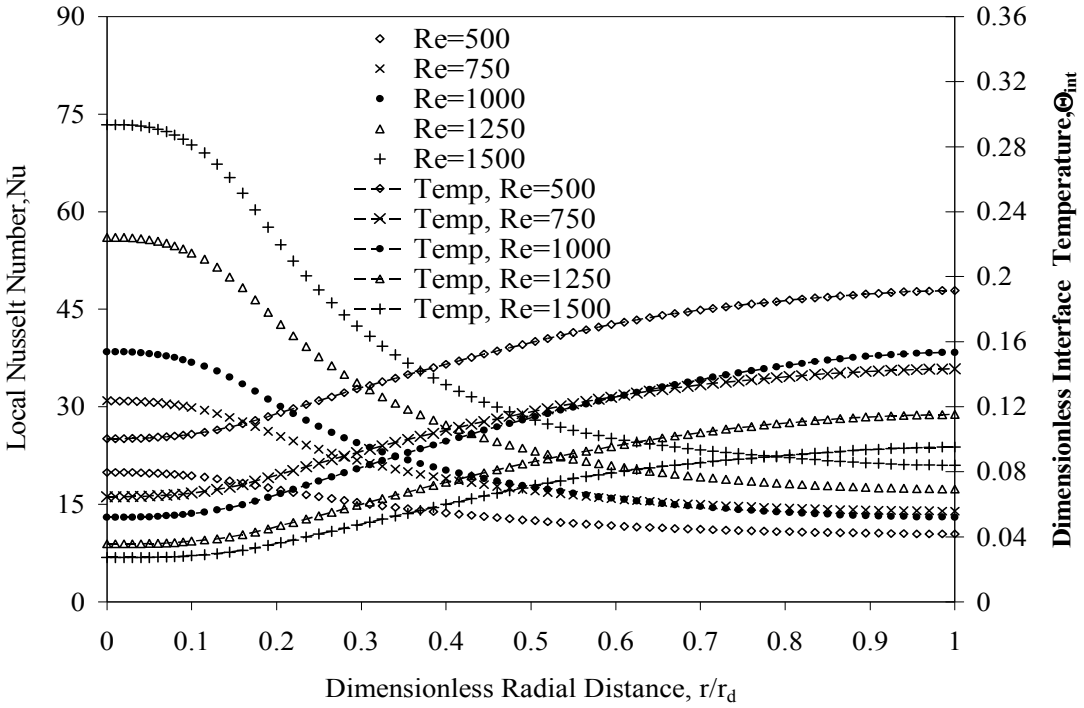

Figure 5.11 Local Nusselt number and dimensionless interface temperature distributions for a silicon disk with water as the cooling fluid for different Reynolds numbers (Ek=4.25x10^{-4}, β=2.0, b/d_n=0.25).

At any Reynolds number, the dimensionless interface temperature has the lowest value at the stagnation point (underneath the center of the axial opening) and increases radially downstream reaching the highest value at the end of the disk. This is due to the development of thermal boundary layer as the fluid moves downstream from the center of the disk. The thickness of the thermal boundary layer increases with radius and causes the interface temperature to increase. The increment of the dimensionless interface temperature coincides with the thickening of thermal boundary layer. A lower interface temperature distribution at Re=750 is attained in comparison to Re=1,000 for the dimensionless radial distance, r/r_d> 0.6. This is due to the fact that the tangential velocity

from the top plate penetrates into the thermal boundary layer thickness adjacent to the heated stationary disk. This effect remains stronger when the momentum of the jet fluid is lower. At higher Reynolds numbers (i.e., Re≥ 1,000), the jet fluid momentum overcomes the tangential velocity effects and increases the dimensionless interface temperature. Figures 5.11 confirm to us how an increasing Reynolds number contributes to a more effective cooling. Similar profiles have been documented by Garimella and Nenaydykh [77] and Ma et al. [69, 81].

Figure 5.12 plots the average Nusselt number as a function of Reynolds number for low, intermediate, and high Ekman numbers. It may be noted that average Nusselt number increases with Reynolds number. As the flow rate (or Reynolds number) increases, the magnitude of fluid velocity near the solid–fluid interface that controls the convective heat transfer rate increases. Furthermore, at a particular Reynolds number, the Nusselt number decrease with Ekman number (or gradually increases with the increment of disk spinning rate). This behavior confirms the positive influence of the rotational rate on the average Nusselt number down to $Ek=1.52x10^{-4}$ that corresponds to a spinning rate of 350 RPM.

However at $Ek=1.06x10^{-4}$ (spinning rate of 500 RPM) the average Nusselt number is lower than the stationary disk ($Ek=\infty$). At high spinning rate the thermal boundary layer thickness increases due to suction created by the spinning motion of the confinement plate. Therefore the heat transfer coefficient decreases compared to the stationary disk; the average Nusselt numbers decreases by 39% at Re=750 and by 2% at Re=1.500. It may be also noticed that the average Nusselt number plots gets closer to

each other as the Reynolds number increases indicating that curves will intersect at higher Reynolds numbers.

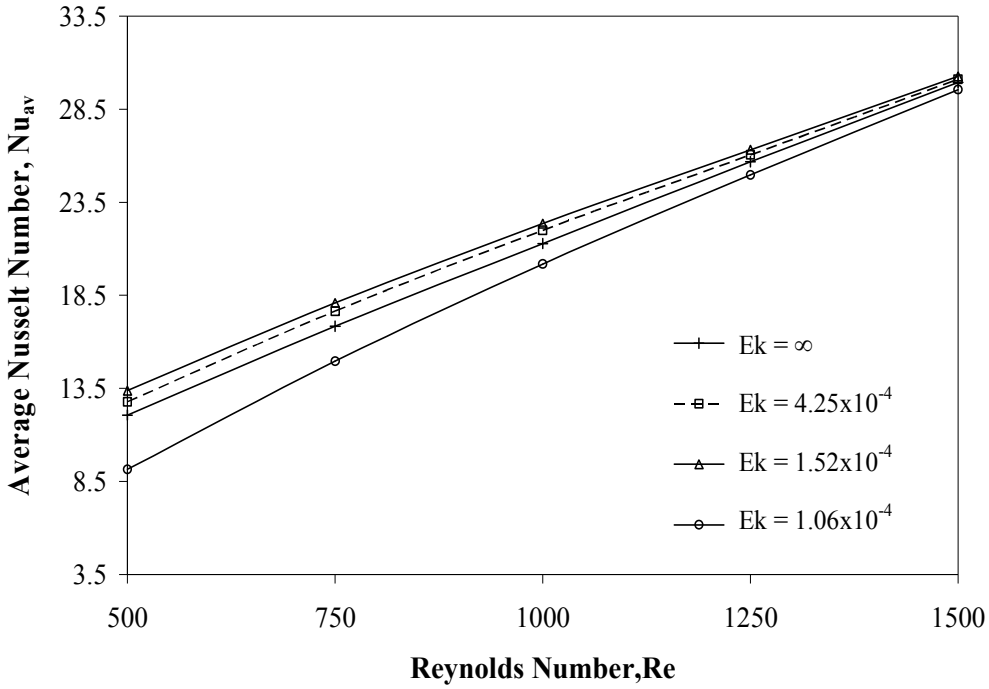

Figure 5.12 Average Nusselt number variations with Reynolds number at different Ekman numbers for a silicon disk with water as the cooling fluid (β=2.0, b/d_n=0.25).

These intersections indicate the presence of a liquid jet momentum dominated region at higher Reynolds numbers. From the numerical results it was observed that the heat transfer is dominated by impingement when $Re \cdot Ek > 0.11$ and dominated by disk rotation when $Re \cdot Ek < 0.07$. In between there limits, both of these effects play important roles in determining the variations of average Nusselt number. This type of behavior is consistent with the experimental results of Brodersen et al. [38] where the ratio of jet and rotational Reynolds numbers was used to characterize the flow regime.

The rotational rate effects on the local Nusselt number and solid–fluid dimensionless interface temperature are illustrated in figures 5.13 and 5.14 for a Reynolds number of 750 and dimensionless nozzle to target spacing (β) equal to 3.

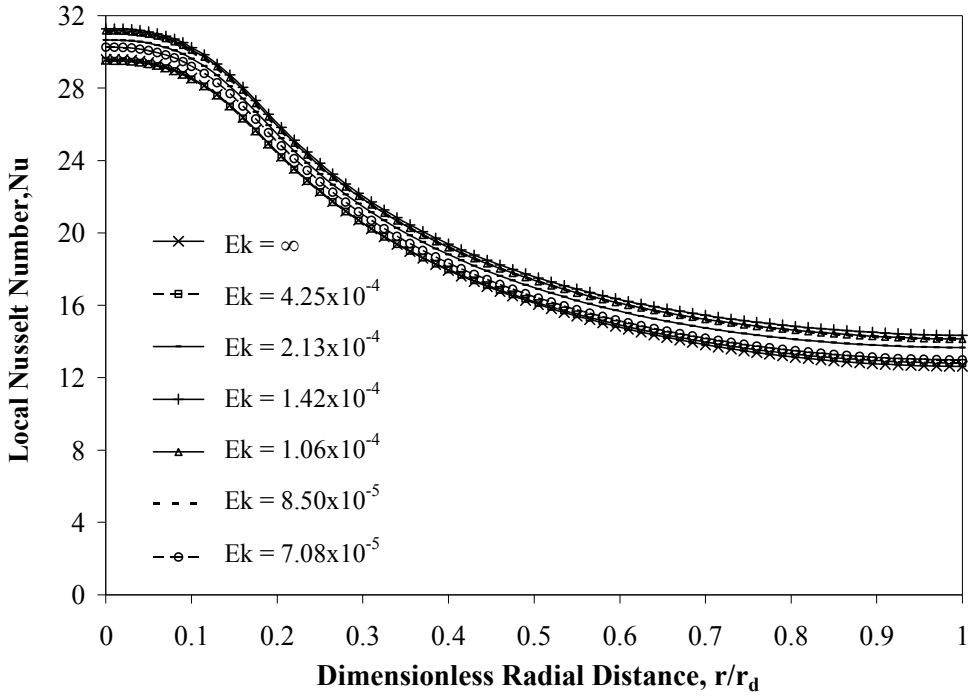

Figure 5.13 Local Nusselt number distributions for a silicon disk with water as the cooling f1uid at different Ekman numbers (Re=750, β=3.0, b/d_n=0.25).

It may be noted that rotational effect increases local Nusselt number and generates lower temperature over the entire solid–fluid interface with somewhat less intensity in comparison with the Reynolds number effect. Figure 5.14 shows that dimensionless interface temperature decreases with the increment of the rotational rate; as the Ekman number decreases from ∞ to $1.42\text{x}10^{-4}$ the local Nusselt number increases by an average 5.56% in figure 5.13 and the dimensionless interface temperature decreases by an average 2.32% in figure 5.14 under a Reynolds number of 750.

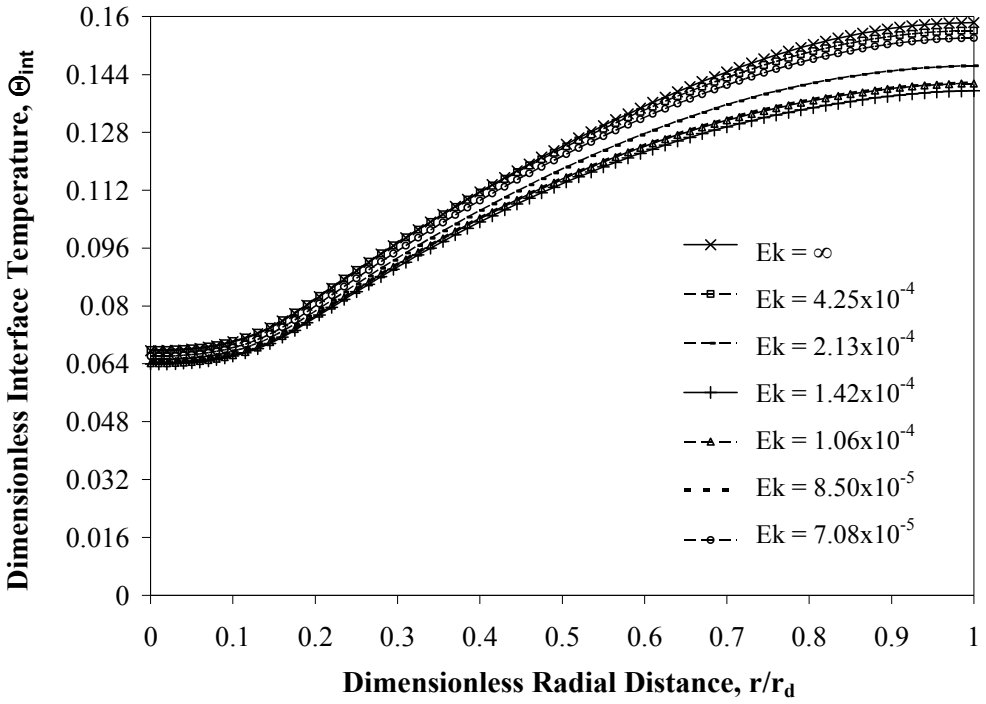

Figure 5.14 Dimensionless interface temperature distributions for a silicon disk with water as the cooling fluid at different Ekman numbers (Re=750, β=3.0, b/d_n=0.25).

The enhancement of Nusselt number due to rotation is primarily caused by enhancement of local fluid velocity adjacent to the heated disk surface. The tangential velocity due to rotation combined with axial and radial velocities due to jet momentum results in an increased magnitude of velocity vector starting from the center of the disk.

The effects of disk thickness variation on the solid–fluid dimensionless interface temperature and local Nusselt number are shown in figures 5.15 and 5.16 respectively. In these plots, silicon has been used as the disk material and water as the cooling fluid for Reynolds number of 1,500 and rotational rate of 350 RPM (Ek=$1.52\text{x}10^{-4}$). The dimensionless solid–fluid interface temperature increases from the impingement region all the way to the end of the disk.

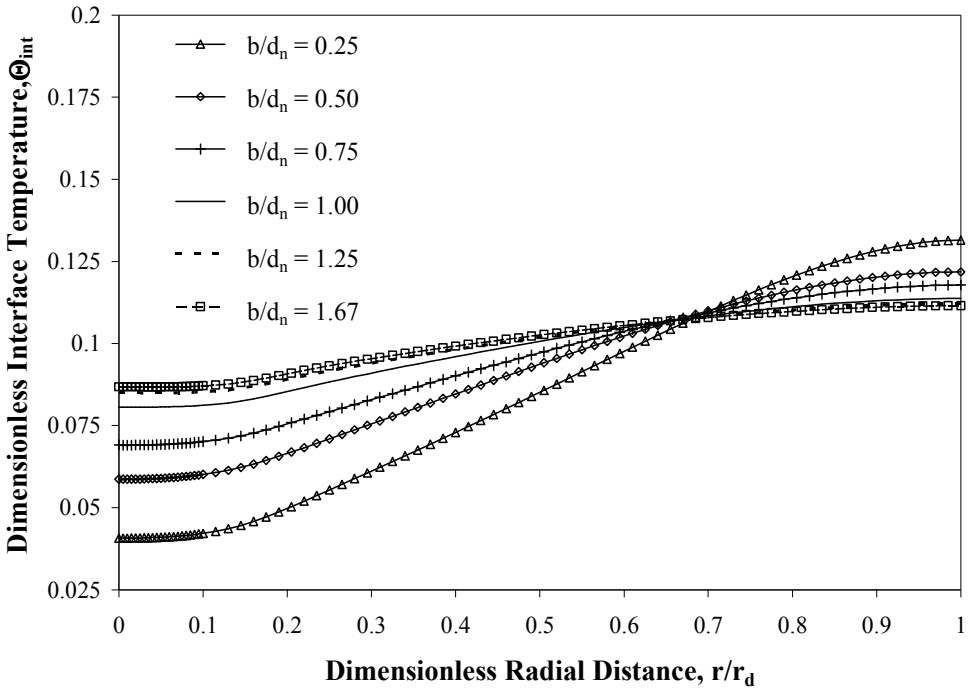

Figure 5.15 Dimensionless interface temperature distributions for different silicon disk thicknesses with water as the cooling fluid (Re=1,500, Ek=1.52x10^{-4}, β=2.0).

When temperature is lower in the stagnation region a higher outflow temperature is obtained. This is quite expected since the total heat transferred to the disk as well as the fluid flow rates are the same for all the cases. It may be noted that the disk thickness variation results intersect with each other around dimensionless radial distance of r/r_d=0.65. Thicker disks generate more uniform dimensionless interface temperature due to larger radial conduction within the disk. The local Nusselt number plots in figure 5.16 change significantly with the variation of disk thickness. In all cases, it is evident that the Nusselt number is sensitive to the solid thickness especially at smaller radii where higher Nusselt number are obtained due to rapid development of thermal boundary layer.

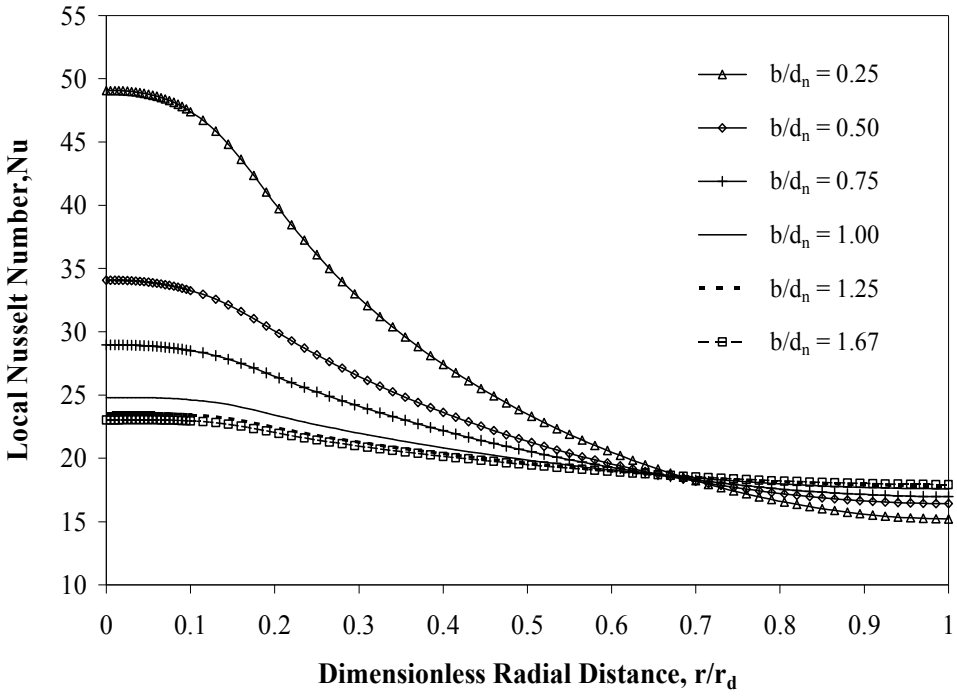

Figure 5.16 Local Nusselt number distributions for different silicon disk thicknesses with water as the cooling fluid (Re=1,500, Ek=1.52x10^{-4}, β=2.0).

Eight different nozzle–to–plate spacing ratio (β) from 0.25 to 5 were modeled for water as the coolant and silicon as the disk material. The effects of nozzle to target spacing on the dimensionless interface temperature and local Nusselt number distributions at a spinning rate of 125 RPM or (Ek=4.25x10^{-4}) and Reynolds number of 750 are shown in figures 5.17 and 5.18. It may be noticed that the impingement height quite significantly affects the Nusselt number distribution particularly at the stagnation region. It may be noticed that a higher local Nusselt number at the stagnation region is obtained when the nozzle is brought close to the heated disk (β=0.25). The spinning motion of the confinement disk really penetrates through the thermal boundary layer adjacent to the heated stationary disk and provides a larger fluid velocity and therefore a larger rate of convective heat transfer.

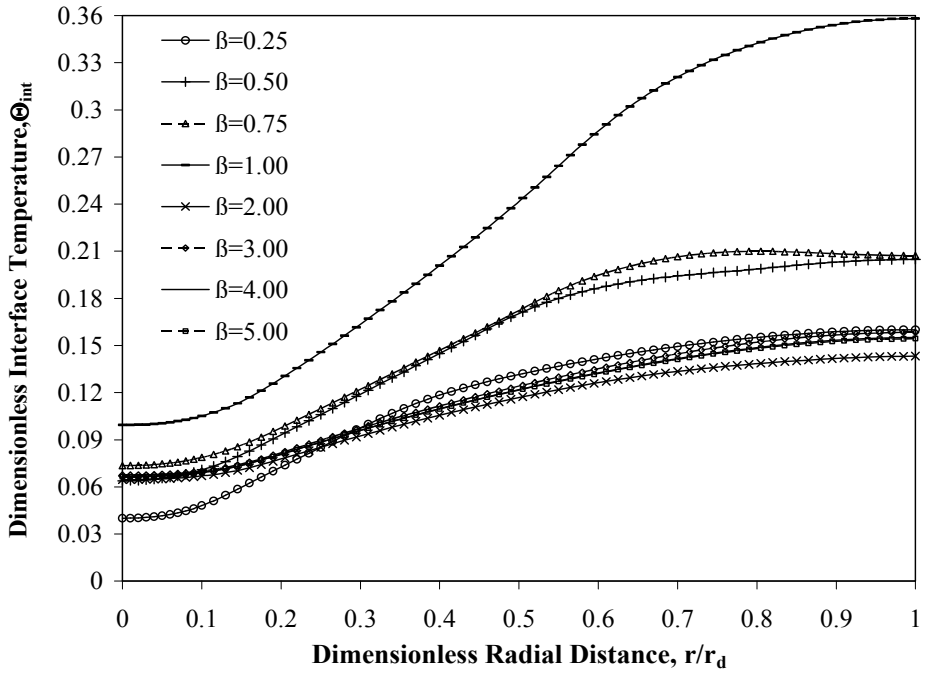

Figure 5.17 Dimensionless interface temperature distributions for a silicon disk with water as the cooling fluid for different nozzle to target spacings (Re=750, Ek=4.25x10^{-4}, b/d$_n$=0.25).

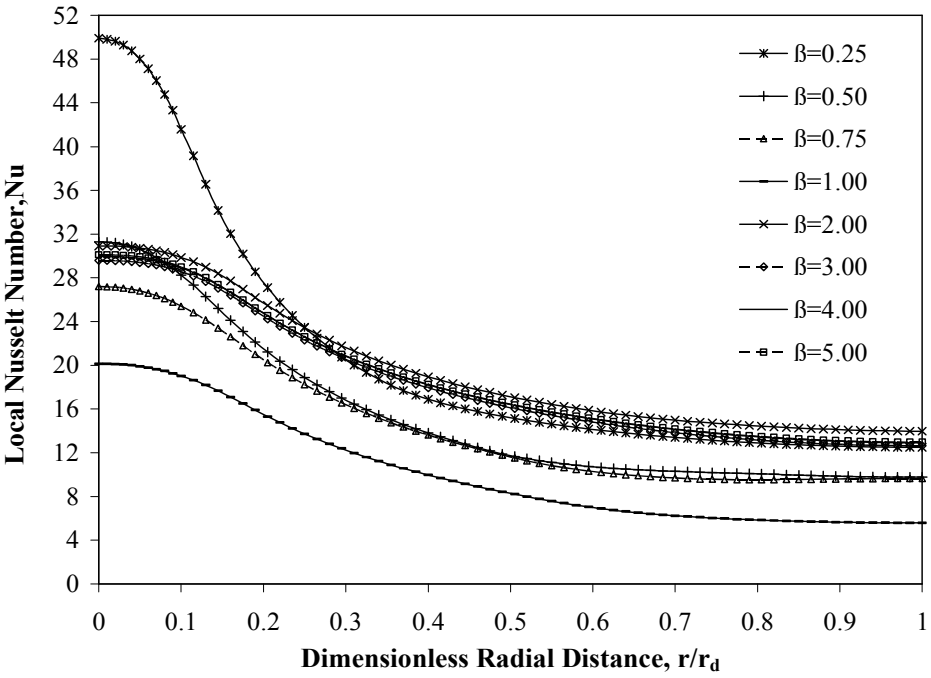

Figure 5.18 Local Nusselt number distributions for a silicon disk with water as the cooling fluid for different nozzle to target spacings (Re=750, Ek=4.25x10^{-4}, b/d$_n$=0.25).

As the nozzle is moved away from the disk (β=0.25–1), the local Nusselt number decreases. This is due to smaller effect of the rotational velocity of the confinement disk. Also, as the spacing is increased, the jet fluid needs to travel a larger distance through the existing fluid column between target and confinement disks and thereby loses its momentum. The minimum stagnation Nusselt number is seen for β=1 and also the shape of the curve somewhat changes. The nozzle to target ratio of β=2 generates an optimal mix of the impinging jet flow with the rotationally induced flow resulting in higher heat transfer rate. There is only small change in Nusselt number values at spacings greater than β=2. This observation is in–line with the previous study by Hung and Lin [74] for a confined jet impingement with a stationary disk.

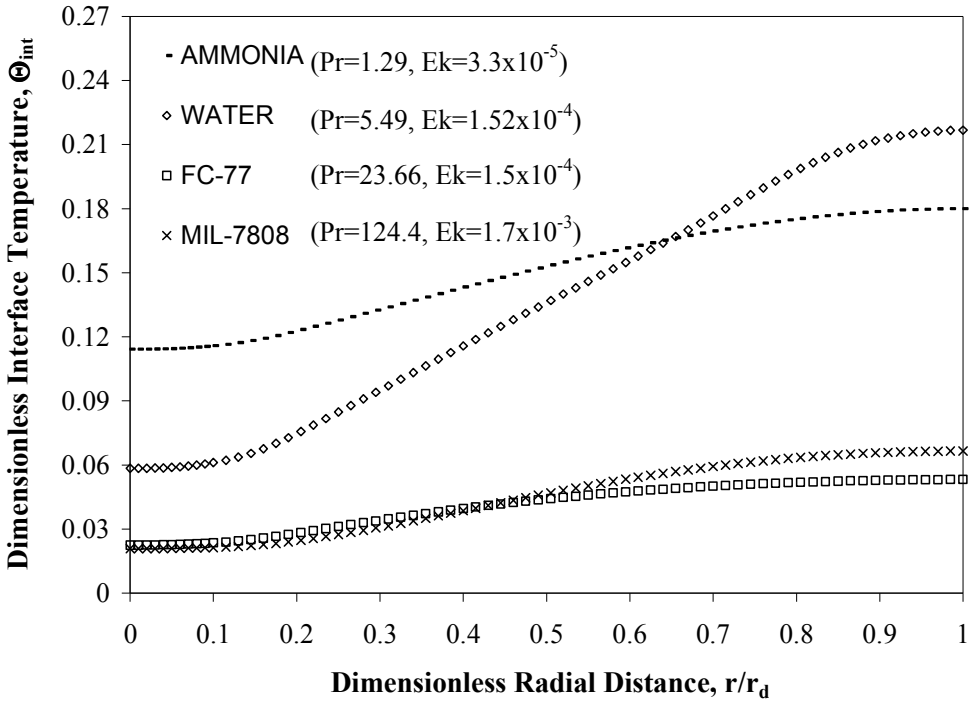

Figure 5.19 Dimensionless interface temperature distributions for different cooling fluids with silicon as the disk material (Re=1,000, β=2.0, b/d_n=0.25).

Figures 5.19 compares the dimensionless solid–fluid interface temperature results of the present working fluid (water) with three other coolants that have been considered in previous thermal management studies, namely ammonia (NH_3), flouroinert (FC–77), and oil (MIL–7808) under a Reynolds number of 1,000. Even though the rotational rate (Ω) for the top confining wall was set at 350 RPM the variation of Ekman number occurred since the density (ρ) and dynamic viscosity (μ) are different for each fluid. The interface temperature distribution of figure 5.19 shows similar results for FC–77 and MIL–7808. It may be noticed that both ammonia and water present higher dimensionless interface temperature distribution in comparison with MIL–7808 and FC–77. Water shows a larger variation of dimensionless interface temperature along the radius of the disk. The water and ammonia curves intersect at a dimensionless radial distance of r/r_d=0.65.

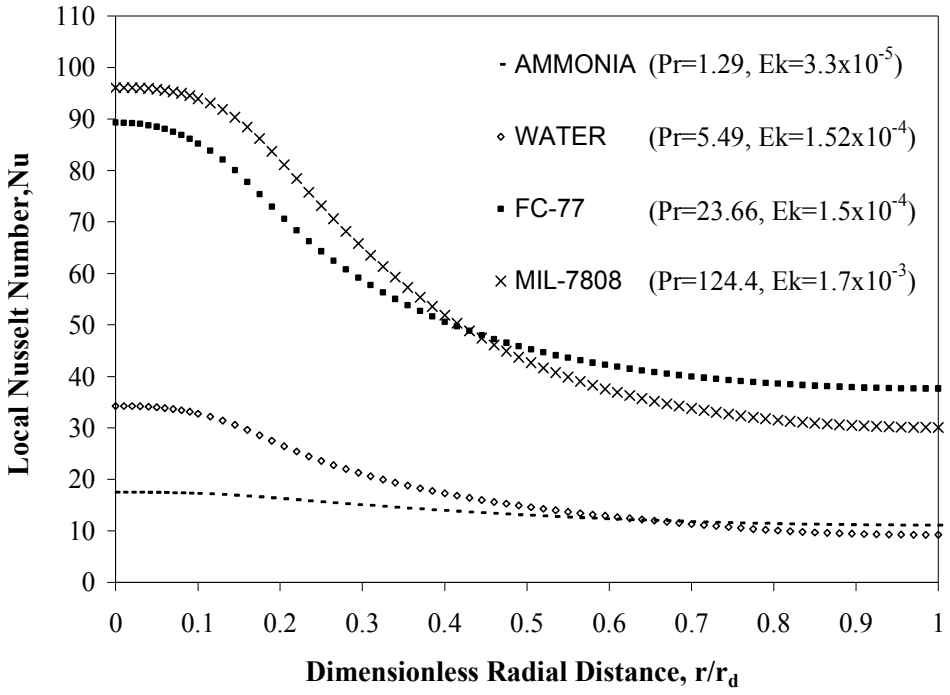

Figure 5.20 Local Nusselt number distributions for different cooling fluids with silicon as the disk material (Re=1,000, β=2.0, b/d_n=0.25).

Figure 5.20 shows the corresponding local Nusselt number distributions. It may be noticed that MIL–7808 presents the highest local Nusselt number values in comparison with water, NH_3 and FC–77 for a dimensionless radial distance, $r/r_d < 0.45$. Only FC–77 exhibits a higher heat removal rate beyond this point. MIL–7808 shows the largest variation of local Nusselt number primarily because of its large variation of viscosity with temperature. Ammonia provides the lowest Nusselt number because of its small Prandtl number. Higher Prandtl number fluids lead to a thinner thermal boundary layer, and more effective heat removal rate at the interface. Present working fluid results are in agreement with Li et al. [80] findings where larger Prandtl number corresponded to a higher recovery factor. Thus, different Prandtl numbers represent different thermal boundary layer thicknesses and different heat generations by viscous dissipation of the fluids.

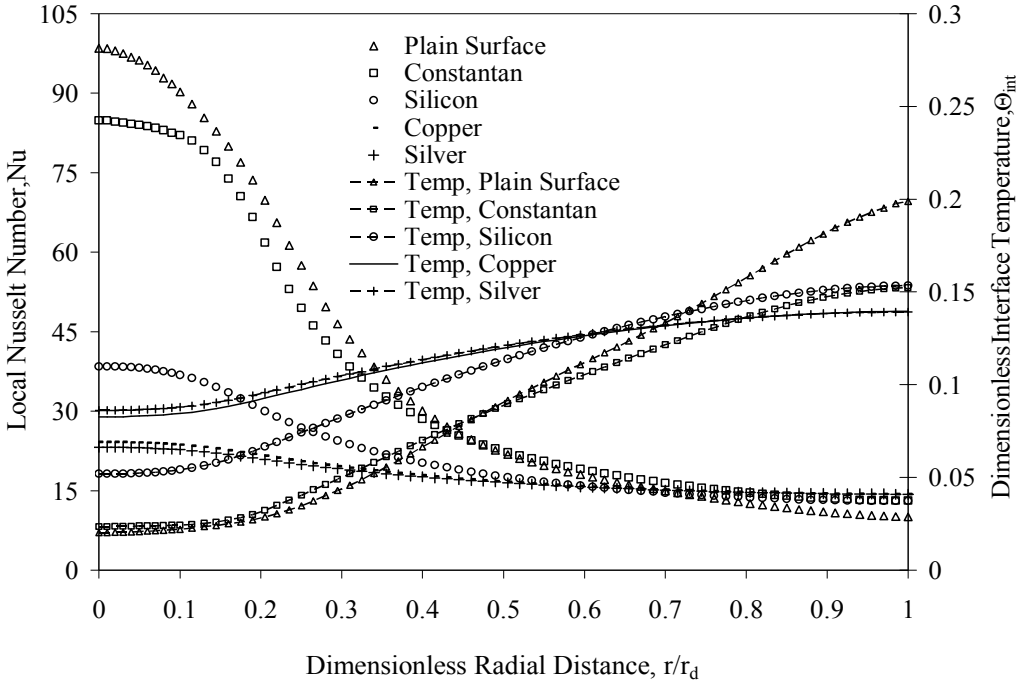

Figure 5.21 Local Nusselt number and dimensionless interface temperature distributions for different solid materials with water as the cooling fluid (Re=1,000, $Ek=4.25\times10^{-4}$, $\beta=2.0$, $b/d_n=0.25$).

The dimensionless solid–fluid interface temperature and local Nusselt number distribution plots as a function of a dimensionless radial distance (r/r_d) measured from the axis–symmetric impingement axis for different solid materials with water as the working fluid are plotted in figure 5.21. The numerical simulation was carried out for a set of materials, namely copper, silver, Constantan, and silicon, having different thermo–physical properties at Reynolds number of 1,000 and Ekman number of 4.25×10^{-4}. Results for plain surface (zero thickness of the disk) are also plotted to identify the extent of conjugate effects. The temperature distribution plots reveal how the thermal conductivity of the solid affects the heat flux distribution that controls the local interface temperature. It may be noted that plain surface has the lowest temperature at the impingement axis and the highest at the outer edge of the disk.

The interface temperature variation for Constantan is also quite large due to its lower thermal conductivity. As the thermal conductivity increases, the thermal resistance within the solid becomes lower and the interface temperature becomes more uniform as seen in the plots corresponding to copper and silicon. The cross–over of the curves of the four materials and plain surface occurred due to a constant fluid flow and heat input rate that provides a constant thermal energy transfer for all circumstances. Narrow and elevated bell shape pattern is seen in figure 5.21 for solid materials with lower thermal conductivity. As the thermal conductivity is increased, a more uniform Nusselt number distribution is obtained.

One of the goals of this work was to develop a predictive trend of the average heat transfer coefficient. A correlation for the average Nusselt number was developed as a function of thermal conductivity ratio, nozzle to target spacing, disk thickness, Ekman

number, and Reynolds number to accommodate most of the transport characteristics of a confined liquid jet impingement cooling process. A correlation that best fitted the numerical data can be placed in the following form:

$$Nu_{av}=1.9762\cdot\beta^{-0.01}\cdot Re^{0.75}\cdot Ek^{-0.111}\cdot(b/d_n)^{-0.05}\cdot\varepsilon^{-0.69} \quad (5.2)$$

In developing this correlation, all average Nusselt number data corresponding to the variation of different parameters were used. Only data points corresponding to water as the fluid were used because the number of average heat transfer data points for other fluids was small. Figure 5.22 gives the comparison between the numerical average Nusselt numbers to average Nusselt numbers predicted by equation 5.2.

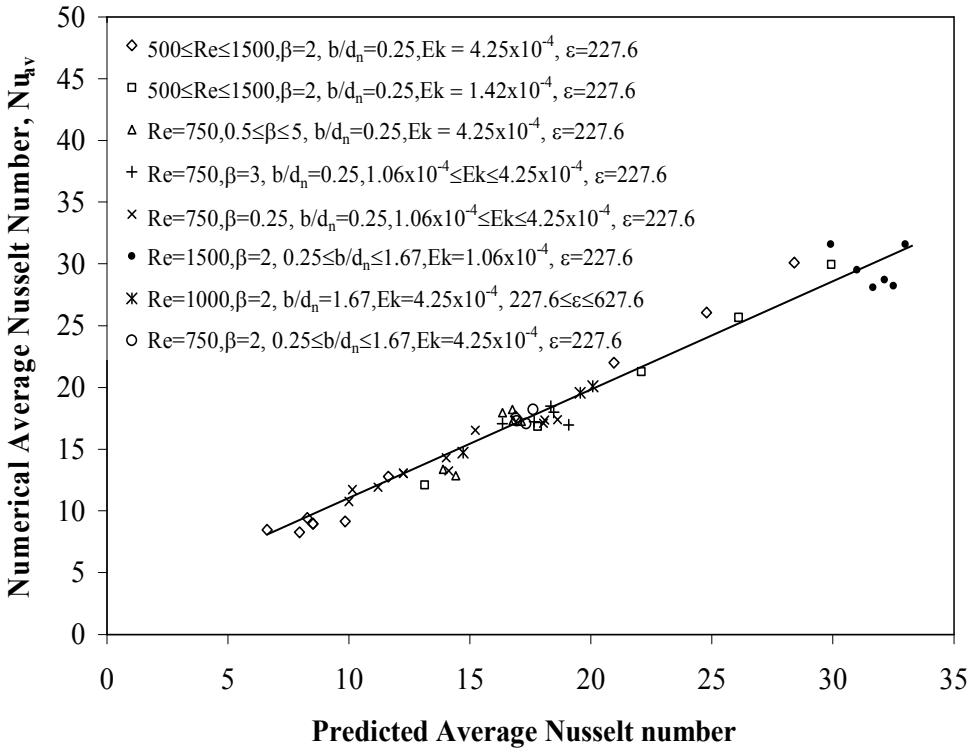

Figure 5.22 Comparison of predicted average Nusselt number of equation 5.2 with present numerical data.

The percent difference of the predicted average Nusselt number was defined as: $\%diff = ((Nuav_{pred} - Nuav_{num})/Nuav_{num}) \times 100$. The average Nusselt number deviates in the range of –13.8% to +15.3% from the average Nusselt numbers predicted by equation 5.2. The mean deviation of the correlation was equal to 6.8%. The ranges of the dimensionless variables used are: $500 \leq Re \leq 1{,}500$, $4.25 \times 10^{-5} \leq Ek \leq 1.06 \times 10^{-4}$, $0.25 \leq \beta \leq 5$, $Pr = 5.49$, $0.25 \leq b/d_n \leq 1.67$, and $227.6 \leq \varepsilon \leq 627.6$. It should be noted from figure 5.22 that a large number of data points are well correlated by equation 5.2. This correlation provides a convenient tool for the prediction of average heat transfer coefficient under liquid jet impingement with a spinning confinement disk. The major difference between past studies and the present investigation is the accounting for conduction within the solid wafer and fluid for various materials, the spinning rate of the confinement disk, and the nozzle to target spacing ratio as a part of the correlation.

Three other papers used for the validation of this numerical study were the analytical works carried out by Scholtz and Trass [6], Nakoryakov et al. [68], and Liu et al. [17] using fluids with Prandtl number greater than unity as coolants. The fluids were tested for heat removal under free liquid jet impingement on a heated flat surface maintained at uniform heat flux. The graphical representation of actual numerical Nusselt number results at the stagnation point at different Reynolds number are shown in figure 5.23. The results shown in figure 5.23 were on average within 8.17% of Scholtz and Trass [6], within 6.67% of Nakoryakov et al. [68], and within 6.75% of Liu et al. [17].

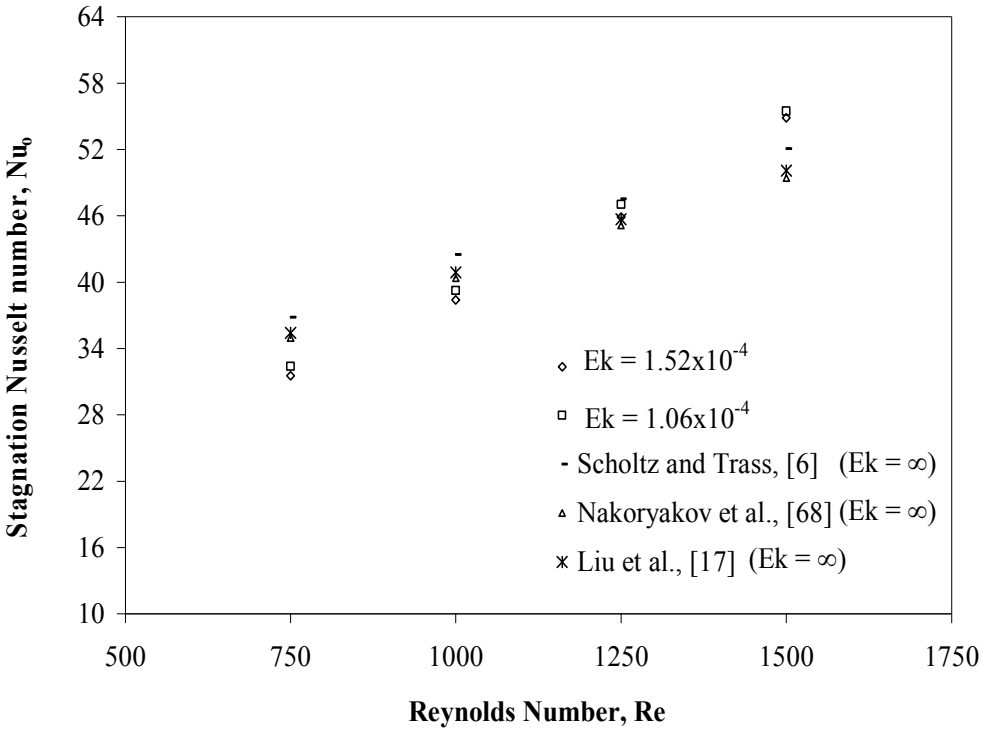

Figure 5.23 Stagnation Nusselt number comparison of Scholtz and Trass [6], Nakoryakov et al. [68], and Liu et al. [17] with actual numerical results under different Reynolds and Ekman numbers (d_n=1.2 mm, b=0.3 mm).

The percent difference of the predicted of local Nusselt number at the stagnation was defined as: $\%diff = ((Nuo_{num} - Nuo_{exp})/ Nuo_{exp}) \times 100$. The local Nusselt number under Reynolds numbers of 750, 1,000, 1,250 and 1,500 correlates with an average difference margin of 11.83%, 6.31%, 2.26%, and 8.40% respectively. Considering the inherent discretization and round off errors, this comparison of Nusselt number at the stagnation point is also quite satisfactory.

Chapter 6 Partially–confined Liquid Jet Impingement Model Results

6.1 Steady State Cooling of Spinning Target

The numerical results of conjugate heat transfer of a steady laminar flow by a partially–confined liquid jet impingement on a uniformly heated and spinning disk of finite thickness and radius are presented in terms of its dimensionless interface temperature distributions and local as well as average Nusselt number variation. The examine parameters are: several flow rates or jet Reynolds numbers, six spinning rates or Ekman number, five different disk thicknesses and four nozzle to target spacings.

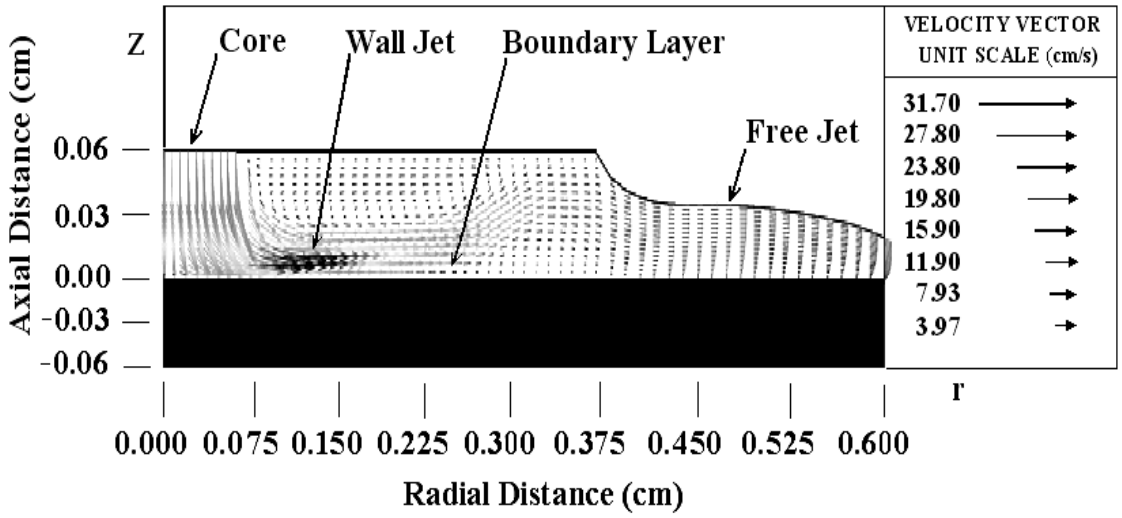

Figure 6.1 Velocity vector distribution for a partially–confined jet impingement on a silicon disk with water as the cooling fluid (Re=475, Ek=4.25x10^{-4}, r_p/r_d=0.5, β=0.5, b/d_n=0.5).

A typical velocity vector distribution is shown in figure 6.1. It can be seen that the velocity remains almost uniform at the potential core region of the jet. The velocity

decreases as the fluid jet expands in the radial direction as it approaches the target plate during the impingement process. The direction of motion of the fluid particles shifts by as much as 90^{o}. After this, the fluid accelerates creating a region of high velocity wall jet within the confined fluid medium. It can be noticed that as the boundary layer thickness increases downstream and the frictional resistance from the walls are eventually transmitted to the entire film thickness. This effect is observed once the fluid leaves the confined region and moves downstream with a free surface on the top. The vectors in the viscous zone show a parabolic profile going from a minimum value at the solid–fluid interface to a maximum at the free surface. The boundary layer develops rapidly and the velocity of the fluid decreases as it spreads radially along the disk. It may be noted, however, that due to spinning streamlines are not aligned along the disk radius, rather the fluid moves at an angle based on the rate of rotation. The three different regions observed in the present investigation are in agreement with the experiments of Liu et al. [17].

Figure 6.2 presents the free surface height distribution for different plate to disk confinement ratios when the jet strikes the center of the disk while it is spinning at a rate of 125 RPM ($Ek=4.25x10^{-4}$). It can be seen that the fluid spreads out radially as a thin film. The film thickness decreases as the plate to disk confinement ratio decreases under the same spinning rate and flow rate. This behavior occurs due to dominance of surface tension and gravitational forces that form the free surface as the fluid leaves the confinement zone and moves downstream. When r_p is increased, the frictional resistance from both walls slows down the momentum and results in greater film thickness. For the conditions considered in the present investigation, a sudden drop in fluid height occurs for $r_p/r_d < 0.333$ because the equilibrium film height for free surface motion is

significantly lower than confinement height. In this situation, liquid may not cover all the way to the end of the confinement disk and free surface may start to form within the confinement region to provide a smooth streamline for the free surface. At $r_p/r_d \geq 0.5$, the confinement region is fully covered with fluid and a smooth transition is seen in film height distribution after exit.

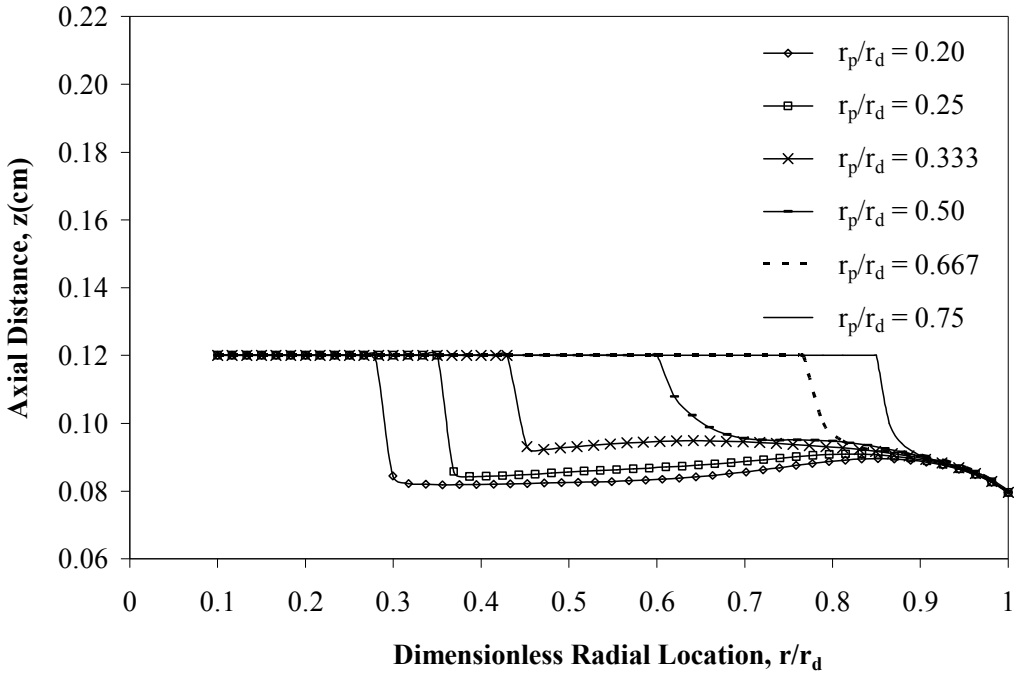

Figure 6.2 Free surface height distribution for different plate to disk confinement ratio with water as the cooling f1uid (Re=450, Ek=4.25x10^{-4}, β=0.5, b/d_n=0.5).

Figure 6.3 shows the local Nusselt number and the dimensionless interface temperature variation for different Reynolds number under a rotational rate of 125 RPM (Ek=4.25x10^{-4}). The plots reveal that dimensionless interface temperature decreases with jet velocity (or Reynolds number). At any Reynolds number, the dimensionless interface temperature has the lowest value at the stagnation point (underneath the center of the axial opening) and increases radially downstream reaching the highest value at the end of

the disk. This is due to the development of thermal boundary layer as the fluid moves downstream from the center of the disk. The thickness of the thermal boundary layer increases with radius and causes the interface temperature to increase. All local Nusselt number distributions are half–bell shaped with a peak at the stagnation point. Figure 6.3 confirm to us how an increasing Reynolds number contributes to a more effective cooling. Similar profiles have been documented by Garimella and Nenaydykh [77] and Ma et al. [69, 81].

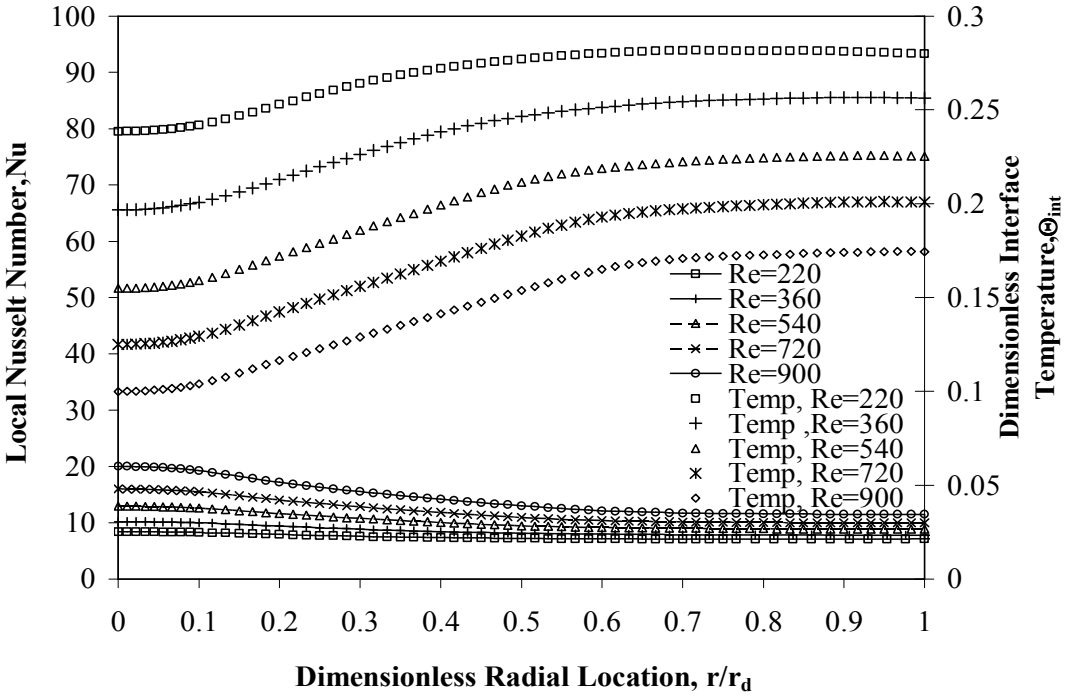

Figure 6.3 Local Nusselt number and dimensionless interface temperature distributions for a silicon disk with water as the cooling fluid for different Reynolds numbers (Ek=4.25x10^{-4}, β=0.5, b/d_n=0.5, r_p/r_d=0.667).

Figure 6.4 plots the average Nusselt number as a function of Reynolds number for low, intermediate, and high Ekman numbers. It may be noted that average Nusselt number increases with Reynolds number. As the flow rate (or Reynolds number) increases, the magnitude of fluid velocity near the solid–fluid interface that controls the

convective heat transfer rate increases. Furthermore, at a particular Reynolds number, the Nusselt number gradually increases with the increment of disk spinning rate.

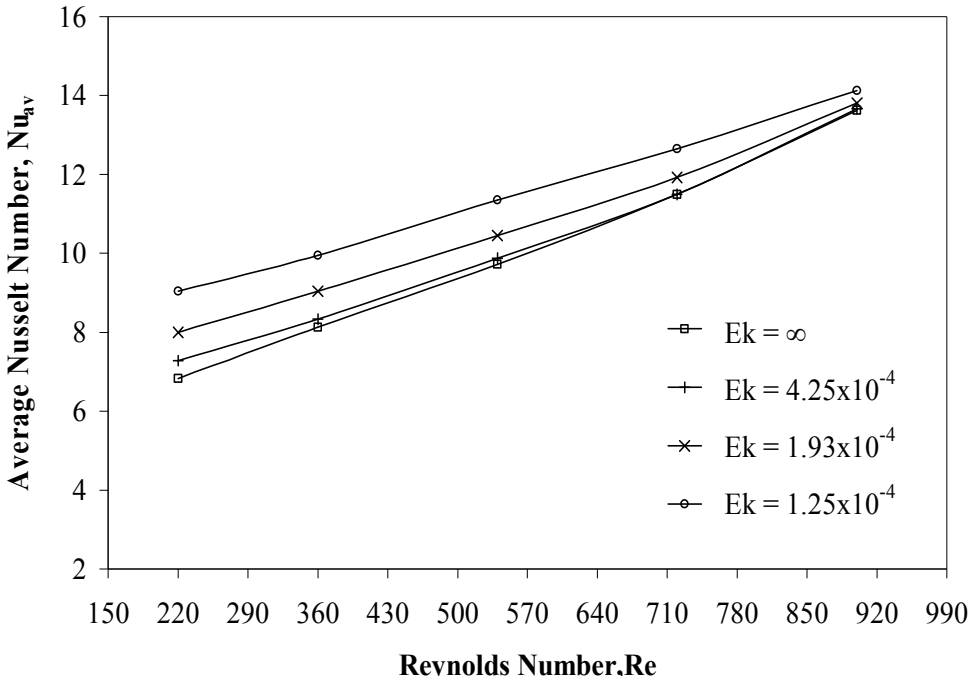

Figure 6.4 Average Nusselt number variations with Reynolds number at different Ekman numbers for a silicon disk with water as the cooling fluid (β=0.5, b/d_n=0.5, r_p/r_d=0.667).

This behavior confirms the positive influence of the rotational rate on the average Nusselt number down to $Ek=1.25x10^{-4}$ that corresponds to a spinning rate of 425 RPM. It may be also noticed that the average Nusselt number plots get closer to each other as the Reynolds number increases indicating that curves will intersect at higher Reynolds numbers. These intersections indicate the presence of a liquid jet momentum dominated region at higher Reynolds numbers. From the numerical results it was observed that the heat transfer is dominated by impingement when $Re \cdot Ek > 0.124$ and dominated by disk rotation when $Re \cdot Ek < 0.092$. In between there limits, both of these effects play an important role in determining the variations of average Nusselt number. This type of

behavior is consistent with the experimental results of Brodersen et al. [38] where the ratio of jet and rotational Reynolds numbers was used to characterize the flow regime.

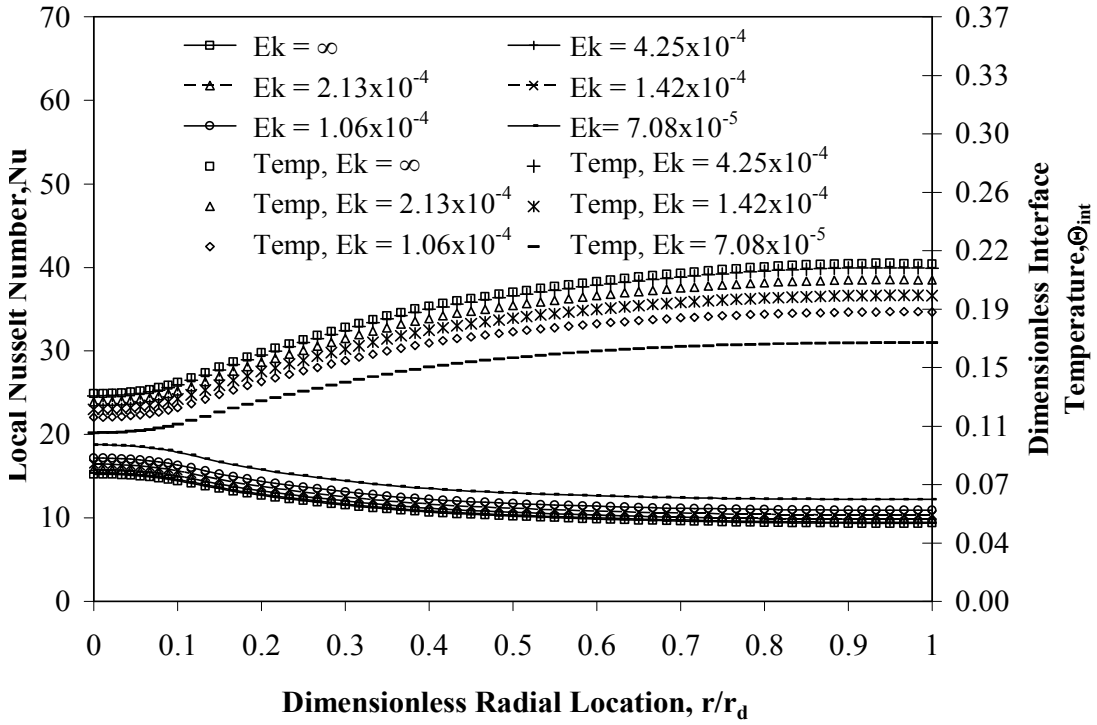

Figure 6.5 Local Nusselt number and dimensionless interface temperature distributions for a silicon disk with water as the cooling f1uid at different Ekman numbers (Re=540, β=0.25, b/d_n=0.5, and r_p/r_d=0.667).

The rotational rate effects on the local Nusselt number and dimensionless interface temperature are illustrated in figure 6.5 for a Reynolds number of 540 and dimensionless nozzle–to–plate spacing (β) equal to 0.25. It may be noted that rotational effect increases local Nusselt number and generates lower temperature over the entire solid–fluid interface with somewhat less intensity in comparison with the Reynolds number effect. In addition, figure 6.5 shows that as the Ekman number decreases from ∞ to $7.08\text{x}10^{-5}$ the local Nusselt number increases by an average of 24.02% and the dimensionless interface temperature decreases by an average of 8.34%. The enhancement of Nusselt number due to rotation is primarily caused by enhancement of local fluid

velocity adjacent to the rotating disk surface. The tangential velocity due to rotation combined with axial and radial velocities due to jet momentum increases the magnitude of the velocity vector starting from the center of the disk.

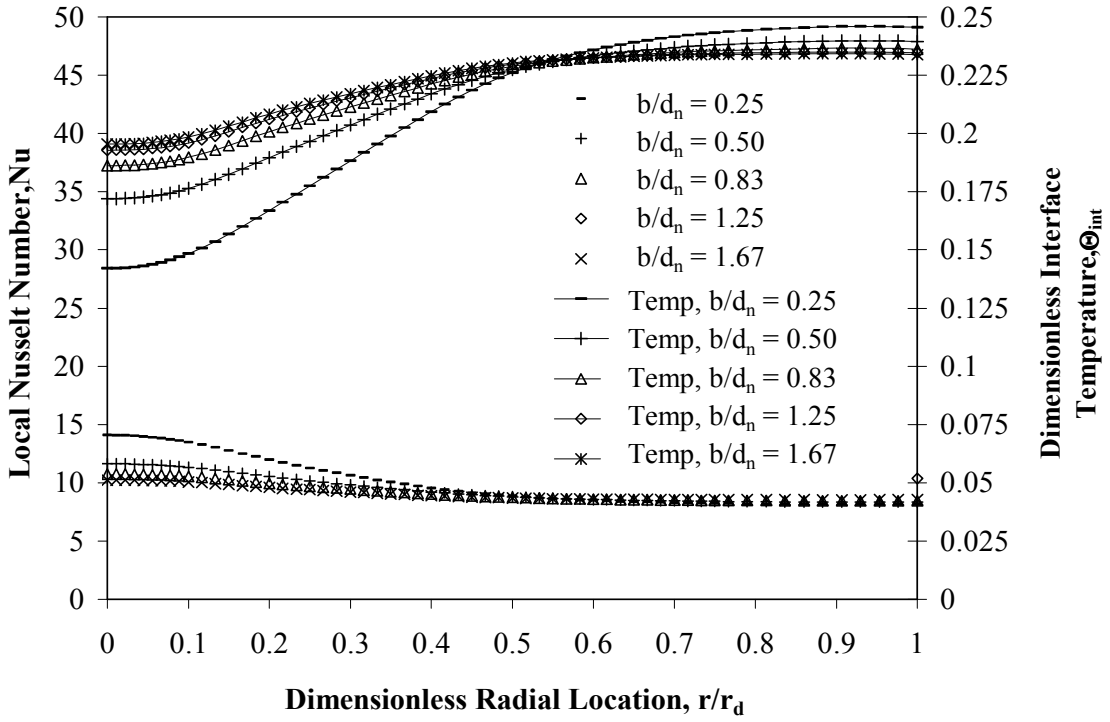

Figure 6.6 Local Nusselt number and dimensionless interface temperature distributions for different silicon disk thicknesses with water as the cooling fluid (Re=450, Ek=4.25x10^{-4}, β=0.5, r_p/r_d=0.667).

The effects of disk thickness variation on the dimensionless interface temperature and local Nusselt number are shown in figure 6.6. The dimensionless interface temperature increases from the impingement region all the way to the end of the disk. It may be noted that the curves intersect with each other at a dimensionless radial distance of r/r_d=0.55. The thicker disks generate more uniform dimensionless interface temperature due to larger radial conduction within the disk. The local Nusselt number plots change slightly with the variation of disk thickness. In all cases, it is evident that the Nusselt number is more sensitive to the solid thickness at the core region where higher

values are obtained. For a lower stagnation temperature, the outlet temperature tends to be relatively higher under constant flow rate and heat flux conditions. This is quite expected because of the overall energy balance of the system. This phenomenon has been documented by Lachefski et al. [54].

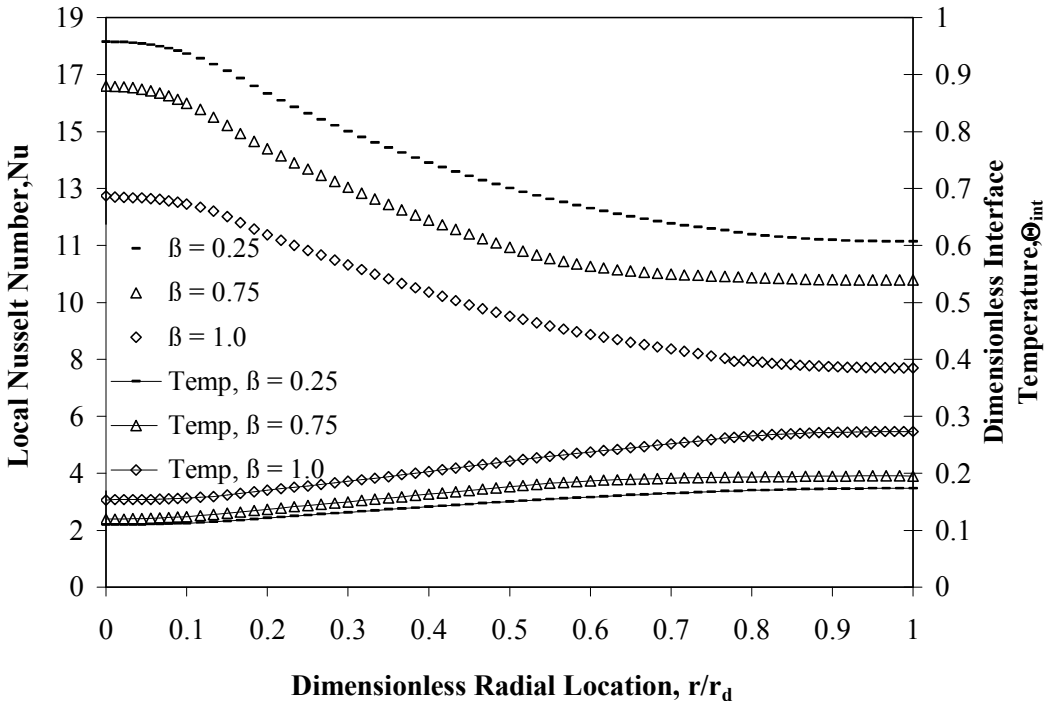

Figure 6.7 Local Nusselt number and dimensionless interface temperature distributions for a silicon disk with water as the cooling fluid for three different nozzle to target spacing ratio (Re=750, Ek=4.25×10^{-4}, b/d_n=0.5, r_p/r_d=0.667).

Three different nozzle to target spacing ratios (β) from 0.25 to 1 were modeled and the results are shown in figure 6.7. It may be noticed that the impingement height quite significantly affects the Nusselt number distribution. A higher local Nusselt number is obtained when the nozzle is brought close to the heated disk (β=0.25). The smaller gap between the nozzle and the target disk avoids loss of momentum as the jet travels through the confined fluid medium and results in a larger fluid velocity and therefore a larger rate of convective heat transfer. As the nozzle is moved away from the disk, the local Nusselt

number decreases. This observation is in–line with the previous study by Hung and Lin [74] for a confined jet impingement on a stationary disk.

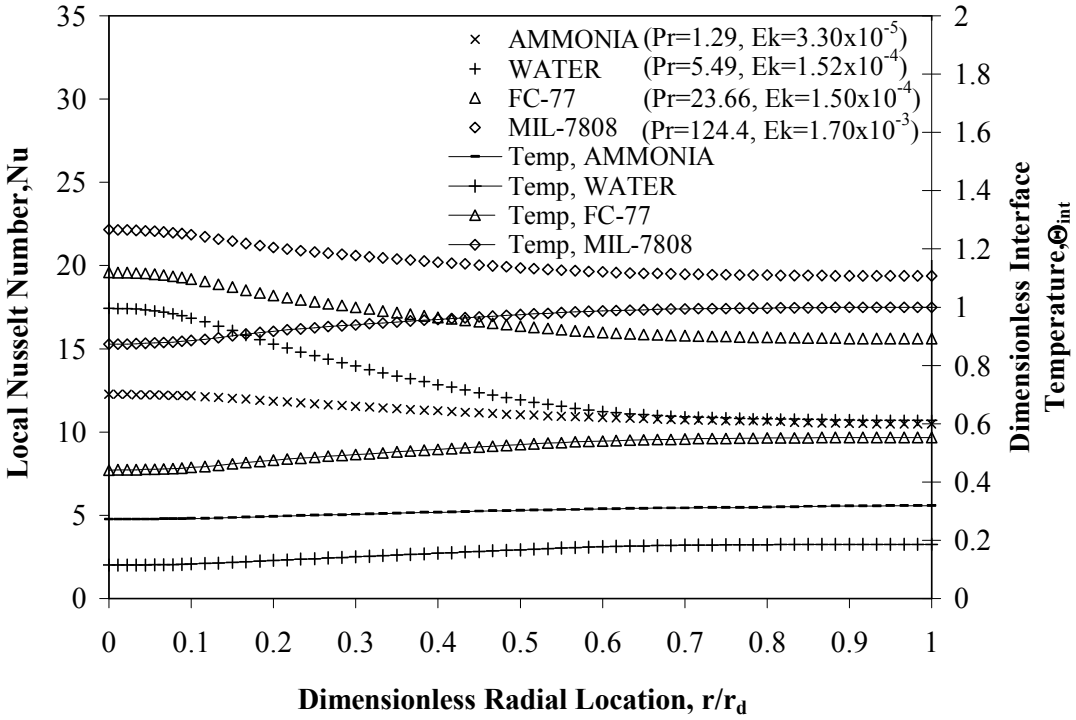

Figure 6.8 Local Nusselt number and dimensionless interface temperature distributions for different cooling fluids for silicon as the disk material (Re=750, β=0.5, b/d_n=0.5, r_p/r_d=0.667).

Figure 6.8 compares the dimensionless interface temperature and local Nusselt number results of the present working fluid (water) with three other coolants, namely ammonia (NH_3), flouroinert (FC–77) and oil (MIL–7808) under a Reynolds number of 750. Even though the rotational rate (Ω) for the impingement disk was set at 350 RPM the variation of Ekman number occurred since the density (ρ) and dynamic viscosity (μ) are different for each fluid. It may be noticed that MIL–7808 presents the highest dimensionless interface temperature and water has the lowest value. Ammonia shows the most uniform distribution of temperature along the radius of the disk. MIL–7808 presents the highest local Nusselt number values over the entire radial distance. Ammonia on the

other hand provides the lowest Nusselt number. Higher Prandtl number fluids lead to a thinner thermal boundary layer and therefore more effective heat removal rate at the interface. Present working fluid results are in agreement with Li et al. [80] findings where a larger Prandtl number corresponded to a higher recovery factor.

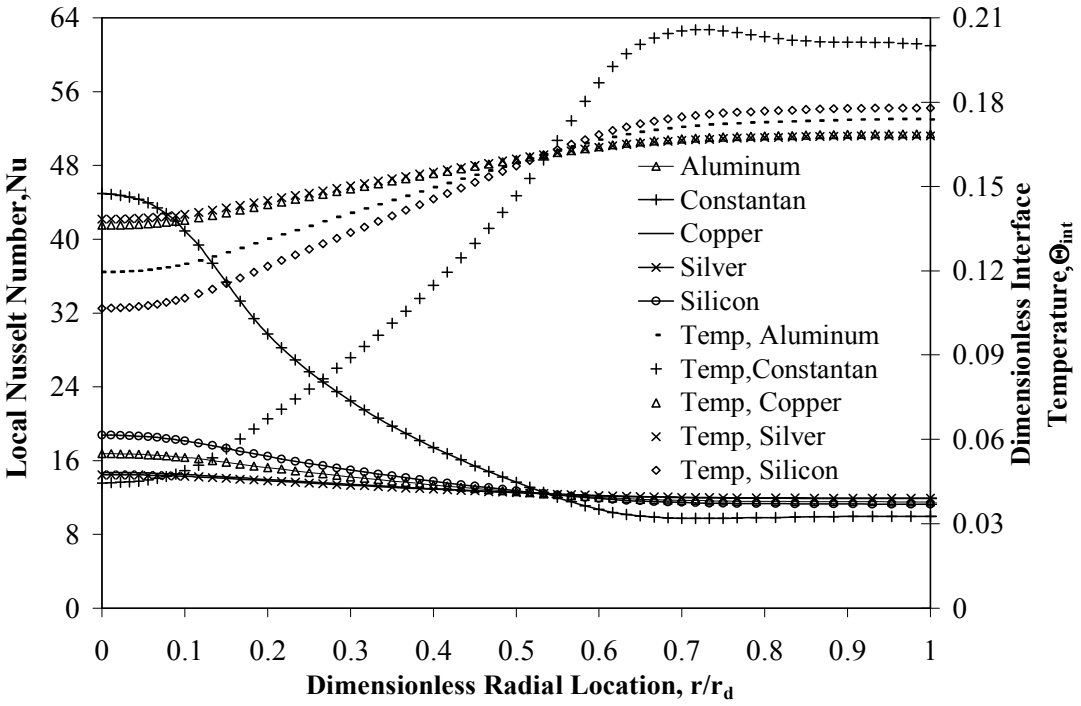

Figure 6.9 Local Nusselt number and dimensionless interface temperature distributions for different solid materials with water as the cooling fluid (Re=875, Ek=$4.25\text{x}10^{-4}$, β=0.5, b/d_n=0.5, r_p/r_d=0.667).

Figure 6.9 shows the dimensionless interface temperature and local Nusselt number distribution plots as a function of dimensionless radial distance (r/r_d) measured from the axis–symmetric impingement axis for different solid materials with water as the working fluid. The dimensionless temperature distribution plots reveal how the thermal conductivity affects the heat flux distribution. Constantan shows the lowest temperature at the impingement zone or stagnation point and the highest dimensionless temperature at the outlet in comparison with other solid materials. Copper and silver show a more

uniform distribution and higher temperature values at the impingement zone due to their higher thermal conductivity. The dimensionless temperature and local Nusselt number distributions of these two materials are almost identical due to their similar thermal conductivity values. The cross–over of curves for all five materials occurred due to a constant fluid flow and heat flux rate that reaches a thermal energy balance. A solid material with lower thermal conductivity shows higher maximum local Nusselt number.

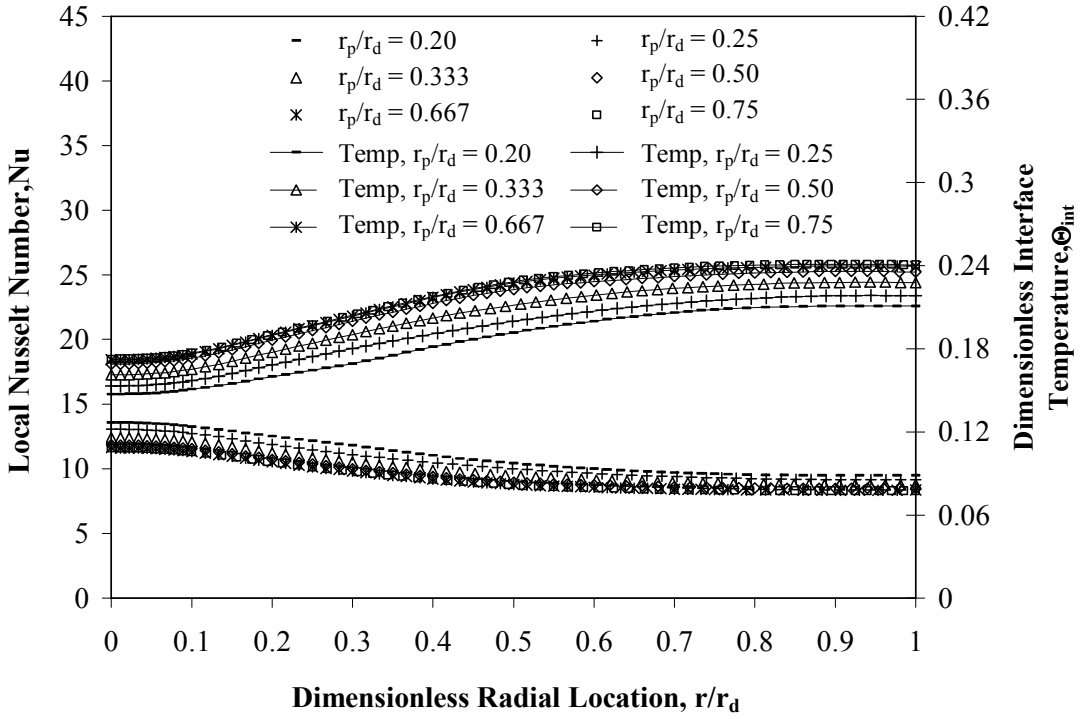

Figure 6.10 Local Nusselt number and dimensionless interface temperature distributions for different plate to disk confinement ratio (Re=450, Ek=4.25x10^{-4}, β=0.5, b/d_n=0.5).

Six different plate–to–disk confinement ratios (r_p/r_d) from 0.2 to 0.75 were modeled for water as the coolant and silicon as the disk material. The effects of plate–to–disk confinement ratio on the dimensionless interface temperature and local Nusselt number are shown in figure 6.10. The dimensionless interface temperature increases with the increment of the plate–to–disk confinement ratio (r_p/r_d). This increment coincides

with the increment of liquid film thickness in the free jet region as seen in figure 6.2. Under the same spinning and flow rates, when r_p is increased the higher frictional resistance from the confinement disk slows down the fluid momentum. In addition, a thinner film thickness for the same flow rate results in higher fluid velocity near the solid–fluid interface resulting in a higher rate of convective heat transfer. This is seen in the distribution of local Nusselt number which increases with the decrease of plate–to–disk confinement ratio.

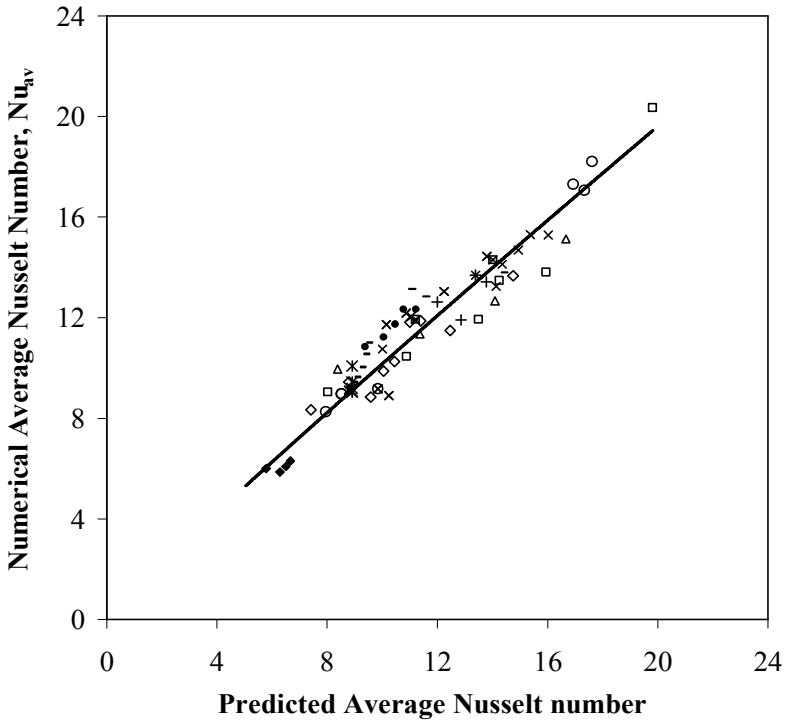

Figure 6.11 Comparison of predicted average Nusselt numbers of equation 6.1 with present numerical data.

Figure 6.11 gives the comparison between the numerical average Nusselt numbers to average Nusselt numbers predicted by equation 6.1. A correlation for the average Nusselt number was developed as a function of confinement ratio, thermal conductivity ratio, and dimensionless nozzle to target spacing ratio, Ekman number, and Reynolds

number to accommodate most of the transport characteristics of a semi–confined liquid jet impingement cooling process. The correlation that best fitted the numerical data can be placed in the following form:

$$Nu_{av}=1.94282\cdot\beta^{0.1}\cdot Re^{0.75}\cdot Ek^{-0.1}\cdot\varepsilon^{-0.7}\cdot(r_p/r_d)^{-0.05} \quad (6.1)$$

In developing this correlation, all average Nusselt number data corresponding to the variation of different parameters were used. Only data points corresponding to water as the fluid were used because the number of average heat transfer data for other fluids were small. The least square curve–fitting technique was used in developing this equation. The sign of the exponents was determined from the trend of variation of average Nusselt number with each parameter. In addition, the percent difference of the predicted average Nusselt number was defined as: $\%\ diff = ((Nuav_{pred} - Nuav_{num})/Nuav_{num}) \times 100$. The average Nusselt number deviates in a range of –15.13% to +15.61% from the average numerical results predicted by equation 6.1. The mean deviation of the above correlation was equal to 6.94%. The ranges of the dimensionless variables in this study are: $360 \le Re \le 900$, $1.06\text{x}10^{-4} \le Ek \le 4.25\text{x}10^{-4}$, $0.25 \le \beta \le 1$, $0.2 \le r_p / r_d \le 0.75$, $Pr=5.49$, $227.6 \le \varepsilon \le 627.6$. A large number of data points are well correlated with equation 6.1, as shown in figure 6.11. This correlation provides a convenient tool for the prediction of average heat transfer coefficient for a partially–confined liquid jet impingement on top of a spinning disk.

6.2 Steady State Cooling of Spinning Confined Wall and Target

Figure 6.12 shows the variation of the dimensionless interface temperature and the local Nusselt number distributions for different Reynolds numbers under a rotational rate of 275 RPM ($Ek_{1,2}=1.93x10^{-4}$).

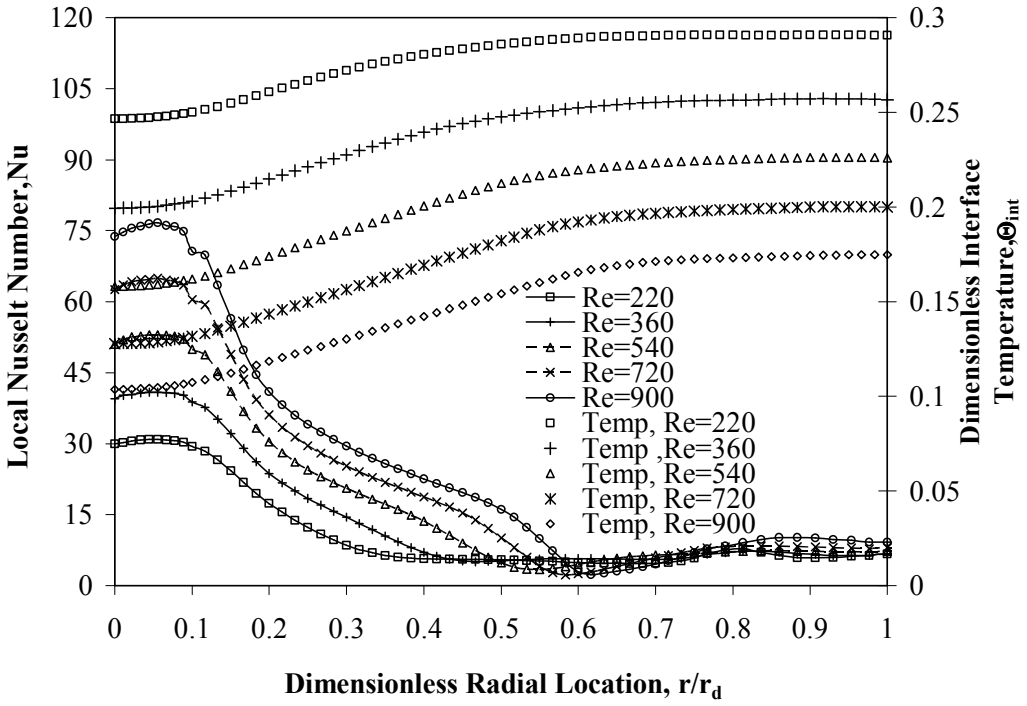

Figure 6.12 Effects of Reynolds number on local Nusselt number and dimensionless solid–fluid interface temperature variation for a silicon disk with water as the cooling fluid ($\beta=0.5$, $b/d_n=0.5$, $r_p/r_d=0.667$, $Ek_{1,2}=1.93x10^{-4}$).

The plots in figure 6.12 reveal that dimensionless interface temperature decreases with jet velocity (or Reynolds number). At any Reynolds number, the dimensionless interface temperature has the lowest value at the stagnation point (underneath the center of the axial opening) and increases radially downstream reaching the highest value at the end of the disk. At a Reynolds number of 220, the temperature becomes practically uniform after $r/r_d > 0.667$. The thickness of the thermal boundary layer increases with radius and causes the interface temperature to increase. The increment of the dimensionless interface

temperature up to the end of its confinement coincides with the thickening of the thermal boundary layer. Afterward it becomes more uniform beneath the free surface. As noted in figure 6.2, there is a significant re–adjustment of fluid layer thickness as the flow comes out of the confinement and moves downstream with a free surface at the top.

Figure 6.12 shows how the local Nusselt number distributions increases over a small distance (core region) measured from the stagnation point, reaching a maximum around r/r_d=0.05, and then decreases along the radial distance as the boundary layer develops further downstream up to the end of the confined spinning plate or $r_p/r_d \approx 0.667$. After this location, the Nusselt number increases downstream and reaches a uniform value at larger radial locations of the disk. The location of the maximum Nusselt number can be associated with the transition of the flow from the vertical impingement to horizontal displacement where the boundary layer starts to develop. The increase of Nusselt number after the exit from the confinement is a result of significant decrease of film thickness that also decreases the thickness of the thermal boundary layer until it reaches a new equilibrium. It may be noticed that at low values of Reynolds number (Re=220 in particular), local Nusselt number remains almost constant over a good portion of the disk including a portion within the confinement region. This is because at low Reynolds number, the jet momentum dies down and the flow is driven by rotational motion of the disks. Figure 6.12 confirms to us how an increasing Reynolds number contributes to a more effective cooling. The observations are in–line with the previous studies by Garimella and Nenaydykh [77] and Saniei et al. [39].

Figure 6.13 plots the average Nusselt number as a function of Reynolds number for low, intermediate, and high Ekman numbers of the solid disk. The spinning of the

confined plate was done at a constant rate of 125 RPM or $Ek_2=4.25x10^{-4}$. It may be noted that average Nusselt number increases with Reynolds number. As the flow rate (or Reynolds number) increases, the magnitude of fluid velocity near the solid–fluid interface that controls the convective heat transfer rate increases. Furthermore, at a particular Reynolds number, the Nusselt number gradually increases with the increment of disk spinning rate. This behavior confirms the positive influence of the rotational rate of the solid disk on the average Nusselt number down to $Ek_1=1.25x10^{-4}$ that corresponds to a spinning rate of 425 RPM.

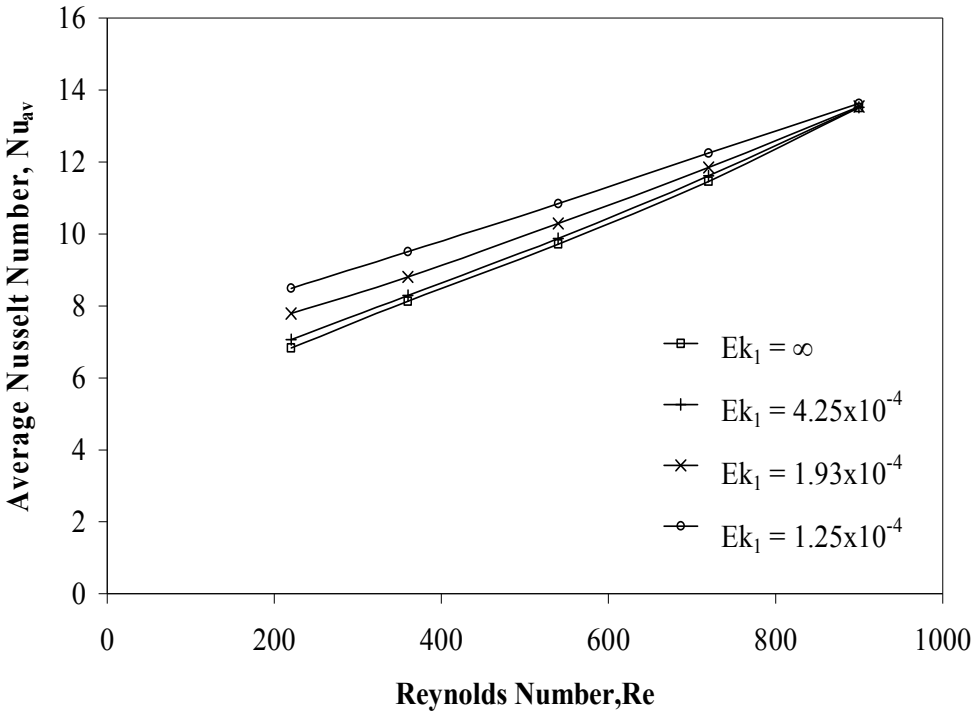

Figure 6.13 Effects of Reynolds number on average Nusselt number at different Ekman numbers for a silicon disk with water as the cooling fluid ($\beta=0.5$, $b/d_n=0.5$, $r_p/r_d=0.667$, $Ek_2=4.25x10^{-4}$).

It may be also noticed that the average Nusselt number plots gets closer to each other as the Reynolds number increases indicating that curves will intersect at higher Reynolds numbers. These intersections indicate the presence of a liquid jet momentum

dominated region at higher Reynolds numbers. From the numerical results it was observed that the heat transfer is dominated by impingement when $Re \cdot Ek_1 > 0.113$ and dominated by disk rotation when $Re \cdot Ek_1 < 0.09$. In between there limits, both of these effects play an important role in determining the variation of average Nusselt number. This type of behavior is consistent with the experimental results of Brodersen et al. [39] where the ratio of jet and rotational Reynolds numbers was used to characterize the flow regime.

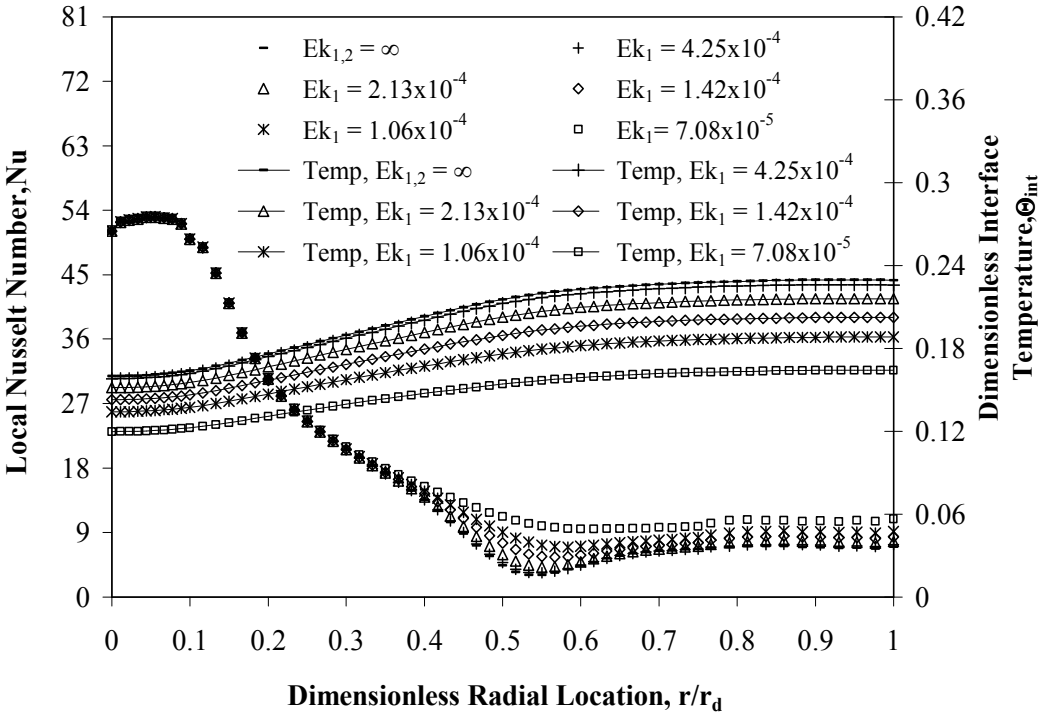

Figure 6.14 Effects of Ek_1 variation on local Nusselt number and dimensionless interface temperature distributions for a silicon disk with water as the cooling f1uid (Re=540, β=0.5, b/d_n=0.5, r_p/r_d=0.667, $Ek_2=4.25x10^{-4}$).

The rotational rate effects of the solid disk under the influence of a constant spinning rate of the confinement plate on the local Nusselt number and dimensionless interface temperature are illustrated in figure 6.14 for a Reynolds number of 540 and

dimensionless nozzle–to–plate spacing (β) equal to 0.5. It may be noted that the local Nusselt number remains the same over the distance $0 < r/r_d < 0.35$ and increases with rotational rate (decreases with Ekman number) further downstream. This is because the flow is highly dominated by jet inlet momentum at $r/r_d < 0.35$, and the centrifugal forces generated by rotation of the disks can influence the transport only at $r/r_d > 0.35$. It may also be noted that a higher rotational rate provides a lesser amount of undershoot in Nusselt number and a higher equilibrium value at large disk radii. Figure 6.14 shows that dimensionless interface temperature decreases with the increment of the rotational rate in comparison with the stationary case due to the enhancement of local fluid velocity adjacent to the disk. The local Nusselt number increases by an average of 33.78% in figure 6.14; as the Ekman number of solid spinning disk decreases from ∞ to 7.08×10^{-5} under the influence of a constant spinning rate of 125 RPM ($Ek_2 = 4.25 \times 10^{-4}$) of the top confinement disk. The dimensionless interface temperature decreases by an average of 10.85% in figure 6.14 under a Reynolds number of 540. The enhancement of Nusselt number due to rotation is primarily caused by enhancement of local fluid velocity adjacent to the rotating disk surface. The tangential velocity due to rotation combined with axial and radial velocities due to jet momentum increases the magnitude of the velocity vector.

Figure 6.15 shows the rotational rate effects of the top confinement disk in conjunction with a constant spinning rate of the solid impingement disk on local Nusselt number and dimensionless interface temperature distributions for a Reynolds number of 540 and dimensionless nozzle–to–plate spacing (β) equal to 0.5. It may be noted that rotational effect up to a spinning rate of 375 RPM or ($Ek_2 = 1.42 \times 10^{-4}$) increases the local

Nusselt number and generates lower temperature over the entire solid–fluid interface with less intensity in comparison with the Reynolds number effect shown in figure 6.12 and the solid disk rotational rate effect under a constant spinning of the confinement plate shown in figure 6.14.

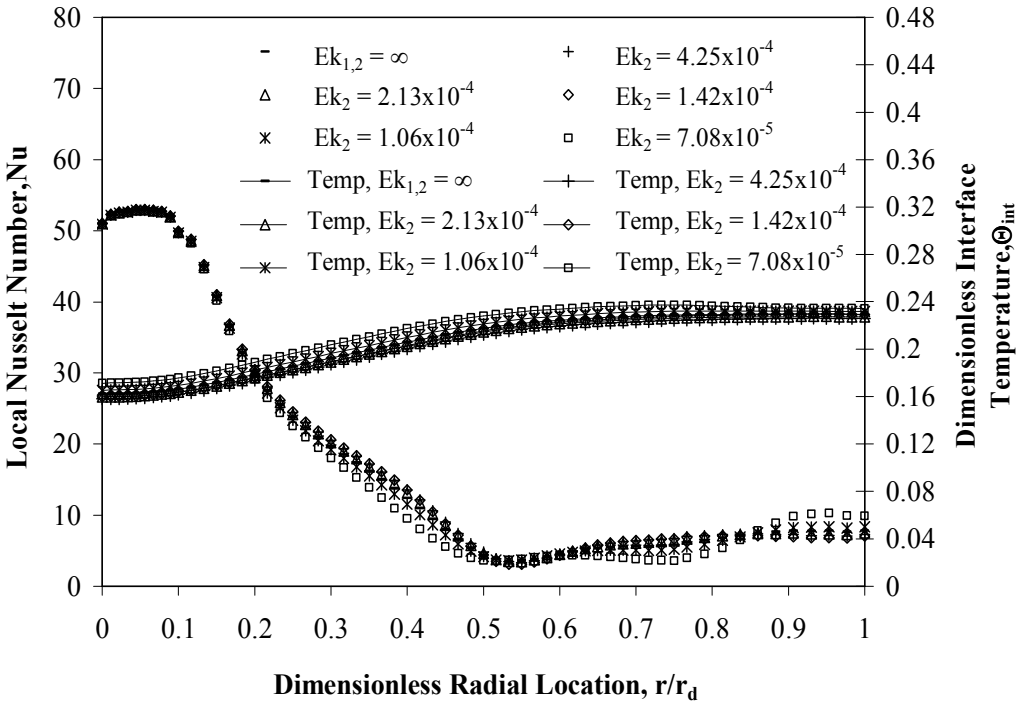

Figure 6.15 Effects of Ek_2 variation on local Nusselt number and dimensionless interface temperature distributions for a silicon disk with water as the cooling f1uid (Re=540, β=0.5, b/d_n=0.5, r_p/r_d=0.667, $Ek_1=4.25x10^{-4}$).

Figure 6.15 shows that dimensionless interface temperature decreases with the increment of the rotational rate up to a spinning rate of 375 RPM ($Ek_2=1.42x10^{-4}$) in comparison with the stationary case due to the enhancement of local fluid velocity adjacent to the disk. The local Nusselt number increases by an average of 5.92% and the dimensionless interface temperature decreases by an average of 0.40% in figure 6.15; as the Ekman number of the top confined plate decreases from ∞ to $1.42x10^{-4}$ under the influence of a constant spinning rate of 125 RPM ($Ek_1=4.25x10^{-4}$) of the solid

impingement disk. However, exceptions occur for spinning rates of 500 and 750 RPM (Ek_2=1.06x10^{-4} and 7.08x10^{-5}) where higher values for dimensionless interface temperature and lower values for Nusselt number are found for the most part of the solid–fluid interface. In these particular cases, the rotation generates a negative effect within the confined region. At these high rotational rates of the top disk (4 and 6 times compared to the bottom disk) the thermal boundary layer structure at the heated bottom disk tends to get swept away by the strong rotational motion of the top disk. Therefore a lower Nusselt number is achieved compared to other cases in the confined region. However, when the flow gets out of the confinement at (r/r_d=0.667), the added momentum exerted by the top disk results in rise of heat transfer coefficient from this point all the way to the end of the disk. Therefore, the proper selection of two spinning rates is crucial in a design process. This type of behavior is consistent with the observations of Popiel and Boguslawski [36].

The effects of disk thickness variation on the dimensionless interface temperature and local Nusselt number are shown in figure 6.16. In these plots, silicon has been used as the disk material and water as the cooling fluid for Reynolds number of 450 and spinning rate of 125 RPM ($Ek_{1,2}$=4.25x10^{-4}). The dimensionless interface temperature increases from the impingement region all the way to the end of the disk. It may be noted that the disk thickness variation curves from the 0.25 to 1.67 intersect with each other at a dimensionless radial distance of r/r_d=0.55. The thicker disks generate more uniform dimensionless interface temperature due to a larger radial conduction within the disk.

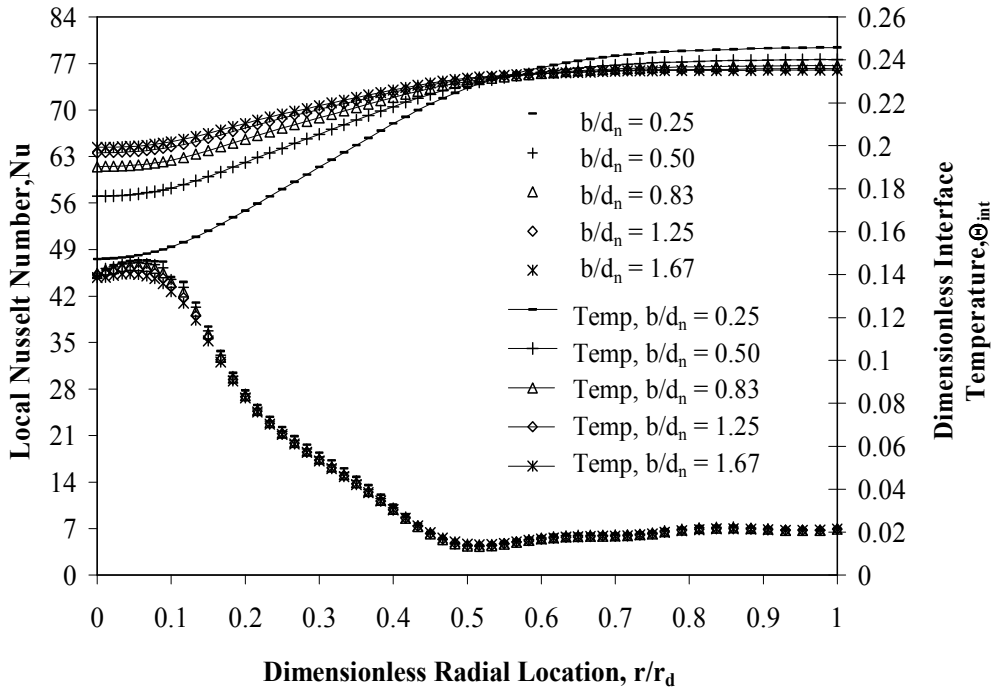

Figure 6.16 Effects of thickness variation on local Nusselt number and dimensionless interface temperature distributions for a silicon disk with water as the cooling f1uid (Re=450, β=0.5, $Ek_{1,2}=4.25x10^{-4}$, $r_p/r_d=0.667$).

Since the flow rate and heat input at the bottom of the disk are kept constant, the global energy balance dictates that average interface temperature changes only slightly as the thermal resistance offered by the disk changes with the variation of disk thickness. It may be observed from figure 6.16 that average interface temperature slightly increases with the increment of disk thickness. The local distribution of interface temperature is primarily controlled by the re–distribution of input heat within the solid. A thinner plate offers a smaller opportunity for heat flux re–distribution and therefore a larger variation controlled by convection and local fluid temperature is seen. For a thicker plate, more opportunity for radial conduction results in higher interface heat flux in the impingement region where the fluid is cooler and gradually smaller interface heat flux as the fluid moves downstream. This results in more uniform interface temperature as shown in

figure 6.16. The combined effects only slight change in average interface temperature whereas large change in local distribution with the variation of thickness results in plots intersecting each other in figure 6.16. Local Nusselt number plots in figure 6.16 change slightly with the variation of disk thickness. In all cases, it is evident that the Nusselt number is sensitive to the solid thickness especially at the core region where higher Nusselt number values are obtained. It may be noted that local Nusselt number was calculated by using local temperature and local heat flux at the interface, both of which became larger in the impingement region with increase of disk thickness. Therefore the net effect was almost same Nusselt number distribution for all the thicknesses. This phenomenon has also been documented by Lachefski et al. [54] for jet impingement on a stationary disk.

Four different nozzle to target spacing ratio (β) from 0.25 to 1 were modeled using water as the coolant and silicon as the disk material. The effects of nozzle to target spacing on local Nusselt number and dimensionless interface temperature at a spinning rate of 125 RPM ($Ek_{1,2}=4.25x10^{-4}$) and Reynolds number of 900 are shown in figure 6.17. It may be noticed that the impingement height quite significantly affects the Nusselt number distribution particularly at the stagnation region. A higher local Nusselt number at the core region is obtained when the nozzle is brought close to the heated disk (β=0.25).

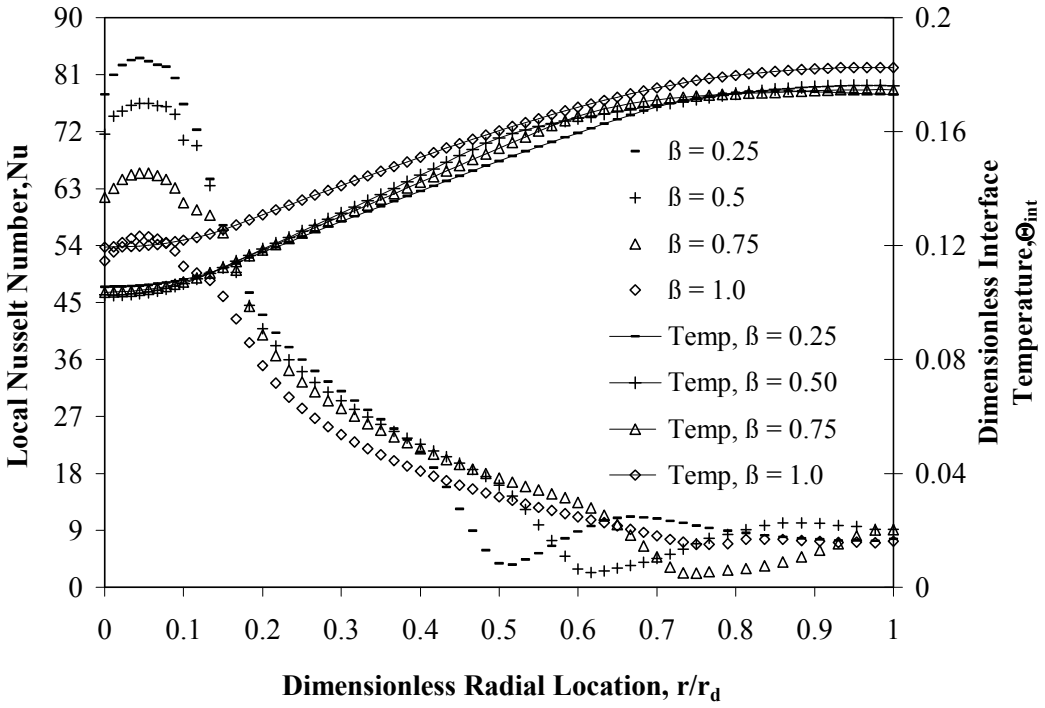

Figure 6.17 Effects of nozzle to target spacing ratio on local Nusselt number and dimensionless interface temperature distributions for a silicon disk with water as the cooling fluid (Re=900, b/d_n=0.5, $Ek_{1,2}$=4.25x10^{-4}, r_p/r_d=0.667).

A lower distance between nozzle and impingement plate provides lower loss of momentum as the jet travels for a shorter distance through the surrounding liquid medium. In addition, a smaller gap provides quicker propagation of centrifugal force from the spinning disks into the fluid medium increasing the net transport rate. It may be also noticed that in figure 6.17, curves for β=0.25–0.75 are close together whereas, at β=1, a higher temperature is obtained all along the disk. In figure 6b, it can be noticed that minimum in Nusselt number moves downstream with increase in gap and no minimum is observed at β=1. Therefore, rotational effects cannot propagate well when the gap between impingement and confinement plates is large. The local maximum is associated with the transition of flow structure from vertical stagnation flow to horizontal

boundary layer flow adjacent to the heated disk. The Nusselt number is maximum at the start of the thermal boundary layer. The minimum is associated with the transition from jet momentum dominated flow to rotation dominated flow. As the fluid moves downstream, boundary layer grows in thickness and jet momentum diminishes. On the other hand, the centrifugal force generated by disk rotation increases as the fluid moves to a larger radial location. The balance of these simultaneous effects results in the minimum in local Nusselt number. As both disks are rotating, a smaller vertical gap between disks causes a stronger propagation of rotational effects to the fluid and therefore earlier transition from momentum dominated to rotation dominated flow.

Figure 6.18 compares the dimensionless interface temperature results of the present working fluid (water) with three other coolants that have been considered in previous heat transfer studies, namely ammonia (NH_3), flouroinert (FC–77) and oil (MIL–7808) under a Reynolds number of 750. Even though the rotational rate ($\Omega_{1,2}$) for the impinging solid disk and confinement plate was set at 350 RPM the variation of Ekman number occurred since the density (ρ) and dynamic viscosity (μ) are different for each fluid. It may be noticed that MIL–7808 presents the highest dimensionless interface temperature and ammonia has the lowest value. Ammonia shows the most uniform distribution of temperature along the radius of the disk.

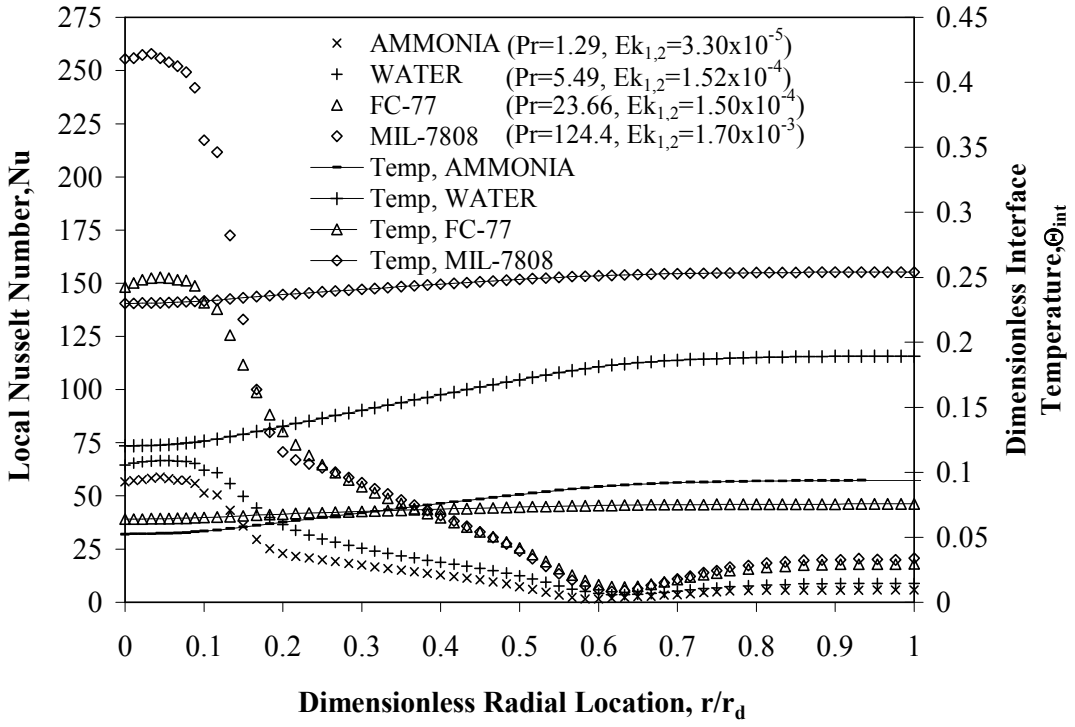

Figure 6.18 Effects of different cooling fluids with silicon as the disk material on local Nusselt number and dimensionless interface temperature (Re=750, β=0.5, b/d_n=0.5, r_p/r_d=0.667).

Figure 6.18 shows the corresponding local Nusselt number distributions. It may be noticed that MIL–7808 presents the highest local Nusselt number values over the entire dimensionless radial distance. Ammonia on the other hand provides the lowest Nusselt number. The Nusselt number trend is well correlated with the variation of Prandtl number. A higher Prandtl number fluid leads to a thinner thermal boundary layer and therefore more effective heat removal rate at the interface. The present working fluid results are in agreement with Li et al. [80] and Ma et al. [81] findings where a larger Prandtl number corresponded to a higher recovery factor.

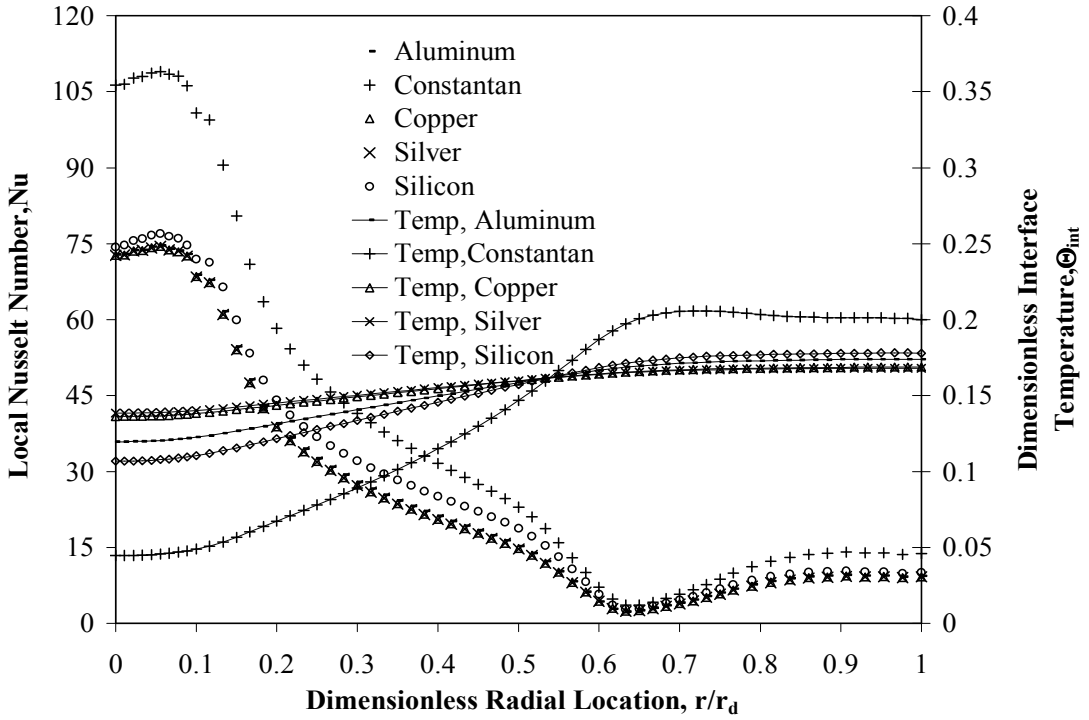

Figure 6.19 Effects of different solid materials with water as the cooling fluid on local Nusselt number and dimensionless interface temperature (Re=875, $Ek_{1,2}=1.77x10^{-4}$, $\beta=0.5$, $b/d_n=0.5$, and $r_p/r_d=0.667$).

Figure 6.19 shows the dimensionless interface temperature and local Nusselt number distribution plots as a function of dimensionless radial distance (r/r_d) measured from the axis–symmetric impingement axis for different solid materials with water as the working fluid. The studied materials were aluminum, Constantan, copper, silicon, and silver having different thermo–physical properties. The dimensionless temperature distribution plots reveal how the thermal conductivity affects the heat flux distribution. Constantan shows the lowest temperature at the impingement zone or stagnation point and the highest dimensionless temperature at the outlet in comparison with other solid materials. Copper and silver show a more uniform distribution and higher temperature values at the impingement zone due to their higher thermal conductivity. The dimensionless temperature and local Nusselt number distributions of these two materials

are almost identical due to their similar thermal conductivity values. The cross–over of curves for all five materials occurred around $r/r_d \approx 0.525$. This cross–over is expected because of thermal energy balance for constant fluid flow and heat input rates. A solid material with a lower thermal conductivity (Constantan) shows a higher maximum local Nusselt number. For all solid materials, the local Nusselt number distribution increases rapidly over a small distance (core region) measured from the stagnation point, reaches a maximum around $r/r_d=0.50$, and then decreases along the radial distance up to $r_p/r_d \approx 0.63$. Further downstream when the film encounters a free surface at the top along with the rotation of the solid disk at the bottom, the local Nusselt values for all materials gradually increase due to the increment of the tangential velocity and thinner thermal boundary layer that enhances the heat transfer on the solid disk surface.

Six different plate–to–disk confinement ratios (r_p/r_d) from 0.2 to 0.75 were modeled using water as the coolant and silicon as the disk material. The effects of plate–to–disk confinement ratio on the dimensionless interface temperature and local Nusselt number at a spinning rate of 125 RPM or $Ek_{1,2}=4.25\text{x}10^{-4}$ and Reynolds number of 450 are shown in figure 6.20. The plots in figure 6.20 reveal that the dimensionless interface temperature increases with the increment of the plate–to–disk confinement ratio (r_p/r_d). This increment coincides with the increment of liquid film thickness in the free jet region seen in figure 6.2. A thinner film thickness for the same flow rate results in higher fluid velocity near the solid–fluid interface resulting in a higher rate of convective heat transfer. This is seen in the distribution of local Nusselt number plotted in figure 6.20. The local Nusselt number increases with the decrease of plate–to–disk confinement ratio.

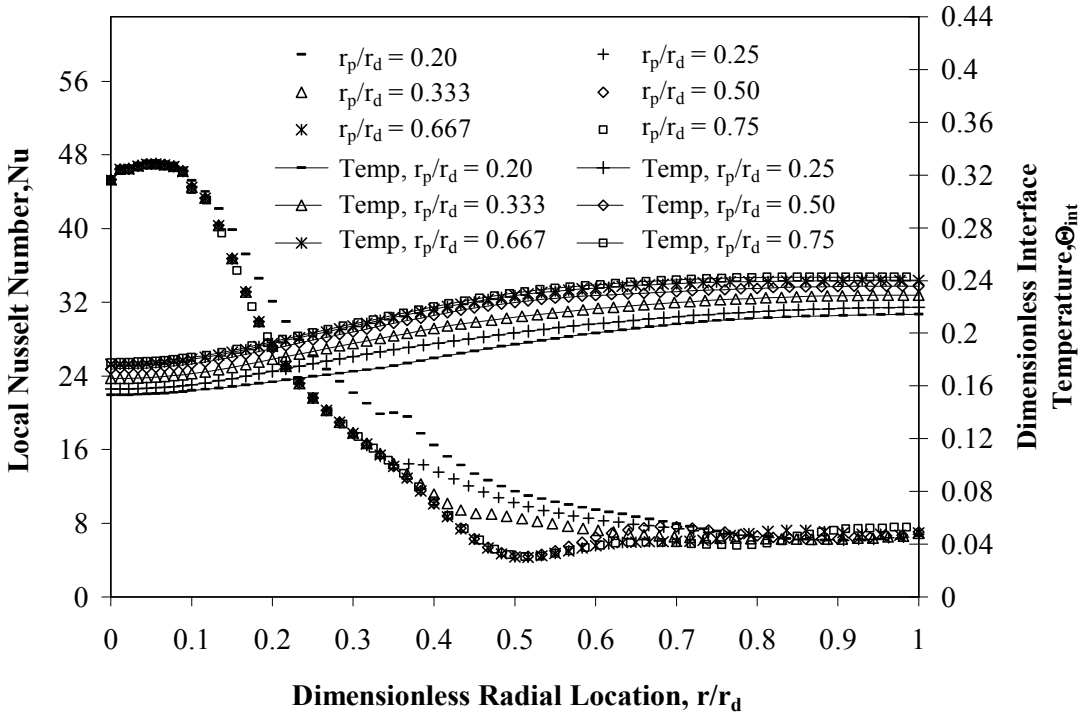

Figure 6.20 Local Nusselt number and dimensionless interface temperature distributions for different plate to disk confinement ratio (Re=450, $Ek_{1,2}=4.25x10^{-4}$, $\beta=0.5$, $b/d_n=0.5$).

A correlation for the average Nusselt number was developed as a function of confinement ratio, thermal conductivity ratio, dimensionless nozzle to target spacing, Ekman number, Reynolds number, and confinement plate to disk radius ratio to accommodate most of the transport characteristics of a semi–confined liquid jet impingement cooling process. The correlation that best fitted the numerical data can be placed in the following form:

$$Nu_{av}=1.94282\cdot\beta^{-0.01}\cdot Re^{0.75}\cdot Ek_1^{-0.0465}\, Ek_2^{-0.047}\cdot\varepsilon^{-0.69}\cdot(r_p/r_d)^{-0.05} \qquad (6.2)$$

In developing this correlation, all average Nusselt number data corresponding to the variation of different parameters were used. Only data points corresponding to water as the fluid were used because the number of average heat transfer data for other fluids

were small. Also data points corresponding to both disks rotating at the same rate were used.

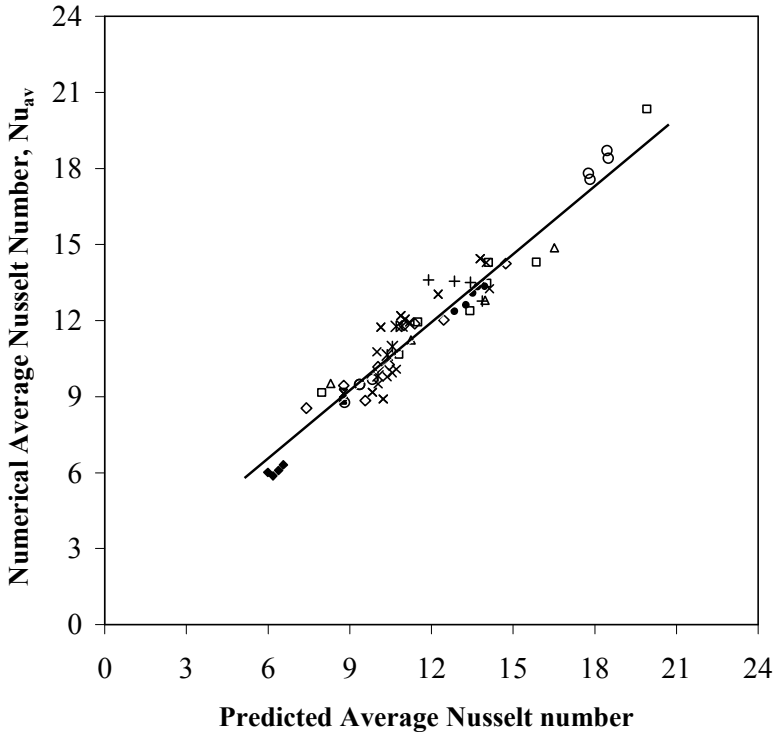

Figure 6.21 Comparison of predicted average Nusselt numbers of equation 6.2 with present numerical data.

Figure 6.21 gives the comparison between the numerical average Nusselt numbers to average Nusselt numbers predicted by equation 6.2. The percent difference of the predicted average Nusselt number was defined as: % diff = $((Nuav_{pred} - Nuav_{num})/Nuav_{num}) \times 100$. The predicted average Nusselt number values from equation 6.2 deviates in a range of –14.76% to +13.08% from the actual numerical results obtained in present dissertation study. The mean deviation of the predicted average Nusselt results was equal to 6.37%. The ranges of the dimensionless variables in this study are: $360 \leq Re \leq 900$, $4.25 \times 10^{-4} \leq Ek_1 \leq 7.08 \times 10^{-5}$, $4.25 \times 10^{-4} \leq Ek_2 \leq 7.08 \times 10^{-5}$, $0.25 \leq \beta \leq 1$, $0.2 \leq r_p/r_d \leq 0.75$, $Pr=5.49$, $227.6 \leq \varepsilon \leq 627.6$. It should be noted from figure 6.21 that a large number of data points

are well correlated with equation 6.2. This correlation can be a convenient tool for the prediction of average heat transfer coefficient.

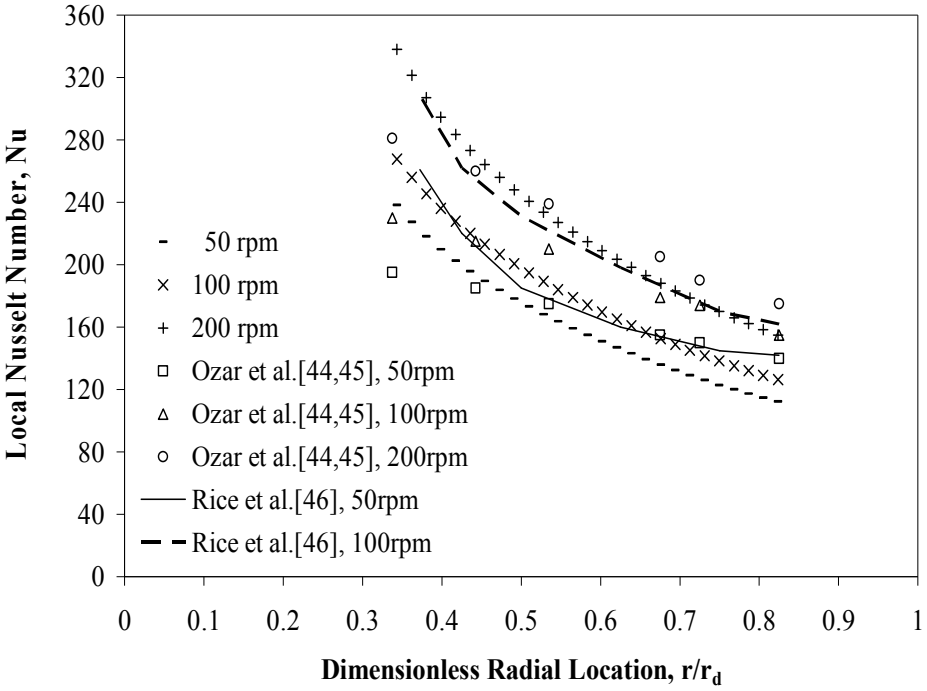

Figure 6.22 Comparison of numerical and experimental local Nusselt number distributions at different spinning rates for an aluminum disk with water as the cooling fluid (T_j=293 K, Re=238, H_n=0.000254 m, b=0.00635 m, b/d_n=0.125, r_p=0.0508 m, and r_p/r_d=0.25).

Figure 6.22 shows a comparison of local Nusselt numbers obtained in present numerical simulation with the experimental data obtained by Ozar et al. [44, 45] and numerical results of Rice et al. [46] at various rotational speeds. A rotating disk with a heat flux of 32kW/m^2, cooled by a round single water jet impingement at a flow rate of 3 liter/min (Re=238) and spinning at speeds of 50, 100, 200 RPM were compared. The computation was conducted for jet temperature (T_j) of 293 K; the nozzle to target spacing was set to 0.00254 m, with a nozzle diameter of 0.0508 m and for collar (or confinement) that extended over a radial distance of 0.051 m. The spinning disk had a diameter of

0.4064 m and thickness of 0.00635 m. The disk was made of aluminum, a material with a thermal conductivity of 202.4 W/mK. As seen in figure 6.22, the agreement of the local Nusselt number results of Ozar et al. [44, 45] and Rice et al. [46] with the present numerical simulation is satisfactory. In those studies higher Nusselt numbers were found at the inner portions of the disk, close to the collar, and decreased towards the outer edge. This was due to the radial spread of the flow, and lower convective heat transfer removal of the liquid due to a more pronounced backflow effect on the upper confinement plate at a large ratio of confinement, including the sluggish development of the thermal boundary layer thickness. The same behavior was observed as part of our numerical study just with a slight cutback effect on local Nusselt number distributions at large ratios of confinement. The percent difference of present local Nusselt number results was defined as: $\%\ \text{diff} = ((Nu_{num} - Nu_{exp})/Nu_{exp}) \times 100$. The difference in local Nusselt number between Ozar et al. [44, 45] and the present simulation is in the range of –18.55% to 22.07% with an average difference of 12.33%. The difference in local Nusselt number between Rice et al. [46] and the present simulation falls in the range of –22.08% to –5.01% with an average difference of 14.9%. The Nusselt number at the stagnation region was compared with the stagnation Nusselt number correlation developed by Liu et al. [17] for liquid jet impingement over a stationary disk. For the Reynolds number and rotational rates considered in our study, the average difference was 13.14%. The rotation always enhances the stagnation Nusselt number compared to the stationary disk.

6.3 Transient Cooling of Spinning Target

Figure 6.23 shows the local Nusselt number and the dimensionless interface temperature variation for different time instants. It can be observed that at the earlier part

of the transient heat transfer process, the solid–fluid interface maintains a more uniform temperature. The difference of dimensionless maximum and minimum temperature at the solid–fluid interface increases from 0.016 at Fo=0.051 to 0.05 when the steady state condition reached at Fo=0.369. After the power is turned on, the heat is first absorbed by the solid as it is transmitted through the solid and dissipated to the fluid. At the solid–fluid interface, the fluid absorbs heat and carries it as it moves downstream. At the start of the transient, the thickness of the thermal boundary layer is zero. As time goes on, the thickness of the thermal boundary layer increases and therefore the temperature rises. The interface temperature responds to the boundary layer thickness that increases downstream. Therefore, the temperature becomes minimum at the impinging point and maximum at the outer edge of the spinning disk.

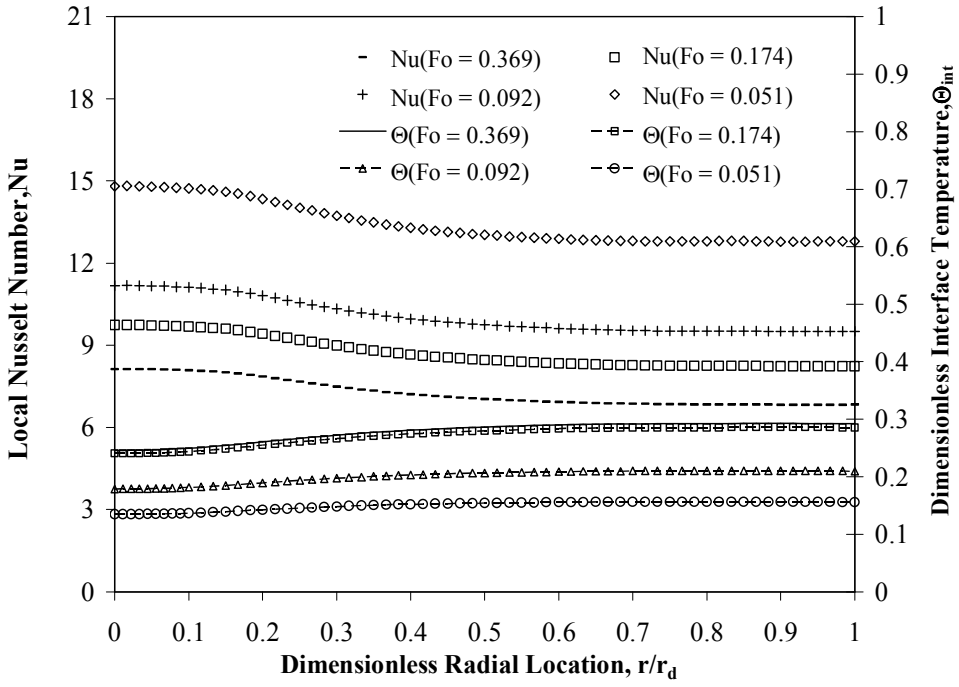

Figure 6.23 Local Nusselt number and dimensionless interface temperature distributions for a silicon disk with water as the cooling fluid for different Fourier numbers (Re=275, Ek=4.25×10^{-4}, β=0.5, b/d_n=0.5, r_p/r_d=0.667).

The local Nusselt number is controlled by local temperature and heat flux at the solid–fluid interface. It shows a higher value at early stages of the transient process due to smaller temperature difference between the liquid jet and disk solid–fluid interface. This essentially means that all heat reaching the solid–fluid interface via conduction through the solid is more efficiently convected out as the local fluid temperature is low everywhere at the interface. The local Nusselt number is maximum at the center of the disk, and decreases along the radial distance as the boundary layer thickness increases downstream. The local Nusselt number decreases with time until it reaches the steady state equilibrium distribution.

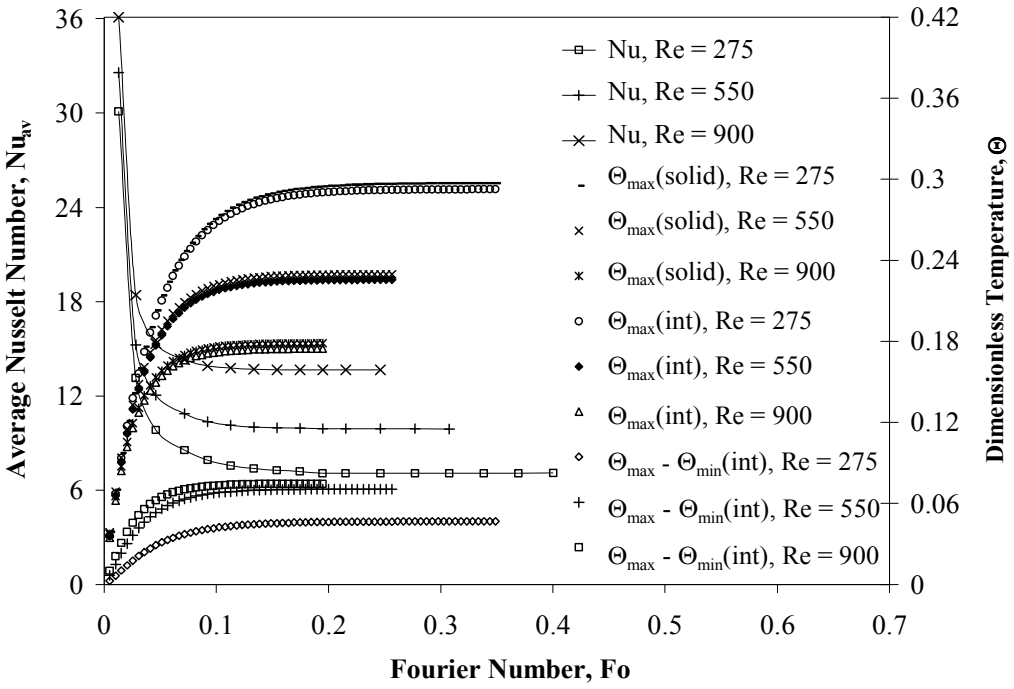

Figure 6.24 Average Nusselt number and dimensionless temperature variations with time for different Reynolds numbers (Ek=4.25x10^{-4}, β=0.5, silicon disk, b/d_n=0.5, and r_p/r_d=0.667).

The integrated average Nusselt number and the variation of dimensionless maximum temperature at the interface, maximum temperature inside the solid and

maximum–to–minimum temperature difference at the interface for different Fourier numbers at different values of Reynolds number are shown in figure 6.24. The average Nusselt number is large at the early part of the transient and monotonically decreases with time ultimately reaching the value for the steady state condition.

A higher Reynolds number increases the magnitude of fluid velocity near the solid–fluid interface that controls the convective heat transfer and therefore increases the average Nusselt number. The control of maximum temperature is important in many critical thermal management applications including electronic packaging. As expected, the temperature increases everywhere with time starting from the initial isothermal condition. A rapid increment is seen at the earlier part of the transient, and it levels off as the thermal storage capacity of the solid diminishes and become zero at the steady state condition. It maybe noted that the time required to reach the steady state condition is lower at a higher Reynolds number because the higher velocity of the fluid helps to enhance the convective heat transfer process. This is due to quicker dissipation of heat with higher flow rate. The steady state Fourier number (Fo_{ss}) was defined as the time needed to approach 99.99% of the steady state local Nusselt number over the entire solid–fluid interface. It was found that Fo_{ss} decreases from 0.369 at Re=275 to 0.195 at Re=900.

Figure 6.25 provides the variations of average Nusselt number and the dimensionless maximum temperature at the interface, maximum temperature inside the solid, and maximum–to–minimum temperature difference at the interface with the progression of time at different Ekman numbers. The average Nusselt number is large at the early part of the transient and monotonically decreases with time ultimately reaching

the value for the steady state condition. Throughout the transient heating process, the average Nusselt number is more at larger spinning rate or smaller Ekman number.

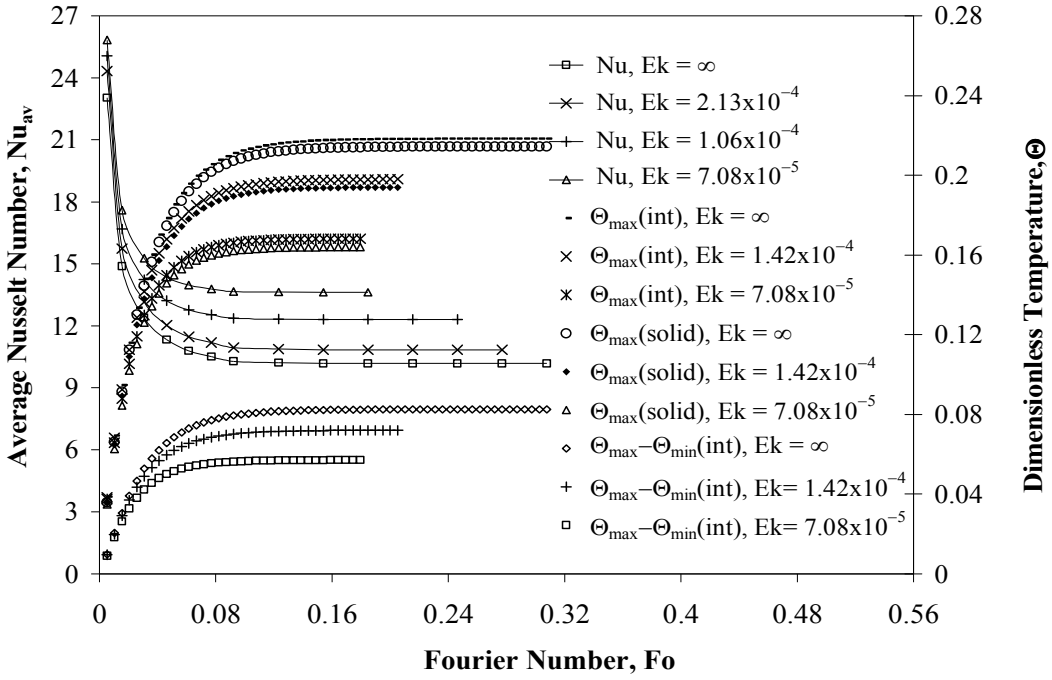

Figure 6.25 Average Nusselt number and dimensionless temperature variations with time for different Ekman numbers (Re=550, β=0.25, silicon disk, b/d_n=0.5, and r_p/r_d=0.667).

As the Ekman number decreases from ∞ to 7.08x10^{-5} the average Nusselt number increases by an average of 27.47% when the Reynolds number is kept constant at 550. The maximum temperature within the solid was encountered at the outlet adjacent to the heated surface (z= –b, r=r_d). The temperatures rise with time as the solid disk and the fluid store heat showing a rapid response at the earlier part of the heating process until the thermal storage capacity reaches its limit at the steady state condition. It may be noted that the magnitude of the dimensionless temperature as well as the time required to reach the steady state condition become smaller as the Ekman number decreases. This is because the magnitude of fluid velocity near the solid–fluid interface that controls the

convective heat transfer rate increases with the increment of the rotational rate of the disk or the reduction of Ekman number. These observations are in agreement with the numerical solutions of Rice et al. [46].

The effects of nozzle to target spacing for water as the coolant and silicon as the disk material at a spinning rate of 125 RPM or Ek=4.25x10^{-4} and Reynolds number of 750 is demonstrated in figure 6.26. It may be noticed that a higher average Nusselt number and a smaller maximum temperature are obtained over the entire transient process when the nozzle is brought closer to the heated disk.

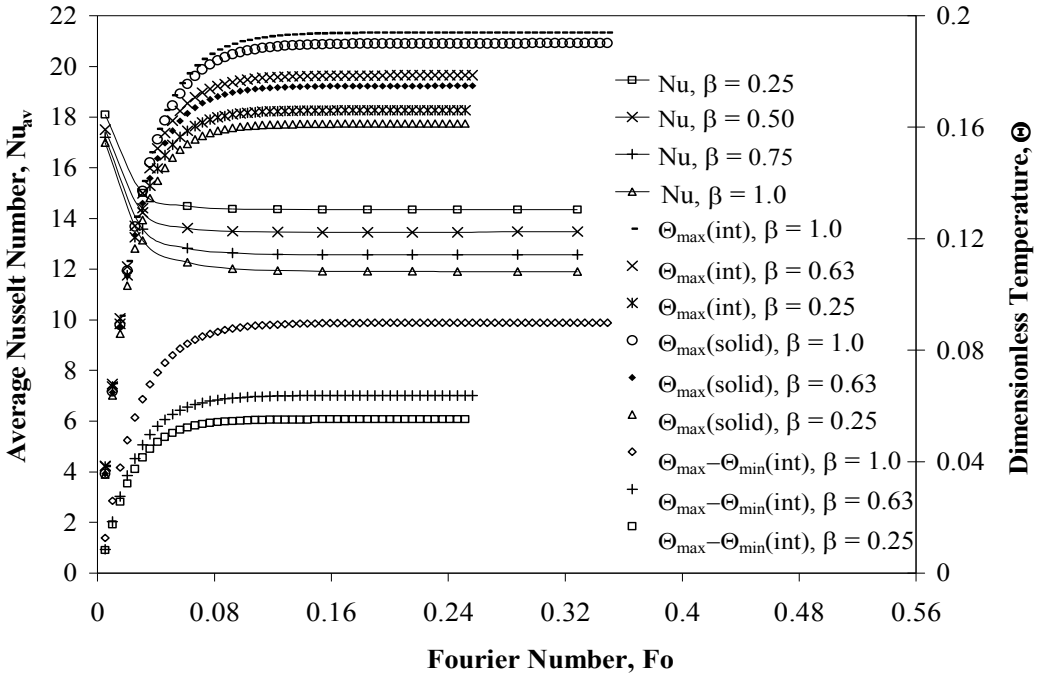

Figure 6.26 Average Nusselt number and dimensionless temperature variations with time for different nozzle–to–plate spacing (Re=750, Ek=4.25x10^{-4}, silicon disk, b/d_n=0.5, and r_p/r_d=0.667).

The smaller gap between the nozzle and the target disk avoids the loss of momentum as the fluids travels through the confined medium. This results in a larger rate of convective heat transfer with higher fluid velocity. As the nozzle to target spacing decreases from 1

to 0.25 the average Nusselt number increases by an average of 12.71% when the Reynolds number is kept at 750.

Different plate–to–disk confinement ratios (r_p/r_d) from 0.2 to 0.75 were investigated for water as the coolant and silicon as the disk material. The effects of plate–to–disk confinement ratio on the variation of dimensionless maximum temperature at the interface, maximum temperature inside the solid, and maximum–to–minimum dimensionless temperature difference at the interface and average Nusselt number are shown in figure 6.27.

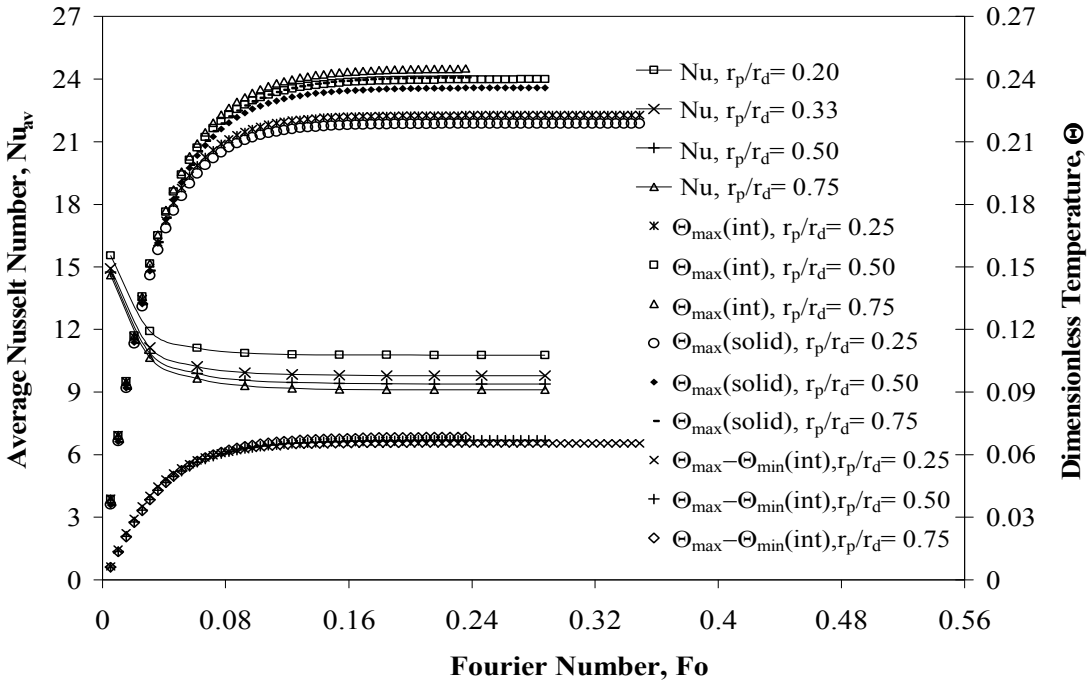

Figure 6.27 Average Nusselt number and dimensionless temperature variations with time for different plate to disk confinement ratios (Re=450, Ek=4.25x10^{-4}, β=0.5, silicon disk, b/d_n=0.5).

The average Nusselt number increases with the reduction of the plate–to–disk confinement ratio. When r_p is increased, the frictional resistance from both walls slows down the momentum and results in higher film thickness at the free surface region for

any given spin rate and flow rate. A lower fluid velocity obviously results in smaller convective heat transfer rate. As the plate–to–disk confinement ratio decreases from 0.75 to 0.2, the average Nusselt number increases by an average of 18.07% when the Reynolds and Ekman numbers are kept constant at 450 and 4.25×10^{-4} respectively. When the ratio of confinement was reduced from 0.75 to 0.25, under the same numerical conditions like flow and spinning rates, it was found that the maximum temperature inside the solid decreases by 8.96%.

The effects of solid material properties on transient heat transfer are presented in figure 6.28. The studied materials were aluminum, Constantan, copper, silicon, and silver having different thermo–physical properties.

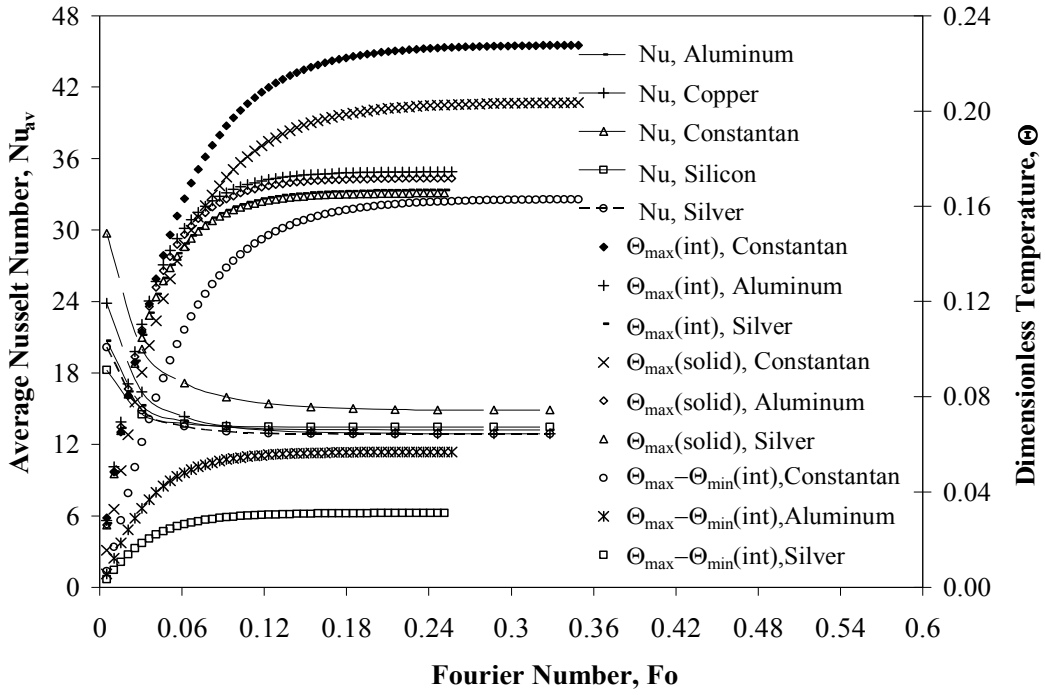

Figure 6.28 Average Nusselt number and dimensionless temperature variations with time for different solid materials (Re=875, $Ek=2.13 \times 10^{-4}$, $b/d_n=0.5$, $\beta=0.5$, and $r_p/r_d= 0.667$).

For all materials the temperature changes occur faster at the earlier part of the heating process and the slope gradually decays when the steady state conditions approaches. It can be observed that a material having a lower thermal conductivity such as Constantan maintains a higher temperature at the solid disk interface and within the solid as the thermal conductivity controls how effectively the heat flows and distributes through the material. For the same reason, the maximum temperature within the solid and that at the interface are significantly different for Constantan, whereareas about the same for both silver and aluminum. The thermal diffusivity of the material also contributes to the transient heat transfer process. Silver and aluminum reach the steady state faster than Constantan due to their higher thermal diffusivity. The values of thermal diffusivity for these materials at 303 K are α_{silver}=1.74 x10^{-4} m^2/s, $\alpha_{aluminum}$=8.33 x10^{-5} m^2/s, and $\alpha_{Constantan}$=6.20x10^{-6} m^2/s.The magnitude of the temperature non–uniformity at the interface at steady state is controlled by thermal conductivity of the material. It may be noted that Constantan ($k_{Constantan}$=22.7 W/m·K) has an average maximum–to–minimum temperature difference of 17.24 K, whereareas silver (k_{silver}=429 W/m·K) has only an average 3.34 K temperature difference at the interface. Figure 6.28 also shows the distribution of average Nusselt number with time for the five materials used in this study. Constantan shows a higher average heat transfer coefficient compared to the other materials over the entire transient process due to its lower thermal conductivity.

Another important factor that controls the transient heat transfer process is the thickness of the disk. Its effects on the variation of the dimensionless maximum temperature at the interface, maximum temperature inside the solid, and maximum–to–minimum dimensionless temperature difference at the interface and average Nusselt

number are shown in figure 6.29. In these plots, silicon has been used as the disk material and water as the cooling fluid. The disk thickness significantly affects the temperature distribution. It may be noted that as the thickness of solid disk increases, the time needed to achieve the steady state condition increases. This is due to more storage capacity of heat within the solid. The radial conduction becomes stronger as the disk thickness increases generating a more uniform heat distribution at the interface. However, the increment of solid thickness creates more thermal resistance to the heat transfer process. The average Nusselt number is higher for a thinner disk.

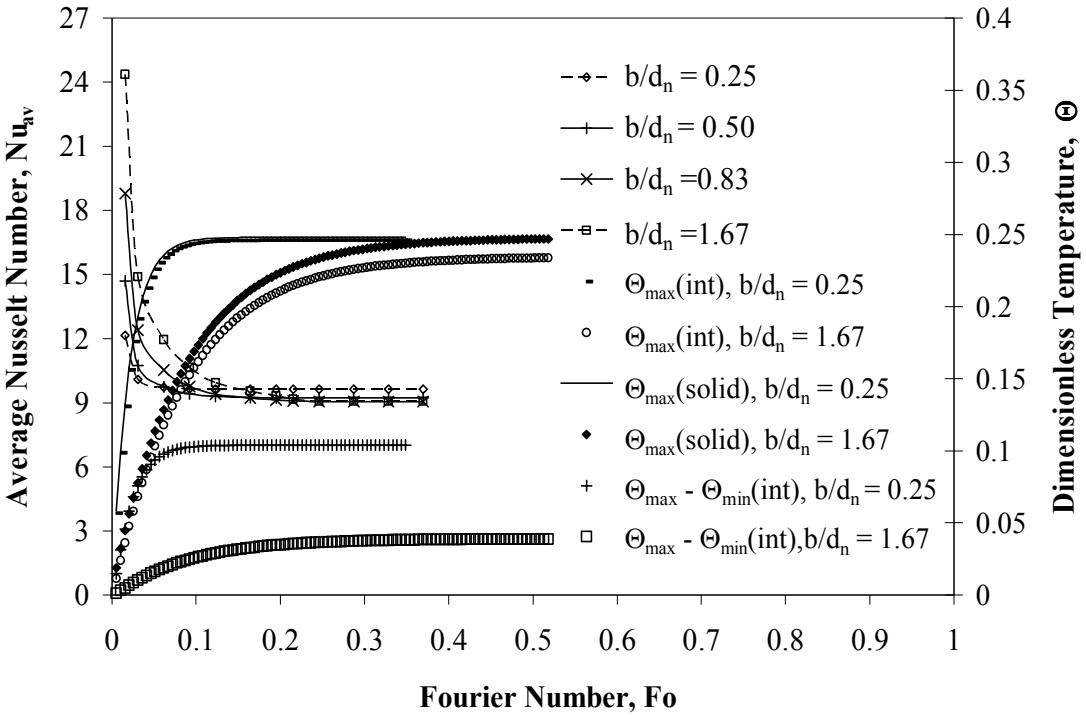

Figure 6.29 Average Nusselt number and dimensionless temperature variations with time for different silicon disk thicknesses (Re=450, Ek=4.25×10^{-4}, β=0.5, and r_p/r_d=0.667).

Based on our numerical data, a correlation for the average Nusselt number was developed as a function of confinement ratio, thermal conductivity ratio, dimensionless disk thickness, nozzle to target spacing, Ekman number, Reynolds number, and Fourier

number to accommodate most of the transport characteristics of a transient partially–confined liquid jet impingement cooling process on a thick solid disk spinning at a constant angular velocity. The correlation that best fitted the data can be placed in the following form:

$$Nu_{av}=1.94282\cdot\beta^{-0.01}\cdot Re^{0.74}\cdot Ek^{-0.1}\cdot\varepsilon^{-0.7}\cdot(b/d_n)^{-0.05}\cdot(r_p/r_d)^{-0.05}\cdot Fo^{-0.01} \quad (6.3)$$

In developing this correlation, all average Nusselt number data corresponding to the variation of different parameters were used. The least squares curve fitting method was used. Figure 6.30 gives a graphical comparison between the numerical average Nusselt numbers to the average Nusselt numbers predicted by equation 6.3.

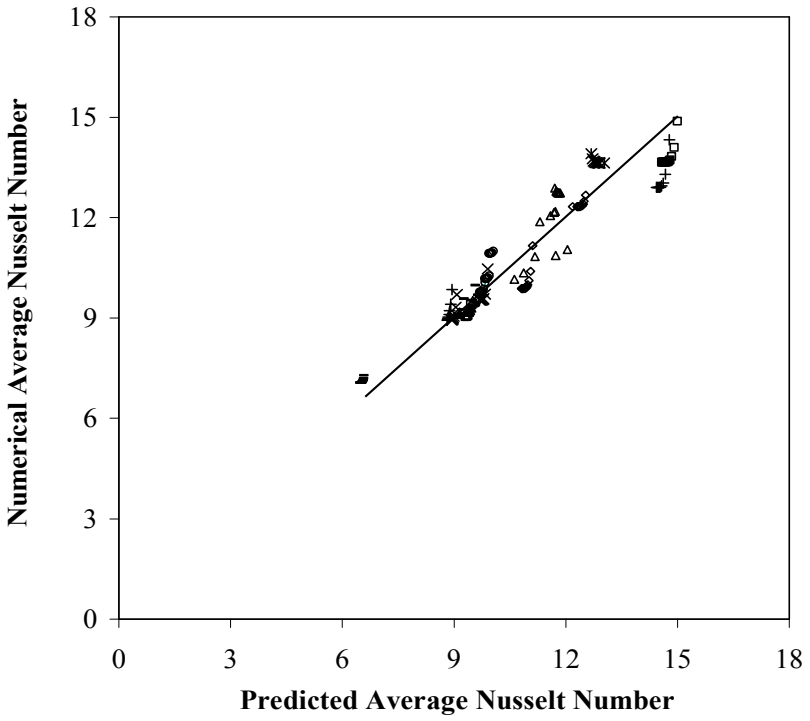

Figure 6.30 Comparison of predicted average Nusselt number of equation 6.3 with present numerical data.

The percent difference of the predicted average Nusselt number was defined as: $\%diff = ((Nuav_{pred} - Nuav_{num})/Nuav_{num}) \times 100$. The predicted average Nusselt number

differences between numerical and predicted values are in the range of –9.21% to +13.61%. The average Nusselt correlation mean difference was equal to 4.98%. The values of the dimensionless variables used for this correlation are: 225 ≤Re≤ 900, $7.08x10^{-5}$ ≤Ek≤ $4.25x10^{-4}$, 0.25 ≤β≤ 1.0, Pr=5.49, 227.6 ≤ε≤ 376.7, 0.25 ≤b/d_n≤ 1.67, 0.2 ≤r_p/r_d≤ 0.75, and 0.045 ≤Fo≤ 0.72. It should be noted from figure 6.30 that a large number of data points are well correlated with equation 6.3. This correlation provides a convenient tool for the prediction of average heat transfer coefficient during the transient heat transfer process.

A comparison of the present numerical results with the experimental data of Ozar et al. [44, 45] for various spinning rates of the target disk is presented in Table 6.1. To match with the experimental conditions, the combination of the parameters used was: q_w=32 kW/m^2, Re=238, T_j=293 K, H_n=0.00254 m, d_n=0.0508 m, r_p=0.051 m, r_d=0.2032 m and b=0.00635 m. Water was used as the working fluid. The disk was made of aluminum, a material with a thermal conductivity of 202.4 W/mK. The local percent difference of present numerical Nusselt number results of Table 6.1 was defined in term of: % diff = $((Nu_{num} – Nu_{exp})/Nu_{exp}) \times 100$. As seen in Table 6.1, the differences in the value of local Nusselt number results were in the range of –14.14% to 4.34% with an average difference of 6.91%.

In Ozar's research [44, 45] higher Nusselt numbers were found at the inner portions of the disk, close to the collar, and decreased towards the outer edge. This was due to the radial spread of the flow, and lower convective heat transfer removal of the liquid due to a more pronounced backflow effect on the upper confinement plate at a large ratio of confinement, including the sluggish development of the thermal boundary

layer thickness. The same behavior was observed as part of our numerical study just with a slight cutback effect on local Nusselt number distributions at large ratios of confinement. Considering the uncertainty of experimental measurements and round off and discretization errors in numerical computation, the overall comparison between test data and numerical results can be considered to be quite satisfactory.

Table 6.1 Local Nusselt number comparison between experimental data of Ozar et al. [44, 45] and present numerical results (T_j=293 K, q_w=32 kw/m^2, b=0.00635 m, Re=238, H_n=0.000254 m, r_p/r_d=0.25, b/d_n=0.125, $r_{hin}=r_p$=0.0508 m).

Confinement ratio, r/r_{hin}	Spinning rate, 50 RPM		Percent difference
	Numerical	Experimental	
1.8	193.40	185	4.34
2.15	166.56	175	–5.07
2.7	135.80	155	–14.14
	Spinning rate, 100 RPM		
	Numerical	Experimental	
1.8	217.58	215	1.19
2.15	197.39	205	–6.39
2.7	152.78	169	–10.62
	Spinning rate, 200 RPM		
	Numerical	Experimental	
1.8	261.09	260	0.42
2.15	224.86	249	–10.73
2.7	183.33	205	–11.82
		Average	6.91

Chapter 7 Chemical Mechanical Polishing Model Results

7.1 Steady State Process

A three dimensional steady state FEM model was used to acquire the temperature profile of the substrate and pad surfaces during a CMP process. Figure 7.1a shows the steady state maximum and minimum temperature contour distributions for the control volume under a slurry flow rate of Q_{sl}=15 cc/min. It can be seen from figure 7.1a that a considerable region of the trailing edge along the 2, 3, and 4 o'clock positions reaches up to a temperature difference of 6 degrees at the wafer and pad surfaces, including the slurry region. A second numerical run with the same polishing conditions except for the amount of slurry flow rate of (Q_{sl}=30 cc/min) are shown in figure 7.1b. Figure 7.1b shows a temperature difference of 4.5 degrees that extends along the trailing edge from the 2 to 4 o'clock positions at the wafer and pad surfaces along the slurry interface.

Figure 7.1c illustrates the same pattern as figures 7.1a and 7.1b with a temperature difference slightly smaller, around 4 degrees, at few areas of the trailing edge, along the 2, 3, and 4 o'clock positions at the wafer and pad surfaces as well as the slurry region. The steady state temperature contour plots of figure 7.1 were done for an abrasive film thickness of 40 μm, under a constant pressure load of P=24.35 kPa, and coefficient of friction (μ_{fr} =0.4), with a variable heat flux that ranges from 3.6 to 8.3 (kW/m^2), under a pad and carrier spinning rate of 120 and 30 RPM respectively.

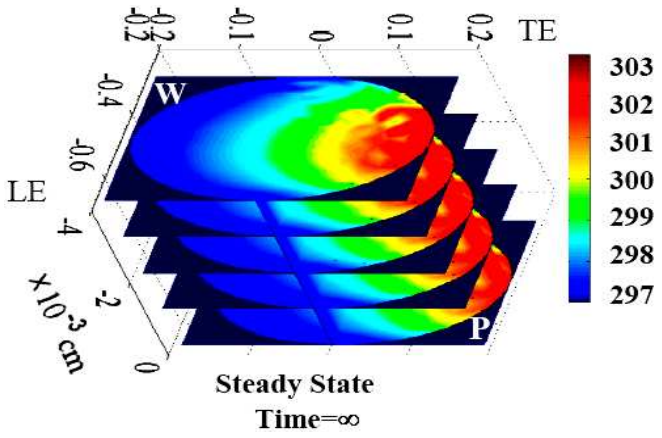

(a)

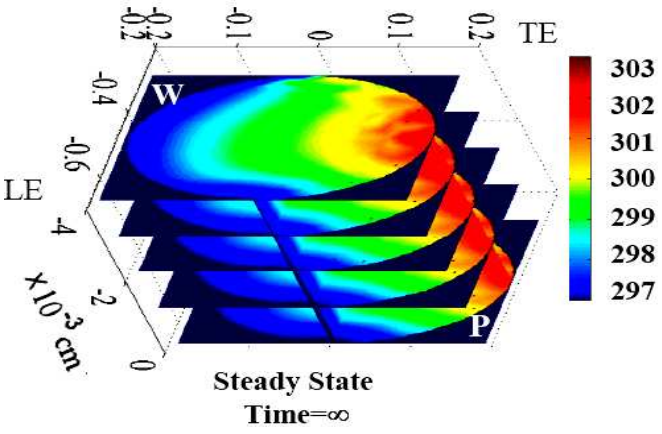

(b)

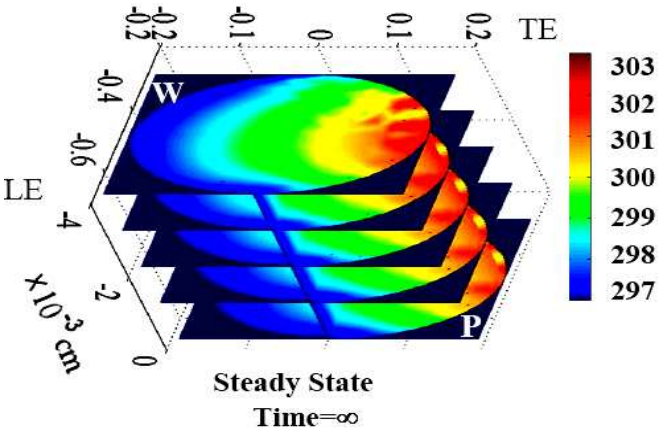

(c)

Figure 7.1 Steady state temperature contour plots for alumina (slurry), the substrate and pad surfaces at various slurry flow rates, (a) Q_{sl}=15 cc/min, (b) Q_{sl}=30 cc/min, and (c) Q_{sl}=75 cc/min.

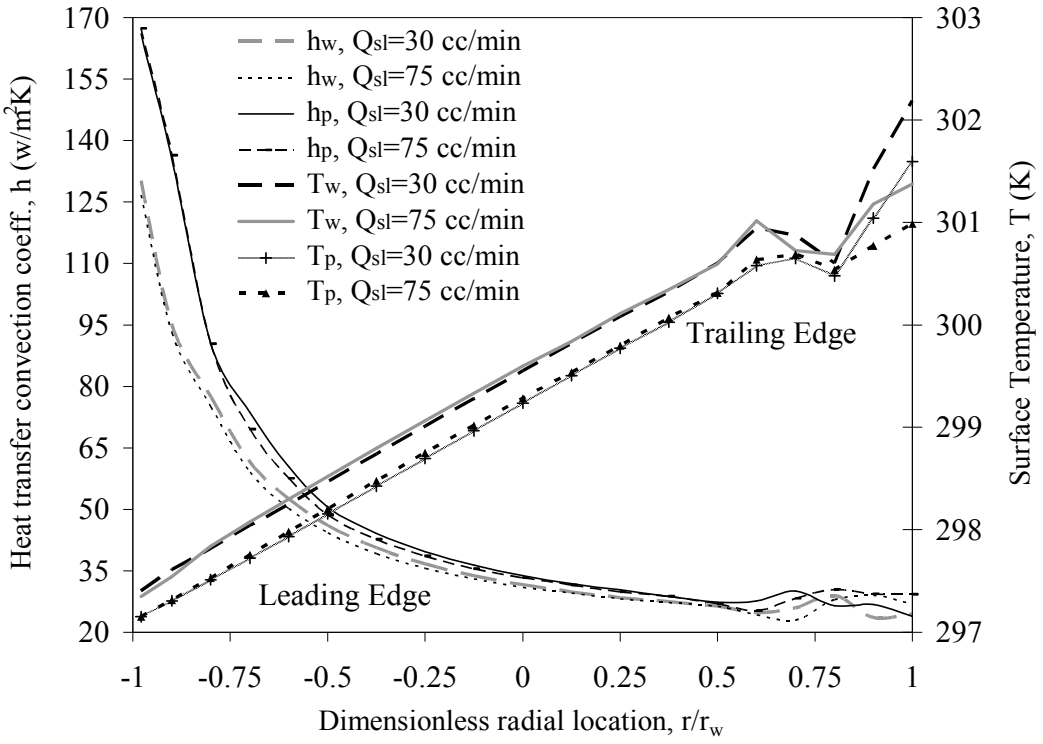

Figure 7.2 Cross–sectional wafer and pad temperature distributions and local heat transfer convection coefficients along the center of pad and substrate surfaces for two different slurry flow rates.

Figure 7.2 shows the cross–sectional wafer and pad surfaces temperature distributions and the local heat transfer convection coefficients along the dimensional radial distance from the leading to the end of the trailing edge of the control volume under study, for two characteristic slurry flow rates under the same polishing conditions described in figures 7.1. The substrate and pad temperature distributions for a higher slurry flow rate are slightly smaller compared to the lower slurry flow rate results in figure 7.2. The temperature difference can be seen at a wafer dimensionless radial distance around r/r_w=0.7 towards the end of its trailing edge, where the temperature of the pad and wafer drops and then increases significantly, due to the backflow effect of the slurry observed by Muldowney [147]. A backflow effect is linked to the rotational motion

of the slurry and the shear effect of frictional forces due to the surface tension of the slurry particles along such a small gap.

The heat transfer convection coefficients for wafer and pad surfaces follow a higher profile pattern that stars at the leading edge and decreases along the radial distance up to the trailing edge of both surfaces. The wafer heat transfer convection coefficient values range from 130 to 24 (W/m^2K). The average values of the heat transfer convection coefficient for the wafer along the surface were approximately equal to 43.64 and 44.11 (W/m^2K) under lower and higher flow rate conditions. The pad heat transfer convection coefficient values range from 170 to 30 (W/m^2K). The average values of the heat transfer convection coefficient for the pad along the surface were approximately equal to 51.25 and 51.95(W/m^2K) under lower and higher flow rate conditions. The temperature contour plots in figure 7.1 and radial surface temperature distributions of figure 7.2 reveal that the wafer and pad temperature profile decreased by a slightly margin with the increment of the slurry velocity. In addition, the figures reveal that the heat transfer convection coefficients are higher at the pad surface than the substrate surface, which is due to its lower thermal conductivity that results in a lower temperature gradient between the incoming slurry and pad surface. This effect results in higher convective coefficients for the pad by an average margin of 17.21% under lower and higher slurry rates. Present numerical results are in agreement with Sampurno et al. [121].

Figure 7.3 shows the cross–sectional wafer and pad temperature rise and the local heat transfer convection coefficient distributions along the dimensional radial distance from the leading to end of the trailing edge of the substrate and pad surfaces for two characteristic pressure loads of 17.24 kPa (2.5psi) and 41.37 kPa (6psi) respectively. The

steady state temperature results were done for an abrasive film of alumina through a film thickness of 40 μm, under a constant slurry flow rate of Q_{sl}=85 cc/min, with a pad coefficient of friction of μ_{fr} =0.4, under a pad and carrier spinning rate of 200 and 30 RPM respectively. The change in pressure will directly affect the amount of heat dispersed beneath the wafer as a result of the greater slurry, pad, and substrate shear stress interaction during polishing. For a load of 17.24 kPa the heat flux input into the system covers a range of (q_{sl} =4.1–9.8 kW/m^2) along the leading edge towards the end of the wafer trailing edge. The increment of the load up to 41.37 kPa as part of the modeling set up, will increase the limits of a variable heat flux from 10 to 23.4 (kW/m^2) along the dimensionless radial distance of the control volume under study. The temperature rise of the wafer under a load of 41.37 and 17.24 kPa were approximately equal to 8.2 and 3.85 degrees respectively at the end of the wafer trailing edge. The substrate and pad temperature distributions increased under a higher pressure load due to the increment of the heat flux generated per unit area. Taking into consideration this temperature gradient, we can expect that the MRR will increase by a factor of 27% and 55% at the trailing edge region along the 2 to 4 o'clock positions according to experimental measurements of Li et al. [124], where the increment of 1 C or K increased the MRR by 7%. In addition, figure 7.3 shows that the backflow effect on the temperature rise was quite gone under the CMP parameters input for this numerical run. One reasonable explanation for the absence of the backflow effect observed by Muldowney [147] is that the increment of pad spinning rate overcame the surface tensional forces beneath the substrate and pad, as shown in figure 7.3. The hotter slurry was driven out towards the end of the platen at a faster rate.

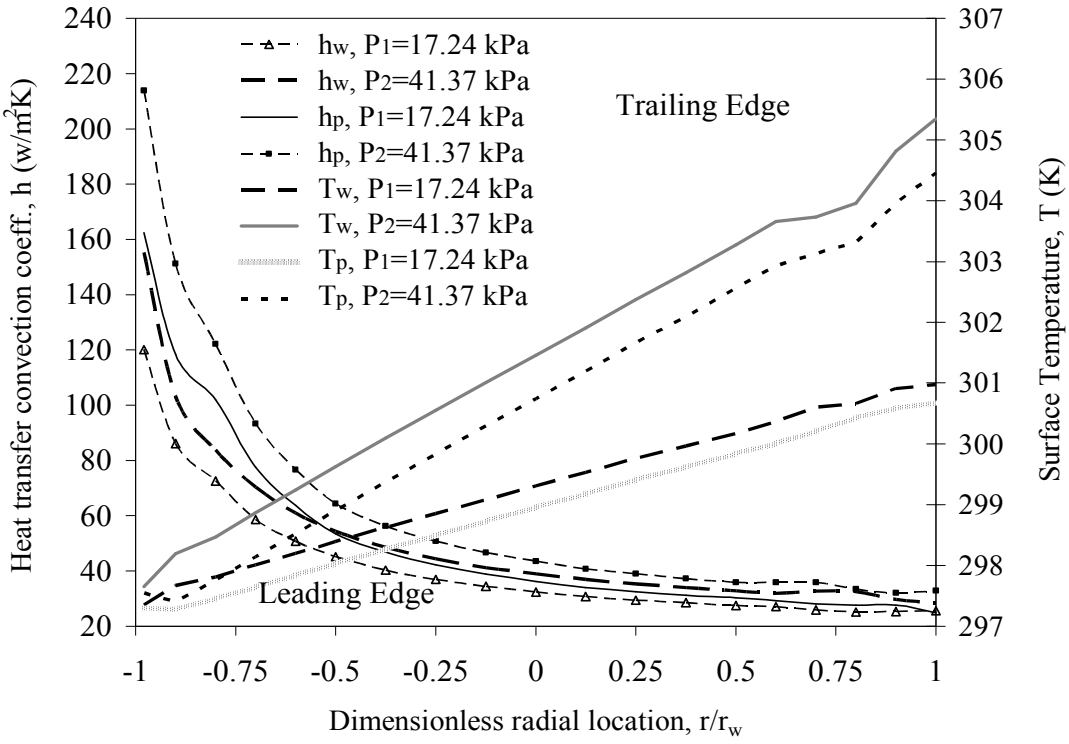

Figure 7.3 Cross–sectional wafer and pad temperature distributions and local heat transfer convection coefficients along the center of pad and substrate surfaces under two characteristic CMP pressure loads.

The heat transfer convection coefficients for wafer and pad surfaces follow the same pattern as shown in figure 7.2. The wafer heat transfer convection coefficient values range from 159 to 31(W/m^{2}K) of both loads of applied pressure. Additionally, the figures reveal that the wafer heat transfer convection coefficients decrease by an average margin of 80% for both loads of 17.24 and 41.37 kPa respectively, once it reaches the wafer outer edge at the trailing region. The average values of the wafer heat transfer convection coefficient along the surface were approximately equal to 43.32 and 54.32 (W/m^{2}K) under a load of 17.24 and 41.37 kPa respectively. The pad heat transfer convection coefficient values range from 215 to 30 (W/m^{2}K). In addition, the figures reveal that the pad heat transfer convection coefficients decrease by an average margin of 85% for both

loads of 17.24 and 41.37 kPa respectively, once it reaches the wafer outer edge at the trailing region. The average pad values of the heat transfer convection coefficient along the surface were approximately equal to 53.01 and 65.37(W/m^2K) for the smaller and higher load respectively. Low heat transfer convection coefficients at a particular region indicate the presence of a larger temperature gradient between the incoming slurry at the pad or substrate surfaces. The average heat transfer convection coefficients obtained are in agreement with the earlier experimental works of Borucki et al. [127, 128].

The temperature contour distributions of the wafer and pad surfaces under two characteristic carrier spinning rates of 15 and 75 RPM are shown in figures 7.4a and 7.4b. The steady state temperature contour plots were done for an abrasive film thickness of 40 μm of alumina, under a constant slurry flow rate of (Q_{sl}=60 cc/min), with a pad coefficient of friction (μ_{fr} =0.4), for a constant load of 34.48 kPa that generates a variable heat flux (q_{sl} =6–14.1 kW/m^2), and pad spinning rate of 150 RPM. The steady state temperature contour distributions in figure 7.4a reach up to a temperature difference of 5.5 degrees for a small fraction of the upper region at the 12, 3 and 4 o'clock positions of the trailing edge of the wafer and pad surfaces including the slurry. Figure 7.4b illustrates a temperature gradient of 5 degrees for a carrier spinning rate of 75 RPM. The temperature gradient extends at few areas around the 12, and 3 to 4 o'clock positions of the trailing edge of the wafer and pad surfaces among the slurry.

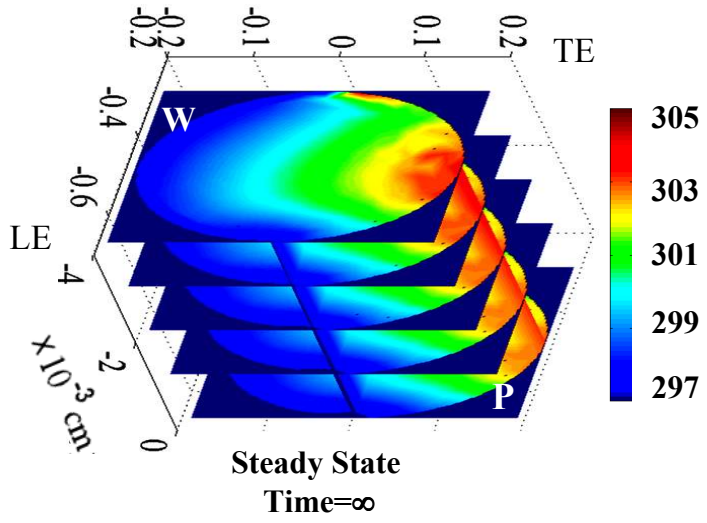

(a)

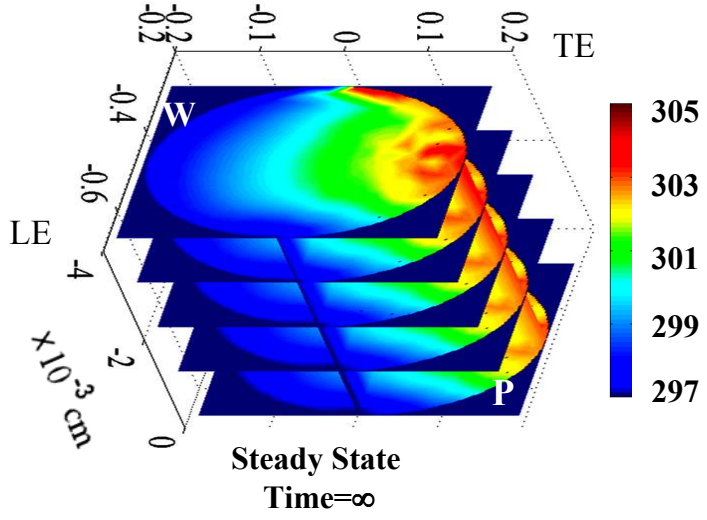

(b)

Figure 7.4 Steady state wafer, and pad temperature contour distributions for two different carrier spinning rates equal to: (a) Ω_c=15 RPM and (b) Ω_c=75 RPM.

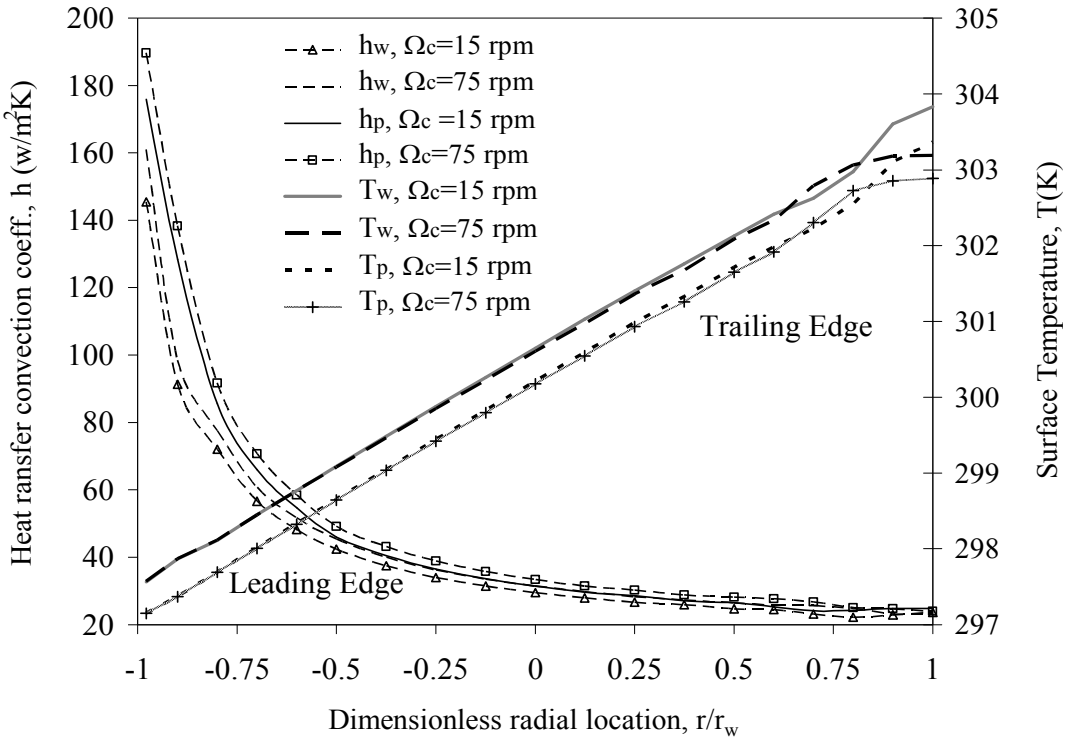

Figure 7.5 Cross–sectional temperature distributions and local heat transfer convection coefficients along the center of pad and substrate surfaces under two different carrier spinning rates.

The cross–sectional wafer and pad surface temperatures rise, and the local heat transfer convection coefficient distributions along the dimensional radial distance that extend from the leading to the end of the trailing edge of both surfaces for two characteristic carrier spinning rates of 15 and 75 RPM, are shown in figure 7.5 under the same polishing conditions of figures 7.4a and 7.4b. The substrate and pad temperature distributions for a carrier spinning rate (Ω_c) of 75 RPM are slightly smaller compared to a carrier spinning rate (Ω_c) of 15 RPM, as shown in figure 7.5. The temperature difference could be seen at a wafer dimensionless radial distance around r/r_w =0.8 towards the end of trailing edge, where the temperature of the pad and wafer drops for a carrier spinning rate (Ω_c) of 75 RPM, and rise for a carrier spinning rate (Ω_c) of 15 RPM. The carrier that

spins at 75 RPM drives out the hot slurry from the backflow region overcoming the surface tensional forces caused by the shear stress. Conversely, the carrier that spins at a spinning rate of 15 RPM allows a greater hot slurry recirculation at the backflow region observed by Muldowney [147], causing an increment of 0.825 degrees at the 3 o'clock position of the substrate trailing edge. A backflow effect is linked to the rotational motion of the slurry and the shear effect of frictional forces due to the surface tension and viscosity of the slurry particles along such a small gap. The average temperature rise of the wafer and pad under a carrier spinning rate of 75 and 15 RPM were approximately equal to 3.4, 3.5, and 3 degrees respectively along the wafer and pad trailing edges.

The heat transfer convection coefficients for wafer and pad surfaces follow a higher heat transfer rate pattern that starts at the surfaces leading edge and decreases along the radial distance up to the surfaces trailing edge. The wafer heat transfer convection coefficient values range from 162 to 24 (W/m^2K). The average values of the heat transfer convection coefficient for the wafer along the surface were approximately equal to 42.61 and 45.79 (W/m^2K) under lower and higher carrier spinning rate conditions. The pad heat transfer convection coefficient values range from 190 to 25 (W/m^2K). The average values of the heat transfer convection coefficient for the pad along the surface were approximately equal to 49.15 and 52.43(W/m^2K) under carrier spinning rates of 15 and 75 RPM. This effect results in higher convective coefficients for the pad by an average margin of 14.93% under a lower and higher carrier spinning rate respectively.

The cross–sectional wafer and pad surfaces temperature rise and the local heat transfer convection coefficient distributions along the dimensional radial distance of the

control volume under study for three characteristic slurry film thicknesses are shown in figures 7.6 and 7.7. The temperature distribution and the local heat transfer convection coefficients were set for a constant alumina slurry flow rate of 65 cc/min, with a pad coefficient of friction (μ_{fr} =0.4), under a constant load of P= 28 kPa, for a variable heat flux rate of 5 to 11.65 kW/m^2, with pad and carrier spinning rates of 150 and 40 RPM. Figure 7.6 shows how the temperature distribution along the pad and wafer surface decreases with the increment of the slurry film thickness.

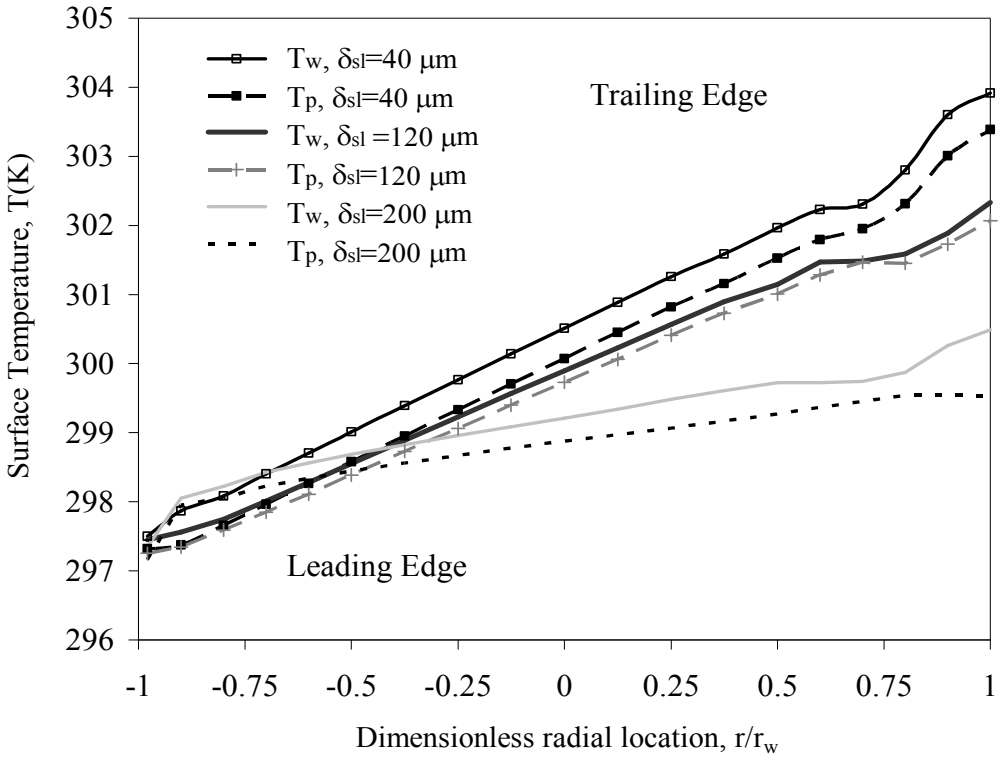

Figure 7.6 Temperature distributions along the center of pad and substrate surfaces for three characteristic slurry film thicknesses.

The average wafer temperature results of figure 7.6 along the radial distance were approximately equal to 299.12, 299.86, and 301.15 degrees K for the abrasive film thicknesses (δ_{sl}) of 200, 120, and 40 μm respectively. As seen in figure 7.6, the wafer

temperature distributions of thicker film are lower and more uniform due to an increment of the volumetric flow rate of the slurry that moves beneath the substrate and pad surfaces. The increment of the volumetric flow rate increases the heat advection per unit area, therefore increasing the heat transfer effect on the pad and substrate surfaces. This effect reduces the overall temperature of the wafer and pad at the control volume under study.

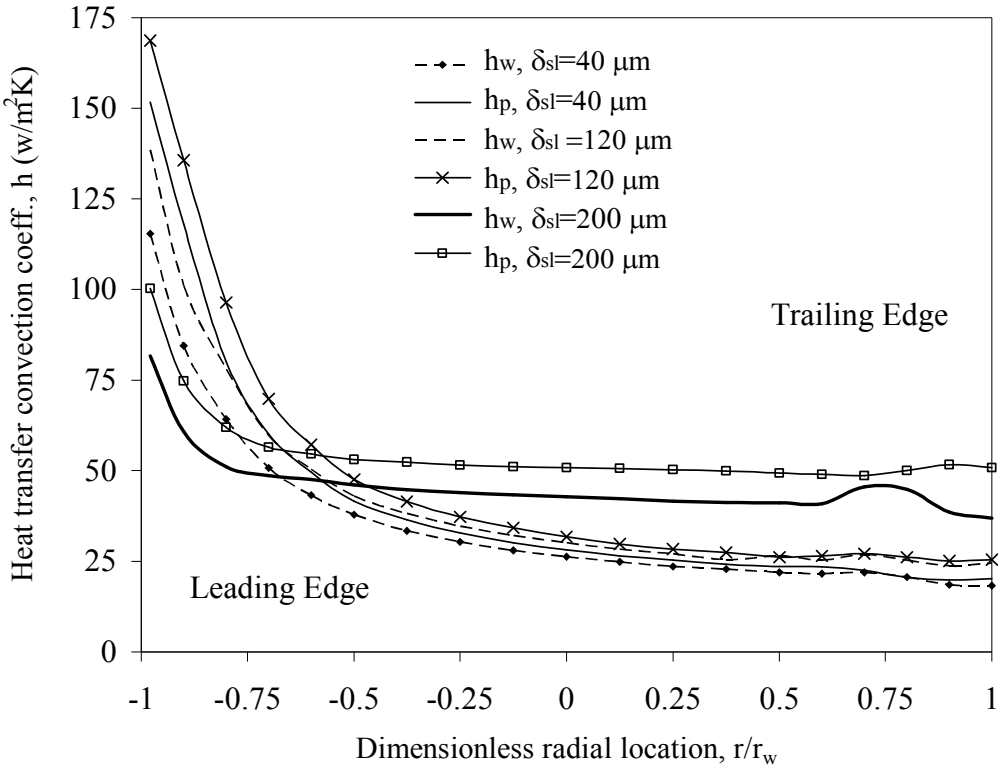

Figure 7.7 Local heat transfer convection coefficient distributions along the center of pad and substrate surfaces for three characteristic slurry film thicknesses.

Figure 7.7 illustrates the increment of the heat transfer convection coefficients of pad and wafer under thicker slurry films. The average heat transfer convection coefficients of the pad surfaces in figure 7.7 were equal to 55.91, 50.62, and 48.99 W/m^2K and the average heat transfer convection coefficients of the substrate surfaces were equal to 46.49, 44.13, and 39.29 W/m^2K for the abrasive film thicknesses (δ_{sl}) of

200, 120, and 40 μm respectively. The average pad heat transfer convection coefficients obtained were higher than the average wafer heat transfer convection coefficients by 20.26%, 14.71% and 24.69% for the slurry film thicknesses (δ_{sl}) of 200, 120, and 40 μm respectively. Present results are in agreement with Mudhivarthi [146] and Borucki [127] findings where the increment of the film thickness reduced the mechanical contact, and increased the amount of slurry interaction resulting in lower temperature profiles, increasing the heat transfer convection along the wafer region exposed to the abrasive–pad interface.

Figures 7.8a and 7.8b illustrate the temperature contour distributions of the wafer and pad surfaces under two characteristic pad spinning rates of 100 and 200 RPM. The steady state temperature contour plots were set for an abrasive film thickness of 40 μm of alumina, at constant slurry flow rate of 50 cc/min, under a constant load of 24.35 kPa, for a variable heat flux range of 6 to 8.5 kW/m^2, and a carrier spinning rate of 30 RPM. Figure 7.8a shows the steady state temperature difference of 6 degrees at a small region of the slurry, wafer, and pad surfaces at the 2 and 3 o'clock positions for a pad spinning rate of 100 RPM.

Figure 7.8b shows a temperature gradient of 4.5 degrees for a pad spinning rate of 200 RPM. The temperature gradient extends at a small fraction of the 3 and 4 o'clock positions of the trailing edge of the substrate surface and a small portion of the slurry region beneath the same wafer orientation.

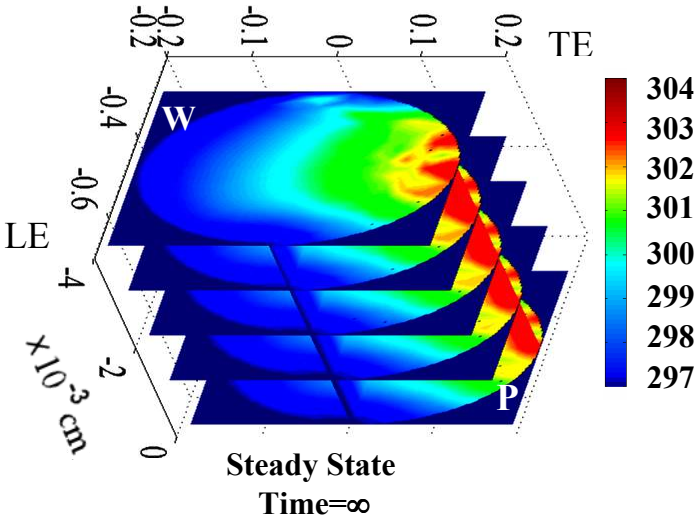

(a)

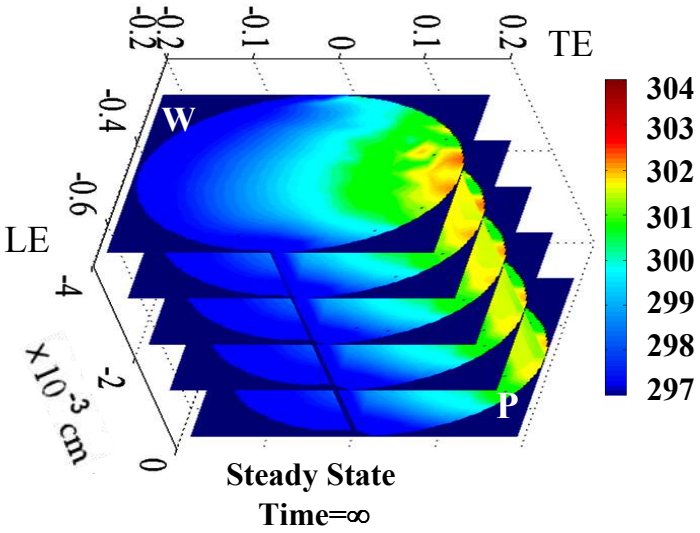

(b)

Figure 7.8 Steady state wafer, and pad temperature contour distributions for two characteristic pad spinning rates equal to: (a) Ω_p=100 RPM and (b) Ω_p=200 RPM.

The temperature rise and the local heat transfer convection coefficient distributions of the wafer and pad surfaces under two characteristic pad spinning rates of

100 and 200 RPM, are shown in figure 7.9 under the same polishing conditions described in figures 7.8a and 7.8b.

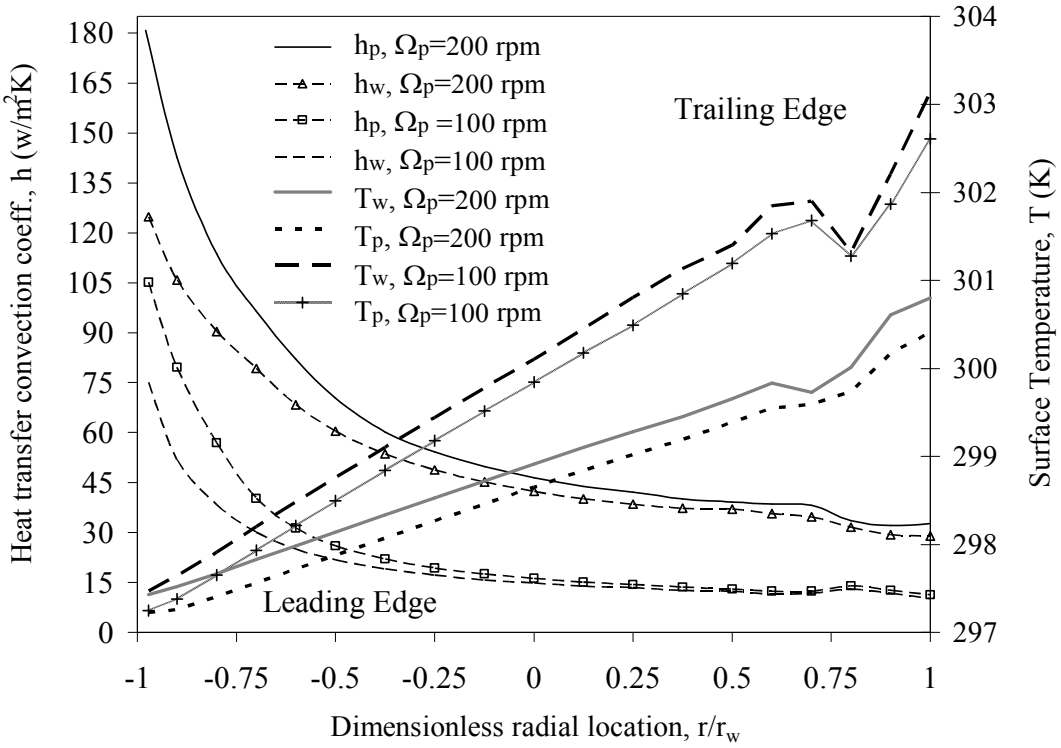

Figure 7.9 Cross–sectional temperature distributions and local heat transfer convection coefficients along the center of pad and substrate surfaces under two different pad spinning rates.

The substrate and pad temperature distributions for a pad spinning rate (Ω_p) of 200 RPM decreased in comparison with the results of a pad spinning rate (Ω_p) of 100 RPM, as shown in figure 7.9. The pad that spins at 200 RPM drive out the hot slurry from the backflow region overcoming the surface tension forces caused by the shear stress. Conversely, the pad that spins at a spinning rate of 100 RPM allows a major hot slurry recirculation at the backflow region, causing an increment of 1.25 degrees at the 3 o'clock position of the substrate trailing edge. A backflow effect is linked to the rotational motion of the slurry and the shear effect of frictional forces due to the surface

tension and viscosity of the slurry particles along such a small gap. The average temperature rise of the wafer and pad under a pad spinning rate of 200 and 100 RPM were approximately equal to 3.4, 3.5, and 3 degrees respectively along the wafer and pad trailing edges.

The heat transfer convection coefficients for wafer and pad surfaces follow the same pattern as figures 7.2, 7.3, 7.5 and 7.6. The wafer heat transfer convection coefficient values range from 130 to 14 (W/m^2K). The average values of the heat transfer convection coefficient for the wafer along the surface were approximately equal to 33.07 and 53.06 (W/m^2K) under lower and higher pad spinning rate conditions respectively. The pad heat transfer convection coefficient values range from 180 to 15 (W/m^2K). The average values of the heat transfer convection coefficient for the pad along the surface were approximately equal to 38.05 and 64.03(W/m^2K) under a pad spinning rate of 100 and 200 RPM respectively. This effect results in higher convective coefficients for the pad by an average margin of 15.06% and 20.67% under lower and higher pad spinning rates.

A lower pad spinning rate of Ω_p=100 RPM increased the backflow recirculation for a dimensionless radial distance $0.75 < r/r_w \leq 1$. However, the increment of the pad spinning rate reduces the backflow effect observed by Muldowney [147], as shown in the pad and wafer temperature distributions in figure 7.9 for a pad spinning rate of 200 RPM. This thermal effect is consistent with the findings of Hong et al. [132] that point out that polishing temperature varies in parallel with their speed integral. The increment of the angular velocity of the platen generates more heat dissipation during the chemical mechanical polishing process due to the increment of the tangential velocity at the

thermal boundary layer thickness of the slurry that is force out through the polishing, which is replaced simultaneously with fresh, cool slurry that enters beneath the polished wafer around its perimeter. The minimum heat–transfer slurry–wafer interaction occurred close to the wafer trailing edge area. Hot spots can be observed along the trailing edge and some inner regions where part of the slurry got trapped due to the emerging rotational flow patterns. Similar temperature profile patterns have been documented by Borucki et al. [127, 128].

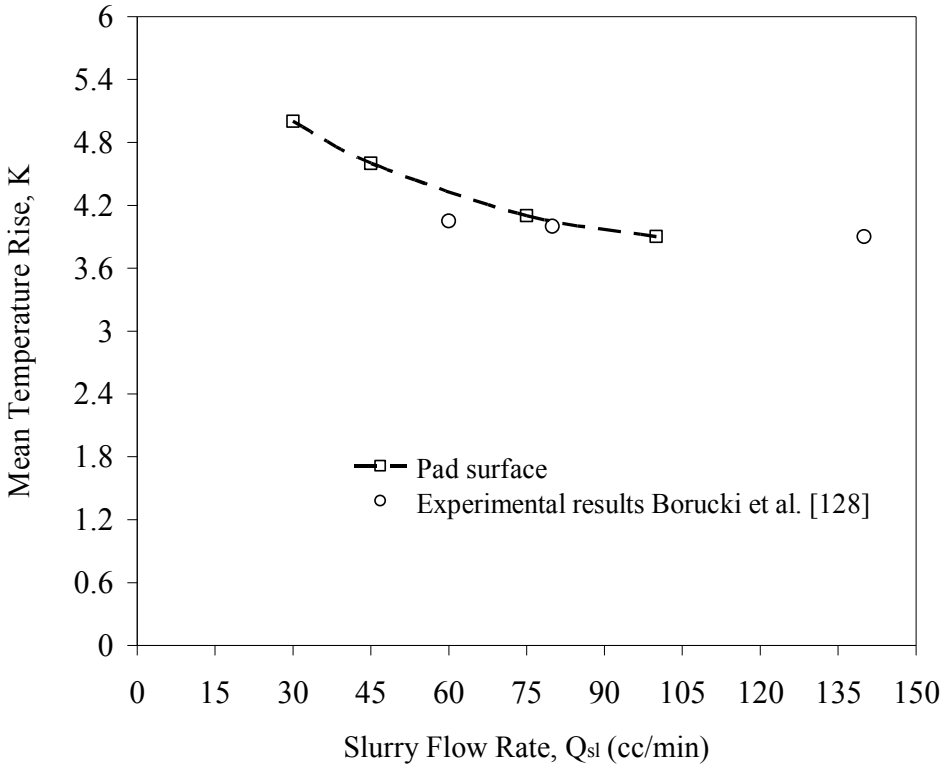

Figure 7.10 Comparison of mean temperature rise of pad at different slurry flow rates of present results with experimental results of Borucki et al. [128].

Figure 7.10 shows the numerical results of mean pad temperature rise at different flow rates along the substrate edge compared to the results from the experimental work by Borucki et al. [128]. As seen in figure 7.10, the agreement of the experimental mean temperature rise obtained by Borucki et al. [128] with the present numerical data is quite

good. The temperature rise under slurry flow rates of 60, and 80 cc/min correlates with an average margin of 6.92%, and 4.73% respectively. Note that numerical predictions are within an average percentage off error of 5.83%.

One of the papers used for the validation of this numerical study was the experimental work by Borucki et al. [127] using a JSR Corp. flat pad with a commercial silica slurry under a flow rate equal to Q_{sl}=60 cc/min. The nominal wafer pressures used were 2.5 and 6 (psi) or (17.24 and 41.37 kPa) respectively, and the co–rotation rates for the carrier and pad range from 120 to 140 RPM. The average heat transfer convection coefficients from the present numerical simulation for different combinations of CMP parameters and input heat flux are listed in Table 7.1. The heat transfer convection coefficients for the JSR Corp. flat pad were correlated with the present numerical results of runs #12 and #13 versus experimental results presented by Borucki et al. [127] on runs #14 and #15 under the CMP parameters described in Table 7.1. Present numerical heat transfer results of runs #12 and #13 correlate with an average margin of 8.69%, and 5.57% respectively. Note that numerical predictions are within an average percentage off error of 7.13%. The numerical results reveal a better correlation at larger flow rates. The factor of working at the micrometer scale under the influence of two spinning surfaces about different axis of rotation, the complexity of flow under such type of boundary conditions, and the range of flow parameters may contribute to the discrepancy between experimental and numerical data. In addition, computational errors can be introduced because of round off and discretization of the mesh. Considering these factors, the overall comparison with test and numerical results of previous studies is satisfactory.

Table 7.1 Average substrate and pad heat transfer convection coefficients and experimental data of Borucki et al. [127] under different CMP parameters and variable input heat flux along the surfaces.

Runs	Q_{sl} (cc/min)	Ω_p (RPM)	Ω_c (RPM)	δ_{sl} (μm)	P (kPa)	q_{sl} (kW/m^2)	COF μ_{fr}	h_{avp} (W/m^{2}K)	h_{avw} (W/m^{2}K)
1	30	120	30	40	24.35	3.6–8.3	0.4	51.25	43.64
2	75	120	30	40	24.35	3.6–8.3	0.4	51.95	44.11
3	85	200	30	40	17.24	4.1–9.8	0.4	53.01	43.32
4	85	200	30	40	41.37	10.1–23.4	0.4	65.37	54.32
5	60	145	15	40	34.48	6–14.1	0.4	49.15	42.61
6	60	145	75	40	34.48	6–14.1	0.4	52.43	45.79
7	65	150	40	40	28	5–11.65	0.4	48.99	39.29
8	65	150	40	120	28	5–11.65	0.4	50.62	44.13
9	65	150	40	200	28	5–11.65	0.4	55.91	46.49
10	50	100	30	40	24.35	3.8–8.75	0.49	38.05	33.07
11	50	200	30	40	24.35	3.8–8.75	0.257	64.03	53.06
12	60	10	140	40	17.24	2.6–6	0.35	35.65	30.26
13	60	10	120	40	41.37	3.56–8.25	0.2	42.86	40.09
14	60	N/D	140	N/D	17.24	N/D	0.35	32.80	N/D
15	60	N/D	120	N/D	41.37	N/D	0.2	40.60	N/D

7.2 Transient Process

Transient temperature profiles and the heat transfer convection coefficients of substrate and pad surfaces during a CMP process were acquired using a three dimensional FEM model. Figure 7.11a shows the maximum and minimum temperature contour distributions for the control volume under study for a slurry flow rate of Q_{sl}=30 cc/min. During the early part of the transient process the slurry, the wafer and pad surfaces reached a temperature difference of 6 degrees at a considerable region of the wafer trailing edge at the 2, 3, and 4 o'clock positions. After a short period of 100 sec the transient temperature difference of 6 degrees remains the same at smaller areas of the wafer trailing edge along the 2, 3, and 4 o'clock positions. A second numerical run with

the same polishing conditions except for the amount of slurry flow rate (Q_{sl}=75 cc/min) are shown in figure 7.11b. Figure 7.11b shows a temperature difference of 10 degrees at a small fraction of the upper region of the trailing edge during the entire polishing process.

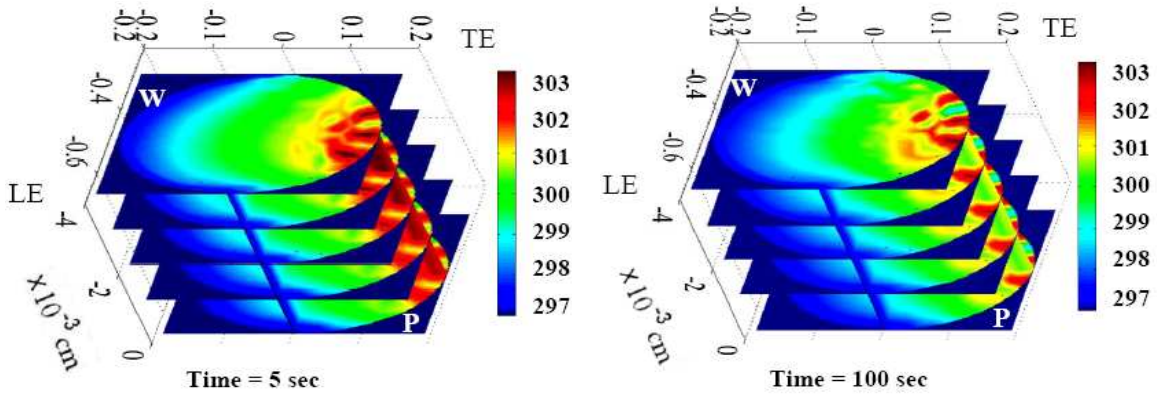

(a)

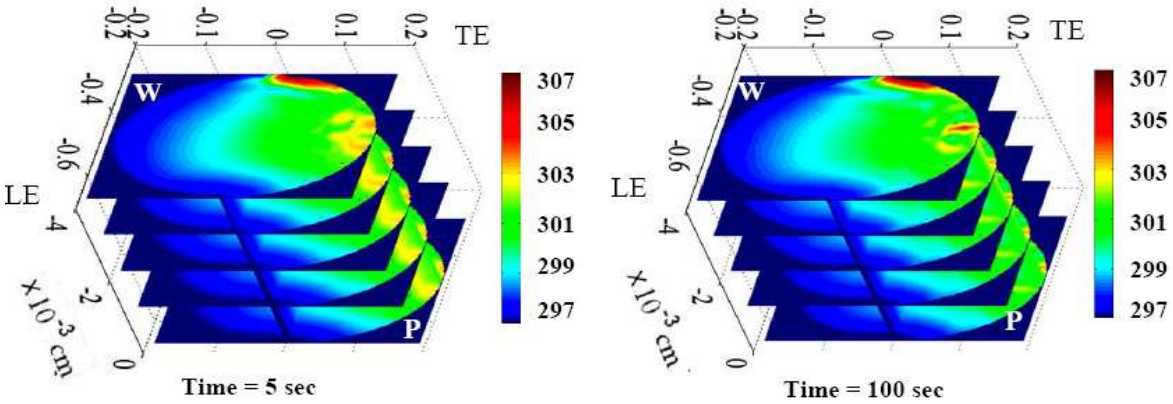

(b)

Figure 7.11 Slurry (alumina), wafer, and pad surfaces temperature contour distributions for a flow rate value of: (a) Q_{sl}=30 cc/min and (b) Q_{sl}=75 cc/min.

In general, the temperature distributions of the wafer–pad interface are smaller for a slurry rate of Q_{sl}=75 cc/min just with the exception of two regions close to the trailing edge of the wafer exposed to the backflow effect of the slurry observed by Muldowney [147]. A backflow effect is linked to the rotational motion of the slurry and the shear

effect of frictional forces due to the surface tension of the slurry particles along such a small gap.

The transient substrate temperature variations and wafer–pad temperature difference for two different flow rates at the 3 and 5 o'clock positions are shown in figures 7.12a and 7.12b respectively. The transient temperature results were done for an abrasive film thickness of 40 μm, at a dimensionless radial distance of r/r_w=7/8 under a constant pressure load of P=24.35 kPa, for a variable heat flux (q_{sl}=4.6–10.8 kW/m^2, under a pad and carrier spinning rate of 150 and 30 RPM respectively. The variable heat flux rate (q_{sl}) used for this analysis is a function of the pressure load, pad coefficient of friction, the radial distance measured from the center of the platen, and the relative pad–wafer spinning rate. The wafer temperature results of figure 7.12a for a slurry flow rate of (Q_{sl}=75 cc/min) are slightly lower in comparison with an alumina flow rate of 30 cc/min. That slight change in temperature can be confirmed with the comparison of the average transient wafer temperature differences of both flow rates during the entire process. An average transient wafer temperature difference of 4.35 degrees was attained for a lower slurry flow rate versus the 3.98 degrees acquired under a higher slurry flow rate. The wafer–pad temperature differences showed in figure 7.12a reveals that the pad temperature values are lower compared to the substrate surface results. The wafer–pad temperature differences examined range up to 1.2 degrees K or C for the lower slurry rate and up to 0.6 degrees for the higher slurry flow rate at the radial location under study (r/r_w=7/8). The temperature difference of a slurry flow rate of 75 cc/min was lower and more stable compared with a slurry flow rate of 30 cc/min.

In contrast, figure 7.12b shows lower temperature results for a slurry rate of 30 cc/min at the 5 o'clock position for a radial distance r/r_w=7/8 of the wafer. That slight change in temperature can be corroborated with the comparison of average temperature differences of both slurry flow rates during the entire process. An average wafer temperature difference of 4.25 degrees was attained for a lower slurry flow rate versus a 4.38 degrees acquired under a higher flow rate of alumina. The wafer temperature at the 3 o'clock position is about 1 degree higher than the 5 o'clock position under both slurry flow rates. This radial temperature variation is related to the slurry flow and the heat transfer beneath the wafer surface. Fresh, cool slurry enters beneath the polished wafer around its perimeter. As seen in figure 7.12b, that the 5 o'clock position is in thermal advantage because it is facing the leading edge of the slurry and it is closer to the center of the platen that holds that pad.

In contrast, the 3 o'clock position is facing the trailing edge far away from the center of the platen; consequently it had more heat to transfer due to frictional interaction of pad–slurry particles beneath the wafer. The wafer pad temperature differences examined range up to 0.92 degrees K or C for the lower slurry flow rate and up to 0.37 degrees for the higher slurry flow rate at a radial location of r/r_w=7/8 along the 5 o'clock position, as shown in figure 7.12b. The temperature difference of a 75 cc/min slurry flow rate was lower and more stable compared with a lower slurry flow rate of 30 cc/min. The temperature contour plots in figures 7.11a and 7.11b, and temperature variation of figures 7.12a and 7.12b reveal that the wafer temperature profile decreases with the increment of the slurry velocity. Present numerical results are in agreement with Sampurno et al. [121].

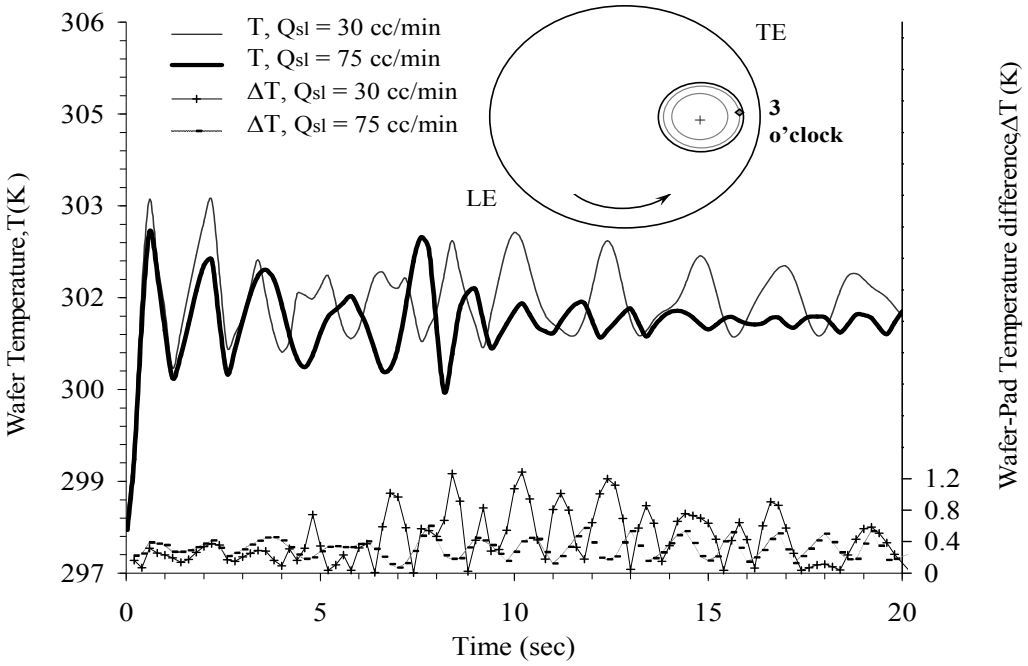

(a)

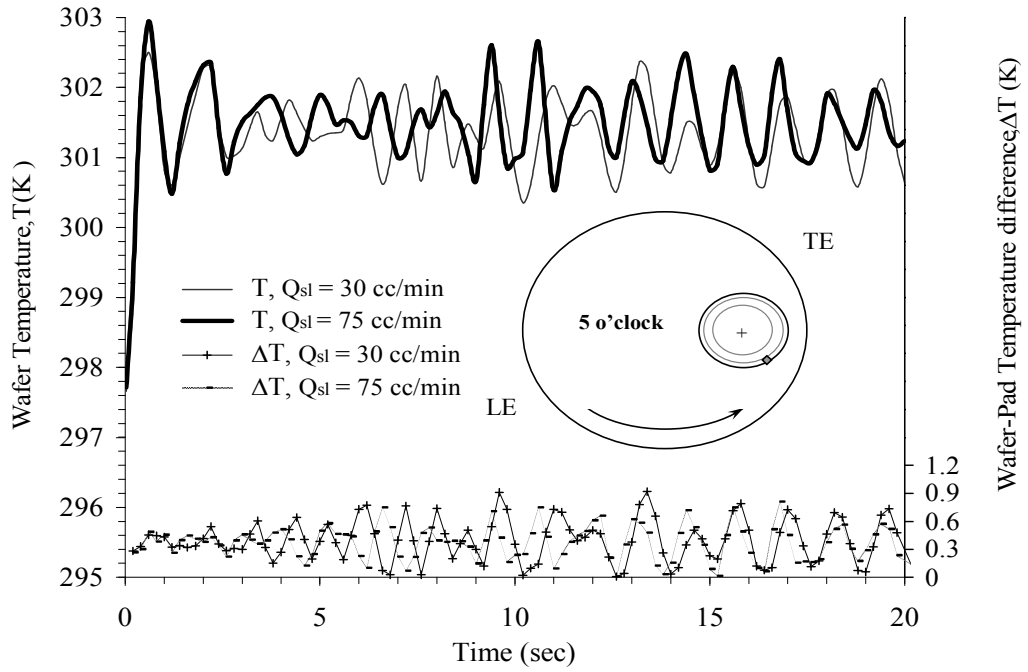

(b)

Figure 7.12 Transient wafer temperature distribution and wafer pad temperature differences for two different flow rates at a radial location of $r/r_w=7/8$ along the: (a) 3 o'clock position and (b) 5 o'clock position.

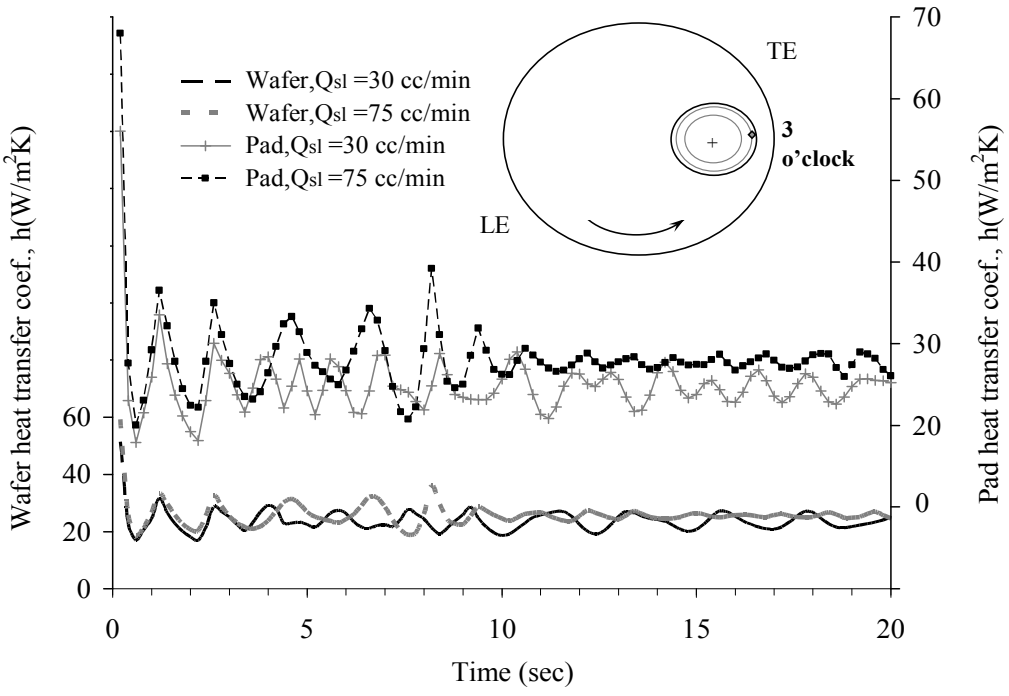

(a)

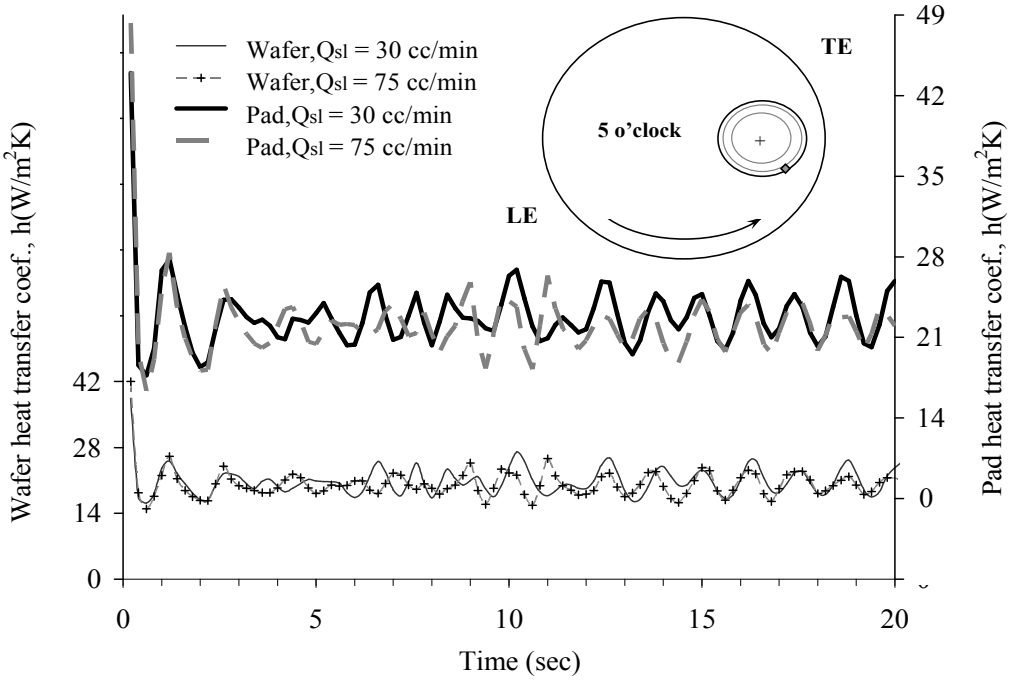

(b)

Figure 7.13 Wafer and pad transient heat transfer convection coefficients for two different flow rates at a radial location of r/r_w=7/8 along the: (a) 3 o'clock position and (b) 5 o'clock position.

Figures 7.13a and 7.13b show the wafer and pad heat transfer convection coefficients at the 3 and 5 o'clock positions respectively for the same conditions of figures 7.12a and 7.12b. The heat transfer convection coefficients in figure 7.13a are slightly higher at the pad than the substrate surface that is due to a lower temperature difference between slurry and pad. This validates the results obtained in figure 7.12a and 7.12b where the temperature difference between the pad and wafer substrate were around 1 C or K smaller. That effect results in higher convective coefficients for the pad by 5.26% and 8.61% under lower and higher slurry flow rates. The average values of the heat transfer convection coefficient for the pad attained at this location were approximately equal to 26.82 and 29.19 W/m^2K under lower and higher slurry flow rate conditions. The heat transfer convection coefficients in figure 7.13b are slightly higher at the pad than the substrate surface due to a lower temperature gradient between the incoming slurry and pad surface. This effect results in higher convective coefficients for the pad by 6.86% and 9.83% under lower and higher slurry flow rates. The average values of the heat transfer convection coefficients for the pad attained at this location were about 22.28 and 23.97 W/m^2K under lower and higher slurry flow rates.

Figures 7.14a and 7.14b show the maximum and minimum temperature contour distributions for the control volume under study at a constant load of 17.24 kPa (2.5psi) and 41.37 kPa (6psi) respectively. The transient temperature contour plots were done for an abrasive film thickness of 40 μm, under a constant slurry flow rate of Q_{sl}=85 cc/min, with a pad coefficient of friction of μ_{fr} =0.4, under a pad and carrier spinning rate of 200 and 30 RPM respectively. This change in pressure directly affects the amount of heat dispersed beneath the wafer as result of the greater slurry, pad, and substrate shear stress

interaction during the polishing. For a load of 17.24 kPa the heat flux input into the system covers a range of (q_{sl}=4.14–9.63 kW/m^2) along the leading to the trailing edge of the wafer, as shown in figure 7.14a. During the early part of the transient process the slurry, the wafer and pad reached up to a temperature difference of 8 degrees at a small fraction of the upper region of the trailing edge. Later on, after a short period of 100 seconds the transient temperature difference decreases slightly to 7 degrees and extends along the trailing edge in small areas from the 12 to 4 o'clock positions.

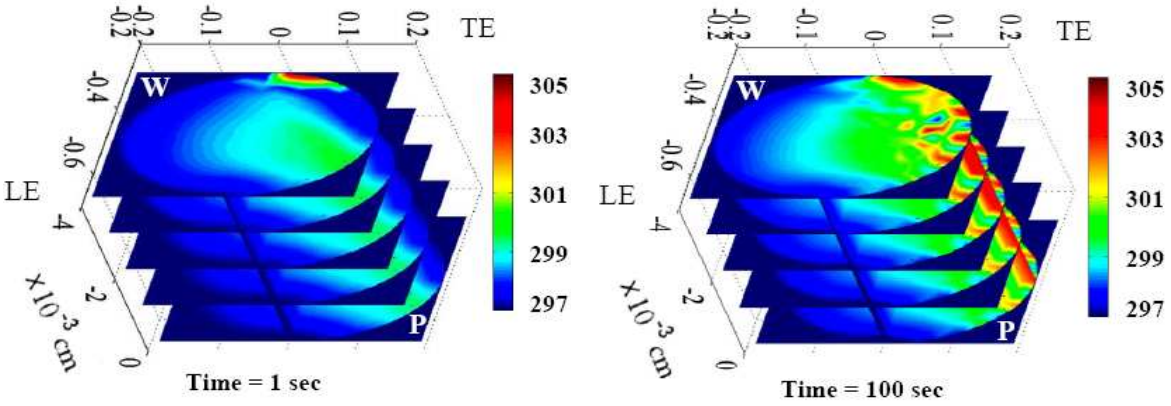

(a)

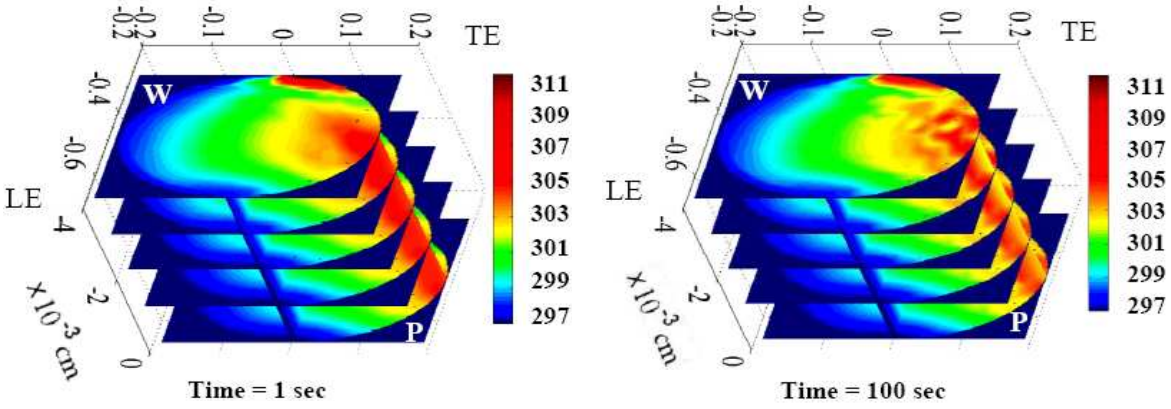

(b)

Figure 7.14 Slurry, wafer, and pad surfaces temperature contour distributions under a constant pressure value of: (a) 17.24 kPa and (b) 41.37 kPa.

A second trial under study is shown in figure 7.14b for the same polishing conditions except for an increment of the applied load to 41.37 kPa as part of the modeling set up. This new applied load set the limits of a variable heat flux that range from 10.38 to 23.12 (kW/m^2) along the leading to the trailing edge of the wafer. Figure 7.14b illustrates a temperature difference of 14 degrees during the early part of the process at a considerable region of the wafer located at the 12 to 5 o'clock position of the trailing edge. After a relative short period of 100 seconds the temperature difference decreases to 12 degrees at various constricted areas more likely at the edge of the wafer, due to the amount of heat transfer with a slurry flow rate under a higher temperature after being exposed to the shear stress and frictional forces as part of the transient CMP process. The effect of adding more pressure to the CMP process produced larger temperature gradients at the wafer–pad interface as a result of more contact to contact abrasion mode of the pad with slurry particles and substrate, as shown in figures 7.14a and 7.14b. Present results are in agreement with Sikder et al. [148]. Their experimental results using an acoustic sensor revealed that the coefficient of friction decreased under a lower applied pressure.

Figures 7.15a and 7.15b show the variable heat transfer effect of two different applied loads of pressure from the universal bench top tribometer during the polishing process on the local transient temperature distributions at different specific radial distances measured from the center of the substrate. The transient wafer temperature results of figure 7.15a under a load of 17.24 kPa are lower in comparison with the results obtained at figure 7.15b under the same dynamic polishing conditions of the model under study in figures 7.14a and 7.14b. The average change in temperature of figure 7.15a

compared with figure 7.15b at the 12 o'clock location for each of the study radial distances were approximately equal to 2.5 degrees at r/r_w=2/3 of the wafer, 4.27 degrees at r/r_w=7/8 and 7.21 degrees along the wafer edge. Average wafer–pad temperature differences of 0.74, 2.24, and 0.69 degrees were attained at each of the following radial locations of 2/3, 7/8, and 1 respectively under a pressure load of 17.24 kPa as shown in figure 7.15a. The wafer–pad temperature differences shown in figures 7.15a and 7.15b range up to 4.5 to 6 degrees respectively. Pad temperature values are lower than wafer substrate results at the polishing surface. The wafer–pad temperature differences at a radial distance around the edge (r/r_w=1) were lower and more stable in comparison with the other two radial locations in figures 7.15a and 7.15b. The temperature differential at the radial location of r/r_w=7/8 was less stable. This instability is part of the fluid dynamics of the slurry that is in continuous re–circulating motion entrapped beneath the wafer and polishing pad surfaces. As part of the mechanics of the CMP process, fresh and cool slurry it is transported continuously from the center of the pad to the surface beneath the substrate, causing a major fluctuation of the temperature gradient. This effect is more pronounced when the heat slurry is getting closer to the starting backflow region underneath the slurry. Conversely, this effect is less pronounced once the outgoing slurry reaches the substrate edge at the outlet and mixes up with fresh and cool slurry. Average wafer–pad temperature differences of 1.76, 3.38, and 1.62 degrees were attained at each of the following radial locations 2/3, 7/8, and 1 respectively under a pressure load of 41.37 kPa, as shown in figure 7.15b.

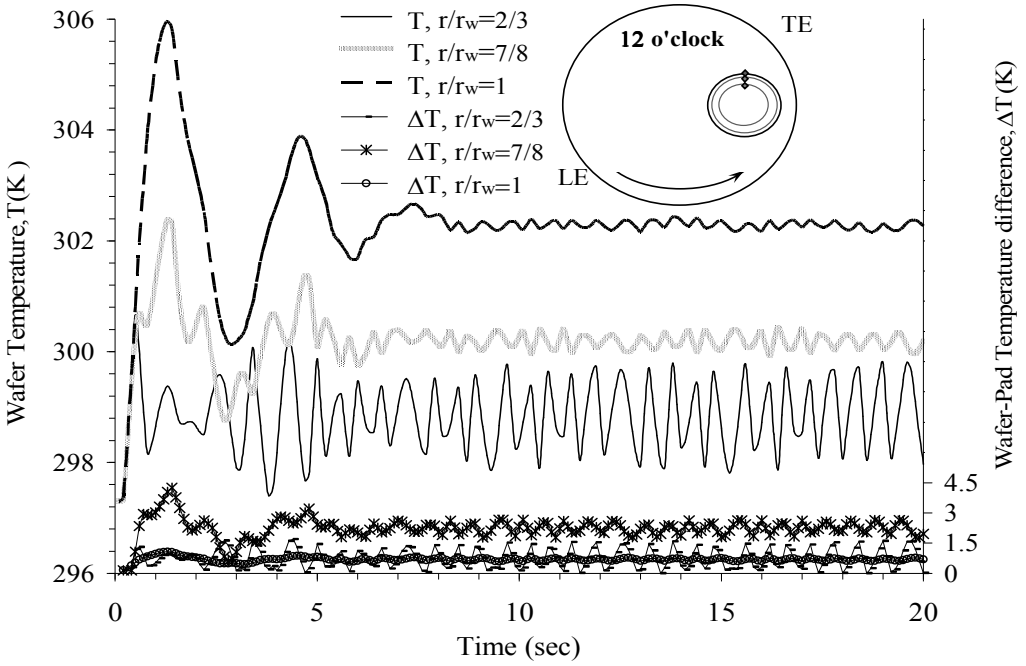

(a)

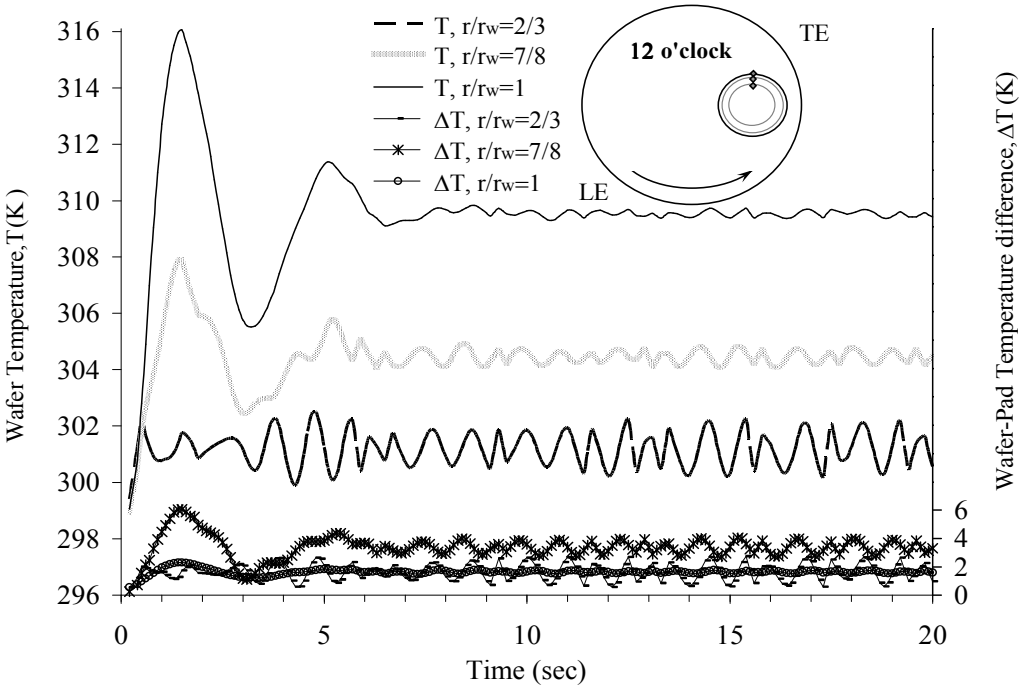

(b)

Figure 7.15 Transient wafer temperature distributions and wafer pad temperature differences at different radial locations along the 12 o'clock position under a constant pressure value of: (a) P=17.24 kPa and (b) P=41.37 kPa.

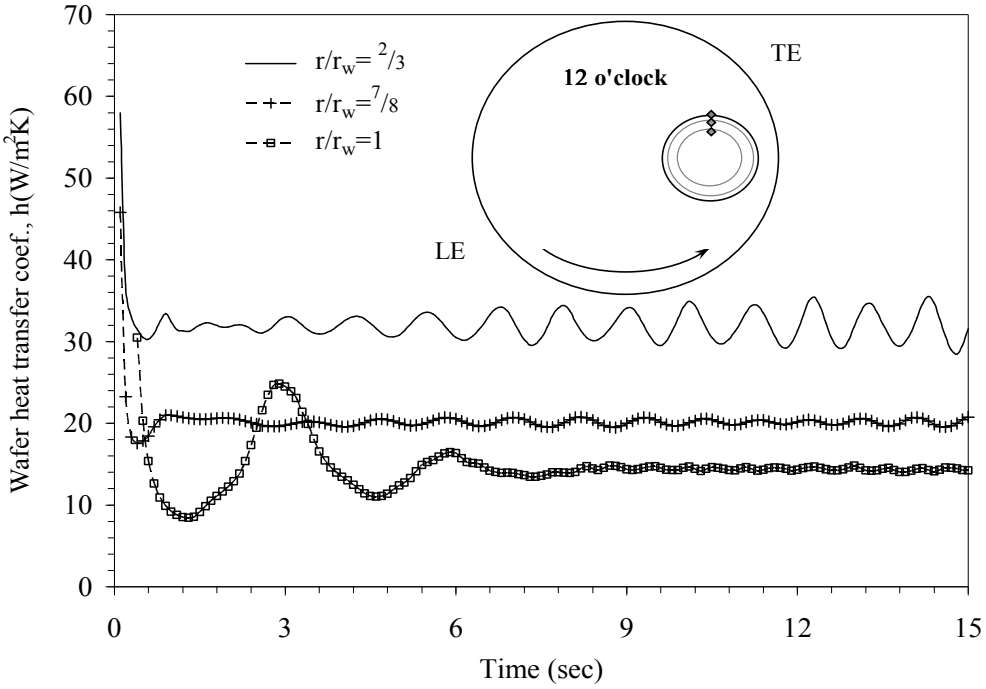

(a)

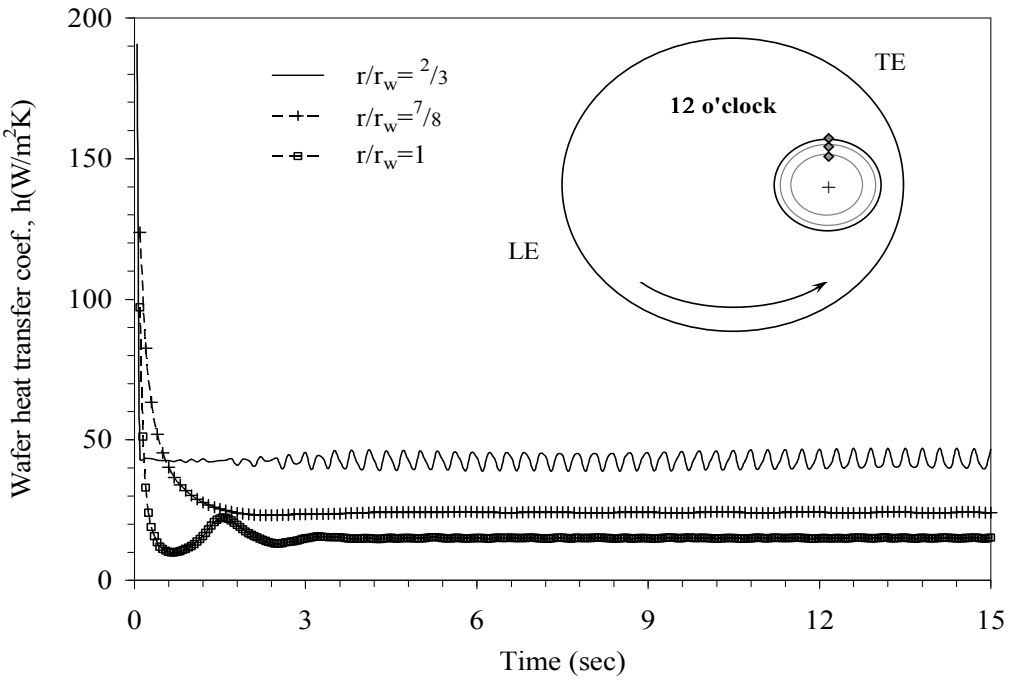

(b)

Figure 7.16 Transient wafer heat transfer convection coefficient at different radial locations along the 12 o'clock position under a constant pressure value of: (a) P=17.24 kPa and (b) P=41.37 kPa.

The wafer heat transfer convection coefficients at three specific radial locations for two distinctive pressure loads are shown in figures 7.16a and 7.16b. Figure 7.16a shows that the pressure effect on the variable heat flux is more intense at the trailing edge of the wafer that is further away from the center of the pad, causing and an uneven heating effect on the substrate surface. The convective heat transfer coefficients effect was more pronounced at a radial distance of $r/r_w=2/3$ with an average value of 32.14 W/m^2K. The average values of the pad heat transfer convection coefficient attained were around 21.3 and 17.62 W/m^2K for the radial locations of $r/r_w=7/8$ and 1 respectively. Figure 7.16b shows the same pattern of figure 7.16a, where the heat transfer convection coefficient effect was more pronounced at a radial distance of $r/r_w=2/3$ with an average value equal to 42.75 W/m^2K. The heat transfer convection coefficient effect decreased by an average margin of 45.05% once it reaches the wafer outer edge at the trailing region. A lower heat transfer convection coefficient at a particular location indicates the presence of a hot spot or a larger temperature gradient between the incoming slurry at the pad or substrate surfaces. The average heat transfer convection coefficients obtained are in agreement with the earlier experimental works of Borucki et al. [127,128].

The temperature contour distributions of the wafer and pad surfaces under two characteristic carrier spinning rates of 15 and 75 RPM are shown in figures 7.17a and 7.17b. The transient temperature contour plots were done for an abrasive film thickness of 40 μm of alumina, under a constant slurry flow rate of (Q_{sl}=60 cc/min), with a pad coefficient of friction (μ_{fr}=0.4), under a constant load of 34.48 kPa, for a variable heat flux (q_{sl}=6.6–15.3 kW/m^2), and pad spinning rate of 145 RPM. During the early part of the transient process in figure 7.17a the slurry, the wafer and pad reached up to a

temperature difference of 9 degrees at a small fraction of the upper region of the trailing edge. Later on, the transient temperature difference decreases slightly to 8 degrees and extends along the trailing edge to series of small areas along the 12 to 3 o'clock positions after a period of 100 seconds, as shown in figure 7.17a. Figure 7.17b illustrates a temperature gradient of 5 degrees during the early part of the process at small areas around the 2 to 4 o'clock positions of the trailing edge. After a short period of 100 seconds the temperature gradient of 5 degrees remains the same around the 3 o'clock position, as shown in figure 7.17b.

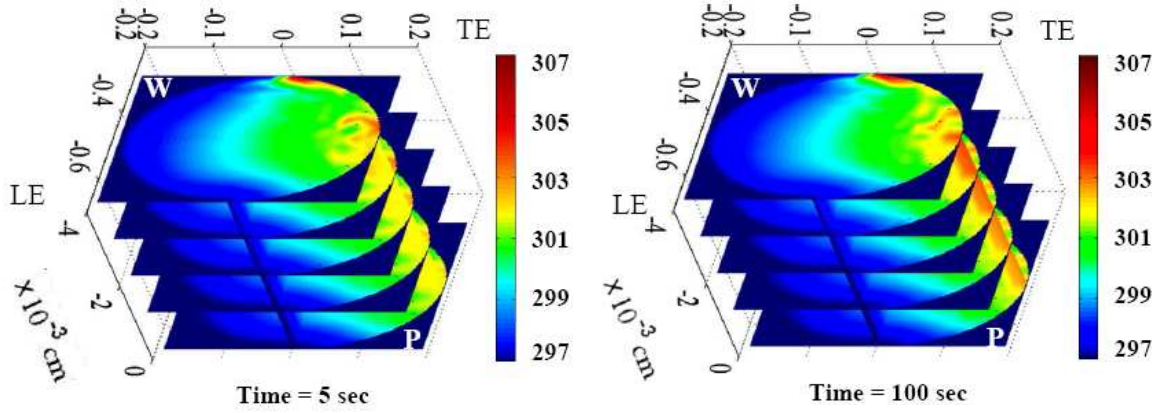

(a)

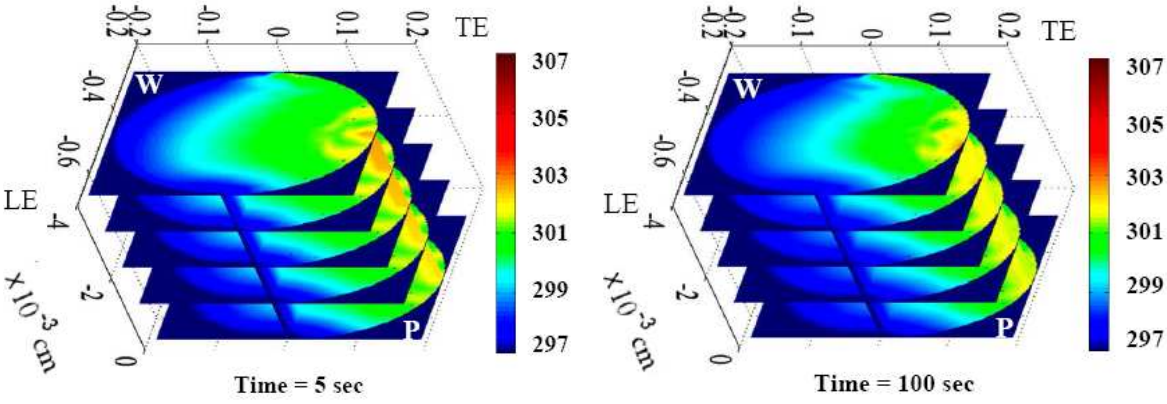

(b)

Figure 7.17 Slurry, wafer, and pad surfaces temperature contour plots for a carrier spinning rate equal to: (a) Ω_c=15 RPM and (b) Ω_c=75 RPM.

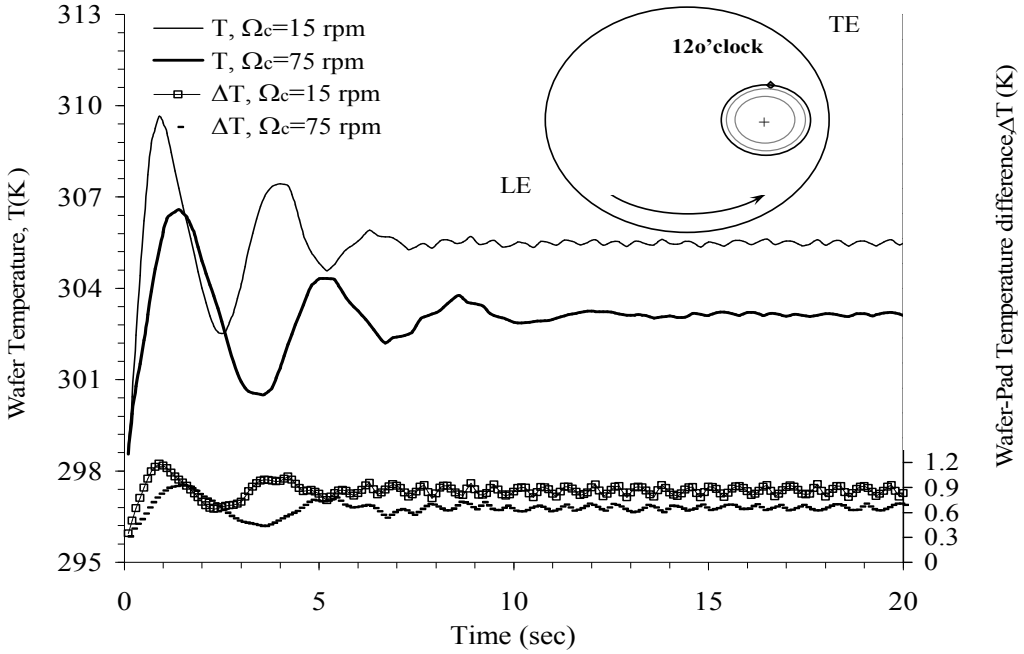

(a)

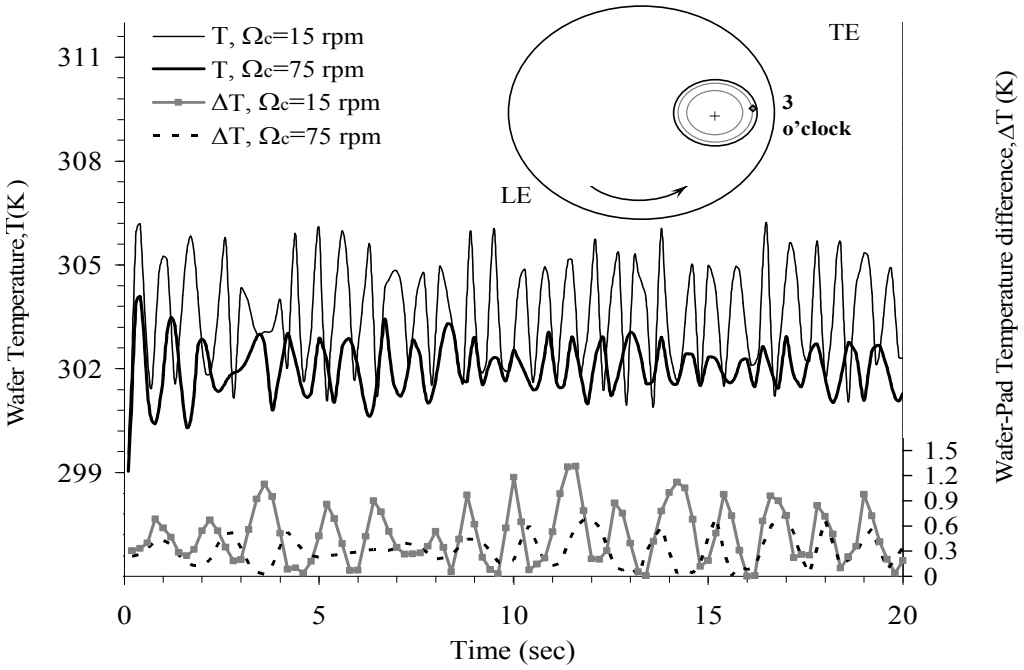

(b)

Figure 7.18 Transient wafer temperature distributions and wafer pad temperature differences for two different carrier spinning rates at a: (a) Radial location of $r/r_w=1$ along the 12 o'clock position and (b) Radial location of $r/r_w=7/8$ along the 3 o'clock position.

Figures 7.18a and 7.18b show the transient substrate temperature variations and wafer–pad temperature differences for two distinctive carrier spinning rates at the 12 and 3 o'clock positions with the same polishing conditions described in figures 7.17a and 7.17b. The average wafer temperature results for a carrier spinning rate of (Ω_c=75 RPM) are 2.59 degrees lower compared to a carrier spinning rate of 15 RPM, as shown in figure 10a. The wafer–pad temperature differences obtained in figure 7.18a range up to 0.86 degrees K or C for the lower carrier spinning rate and up to 0.655 degrees for the carrier at higher spinning rate at the radial location under study of r/r_w=1. An overall average transient wafer temperature difference of 8.56 degrees was obtained under a carrier spinning rate of 15 RPM versus the 5.97 degrees differential acquired for a carrier spinning rate of 75 RPM. The wafer–pad temperature differences examined range up to 0.86 degrees K or C for the lower carrier spinning rate and up to 0.655 degrees for the higher carrier spinning rate at the radial location under study of r/r_w=1.

Figure 7.18b shows that the average transient temperature results for a carrier spinning rate of (Ω_c=75 RPM) were approximately 1.55 degrees lower compared to a carrier spinning rate of 15 RPM along the 3 o'clock position at a radial distance of 7/8 of the wafer radius. The overall average transient wafer temperature differential of 6.63 degrees was attained for a lower carrier spinning rate versus the 5.08 degrees differential acquired for a carrier at higher spinning rate. Figure 7.18b kept the same wafer–pad temperature difference pattern observed in figure 7.18a. The wafer–pad temperature differences examined range up to 0.605 degrees K or C for the carrier at a lower spinning rate and up to 0.31 degrees for the carrier at a higher spinning rate at the radial location under study. The wafer temperature at the 12 o'clock position in figure 7.18a is about 1.5

degrees higher than the temperature observed at the 3 o'clock position for both carrier spinning rates. In general, the radial temperature variations are related to the slurry flow rate and the heat transfer beneath the wafer. Figure 7.18a illustrates that the 12 o'clock position at $r/r_w=1$ is in thermal disadvantage because it is at the back portion of the leading edge of the slurry. In contrast, the 3 o'clock position is between the leading and trailing edge at a radial distance of $r/r_w=7/8$, therefore it had less heat to transfer from the interaction of pad–slurry particles beneath the wafer. Additionally, the wafer–pad temperature differences for a carrier spinning rate of $\Omega_c=75$ RPM were lower and more stable than a carrier under a spinning rate of 15 RPM, as shown in figures 7.18a and 7.18b.

Figures 7.19a and 7.19b show the wafer and pad heat transfer convection coefficients at the 12 and 3 o'clock positions under the same numerical parameters of figures 7.18a and 7.18b. In addition, figures 7.19a and 7.19b show a similar heat transfer convection coefficient trend profile, as shown in figures 7.13a and 7.13b. Therefore, higher heat transfer convection coefficients are observed in figure 7.19a for the pad by a margin of 14.15% and 6.98% for a carrier at higher and lower spinning rates respectively. The average heat transfer convection coefficients for the pad along the 12 o'clock position at a radial location of $r/r_w=1$ were about 27.77 and 19.47 W/m^2K under higher and lower carrier spinning rates, as shown in figure 7.19a.

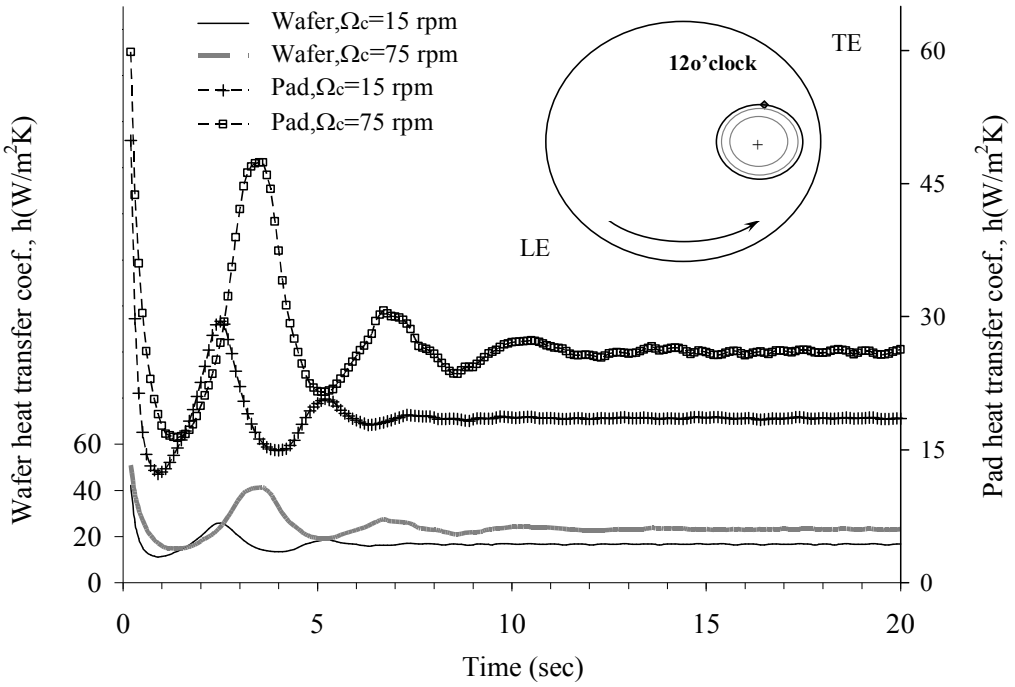

(a)

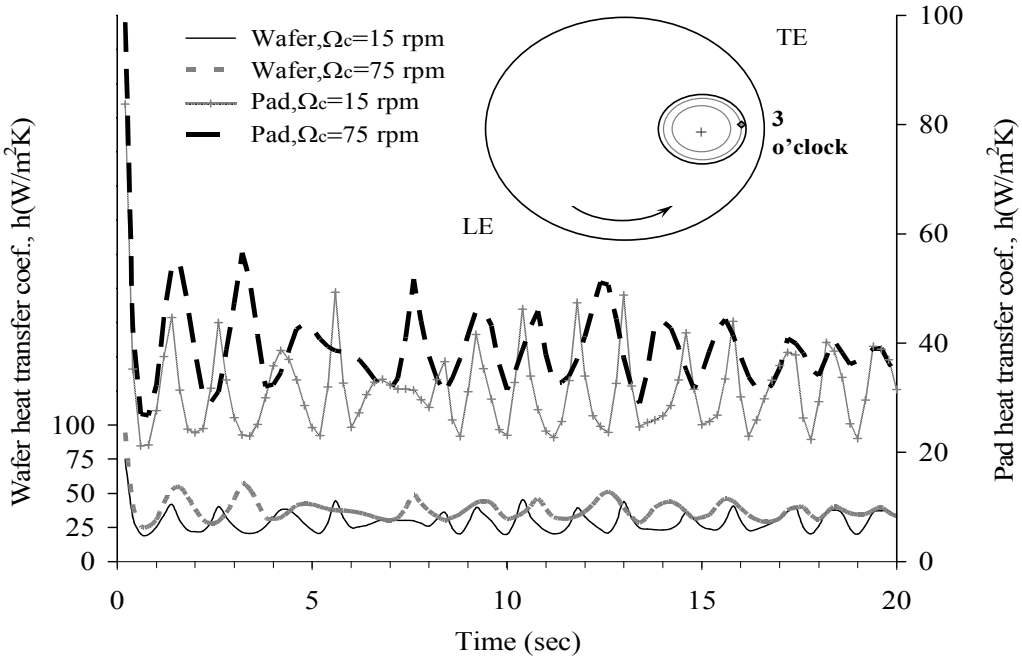

(b)

Figure 7.19 Wafer and pad transient heat transfer convection coefficients for two different carrier spinning rates at a: (a) Radial location of $r/r_w=1$ along the 12 o'clock position and (b) Radial location of $r/r_w=7/8$ along the 3 o'clock position.

Figure 7.19b reveals that the heat transfer convection coefficients for the pad increased by 7.22% and 3.12% for a carrier at higher and lower spinning rates respectively. The average values of the heat transfer convection coefficient for the pad along the 3 o'clock position at a radial location of $r/r_w=7/8$ were approximately equal to 40.24 and 31.36 W/m^2K under higher and lower carrier spinning rate conditions, as shown in figure 7.19b.

The temperature contour plots of the wafer and pad surfaces under two different slurry film thicknesses of (δ_{sl}=40 and 120 μm) are shown in figures 7.20a and 7.20b respectively. The transient temperature contour were prepared for a constant alumina slurry flow rate of 65 cc/min, with a pad coefficient of friction (μ_{fr} =0.4), under a constant load of P= 28 kPa, for a variable heat flux rate of 5.26 to 12.30 kW/m^2, with a pad and carrier spinning rate of 150 and 40 RPM respectively. During the early part of the transient process, as shown in figure 7.20a the wafer and pad reached up to a temperature difference of 9 degrees at a considerable region of the wafer along the 12 to 5 o'clock positions of the trailing edge. This thermal effect is consistent with the findings of Hong et al. [132], which pointed out that polishing temperature varies in parallel with their speed integral. Their finding reveals that the location of the highest predicted temperature by the speed integral match the highest measured temperature on the substrate surface. After a period of 100 sec the temperature gradient of 9 degrees remained the same at a few small areas around the 3 to 4 o'clock positions of the trailing edge of the wafer, as shown in figure 7.20a. Figure 7.20b shows a temperature difference of 6 degrees during the early part of the process at a small fraction of the upper region (12 o'clock) of the trailing edge and a significant region along the 3 to 4 o'clock positions closer to the

center of the substrate. Later on, the transient temperature difference reduced slightly to 5 degrees to three constricted areas near the trailing edge of the wafer at the 12, 3 and 4 o'clock positions. In addition, the temperature gradient for a thicker slurry film at the pad surface showed an overall temperature difference of 3 degrees approximately.

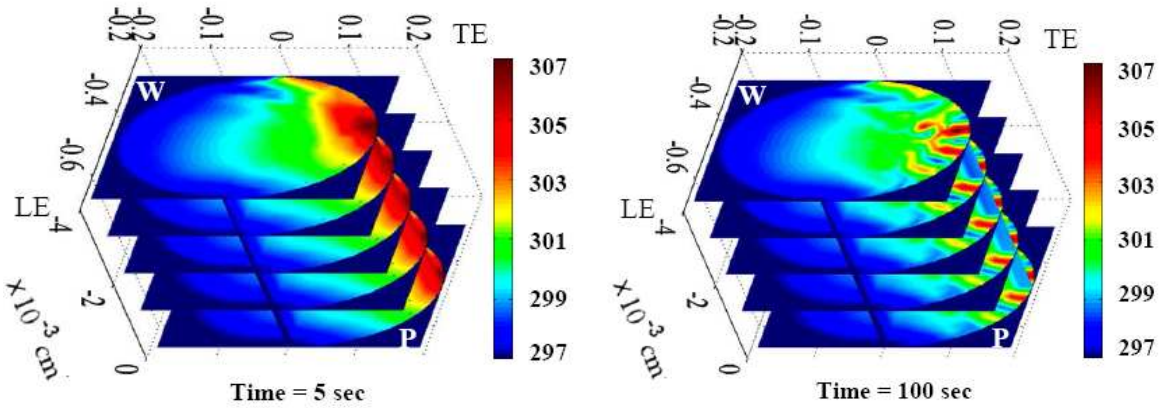

(a)

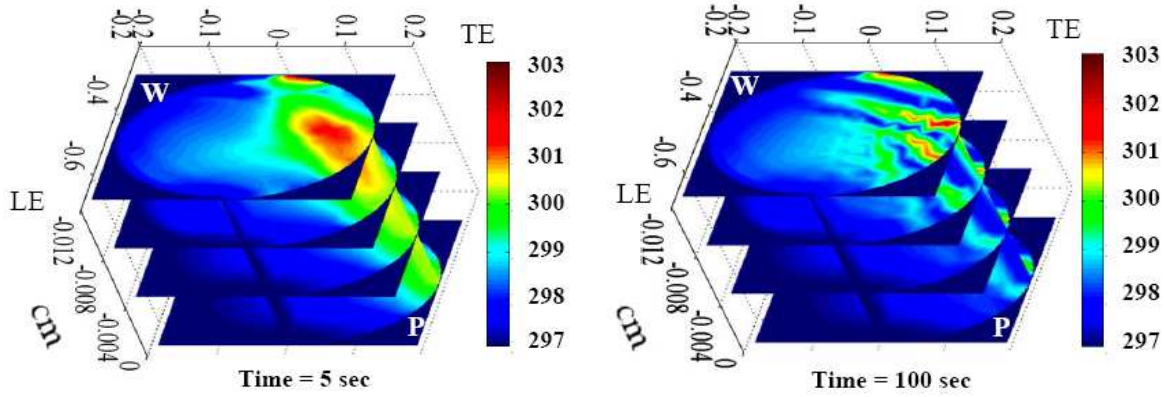

(b)

Figure 7.20 Slurry, wafer, and pad surfaces temperature contour distributions under a slurry film thickness equal to: (a) δ_{sl}=40 μm and (b) δ_{sl}=120 μm.

Figure 7.21 shows the transient substrate temperature variations and wafer–pad temperature differences for three different slurry film thicknesses at the 1 o'clock position, for the same conditions described in the preceding temperature contour plots.

The average transient wafer temperature results of figure 7.21 at a radial distance of r/r_w=7/8 along the 1 o'clock position were approximately equal to 301.38, 301.98, and 303.13 degrees K for the abrasive film thicknesses (δ_{sl}) of 200, 120, and 40 μm. The wafer–pad temperature differences examined range up to 3.03, 1.95, and 0.67 degrees K or C for the following abrasive film thickness (δ_{sl}) of 200, 120, and 40 μm. Conversely, the wafer temperature distributions of thicker film are lower due to an increment of the volumetric flow rate of the slurry that moves beneath the substrate and pad surfaces.

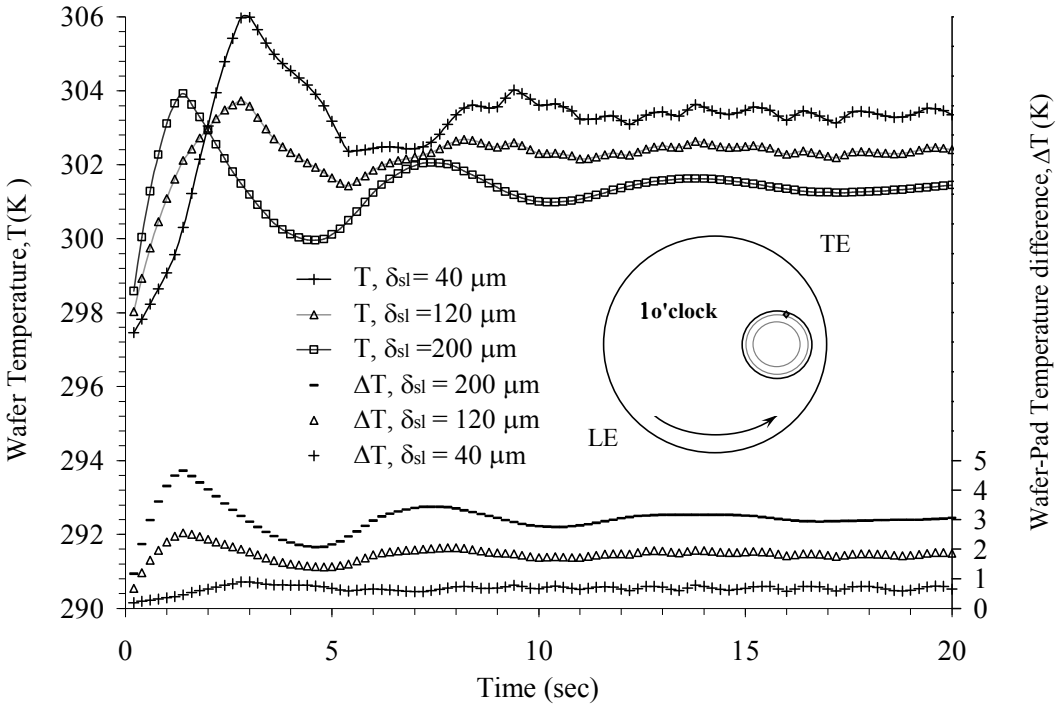

Figure 7.21 Transient wafer temperature distributions and wafer pad temperature differences for 3 different slurry film thicknesses at a radial location of r/r_w=7/8 along the 1 o'clock position.

Figure 7.22 shows the wafer heat transfer convection coefficients at a radial distance of r/r_w=7/8 along the 1 o'clock position for three different slurry film thicknesses. The average heat transfer convection coefficients of the substrate surfaces in

figure 7.22 attained were equal to 28.51, 24.19, and 20.02 W/m^{2}K for the abrasive film thicknesses (δ_{sl}) of 200, 120, and 40 μm respectively. The increment of volumetric flow rate increased the heat advection per unit area; therefore it removes more heat in less time. This effect reduces the overall temperature of the wafer and pad at the control volume under study. Present results are in agreement with the findings of Mudhivarthi [146] and Sikder et al. [148], where the increment of the film thickness reduced the mechanical contact, and increased the amount of slurry interaction, resulting in lower temperature profiles around the trailing area of the wafer region exposed to the abrasive–pad interface.

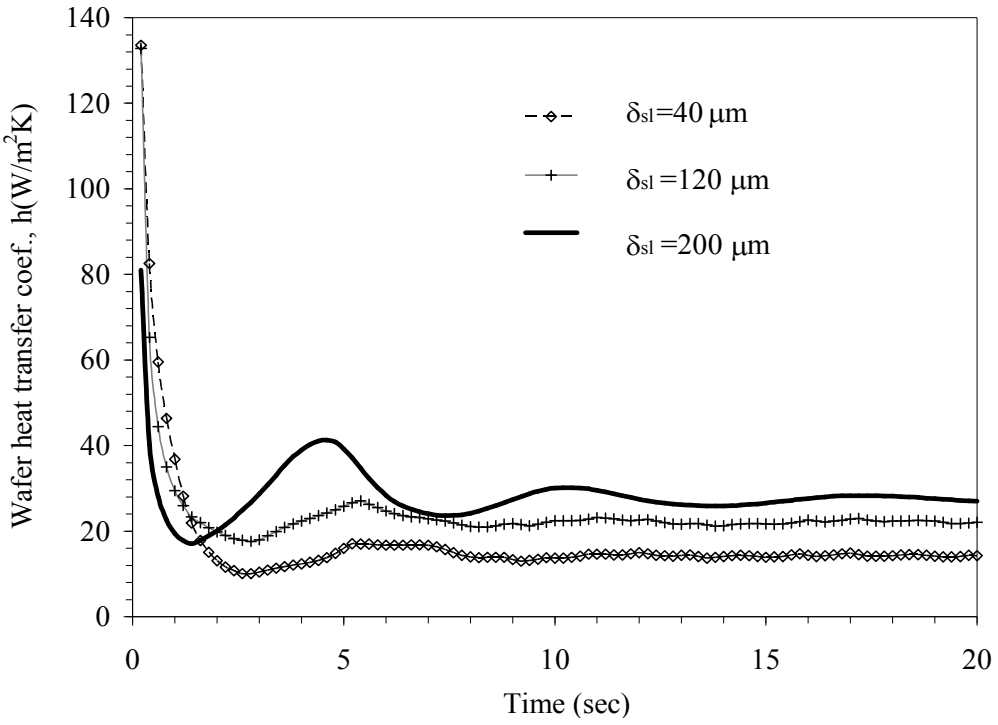

Figure 7.22 Transient wafer heat transfer convection coefficients for three different slurry film thicknesses at a radial location of r/r_w=7/8 along the 3 o'clock position.

The temperature contour distributions of the wafer and pad surfaces under two characteristic pad spinning rates of 175 and 250 RPM are shown in figures 7.23a and 7.23b.

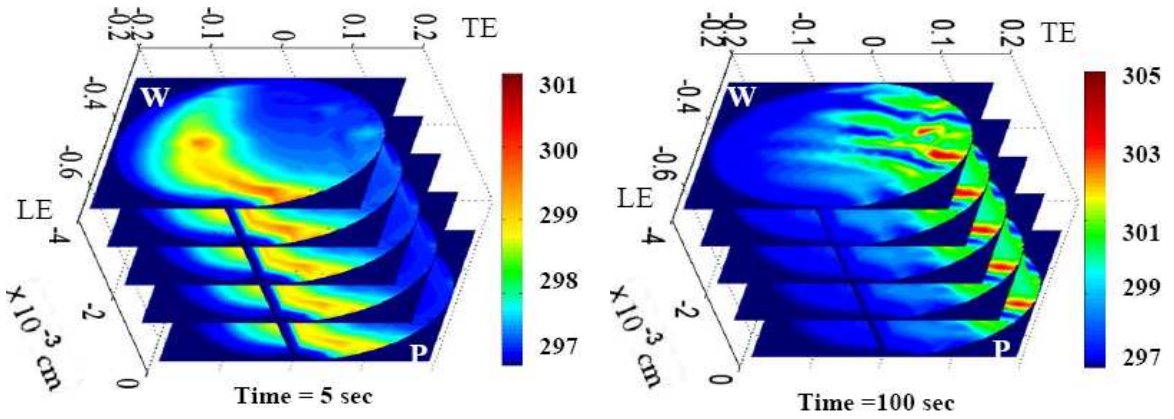

(a)

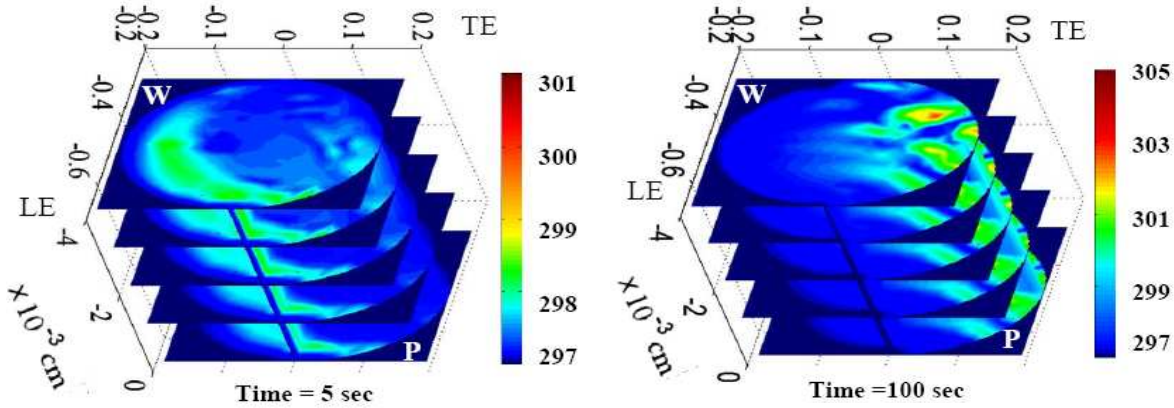

(b)

Figure 7.23 Wafer, and pad temperature contour distributions for a pad spinning rate equal to: (a) Ω_p=175 RPM and (b) Ω_p=250 RPM.

The transient temperature contour plots were set for an alumina abrasive film thickness of 40 μm, at a constant slurry flow rate of 50 cc/min, under a constant load of 24.35 kPa, for a variable heat flux range of 3.9 to 9.14 kW/m^2, and a carrier spinning rate of 30 RPM. During the early part of the transient process in figure 7.23a the slurry, wafer

and pad reached up to a temperature difference of 4 degrees at a small fraction of the lower region of the leading edge at the 6 to 9 o'clock positions. Later on, the transient temperature difference increases around 8 degrees at a small region along the 3 o'clock position for a time frame of 100 seconds, as shown in figure 7.23a. Figure 7.23b shows a temperature gradient of 1.5 degrees at the early part of the process at a small section of the lower region along the leading edge at the 6 to 9 o'clock positions. After a short period of 100 seconds the transient temperature gradient increases by 5.5 degrees at a small area of the wafer trailing edge around the 2 o'clock position.

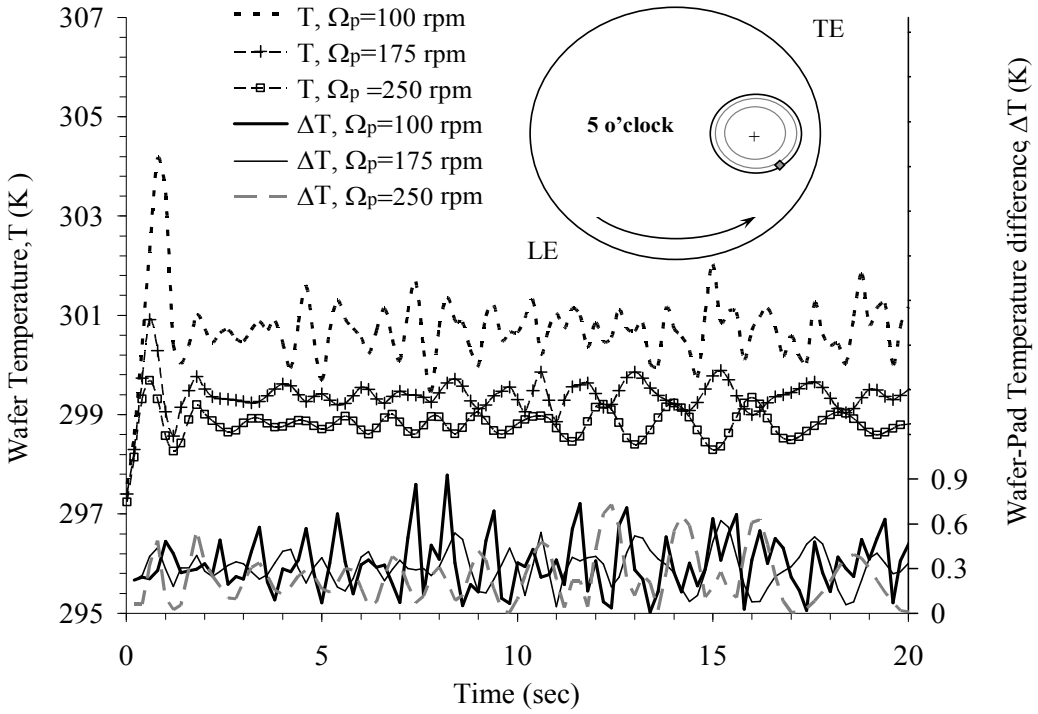

Figure 7.24 Transient wafer temperature distributions and wafer pad temperature differences for three different pad spinning rates at a radial location of r/r_w=7/8 along the 5 o'clock position.

Figure 7.24 shows the transient substrate temperature variations and wafer–pad temperature differences for three characteristic pad spinning rates at the 5 o'clock position, for the same conditions of previous temperature contour plots. The transient

average wafer temperature results of figure 7.24 under a pad spinning rate of (Ω_p=250 RPM) were found to be 2 degrees lower in general. An overall transient average wafer temperature difference of 3.62 degrees was attained under a pad spinning rate of 100 RPM versus a 1.65 degrees differential acquired under a pad spinning rate of 250 RPM. The wafer–pad temperature differences examined range up to 0.43 degrees K or C for the pad under a lower spinning rate and up to 0.27 degrees for the pad under a higher spinning rate at a dimensionless radial location of r/r_w=7/8. Additionally, it was found that the wafer–pad temperature differences for a pad spinning rate of 250 RPM were lower and more stable compared with a pad spinning rate of 100 RPM, as shown in figure 7.24.

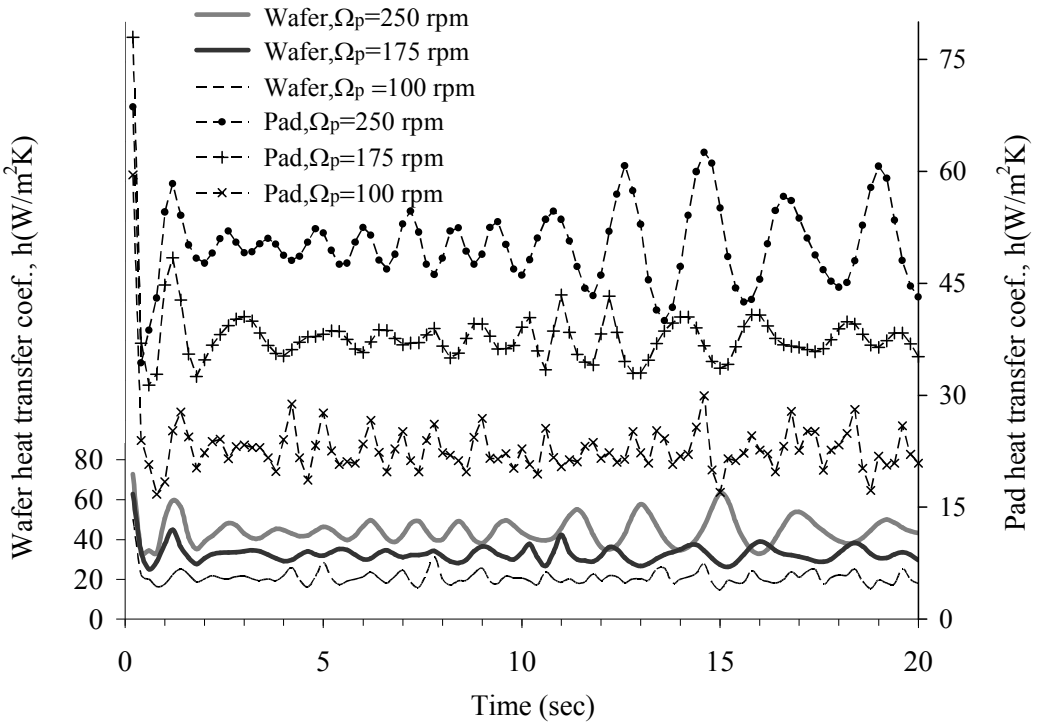

Figure 7.25 Transient wafer heat transfer convection coefficients for three different pad spinning rates at a radial location of r/r_w=7/8 along the 5 o'clock position.

Figure 7.25 show the wafer and pad heat transfer convection coefficients at a radial distance of $r/r_w=7/8$ along the 5 o'clock position. The average heat transfer convection coefficient of the pad in figure 7.25 under a pad spinning rate of 100, 175, and 250 RPM at the radial location under study along the 5 o'clock position were equal to 22.93, 37.91, and 50.19 W/m^2K respectively. The average heat transfer convection coefficients of the wafer under a pad spinning rate of 100, 175, and 250 RPM at a radial location of $r/r_w=7/8$ along the 5 o'clock position were equal to 20.91, 33.86, and 44.53 W/m^2K respectively, as shown in figure 7.25. The results of figure 7.25 showed the substantial enhancement of the heat transfer convection coefficients by the increment of the pad spinning rate up to 250 RPM. It was found that this effect could double the heat transfer removal rate and diminishes the temperature gradient of the pad and wafer surfaces between 2 to 4 degrees during the CMP process.

Present numerical results were compared with the transient experimental test data acquired of the pad temperature rise by Mudhivarthi [146]. The pad surface temperature rises during polishing experiments at different slurry flow rates, as shown in figure 7.26. It can be seen from that figure, that the amount of pad surface temperature decreases with increment of slurry flow rates. Figure 7.27 shows present numerical results of the transient pad temperature distribution at the leading edge along the 5 o'clock position for various slurry flow rates. A comparable trend of the actual pad temperature distributions can be seen in figure 7.27. The pad temperature rise under slurry flow rates of 30, 55, and 75 cc/min correlate with an average margin of 4.05%, 2.84%, and 4.03% respectively. Note that numerical predictions are within an average percentage off error of 3.65%. The numerical results reveal a better correlation at larger flow rates.

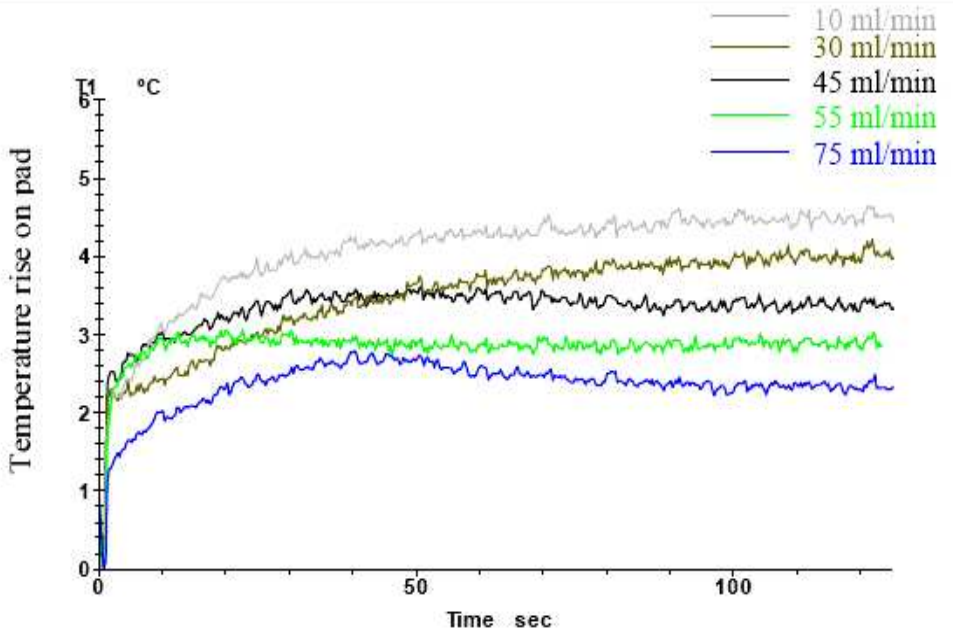

Figure 7.26 Experimental results of pad surface temperature rise during copper polish at different slurry flow rates from Mudhivarthi [146].

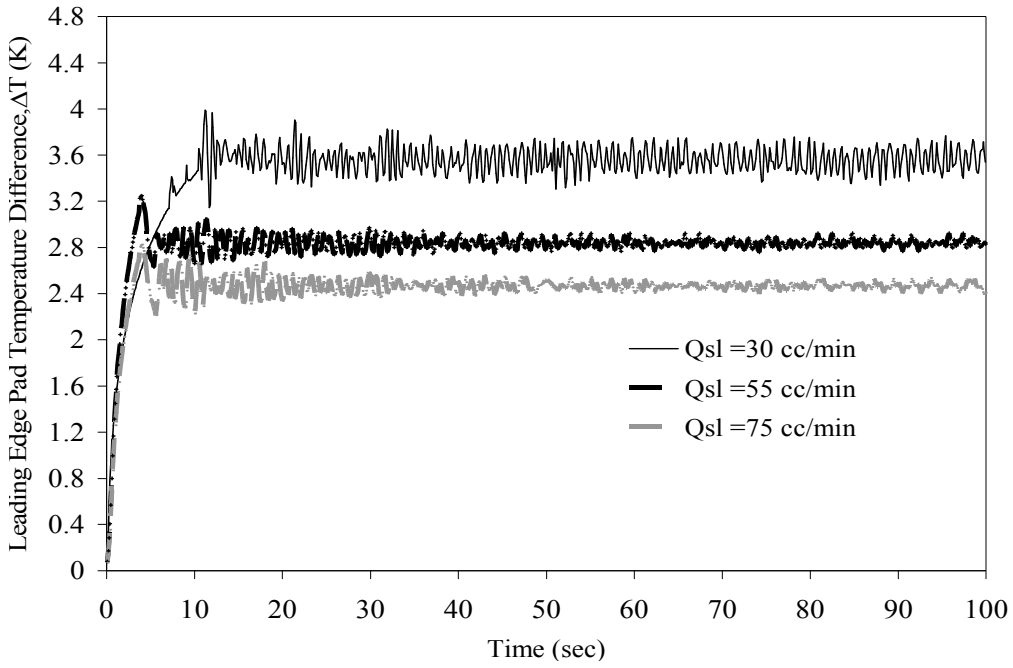

Figure 7.27 Present numerical results of pad temperature rise at the leading edge along the 5 o'clock position for three different slurry flow rates at (Ω_p=150 RPM, Ω_c=30 RPM, T_{sl}=297 K, COF=0.4, P=24.35 kPa, δ_{sl}=40 μm, r_w=1.9 cm, q_{sl}=4.6 to 10.8 kW/m^2).

The factor of working at the micrometer scale under the influence of two spinning surfaces about different axes of rotation, the complexity of flow under such type of boundary conditions, and the range of flow parameters may contribute to the discrepancy between experimental and numerical data. In addition, computational errors can be introduced because of round off and discretization of the mesh. Considering these factors, the overall comparison with test and numerical results of previous studies is satisfactory. The average heat transfer convection coefficients of pad and substrate surfaces from the present numerical simulation under the combination of different CMP parameters and input heat flux are listed in Table 7.2.

Table 7.2 Average substrate and pad heat transfer convection coefficients under different CMP parameters and variable input heat flux at specific radial locations along the surfaces.

Runs	Q_{sl} (cc/min)	Ω_p (RPM)	Ω_c (RPM)	δ_{sl} (μm)	r/r_w	loc. o'clock	P (kPa)	q_{sl} (kW/m^2)	COF μ_{fr}	h_{avp} (W/m^{2}K)	h_{avw} (W/m^{2}K)
1	30	150	30	40	7/8	3	24.35	4.6-10.8	0.4	26.82	25.48
2	75	150	30	40	7/8	3	24.35	4.6-10.8	0.4	29.19	26.87
3	30	150	30	40	7/8	5	24.35	4.6-10.8	0.4	22.28	20.85
4	75	150	30	40	7/8	5	24.35	4.6-10.8	0.4	23.97	21.82
5	85	200	30	40	1	12	17.24	4.14-9.6	0.4	24.75	17.62
6	85	200	30	40	1	12	41.37	10.4-23	0.4	17.85	19.26
7	85	200	30	40	7/8	12	17.24	4.14-9.6	0.4	40.58	21.30
8	85	200	30	40	7/8	12	41.37	10.4-23	0.4	37.75	26.18
9	85	200	30	40	2/3	12	17.24	4.14-9.6	0.4	50.86	32.14
10	85	200	30	40	2/3	12	41.37	10.4-23	0.4	48.39	42.75
11	60	145	15	40	1	12	34.48	6.2-15.3	0.4	19.47	18.19
12	60	145	75	40	1	12	34.48	6.2-15.3	0.4	27.77	24.32
13	60	145	15	40	7/8	3	34.48	6.2-15.3	0.4	31.36	30.41
14	60	145	75	40	7/8	3	34.48	6.2-15.3	0.4	40.24	37.53
15	65	150	40	40	7/8	1	28	5.3-12.3	0.4	39.08	20.02
16	65	150	40	120	7/8	1	28	5.3-12.3	0.4	46.76	24.19
17	65	150	40	200	7/8	1	28	5.3-12.3	0.4	55.32	28.51
18	50	100	30	40	7/8	5	24.35	3.9-9.1	0.5	22.93	20.91
19	50	175	30	40	7/8	5	24.35	3.9-9.1	0.295	37.91	33.86
20	50	250	30	40	7/8	5	24.35	3.9-9.1	0.215	50.19	44.53

Chapter 8 Conclusions and Recommendations

8.1 Free Liquid Jet Impingement

8.1.1 Steady State Cooling of Spinning Target

Local and average Nusselt number and heat transfer coefficient distributions showed a strong dependence on the impingement velocity or Reynolds number; as the velocity increases, the boundary layer or film thickness decreases and Nusselt number increases over the entire solid–fluid interface. In general, the rotational rate diminishes the dimensionless solid–fluid interface temperature and increases the local Nusselt number distribution. The average Nusselt number attained an almost constant value at $b/d_n \geq 0.50$ for all materials indicating that an optimum thickness design condition has been reached. This occurs due to maximum heat redistribution by conduction within the solid disk. All five solid materials showed higher maximum temperature values at smaller thickness to nozzle diameter ratio. A lower thermal conductivity material showed higher local maximum Nusselt number as well as higher average Nusselt number at all studied material thicknesses. On the other hand, plate materials with higher thermal conductivity maintained a more uniform temperature distribution through the solid–fluid interface and facilitated a faster heat transfer rate, lowering the maximum temperature inside the solid and at the interface. A lower dimensionless solid–fluid interface temperature distribution was achieved for a lower Prandtl number fluid. The correlation for average Nusselt number developed under this study may be useful for engineering design.

8.1.2 Transient Cooling of Spinning Target

A number of important conclusions can be derived from the present numerical results. The dimensionless interface temperature increases and Nusselt number decreases with the progression of the transient from the start–up of heating to the equilibrium steady state condition. The location of the maximum Nusselt number can be associated with the transition of the flow from the vertical impingement to horizontal displacement where the boundary layer starts to develop. A higher Reynolds number increases the magnitude of fluid velocity near the solid–fluid interface allowing a quicker dissipation of heat with higher flow rate and lower thermal boundary layer thickness. Consequently, the time required to reach the steady state decreases and Nusselt number increases with Reynolds number. In addition, the maximum temperature inside the solid decreases as the Reynolds number increases. In general, the rotational rate diminishes the dimensionless solid–fluid interface temperature as well as the time required to reach the steady state condition. The average Nusselt number is greater at larger spinning rate or lower Ekman number. As the Ekman number decreases from ∞ to $6.62\text{x}10^{-5}$ the average Nusselt number increases by an average of 20.81%. The increment of solid disk thickness creates more thermal resistance and provides a more uniform interface temperature due to radial heat spreading within the solid. A higher thickness decreases the dimensionless maximum temperature at the interface and within the solid and increases the time to reach the steady state condition. The average Nusselt number is higher for a thinner disk. The magnitude of the temperature non–uniformity and how effectively the heat flows and distributes within the material and at the interface is controlled by the thermal conductivity of the material. A lower thermal conductivity material such as Constantan

maintains a higher average heat transfer coefficient and a higher maximum temperature within the solid over the entire transient process. A disk material with higher thermal diffusivity reaches the steady state faster. The correlation for average Nusselt number during the transient process was developed as a function of Reynolds number, Ekman number, thermal conductivity ratio, and Fourier number. This correlation will be useful for engineering design.

8.2 Confined Liquid Jet Impingement

8.2.1 Steady State Cooling of Stationary Confined Wall with Spinning Target

The solid–fluid dimensionless interface temperature, the local Nusselt number and local heat transfer coefficient shows a strong dependence of the following parameters: Reynolds number, rotational rate, solid material properties, and fluid properties. Increasing the Reynolds number increases the local heat transfer coefficient distribution values over the entire solid–fluid interface. Simultaneously, this effect reduces the solid–fluid temperature and improves the cooling effectiveness of the process. In general, the rotational rate effect increases the local Nusselt number distribution values over the entire solid–fluid interface except for a disk under high spinning rate where the thermal boundary layer separates from the wall and generates an ineffective cooling. Plate materials with a higher thermal conductivity maintained a more uniform temperature distribution at the solid–fluid interface. Highest local Nusselt number occurred at the highest Prandtl number condition. Correlation for average Nusselt number under confined jet impingement cooling of a spinning disk is proposed in terms of Reynolds number, Ekman number, Prandtl number, nozzle–to–plate spacing ratio, and thermal conductivity ratio. The differences between numerical and predicted values are in the

range from –20.36% to +14.47%. The mean value of the error is 7.7%. The numerical results compared well with available experimental measurements.

8.2.2 Steady State Cooling of Spinning Confined Wall with Stationary Target

The solid–fluid dimensionless interface temperature and local Nusselt number showed a strong dependence on Reynolds number, rotational rate, disk thickness, impingement height, fluid properties, and solid material properties. The increment of Reynolds number increases the local heat transfer coefficient distribution values over the entire solid–fluid interface. In general, the rotational rate increases the local Nusselt number distribution values over the entire solid–fluid interface for Ek> 1.52×10^{-4}. A thicker disk provides a more uniform distribution of interface temperature and heat transfer coefficient. As the nozzle to target spacing increases from β=0.25 to 1, the heat transfer coefficient decreases. However, at higher spacing (β=2–5) a higher heat removal rate is obtained due to an optimal mix of the impinging jet flow with the rotationally induced flow. Higher Prandtl number fluids lead to a thinner thermal boundary layer, and therefore higher heat transfer coefficient at the interface. Plate materials with higher thermal conductivity maintained lower thermal resistance within the solid and therefore more uniform temperature distribution results at the interface. Correlation for average Nusselt number under spinning confined jet impingement cooling is proposed in terms of Reynolds number, Ekman number, disk thickness, nozzle to target spacing, and thermal conductivity ratio. The differences between numerical and predicted values are in the range from –13.8% to +15.3%. The mean value of the error is equal to 6.8%. The numerical results compared reasonably well with available analytical predictions and experimental measurements.

8.3 Partially–confined Liquid Jet Impingement

8.3.1 Steady State Cooling of Spinning Target

The solid–fluid dimensionless interface temperature and local Nusselt number showed a strong dependence on Reynolds number, rotational rate, disk thickness, nozzle to target spacing or impingement height, plate–to–disk confinement ratio, fluid properties, and solid material properties. The increment of Reynolds number increases the local heat transfer coefficient distribution over the entire solid–fluid interface. In general, rotation increases the local Nusselt number distribution values over the entire solid–fluid interface for $Ek > 7.08 \times 10^{-5}$. A higher disk thickness provides a more uniform distribution of interface temperature and heat transfer coefficient. As the nozzle to target distance increases from $\beta=0.25$ to 1, the existing fluid column between target and confinement diminishes the liquid jet momentum and therefore the heat removal rate. A decrease in plate to disk confinement ratio increases local Nusselt number at all locations in the disk. A higher Prandtl number fluid leads to a thinner thermal boundary layer and provides a more effective heat removal rate at the interface. Plate materials with higher thermal conductivity maintained lower thermal resistance within the solid and therefore a more uniform temperature distribution happens at the interface. A correlation for average Nusselt number under partially–confined liquid jet impingement over a spinning target is proposed in terms of Reynolds number, Ekman number, dimensionless nozzle to target spacing ratio, thermal conductivity ratio and confinement plate to disk radius ratio. The differences between numerical and predicted values are in the range from –15.13% to +15.61%. The mean value of the error is equal to 6.94%.

8.3.2 Steady State Cooling of Spinning Confined Wall and Target

The following conclusions could be made based on the numerical results of the present investigation.

1. The increment of Reynolds number contributes to a more effective cooling by increasing the local heat transfer coefficient over the entire solid–fluid interface.
2. For $Ek_{1,2} > 7.08 \times 10^{-5}$, a higher rotational speed enhances the local Nusselt number and generates lower temperature over the entire solid–fluid interface.
3. A higher disk thickness provides more uniform interface temperature and heat transfer coefficient.
4. Heat transfer coefficient increases as the nozzle to target distance decreases from β=1.0 to 0.2.
5. A reduction in plate–to–disk confinement ratio increases the local Nusselt number at all locations.
6. A higher Prandtl number fluid leads to a thinner thermal boundary layer and provides a more effective heat removal rate at the solid–fluid interface.
7. Plate materials with higher thermal conductivity maintain lower thermal resistance within the solid and therefore a more uniform temperature distribution is achieved at the solid–fluid interface.
8. A correlation for average Nusselt number is proposed in terms of Reynolds number, Ekman numbers (Ek_1, Ek_2), nozzle to target spacing ratio, thermal conductivity ratio and confinement plate to disk radius ratio. The percent differences between numerical and predicted values are in the range of –14.76%

to +13.08%. The mean deviation of the predicted average Nusselt correlation is equal to 6.37%.

9. The numerical results compared reasonably well with available experimental measurements.

8.3.3 Transient Cooling of Spinning Target

A number of important conclusions can be made based on the results of the present investigation. Local Nusselt number shows a higher value at early stages of the transient process due to smaller temperature difference between the liquid jet and disk solid–fluid interface. The increment of Reynolds number results in higher fluid velocity near the solid–fluid interface that enhances the convective heat transfer rate and reduces the solid–fluid interface temperature. Consequently, the duration of the transient heat transfer process and the maximum temperature inside the solid decreases as the Reynolds number increases. As the Ekman number decreases from ∞ to 7.08×10^{-5} the average Nusselt number increases by an average of 27.47%. As the nozzle to target spacing decreases from 1 to 0.25 the average Nusselt number increases by an average of 12.71%. The increment of confinement ratio (r_p/r_d) increases the frictional resistance from the confinement disk slowing down the fluid momentum and the convective heat transfer rate. The increment of disk thickness decreases the maximum temperature at the interface and within the solid and increases the time needed to achieve the steady state condition. A lower thermal conductivity material maintains a higher average heat transfer coefficient and maximum temperature within the solid over the entire transient process. A disk material with higher thermal diffusivity reduces the duration of the transient heat transfer process and reaches the steady state faster. The correlation for average Nusselt

number during the transient process was developed as a function of confinement ratio, thermal conductivity ratio, and dimensionless disk thickness, nozzle to target spacing, Ekman number, Reynolds number, and Fourier number. This correlation will be useful for engineering design.

8.4 Chemical Mechanical Polishing Model

8.4.1 Steady State and Transient Process

The steady state and transient three dimensional heat transfer model is developed and solved numerically to obtain the pad and wafer surfaces temperature distributions along the radial distance from the leading to trailing edge and specific locations of both surfaces as part of the transient model. The model results include steady state and transient local and average heat transfer convective coefficients of wafer and pad under the influences of various CMP parameters along both surfaces and specific locations.

1. The polishing interface temperatures of pad and substrate and local heat transfer coefficient are significantly affected by slurry flow rate, tribological aspects, and pad spinning rate at the interface.
2. The increment of slurry flow rates and the reduction of the friction coefficient results in lower pad and wafer surfaces temperature. In most cases the pad and wafer surface temperatures are the highest at the trailing edge of the wafer and decrease towards the leading edge.
3. The substrate and pad temperature distributions increase under a higher pressure load due to the increment of the heat flux generated per unit area.

4. The effect of adding more pressure to the CMP process produce larger temperature gradients at the wafer–pad interface as result of more contact to contact abrasion mode of the pad with slurry particles and substrate.
5. The backflow effects increased at lower pad spinning rates, allowing more flow recirculation of the slurry and increase the shear forces effect of slurry particles along the pad and wafer surfaces.
6. The increment of the pad spinning rate overcome the frictional and tensional forces of the slurry beneath the substrate and pad surfaces. The hotter slurry is driven out towards the end of the platen at a faster rate.
7. The increment of the slurry film thickness provides lower and more uniform interface temperatures and heat transfer coefficients across the leading to the trailing edge of the control volume under study.
8. The steady state results reveal that the temperature around the leading edge is about 2 to 3 ^{o}C lower than the inner section and up to 8.5 ^{o}C lower than the wafer trailing edge. The leading edge keeps its temperature close to the initial flow rate value because fresh, cool slurry enters beneath the polished wafer around its perimeter.
9. A lower heat transfer convection coefficient at a particular location indicates the presence of a hot spot or a higher temperature gradient between the incoming slurry at the pad or substrate surfaces under transient and steady state conditions.
10. The heat transfer convection coefficients are higher at the pad surface than the substrate surface, which is due to the lower thermal conductivity of the pad that

results in a lower temperature gradient between the incoming slurry and pad surface under transient and steady state conditions.

11. The transient results reveal that the temperature around the leading edge is about 2 to 3 ^{o}C lower than the inner section and up to 10 ^{o}C lower than the wafer trailing edge. The leading edge keeps its temperature close to the initial flow rate value because fresh, cool slurry enters beneath the polished wafer around its perimeter.
12. The minimum heat–transfer slurry–wafer interaction occurs close to the trailing edge area. Hot spots can be observed along the trailing edge and some inner regions where part of the slurry got trapped due to the emerging rotational flow patterns.
13. The influence of transient temperature of the process with the interaction of the chemical abrasive can be one of the reasons for non–uniformity within the wafer during the CMP process.
14. The results presented are critical to understanding how fluid dynamics affects the CMP process and can be used to improve the design of more thermal stable pads and therefore prolong the life of the pad.

8.5 Future Work and Recommendations

All the problems presented in this work have been done as (CFD) numerical models with prescribed boundary conditions to study the fluid flow and heat transfer phenomena of cooling systems with dimensions that range on the millimeter scale. The millimeter scale includes jet size, free surface height, and nozzle to target spacing of jets, surfaces confinement, and flow film thickness. The analysis presented shows interesting behaviors that can be explored with experiments that involve the design of more efficient

and economic cooling systems. Using the study parameters of this investigation for future reference it will be useful to correlate different fluids and multiple layer materials or coated films, such as polymers with variable properties, diamond coating, and polyurethane coatings. It will be useful to: implement computational studies of free, partially–confined and confined liquid jet impingement technique in specific cooling of electronic applications and compare with present results. The implementation of experiments will be ideal to strengthen and support most of the findings of this work.

In terms of the effect of temperature on the CMP process, this research demonstrates that the increase in removal rate during CMP is due to the increased rate of the dissolvable surface of copper oxides and hydroxides into the slurry. It is noted that the increase in temperature can be used as an index of surface quality. Experimental results demonstrate that scratch depth increased with increment of slurry and substrate surface temperatures. The temperature profiles of this study revealed that the non–uniformity in CMP is a function of a series of dynamic parameters, such as slurry film thickness, pad and carrier spinning rates, applied pressure, and slurry flow rate, which control the slurry flow patterns and recirculation beneath the substrate. The existence of three distinct regimes of temperature effects opens the door to further investigations. The three dimensional model of CMP under study has more room to improve. In a future study, it will be useful to explore parameters like substrate sizes or radii, inlet to outlet ratio, pad groove design, the eccentricity effect of pad to wafer distance, and the thermal properties effects of different slurries, pads and substrates. In addition, it will be useful to correlate temperature profiles and heat transfer convection coefficients to the index of Material Removal Rate (MRR) of substrate.

References

[1] Jairath, R., Desai, M., Stell, M., Tolles, R., and Scherber–Brewer, D., "Advanced Metallization for Devices and Circuits Science, Technology and Manufacturability", Murarka, S.P. Katz, A., Tu, K.N. and Maex, K., Editors, *Materials Research Society Proceedings Series*, Pittsburgh, PA, vol. 337, pp. 121, 1994.

[2] Kuide, Qin, 2003, "Multi–Scale Modeling of the Slurry Flow and the Material Removal in Chemical Mechanical Polishing", Ph.D. Dissertation, University of Florida, Gainesville, Florida.

[3] Glauert, M.B., "The Wall Jet", *Journal of Fluid Mechanics*, vol. 1, no. 6, pp. 625–643, 1956.

[4] Watson, E.J., "The Radial Spread of a Liquid Jet Over a Horizontal Plane", *Journal of Fluid Mechanics*, vol. 20, pp. 481–499, 1964.

[5] Chaudhury, Z.H., "Heat Transfer in a Radial Liquid Jet", *Journal of Fluid Mechanics,* vol. 20, no. 3, pp. 501–511, 1964.

[6] Scholtz, M.T., and Trass, O., "Mass Transfer in a Non–Uniform Impinging Jet: Part 1, Stagnation Flow Velocity and Pressure Distribution", *American Institute of Chemical Engineers Journal,* vol. 16, no. 1, pp. 82–90, 1970.

[7] Metzger, D.E., Cammings, K.N., and Ruby, W.A., "Effects of Prandtl Number on Heat Transfer Characteristics of Impinging Liquid Jets", *Proceedings of the 5th International Heat Transfer Conference*, Tokyo, vol. 2, pp. 20–24. 1974.

[8] Adachi, K., "Laminar Jets of a Plane Liquid Sheet Falling Vertically in the Atmosphere", *Journal of Non–Newtonian Fluid Mechanics*, vol. 24, pp. 11–30, 1987.

[9] Jiji, L.M. and Dagan, Z., "Experimental Investigation of Single Phase Multi–Jet Impingement Cooling of an Array of Microelectronic Heat Sources", *Proceedings of the International Symposium on Cooling Technology for Electronic Equipment*, Pacific Institute for Thermal Engineering, HI, pp. 265–283, 1987.

[10] Liu, X., and Lienhard, J.H., "Liquid Jet Impingement Heat Transfer on a Uniform Flux Surface", *Heat Transfer Phenomena in Radiation, Combustions and Fires, ASME HTD*, vol. 6, pp. 523–530, 1989.

[11] Polat, S., Huang, B., Mujumdar, A.S. and Douglas, W.J.M., "Numerical Flow and Heat Transfer under Impinging Jets: A review", *Annual Review Numerical Fluid Mechanics and Heat Transfer*, vol. 2, pp. 157–197, 1989.

[12] Wang, X.S., Dagan, Z., and Jiji, L.M., "Heat Transfer between a Circular Free Impinging Jet and a Solid Surface with Non–Uniform Wall Temperature or Wall Heat Flux–1, Solution for the Stagnation Region", *International Journal of Heat and Mass Transfer*, vol. 32, no. 7, pp. 1351–1360, 1989.

[13] Wang, X.S., Dagan, Z., and Jiji, L.M., "Heat Transfer between a Circular Free Impinging Jet and a Solid Surface with Non–Uniform Wall Temperature or Wall Heat Flux–2, Solution for the Boundary Layer Region", *International Journal of Heat and Mass Transfer*, vol. 32, no. 7, pp. 1361–1371, 1989.

[14] Wolf, D.H., Viskanta, R., and Incropera, F.P., "Local Convective Heat Transfer from a Heated Surface to a Planar Jet of Water with Non–Uniform Velocity Profile", *Journal of Heat Transfer*, vol. 112, pp. 899–905, 1990.

[15] Vader, D.T., Incropera, F.P., and Viskanta, R., "Local Convective Heat Transfer from a Heated Surface to an Impinging Planar Jet of Water", *International Journal of Heat and Mass Transfer*, vol. 34, no. 3, pp. 611–632, 1991.

[16] Stevens, J., and Webb, B.W., "Local Heat Transfer Coefficients under an Axis–symmetric, Single–Phase Liquid Jet", *Journal of Heat Transfer*, vol. 113, pp. 71–78, 1991.

[17] Liu, X., Lienhard, J.H., and Lombara, J.S., "Convective Heat Transfer by Impingement of Circular Liquid Jets", *Journal of Heat Transfer*, vol. 13, pp. 571–582, 1991.

[18] Womac, D.J., Ramadhyani, S., and Incropera, F.P., "Correlating Equations for Impingement Cooling of Small Heat Sources with Single Circular Liquid Jets", *Journal of Heat Transfer*, vol. 115, no. 1, pp. 106–115, 1993.

[19] Leland, J.E., and Pais, M.R., "Free Jet Impingement Heat Transfer of a High Prandtl Fluid under Conditions of Highly Varying Properties", *Journal of Heat Transfer*, vol. 121, pp. 592–597, 1999.

[20] Rahman, M.M., Bula–Silvera, A.J., and Leland, J.E., "Conjugate Heat Transfer During Free Jet Impingement of a High Prandtl Number Fluid", *Numerical Heat Transfer*, *Part B*, vol. 36, no. 2, pp. 139–162, 1999.

[21] Chattopadhyay, H., and Saha, S.K., "Numerical Investigations of Heat Transfer Over a Moving Surface due to Impinging Knife Jets" , *Numerical Heat Transfer*, *Part A*, vol. 39, no. 5, pp. 531–549, 2001.

[22] Roy, S., Nasr, K., Patel, P., and AbdulNour, B., "Rectangular Jet Impingement Heat Transfer on a Vehicle Windshield", *Journal of Thermophysics and Heat Transfer*, vol. 16, no. 1, pp. 154–157, 2002.

[23] Chan, T.L., Leung, C.W., Jambunathan, K., Ashforth–Frost, S., Zhou, Y., and Liu, M.H., "Heat Transfer Characteristics of a Slot Jet Impinging on a Semi–Circular Convex Surface", *International Journal of Heat and Mass Transfer*, vol. 45, no. 5, pp. 993–1006, 2002.

[24] Aldabbagh, L.B.Y., and Sezai, I., "Numerical Simulation of Three Dimensional Laminar, Square Twin–Jet Impingement on a Flat Plate, Flow Structure", and *Heat Transfer, Numerical Heat Transfer*, *Part A*, vol. 41, no. 8, pp. 835–850, 2002.

[25] Chatterjee, A., Dhingra, S.C., and Kapur, S.S., Laminar Impinging Jet Heat Transfer with a Purely Viscous Inelastic Fluid, *Numerical Heat Transfer, Part A*, vol. 42, no. 1–2, pp. 193–213, 2002.

[26] Yilbas, B.S., Shuja, S.Z., and Budair, M.O., "Jet Impingement onto a Hole with Constant Wall Temperature", *Numerical Heat Transfer*, *Part A*, vol. 43, no. 8, pp. 843–865, 2003.

[27] Tong, A.Y., "A Numerical Study on the Hydrodynamics and Heat Transfer of a Circular Liquid Jet Impinging onto a Substrate", *Numerical Heat Transfer*, *Part A*, vol. 44, no. 1, pp. 1–19, 2003.

[28] Silverman, I., and Nagler, A., "High Heat Flux Cooling with Water Jet Impingement", *Proceedings ASME Heat Transfer/Fluids Engineering Summer Conference*, Charlotte, North Carolina, vol. 1, pp. 277–288, 2004.

[29] Sezai, I., and Aldabbagh, L.B.Y., "Three Dimensional Numerical Investigation of Flow and Heat Transfer, Characteristics of Inline Jet arrays", *Numerical Heat Transfer*, *Part A*, vol. 45, no. 3, pp. 271–288, 2004.

[30] Yang, Y.T., and Hwang, C.H., "Numerical Simulations on the Hydrodynamics of a Turbulent Slot Jet Impinging on a Semi–Cylindrical Convex Surface", *Numerical Heat Transfer*, *Part A*, vol. 46, no. 10, pp. 995–1008, 2004.

[31] Batchelor, G. K., "Note on the Class of Solutions of Navier–Stokes Equations Representing Steady Rotationally–symmetric Flow", *Q.J. Mechanical Applied Mathematics*, vol. 4, pp. 29–41, 1951.

[32] Kreith, F., Taylor, J.H., and Chong, J. P., "Heat and Mass Transfer from a Rotating Disk", *Journal of Heat Transfer*, vol. 81, pp. 95–104, 1959.

[33] Metzger, D.E., and Grochowsky, L.D., "Heat Transfer Between as Impinging Jet and a Rotating Disk", *Journal of Heat Transfer*, vol. 99, pp. 663–667, 1977.

[34] and Deffenbaugh, D.M., "Heat Transfer from a Rotating Disk with Liquid Jet Impingement", *6th International Heat Transfer Conference*, Toronto, Ontario, Hemisphere Public Corp, Washington, DC, vol. 4, pp. 113–118, 1978.

[35] Carper, H.J. Jr., Saavedra, J.J., and Suwanprateep, T., "Liquid Jet Impingement Cooling of a Rotating Disk", *Journal of Heat Transfer,* vol. 108, pp. 540–546, 1986.

[36] Popiel, C.O., and Boguslawski, L., "Local Heat Transfer from a Rotating Disk in an Impinging Round Jet", *Journal of Heat Transfer*, vol.108, pp.357–364, 1986.

[37] Metzger, D.E., Bunker, R.S., and Bosch, G., "Transient Liquid Crystal Measurements of Local Heat Transfer on a Rotating Disk with Jet Impingement", *Journal of Turbomachinery,* vol. 113, no. 1, pp. 52–59, 1991.

[38] Brodersen, S., Metzger, D.E., and Fernando, H.J.S., "Flows Generated by the Impingement of a Jet on a Rotating Surface, Part 1: Basic Flow Patterns", *Journal of Fluids Engineering,* vol. 118, pp. 61–67, 1996.

[39] Saniei, N., Yan, X.T., and Schooley, W., "Local Heat Transfer Characteristics of a Rotating Disk Under Jet Impingement Cooling", *Proceedings 11th International Heat Transfer Conference,* editor Lee, J.S., Korean Society of Mechanical Engineers, Kyongju, Korea, vol. 5, pp. 445–450, 1998.

[40] Saniei, N., and Yan, X.T., "Experimental Study of Heat Transfer from a Disk Rotating in an Infinite Environment Including Heat Transfer Enhancement by Jet Impingement Cooling", *Journal of Enhanced Heat Transfer*, vol. 7, no. 4, pp. 231–245, 2000.

[41] Hung, Y.H., and Shieh, Y.R., "Convective Heat Transfer from a Rotating Ceramic–Based Multichip Disk with Round Jet Impingement", *Proceedings National Heat Transfer Conference*, Anaheim, California, vol. 1, pp. 97–103, 2001.

[42] Kang, H.S., and Yoo, J.Y., "Turbulence Characteristics of the Three Dimensional Boundary Layer on a Rotating Disk with Jet Impingement", *Experiments in Fluids*, vol. 33, no. 2, pp. 270–280, 2002.

[43] Shevchuk, I.V., Saniei, N., and Yan, X.T., "Impingement Heat Transfer over a Rotating Disk: Integral Method", *Journal of Thermophysics and Heat Transfer*, vol. 17, no. 2, pp. 291–293, 2003.

[44] Ozar, B., Cetegen, B.M., and Faghri, A., "Experiments on the Flow of a Thin Liquid Film Over a Horizontal Stationary and Rotating Disk Surface", *Experiments in Fluids,* vol. 34, pp. 556–565, 2003.

[45] Ozar, B., Cetegen, B.M., and Faghri, A., "Experiments on Heat Transfer in a Thin Liquid Film Flowing over a Rotating Disk", *Journal of Heat Transfer,* vol. 126, no. 2, pp. 184–192, 2004.

[46] Rice, J., Faghri, A., and Cetegen, B.M., "Analysis of a Free Surface Film From a Controlled Liquid Impinging Jet Over a Rotating Disk Including Conjugate Effects with and without Evaporation", *International Journal of Heat and Mass Transfer,* vol. 48, no. 25–26, pp. 5192–5204, 2005.

[47] Iacovides, H., Kounadis, D., Launder, B.E., Li, J., and Xu, Z., "Experimental Study of the Flow and Thermal Development of a Row Cooling Jets Impinging on a Rotating Concave Surface", *Journal of Turbomachinery*, vol. 127, no. 1, pp. 222–229, 2005.

[48] Basu, S, and Cetegen, B M, "Analysis of Hydrodynamics and Heat Transfer in a Thin Liquid Film Flowing Over a Rotating Disk by the Integral Method", *Journal of Heat Transfer*, vol. 128, no. 3, pp. 217–225, 2006.

[49] Rahman, M.M., and Lallave, J.C., "A Comprehensive Study of Conjugate Heat Transfer During Free Liquid Jet Impingement on a Rotating Disk", *Numerical Heat Transfer*, *Part A*, vol. 51, no. 11, pp. 1041–1064, 2007.

[50] Moallemi, M.K., and Naraghi, M.N., "An Experimental and Analytical Investigation of Ice Formation from a Circular Water Jet Impinging on a Horizontal Cold Surface", *Journal of Heat Transfer,* vol. 116, no. 4, pp. 1016–1027, 1994.

[51] Van Treuren, K.W., Wang, Z., Ireland, P.T., and Jones, T.V., "Detailed Measurements of Local Heat Transfer Coefficient and Adiabatic Wall Temperature beneath an Array of Impinging Jets", *Journal of Turbomachinery*, vol. 116, no. 3, pp. 369–374, 1994.

[52] Owens, R., and Liburdy, J.A., "Use of Thermochromatic Liquid Crystals in the Study of Jet Impingement Cooling: Sensitivity of Transient Heating Methods", *Proceedings of SPIE*, The International Society of Optical Engineering, Bellingham, WA, USA, pp. 136–144, 1995.

[53] Kumagai, S., Suzuki, S., Kubo, R., and Kawazoe, M., "Transient Cooling of a Hot Metal Plate with an Impinging Water Jet", *Heat Transfer Japanese Research*, vol. 24, no. 6, pp. 538–550, 1995.

[54] Lachefski, H., Cziesla, T., Biswas, G., and Mitra, K., "Numerical Investigation of Heat Transfer by Rows of Rectangular Impinging Jets", *Numerical Heat Transfer, Part A*, vol. 30, no. 1, pp. 87–101, 1996.

[55] Sazhin, S.S., Sazhina, E.M., Faltsi–Saravelou, O., Wild, P., Francis, N.D., and Wepfer, W.J., "Jet Impingement Drying of a Moist Porous Solid", *International Journal of Heat and Mass Transfer*, vol. 39, no. 9, pp. 1911–1923, 1996.

[56] Fujimoto, H., Takuda, H., Hatta, N., and Viskanta, R., "Numerical Simulation of Transient Cooling of a Hot Solid by an Impinging Free Surface Jet", *Numerical Heat Transfer, Part A,* vol. 36, no. 8, pp. 767–780, 1999.

[57] Rahman, M.M., Bula–Silvera, A.J., and Leland, J.E., "Analysis of Transient Conjugate Heat Transfer to a Free Impinging Jet", *Journal of Thermophysics and Heat Transfer,* vol. 14, no. 3, pp. 1–10, 2000.

[58] Rahman, M.M., Bula–Silvera, A.J., and Leland, J.E., "Numerical Modeling of Conjugate Heat Transfer During Impingement of Free Liquid Jet Issuing a from a Slot Nozzle", *Numerical Heat Transfer, Part A,* vol. 38, no. 1, pp. 45–66, 2000.

[59] Liu, L.K., Su, W.S., and Hung, "Transient Convective Heat Transfer of Air Jet Impinging Onto a Confined Ceramic–based MCM Disk", *Journal of Electronic Packaging*, vol. 126, no. 1, pp. 159–172, 2004.

[60] Sarghini, F., and Ruocco, G., "Enhancement and Reversal Heat Transfer by Competing Modes in Jet Impingement", *International Journal of Heat and Mass Transfer*, vol. 47, no. 8–9, pp. 1711–1718, 2004.

[61] Fang, C.J., Wu, M.C., Kuo, Y.M., Lee, C.Y., Peng, C.H., and Hung, Y.H., "Heat Transfer Behavior for a Stationary or Rotating MCM Disk With an Unconfined Round Jet Impingement", *Journal of Electronic Packaging*, vol. 129, no. 4, pp. 400–410, 2007.

[62] McMurray, D.C., Myers, P.S., and Uyehara, O.A., "Influence of Impinging Jet Variables on Local Heat Transfer Coefficients Along a Flat Surface with Constant Heat Flux", *Proceedings of the 3rd International. Heat Transfer Conference*, Chicago, IL, vol. 2, pp. 292–299, 1966.

[63] Korger, M. and Krizek, F., "Mass Transfer Coefficient in Impingement Flow from Slotted Nozzles", *International Journal of Heat and Mass Transfer*, vol. 9, pp. 338–344, 1966.

[64] Kumada, M., and Mabuchi, I., "Studies on the Heat Transfer of Impinging Jets", *Bulletin of JSME*, vol. 13, no. 55, pp. 77–85, 1970.

[65] Miyazaki, H., and Silberman, E., "Flow and Heat Transfer on a Flat Plate Normal to a Two Dimensional Laminar Jet Issuing from a Nozzle of Finite Height", *International Journal of Heat and Mass Transfer*, vol. 15, pp. 2097–2107, 1972.

[66] Sparrow, E.M., and Wong, T.C., "Impingement Transfer Coefficients due to Initially Laminar Slot Jets", *International Journal of Heat and Mass Transfer*, vol. 18, pp. 597–605, 1975.

[67] Saad, N.R., Douglas, J.M., and Mujumdar, A.S., "Prediction of Heat Transfer under an Axis–symmetric Laminar Impinging Jet", *Industrial and Engineering Chemistry Fundamental*, vol. 16, pp. 148–154, 1977.

[68] Nakoryakov, V.E., Pokusaev, B.G., and Troyan, E.N., "Impingement of an Axis–symmetric Liquid Jet on a Barrier", *International Journal of Heat and Mass Transfer,* vol. 21, no. 9, pp. 1175–1184, 1978.

[69] Ma, C.F., Sun, H., Auracher, H., and Gomi, T., "Local Convective Heat Transfer from Vertical Heated Surfaces to Impinging Circular Jets of Large Pr Number Liquids", *Proceedings of the 9th International Heat Transfer Conference,* Hemisphere, Jerusalem, Israel, vol. 2, pp. 441–446, 1990.

[70] Polat, S., Huang, B., Mujumdar, A.S. and Douglas, W.J.M., "Impingement Heat Transfer under a Confined Slot Jet Part 1: Effect of Surface through Flow", *The Canadian Journal of Chemical Engineering*, vol. 69, pp. 266–273, 1991.

[71] Polat, S., Huang, B., Mujumdar, A.S. and Douglas, W.J.M., "Impingement Heat Transfer under a Confined Slot Jet Part 2: Effect of Surface Motion and Through Flow", *The Canadian Journal of Chemical Engineering*, vol. 69, pp. 274–280, 1991.

[72] Moreno, O.A., Katyl, R.H., Jones, J.D., and Moschak, P.A., "Mass Transfer of an Impinging Jet Confined between Parallel Plates", *International Journal of Research and Development*, vol. 37, no. 2, pp. 143–154, 1993.

[73] Chang, C. T., Kocamustafaogullari, G., Landis, F. and Downing, S., "Single and Multiple Liquid Jet Impingement Heat Transfer", *Heat Transfer in Turbulent Flows, ASME HTD*, vol. 246, pp. 43–52, 1993.

[74] Hung, Y.H., and Lin, Z.H., "Effect of Confinement Plate on Heat Transfer Characteristics of a Circular Jet Impingement", *Proceedings of the Fundamentals of Heat Transfer in Forced Convection, ASME HTD,* vol. 285, pp. 101–109, 1994.

[75] Garimella, S.V., and Rice, R., "Confined and Submerged Liquid Jet Impingement Heat Transfer", *Journal of Heat Transfer,* vol. 117, no. 4, pp. 871–877, 1995.

[76] Webb, B.W., and Ma, C.F., "Single Phase Liquid Jet Impingement Heat Transfer", *Advances in Heat Transfer*, vol. 26, pp. 105–117, 1995.

[77] Garimella, S.V., and Nenaydykh, B., "Nozzle–Geometry Effects in Liquid Jet Impingement Heat Transfer", *International Journal of Heat and Mass Transfer,* vol. 39, no. 14, pp. 2915–2923, 1996.

[78] Fitzgerald, J.A. and Garimella, S.V., "Flow Field Effects on Heat Transfer in Confined Jet Impingement", *Journal of Heat Transfer*, vol. 119, pp. 630–632, 1997.

[79] Fitzgerald, J.A., and Garimella, S.V., "A Study of the Flow Field of a Confined and Submerged Impinging Jet", *International Journal of Heat and Mass Transfer,* vol. 41, no. 8–9, pp.1025–1034, 1998.

[80] Li, De–Yu., Guo, Z.Y., and Ma, C.F., "Relationship between the Recovery Factor and the Viscous Dissipation in a Confined, Impinging, Circular Jet of High–Prandtl Number Liquid", *International Journal of Heat and Fluid Flow,* vol. 18, no. 6, pp. 585–590, 1997.

[81] Ma, C.F., Zheng, Q., Lee, S.C., and Gomi, T., "Impingement Heat Transfer and Recovery Effect with Submerged Jets of Large Prandtl Number Liquid 2. Initially Laminar Confined Slot Jets", *International Journal of Heat and Mass Transfer,* vol. 40, no. 6, pp. 1491–1500, 1997.

[82] Abou–Ziyan, A.B., and Hassan, F., "Effect of Jet Characteristics on Heat Transfer by Impingement of Submerged Confined Water Jets", *ASME HTD*, vol. 361, no. 1, pp. 211–218, 1998.

[83] Morris G.K., and Garimella, S.V., "Orifice and Impingement Flow Fields in Confined Jet Impingement", *Journal of Electronic Packaging,* vol. 120, no. 1, pp. 68–72, 1998.

[84] Tzeng, P.Y., Soong, C.Y., and Hsieh, C.D., "Numerical Investigation of Heat Transfer Under Confined Impinging Turbulent Slot Jets", *Numerical Heat Transfer*, *Part A*, vol. 35, no. 8, pp. 903–924, 1999.

[85] Chatterjee, A., and Deviprasath, L.J., "Heat Transfer in Confined Laminar Axis–symmetric Impinging Jets at Small Nozzle–plate Distances: The Role of Upstream Vorticity Diffusion", *Numerical Heat Transfer*, *Part A*, vol. 39, no. 8, pp. 777–800, 2001.

[86] Li, C.Y., and Garimella, S.V., "Prandtl–number Effects and Generalized Correlations for Confined and Submerged Jet Impingement", *International Journal of Heat and Mass Transfer,* vol. 44, no. 18, pp. 3471–3480, 2001.

[87] Rahman, M.M., Dontaraju, P., and Ponnappan, R., "Confined Jet Impingement Thermal Management using Liquid Ammonia as the Working Fluid", *Proceedings of International Mechanical Engineering Congress and Exposition,* ASME, New Orleans, Louisiana, pp. 1–10, 2002.

[88] Ichimiya, K., and Yamada, Y., "Three Dimensional Heat Transfer of a Confined Circular Impinging Jet with Buoyancy Effects", *Journal of Heat Transfer,* vol. 125, no. 2, pp. 250–256, 2003.

[89] Sahoo, D., and Sharif, M.A.R., "Mixed Convective Cooling of an Isothermal Hot Surface by Confined Slot Jet Impingement", *Numerical Heat Transfer*, *Part A*, vol. 45, no. 9, pp. 887–909, 2004.

[90] Qing–Guang, C., Zhong, X., Yu–Lin, W., and Yong–Jian, Z., "Numerical Simulation of Laminar Square Impinging Jet Flows", *Journal of Hydrodynamics*, *Series B*, vol. 17, no. 3, pp. 269–274, 2005.

[91] El–Gabry, L.A., and Kaminski, D.A., "Experimental Investigation of Local Heat Transfer Distribution on Smooth and Roughened Surfaces under an Array of Angled Impinging Jets", *Journal of Turbomachinery*, vol. 172, no. 3, pp. 532–544, 2005.

[92] Salamah, S.A., and Kaminski, D.A., "Modeling of Turbulent Heat Transfer from an Array of Submerged Jets Impinging on a Solid Surface", *Numerical Heat Transfer*, *Part A*, vol. 48, no. 4, pp. 315–337, 2005.

[93] Rahman, M.M., and Mukka, S. K., "Confined Liquid Jet Impingement on a Plate with Discrete Heating Elements", *Proceedings of the ASME Summer Heat Transfer Conference,* San Francisco, CA, vol. 4, pp. 637–647, 2005.

[94] Lin, T.W., Wu, M.C., Liu, L.K., Fang, C.J., and Hung, Y.H., "Cooling Performance of Using a Confined Slot Jet onto Heated Heat Sinks", *Journal of Electronic Packaging*, vol. 128, no. 1, pp. 82–91, 2006.

[95] Thomas, S., Faghri, A., and Hankey, W.L., "Experimental Analysis and Flow Visualization of a Thin Liquid Film on a Stationary and Rotating Disk", *Journal of Fluids Engineering*, vol. 113, no. 1, pp. 73–80, 1991.

[96] Rahman, M.M., and Faghri, A., "Numerical Simulation of Fluid Flow and Heat Transfer in a Thin Liquid Film over a Rotating Disk", *International Journal of Heat and Mass Transfer,* vol. 35, no. 6, pp. 1441–1453, 1992.

[97] Al–Sanea, S., "Numerical Study of the Flow and Heat Transfer Characteristics of an Impinging Laminar Slot Jet Including Crossflow Effects", *International Journal of Heat and Mass Transfer,* vol. 35, no. 10, pp. 2501–2513, 1992.

[98] Rahman, M.M., and Faghri, A., "Analysis of Heating and Evaporation from a Liquid Film Adjacent to a Horizontal Rotating Disk", *International Journal of Heat and Mass Transfer,* vol. 35, no. 10, pp. 2655–2664, 1992.

[99] Faghri, A., Thomas, S., and Rahman, M.M., "Conjugate Heat Transfer from a Heated Disk to a Thin Liquid Film formed by a Controlled Impinging Jet", *Journal of Heat Transfer*, vol. 115, no. 1, pp. 116–123, 1993.

[100] Rahman, M.M., "Analysis of Simultaneous Gas Absorption and Chemical Reaction to a Thin Liquid Film over a Spinning Disk", *International Communications in Heat and Mass Transfer,* vol. 27, no. 3, pp. 303–314, 2000.

[101] Shi, Y.L., Ray, M.B., and Mujumdar, A.S., "Effects of Prandtl Number on Impinging Jet Heat Transfer Under a Semi–Confined Laminar Slot Jet", *International Communications in Heat and Mass Transfer,* vol. 30, no. 4, pp. 455–464, 2003.

[102] Dano, B., Liburdy, J.A., and Kanokjaruvijit, K., "Flow Characteristics and Heat Transfer Performances of a Semi–Confined Impinging Array of Jets: Effect of Nozzle Geometry", *International Journal of Heat and Mass Transfer,* vol. 48, no. 3–4, pp. 691–701, 2005.

[103] Lallave, J.C., and Rahman, M.M., "Modeling of Convective Cooling of a Rotating Disk by Partially–Confined Liquid Jet Impingement", *Journal of Heat Transfer*, vol. 130, no. 10, pp. 102201–102211, 2008.

[104] Steigerwald, J.M., Murarka, S.P., and Guttmann, R.J., *Chemical Mechanical Planarization of Microelectronic Materials*, John Wiley and Sons, New York, 1997.

[105] Fu, G., and Chandra, A., "A Model for Wafer Scale Variation of Material Removal Rate in CMP", *Journal of Electronic Materials*, vol. 31, no. 10, pp. 1066–1073, 2002.

[106] Su, Y.T., **"**Investigation of Removal Rate Properties of a Floating Polishing Process", *Journal of the Electrochemical Society*, vol. 147, no. 6, pp. 2290–2296, 2000.

[107] Zhou, C., Shan, L., Roberts, J., Ng, S.H., and Danyluk, S., "Fluid Pressure and its Effects on Chemical Mechanical Polishing", *Wear*, vol. 253, no. 3–4, pp. 430–437, 2002.

[108] Luo, J. and Dornfeld, D.A., "Material Removal Mechanism in Chemical Mechanical Polishing: Theory and Modeling", *Semiconductor Manufacturing, IEEE Transactions***,** vol. 14, no. 2, pp. 112–133, 2001.

[109] Burthon, R.A., "Effects of Two Dimensional, Sinusoidal Roughness on the Load Support Characteristics of a Lubricant Film", *Journal of Basic Engineering*, vol. 85, pp. 258–264, 1963.

[110] Salant, R.F. "Numerical Analysis of the Flow Field within Lip Seals containing Micro Undulations", *Journal of Tribology*, vol. 114, pp. 485–492, 1992.

[111] Tzeng , S.T., and Saibel, E., "Surface Roughness Effect on Slider Bearing Lubrication", *ASLE Transactions*, vol. 10, pp. 334–338, 1967.

[112] Christensen, H., "Stochastic Models for Hydrodynamic Lubrication of Rough Surfaces", *Proceedings of the Institution of Mechanical Engineers*, vol. 184, no. 1, pp. 1013–1022, 1970.

[113] Christensen H., and Tonder, K., "The Hydrodynamic Lubrication of Rough Bearing Surfaces of Finite Width", *Journal of Lubrication Technology*, vol. 93, pp. 324–330, 1971.

[114] Christensen H., and Tonder, K., "Waviness and Roughness in Hydrodynamic Lubrication", *Proceedings of the Institution of Mechanical Engineers*, vol. 186, no. 72, pp. 807–812, 1972.

[115] Christensen H., "A Theory of Mixed Lubrication", *Proceedings of the Institution of Mechanical Engineers*, vol. 186, no. 41, pp. 421–430, 1972.

[116] Elrod, H.G., "A General Theory for Laminar Lubrication with Reynolds Roughness", *Journal of Lubrication Technology*, vol. 101, pp. 8–14, 1979.

[117] Tripp, J.H., "Surface Roughness Effects in Hydrodynamic Lubrication: The Flow Factor Method", *Journal of Lubrication Technology*, vol. 105, pp. 458–465, 1983.

[118] Fu, G., and Chandra, A., Guha S., and Subhash, G., "A Plasticity–based Model of Material Removal in Chemical Mechanical Polishing (CMP)", *Semiconductor Manufacturing*, *IEEE Transactions*, vol. 14, no. 2, pp. 406–417, 2001.

[119] Thakurta, D.G., Borst, C.L., Schwendeman, D.W., Gutmann, R.J., and Gill, W.N., "Three Dimensional Chemical Mechanical Planarization Slurry Flow Model Based on Lubrication Theory", *Journal of the Electrochemical Society*, vol. 148, no. 4, G207–G214, 2001.

[120] Yang, L., "Modeling CMP for Copper Dual Damascene Interconnects", *Solid State Technology*, vol. 43, no. 6, pp. 111–121, 2000.

[121] Sampurno, Y., Borucki, L., Zhuang, Y., Boning, D., and Philipossian, A., "A Method for Direct Measurement of Substrate Temperature during Copper CMP", *Journal of the Electrochemical Society*, vol. 152, no. 7, G537–G541, 2005.

[122] Renteln, P., and Ninh, T., *Materials Research Society Symposium Proceedings*, vol. 566, pp. 155, 1999.

[123] Sorooshian, J., DeNardis, D., Charns, L., Li, Z., Shadman, F., Boning, D., Hetherington, D., and Philipossian, A., "Arrhenius Characterization of ILD and Copper CMP Processes", *Journal of the Electrochemical Society*, vol. 151, no. 2, G85–G88, 2004.

[124] Li, Z., Borucki, L., Koshiyama, I., and Philipossian, A., *Journal of the Electrochemical Society*, vol. 151, no. 7, G482–G487, 2004.

[125] Mudhivarthi, S., Zantye, P., Kumar, A., Kumar, A., Beerbom, M. and Schlaf, R., *Electrochemistry and Solid State Letters,* vol. 8, no. 9, G241, 2005.

[126] Mudhivarthi, S., Gitis, N., Kuiry, S., Vinogradov M., and Kumar, A., *Journal of the Electrochemical Society*, vol. 153, no. 5, G372, 2006.

[127] Borucki, L., Charns, L., and Philipossian, A., Abstract 918, *Electrochemical Society Meeting Abstracts*, vol. 2003–2, Orlando, Florida, Oct 12–16, 2003.

[128] Borucki, L., Li, Z., and Philipossian, A., *Journal of the Electrochemical Society*, vol. 151, G559, 2004.

[129] White, D., Melvin, J., and Boning, D., *Journal of the Electrochemical Society*, vol. 150, G271, 2003.

[130] Sorooshian, J., Hetherington, D., and Philipossian, A., "Effect of Process Temperature on Coefficient of Friction during CMP", *Electrochemical Solid State Lett.*, vol. 7, no. 10, G222–G224, 2004 .

[131] Wang, Y.L., Liu, C., Feng, M.S., and Tseng, W.T., *Materials Chemistry and Physics*, vol. 52, pp. 17–22, 1998.

[132] Hong, H., Huang, Y.L., and Chenb, L.J., *Journal of the Electrochemical Society*, vol. 146, no. 11, pp. 4236–4239, 1999.

[133] Cornely, J., Rogers, C., Manno, V. and Philipossian, A., *Materials Research Society Symposium. Proceedings*, vol. 767, F1.6.1, 2003.

[134] Bejan, A., *Convection Heat Transfer*, 2nd ed., John Wiley and Sons, New York, Appendix C, pp. 595–602, 1995.

[135] Schlichting, H., *Boundary–layer theory*, 7th ed., McGraw–Hill, New York. Chapters 3 and 5, pp. 53–54 and 84, 1979.

[136] Burmeister, L.C., *Convective Heat Transfer,* 2nd ed., John Wiley and Sons Inc, New York, Appendix C, pp. 581–590, 1993.

[137] White, F.M., *Fluid Mechanics*, 5th ed., McGraw–Hill, New York, 2003.

[138] Bula, A.J., 1999, "Numerical Modeling of Conjugate Heat Transfer during Free Liquid Jet Impingement", Ph.D. Dissertation, University of South Florida, Tampa, Florida.

[139] Ng, S.H., 2005, "Measurement and Modeling of Fluid Pressures in Chemical Mechanical Polishing", Ph.D. Dissertation, Georgia Institute of Technology, Georgia.

[140] Fletcher, C.A.J. *Computational Galerkin Methods*, Springer Verlag, New York, pp. 27 and 205, 1984.

[141] Özisik, M.N., *Heat Conduction,* 2nd ed., John Wiley and Sons, New York, Appendix 1, pp. 657–660, 1993.

[142] Vanyo, J.P., *Rotating Fluids in Engineering and Science,* Butterworth–Heinemann, Stoneham, MA, Chapter 14, pp. 233–264, 1993.

[143] Roache, P.J., K. Ghia, and F. White, "Editorial Policy Statement on the Control of Numerical Accuracy", *Journal of Fluids Engineering,* vol. 108, no. 1, p.2, 1986.

[144] Owosina, T.A., 2002, "Numerical Modeling of Conjugate Heat Transfer During Free and Confined Liquid Jet Impingement", MS Thesis, University of South Florida, Tampa, Florida.

[145] Martin, H., *Heat and Mass Transfer between Impinging Jets and Solid Surfaces, Advances in Heat Transfer*, vol. 13, pp. 1–60, Academic Press, New York, 1977.

[146] Mudhivarthi, S.R., 2007, "Process Optimization and Consumable Development for Chemical Mechanical Planarization (CMP) Processes", Ph.D. Dissertation, University of South Florida, Tampa, Florida.

[147] Muldowney, G., Paper presented at *The 9th International Symposium on Chemical Mechanical Planarization*, Aug.8–11, Lake Placid, New York Center for Advanced Materials Processing, 2004.

[148] Sikder, A.K., Giglio, F., Wood, J., Kumar, A. and Anthony, M., *Journal of Electronic Materials*, vol. 30, no. 12, pp. 1520–1526, 2001.

Appendices

Appendix A: CFD Free Liquid Jet Impingement

```
TITLE (  )
FREE SURFACE JET IMPINGEMENT

/ FIGURE GENERATION SECTION

FI-GEN (ELEM = 1, POIN = 1, CURV = 1, SURF = 1, NODE = 0,
MEDG = 1, MLOO = 1, MFAC = 1, BEDG = 1, SPAV = 1, MSHE = 1,
MSOL = 1, COOR = 1, TOLE = 0.0001)

/ POINTS

POINT( ADD, COOR, X = 0, Y = 0 )
POINT( ADD, COOR, X = -0.06, Y = 0 )
POINT( ADD, COOR, X = -0.24, Y = 0 )
POINT( ADD, COOR, X = -0.24, Y = 0.06 )
POINT( ADD, COOR, X = -0.16, Y = 0.20 )
POINT( ADD, COOR, X = -0.13, Y = 0.38 )
POINT( ADD, COOR, X = -0.13, Y = 0.76 )
POINT( ADD, COOR, X = -0.06, Y = 0.76 )
POINT( ADD, COOR, X = 0, Y = 0.76 )
POINT( ADD, COOR, X = 0, Y = 0.38 )
POINT( ADD, COOR, X = -0.06, Y = 0.06 )
POINT( ADD, COOR, X = -0.06, Y = 0.20 )
POINT( ADD, COOR, X = -0.06, Y = 0.38 )
POINT( ADD, COOR, X = -0.24, Y = 0.76 )

/ LINES (1,2,3,4)

POINT( SELE, ID = 1 )
POINT( SELE, ID = 2 )
CURVE( ADD, LINE )

POINT( SELE, ID = 2 )
POINT( SELE, ID = 3 )
CURVE( ADD, LINE )

POINT( SELE, ID = 3 )
POINT( SELE, ID = 4 )
CURVE( ADD, LINE )

POINT( SELE, ID = 4 )
POINT( SELE, ID = 5 )
POINT( SELE, ID = 6 )
CURVE( ADD, ARC )
```

Appendix A (Continued)

```
CURVE( SELE, ID = 4 )
POINT( SELE, ID = 5 )
CURVE( SPLI )
```

/ LINES (6,7,8,9,10)

```
POINT( SELE, ID = 6 )
POINT( SELE, ID = 7 )
CURVE( ADD, LINE )

POINT( SELE, ID = 7 )
POINT( SELE, ID = 8 )
CURVE( ADD, LINE )

POINT( SELE, ID = 8 )
POINT( SELE, ID = 9 )
CURVE( ADD, LINE )

POINT( SELE, ID = 9 )
POINT( SELE, ID = 10 )
CURVE( ADD, LINE )

POINT( SELE, ID = 10 )
POINT( SELE, ID = 1 )
CURVE( ADD, LINE )

POINT( SELE, ID = 2 )
POINT( SELE, ID = 11 )
CURVE( ADD, LINE )

POINT( SELE, ID = 11 )
POINT( SELE, ID = 12 )
CURVE( ADD, LINE )

POINT( SELE, ID = 12 )
POINT( SELE, ID = 13 )
CURVE( ADD, LINE )

POINT( SELE, ID = 13 )
POINT( SELE, ID = 8 )
CURVE( ADD, LINE )
```

Appendix A (Continued)

```
POINT( SELE, ID = 13 )
POINT( SELE, ID = 6 )
CURVE( ADD, LINE )
```

/ MODEL SURFACE BY POINTS

```
POINT( SELE,ID = 1 )
POINT( SELE,ID = 3 )
POINT( SELE,ID = 9 )
POINT( SELE,ID = 14 )
SURFACE( ADD, POIN, ROWW = 2, NOAD )
```

/ MESH EDGES

```
CURVE( SELE,ID = 1 )
MEDGE( ADD, SUCC, INTE = 6, RATI = 0, 2RAT = 0, PCEN = 0 )
CURVE( SELE,ID = 2 )
MEDGE( ADD, FRST, INTE = 16, RATI = 0.1, 2RAT = 0, PCEN =
0.5 )
CURVE( SELE,ID = 3 )
MEDGE( ADD, LSTF, INTE = 6, RATI = 0, 2RAT = 0, PCEN = 0 )
CURVE( SELE,ID = 5 )
MEDGE( ADD, SUCC, INTE = 14, RATI = 0, 2RAT = 0, PCEN = 0 )
CURVE( SELE,ID = 6 )
MEDGE( ADD, SUCC, INTE = 18, RATI = 0, 2RAT = 0, PCEN = 0 )
CURVE( SELE,ID = 7 )
MEDGE( ADD, SUCC, INTE = 38, RATI = 0, 2RAT = 0, PCEN = 0 )
CURVE( SELE,ID = 8 )
MEDGE( ADD, LSTF, INTE = 16, RATI = 0.1, 2RAT = 0, PCEN =
0.5 )
CURVE( SELE,ID = 9 )
MEDGE( ADD, SUCC, INTE = 6, RATI = 0, 2RAT = 0, PCEN = 0 )
CURVE( SELE,ID = 10 )
MEDGE( ADD, SUCC, INTE = 38, RATI = 0, 2RAT = 0, PCEN = 0 )
CURVE( SELE,ID = 11 )
MEDGE( ADD, SUCC, INTE = 38, RATI = 0, 2RAT = 0, PCEN = 0 )
CURVE( SELE,ID = 12 )
MEDGE( ADD, SUCC, INTE = 6, RATI = 0, 2RAT = 0, PCEN = 0 )
CURVE( SELE,ID = 13 )
MEDGE( ADD, SUCC, INTE = 14, RATI = 0, 2RAT = 0, PCEN = 0 )
CURVE( SELE,ID = 14 )
MEDGE( ADD, SUCC, INTE = 18, RATI = 0, 2RAT = 0, PCEN = 0 )
CURVE( SELE,ID = 15 )
MEDGE( ADD, SUCC, INTE = 38, RATI = 0, 2RAT = 0, PCEN = 0 )
```

Appendix A (Continued)

```
CURVE( SELE,ID = 16 )
MEDGE( ADD, FRST, INTE = 16, RATI = 0.1, 2RAT = 0, PCEN =
0.5 )
```

/ MESH LOOPS

/ LOOP 1

```
CURVE( SELE, ID = 1 )
CURVE( SELE, ID = 12 )
CURVE( SELE, ID = 13 )
CURVE( SELE, ID = 14 )
CURVE( SELE, ID = 15 )
CURVE( SELE, ID = 9 )
CURVE( SELE, ID = 10 )
CURVE( SELE, ID = 11 )
MLOOP( ADD, MAP, VISI, NOSH, EDG1 = 1, EDG2 = 4, EDG3 = 1,
EDG4 = 2 )
```

/ LOOP 2

```
CURVE( SELE, ID = 3 )
CURVE( SELE, ID = 5 )
CURVE( SELE, ID = 6 )
CURVE( SELE, ID = 16 )
CURVE( SELE, ID = 14 )
CURVE( SELE, ID = 13 )
CURVE( SELE, ID = 12 )
CURVE( SELE, ID = 2 )
MLOOP( ADD, MAP, VISI, NOSH, EDG1 = 3, EDG2 = 1, EDG3 = 3,
EDG4 = 1 )
```

/ LOOP 3

```
CURVE( SELE, ID = 16 )
CURVE( SELE, ID = 7 )
CURVE( SELE, ID = 8 )
CURVE( SELE, ID = 15 )
MLOOP( ADD, MAP, VISI, NOSH, EDG1 = 1, EDG2 = 1, EDG3 = 1,
EDG4 = 1 )
```

/ MESH FACES

Appendix A (Continued)

/ FACE1

```
SURFACE( SELE, ID = 1 )
MLOOP( SELE, ID = 1 )
MFACE( ADD )
```

/ FACE2

```
SURFACE( SELE, ID = 1 )
MLOOP( SELE, ID = 2 )
MFACE( ADD )
```

/ FACE3

```
SURFACE( SELE, ID = 1 )
MLOOP( SELE, ID = 3 )
MFACE( ADD )
```

/ MESHING FEATURES

```
MFACE( SELE,ID = 1 )
ELEMENT( SETD, QUAD, NODE = 4 )
MFACE( MESH, MAP, NOSM, ENTI = "silicon" )
MFACE( SELE,ID = 2 )
MFACE( SELE,ID = 3 )
ELEMENT( SETD, QUAD, NODE = 4 )
MFACE( MESH, MAP, ENTI ="water" )
```

/ MESH MAP ELEMENT ID

```
ELEMENT( SETD, EDGE, NODE = 2 )
MEDGE( SELE,ID = 3 )
MEDGE( MESH, MAP, ENTI = "inlet" )
MEDGE( SELE,ID = 7 )
MEDGE( MESH, MAP, ENTI = "outlet" )
MEDGE( SELE,ID )
4
5
6
MEDGE( MESH, MAP, ENTI = "surface" )
MEDGE( SELE,ID )
9
10
MEDGE( MESH, MAP, ENTI = "bottom" )
```

Appendix A (Continued)

```
MEDGE( SELE,ID = 2 )
MEDGE( MESH, MAP, ENTI = "axis" )
MEDGE( SELE,ID )
1
8
MEDGE( MESH, MAP, ENTI = "sides" )
MEDGE( SELE,ID )
11
12
13
14
MEDGE( MESH, MAP, ENTI = "interface" )
END(  )
```

/ FEM PROPERTIES OF (SOLID, LIQUID, OR GAS), ENTITY, PROBLEM TYPE AND BOUNDARY CONDITION DEFINITION

```
FIPREP(  )
```

/ FLUID CONSTANT PROPERTIES

```
DENSITY( ADD, SET = "water", CONS = 0.996 )
CONDUCTIVITY( ADD, SET = "water", CONS = 0.0014699 )
VISCOSITY( ADD, SET = "water", CONS = 0.00798 )
SPECIFICHEAT( ADD, SET = "water", CONS = 0.998137 )
SURFACETENSION( ADD, SET = "water", CONS = 73 )
```

OR

/ FLUID VARIABLE PROPERTIES

```
DENSITY( ADD, SET = "water", TYP2, CONS = 0.996,
TEMPERATURE )

CONDUCTIVITY( ADD, SET = "water", CURVE = 10 )
0 37.0 43.33 48.89 54.44 65.55 76.67 87.78 104.4 115.6
0.00135277247 0.0014699 0.0015224665 0.001539197
0.0015511472 0.0015750478 0.0015965583 0.0016132887
0.0016347992 0.0016371893

VISCOSITY( ADD, SET = "water", CURVE = 10 )
0 37.0 43.33 48.89 54.44 65.55 76.67 87.78 104.4 115.6
0.017900 0.00798 0.00616 0.00562 0.00513 0.00430 0.00372
0.00327 0.00267 0.00244
```

Appendix A (Continued)

```
SPECIFICHEAT( ADD, SET = "water", CURVE = 10 )
0 37.0 43.33 48.89 54.44 65.55 76.67 87.78 104.4 115.6
1.009799235 0.998137 0.99760994 0.99770994 0.99880497
0.99976099 1.00167304 1.003585086 1.007648184

/ MATERIAL PROPERTIES

DENSITY( ADD, SET = "silicon", CONS = 2.33 )
CONDUCTIVITY( ADD, SET = "silicon", CONS = 0.334608 )
SPECIFICHEAT( ADD, SET = "silicon", CONS = 0.17006 )

/ ENTITY DEFINITION

ENTITY( ADD, NAME = "water", FLUI, PROP = "water" )
ENTITY( ADD, NAME = "inlet", PLOT )
ENTITY( ADD, NAME = "outlet", PLOT )
ENTITY( ADD, NAME = "surface", SURF, DEPT = 15, SPIN, STRA,
ANG1 = 10, ANG2 = 180 )
ENTITY( ADD, NAME = "bottom", PLOT )
ENTITY( ADD, NAME = "axis", PLOT )
ENTITY( ADD, NAME = "silicon", SOLI, PROP = "silicon" )
ENTITY( ADD, NAME = "sides", PLOT )
ENTITY( ADD, NAME = "interface", PLOT, ATTA= "water", NATT
= "silicon")
BODYFORCE( ADD, CONS, FX = 981, FY = 0, FZ = 0 )
PRESSURE( ADD, MIXE = 1e-11, DISC )

/ RELAXATION FACTORS (UR, UZ, Uθ, PRESSURE, TEMP, SURFACE)

OPTIONS (ADD, UPWI )
UPWINDING (ADD, STRE )
RELAXATION(  )
  0.3, 0.3, 0.3, 0, 0.05, 0.25

/ BOUNDARY CONDITIONS

BCNODE( ADD, COOR, NODE = 24 )
BCNODE( ADD, SURF, NODE = 24, ZERO )
BCNODE( ADD, VELO, ENTI = "bottom", ZERO )
BCNODE( ADD, URC, ENTI = "inlet", ZERO )
BCNODE( ADD, UZC, ENTI = "inlet", CONS = 80.15 )
BCNODE( ADD, URC, ENTI = "axis", ZERO )
BCNODE( ADD, VELO, ENTI = "interface", ZERO )
BCNODE( ADD, VELO, ENTI = "sides", ZERO )
```

Appendix A (Continued)

```
BCNODE( ADD, VELO, NODE = 24, ZERO )
BCNODE( ADD, UT, NODE = 24, ZERO )
BCNODE( ADD, TEMP, ENTI = "inlet", CONS = 37 )
BCFLUX( ADD, HEAT, ENTI = "bottom", CONS = 5.971 )
BCNODE(UTHETA,POLYNOMIAL=1,ENTITY="silicon")
0 44.5  0 1 0
```

/ INITIAL CONDITION

```
ICNODE( ADD, URC, ENTI = "water", CONS = 30  )
```

/ MINIMUM TEMPERATURE

```
CLIPPING( ADD, MINI )
    0,     0,     0,     0,    37,     0
```

/ PROBLEM DESCRIPTION AND METHOD

```
PROBLEM ( ADD, CYLI, INCO, TRAN, LAMI, NONL, NEWT, MOME,
FREE, SING )
DATAPRINT( ADD, CONT )
EXECUTION( ADD, NEWJ )
PRINTOUT( ADD, NONE, BOUN )
```

/ METHOD TYPE FOR VARIABLE AND CONSTANT PROPERTIES

```
SOLUTION( ADD, N.R. = 50, KINE = 25, VELC = 1e-4, RESC =
1e-4, SURF = 1e-3 )

TIMEINTEGRATION( ADD, BACK, NSTE = 1000, TSTA = 0, DT = 1e-
8, VARI, WIND = 9, NOFI = 10 )
END(  )
```

/ INPUT FILE GENERATION AND RUN

```
CREATE( FISO )
RUN( FISOLV, IDEN = "EXAMPLE1", BACK, AT = "", TIME =
     "NOW", COMP )
```

Appendix B: CFD Confined Liquid Jet Impingement

```
TITLE(  )
CONFINED JET IMPINGEMENT WITH SPINNING TARGET OR SPINNING
CONFINED WALL

/ FIGURE GENERATION SECTION
FI-GEN( ELEM = 1, POIN = 1, CURV = 1, SURF = 1, NODE = 0,
MEDG = 1, MLOO = 1, MFAC = 1, BEDG = 1, SPAV = 1, MSHE = 1,
MSOL = 1, COOR = 1, TOLE = 1e-05 )

/ POINTS

POINT( ADD, COOR, X = 0, Y = 0 )
POINT( ADD, COOR, X = -0.06, Y = 0 )
POINT( ADD, COOR, X = -0.35, Y = 0 )
POINT( ADD, COOR, X = -0.35, Y =0.06 )
POINT( ADD, COOR, X = -0.35, Y = 0.76 )
POINT( ADD, COOR, X = -0.06, Y = 0.76 )
POINT( ADD, COOR, X = 0, Y = 0.76 )
POINT( ADD, COOR, X = 0, Y =0.06 )
POINT( ADD, COOR, X = -0.06, Y =0.06 )

/ LINES (1,2,3)

POINT( SELE,ID = 1 )
POINT( SELE,ID = 2 )
CURVE( ADD, LINE )

POINT( SELE,ID = 2 )
POINT( SELE,ID = 3 )
CURVE( ADD, LINE )

POINT( SELE,ID = 3 )
POINT( SELE,ID = 4 )
CURVE( ADD, LINE )

/ LINES (4,5,6)

POINT( SELE,ID = 4 )
POINT( SELE,ID = 5 )
CURVE( ADD, LINE )

POINT( SELE,ID = 5 )
POINT( SELE,ID = 6 )
CURVE( ADD, LINE )
```

Appendix B (Continued)

```
POINT( SELE,ID = 6 )
POINT( SELE,ID = 7 )
CURVE( ADD, LINE )

/ LINES (7,8,9,10)
POINT( SELE,ID = 7 )
POINT( SELE,ID = 8 )
CURVE( ADD, LINE )

POINT( SELE,ID = 8 )
POINT( SELE,ID = 1 )
CURVE( ADD, LINE )

POINT( SELE,ID = 2 )
POINT( SELE,ID = 9 )
CURVE( ADD, LINE )

POINT( SELE,ID = 9 )
POINT( SELE,ID = 6 )
CURVE( ADD, LINE )

/ MODEL SURFACE BY POINTS

POINT( SELE,ID = 1 )
POINT( SELE,ID = 3 )
POINT( SELE,ID = 7 )
POINT( SELE,ID = 5 )
SURFACE(ADD, POIN,ROWW = 2 )

/ MESH EDGES

CURVE( SELE,ID = 1 )
MEDGE( ADD, SUCC, INTE = 6, RATI = 0, 2RAT = 0, PCEN = 0 )
CURVE( SELE,ID = 2 )
MEDGE( ADD, FRST, INTE = 35, RATI = 0.1, 2RAT = 0, PCEN =
0.5 )
CURVE( SELE,ID = 3 )
MEDGE( ADD, SUCC, INTE = 6, RATI = 0, 2RAT = 0, PCEN = 0 )
CURVE( SELE,ID = 4 )
MEDGE( ADD, SUCC, INTE = 73, RATI = 0, 2RAT = 0, PCEN = 0 )
CURVE( SELE,ID = 5 )
MEDGE( ADD, LSTF, INTE = 35, RATI = 0.1, 2RAT = 0, PCEN =
0.5 )
CURVE( SELE,ID = 6 )
```

Appendix B (Continued)

```
MEDGE( ADD, SUCC, INTE = 6, RATI = 0, 2RAT = 0, PCEN = 0 )
CURVE( SELE,ID = 7 )
MEDGE( ADD, SUCC, INTE = 73, RATI = 0, 2RAT = 0, PCEN = 0 )
CURVE( SELE,ID = 8 )
MEDGE( ADD, SUCC, INTE = 6, RATI = 0, 2RAT = 0, PCEN = 0 )
CURVE( SELE,ID = 9 )
MEDGE( ADD, SUCC, INTE = 6, RATI = 0, 2RAT = 0, PCEN = 0 )
CURVE( SELE,ID = 10 )
MEDGE( ADD, SUCC, INTE = 73, RATI = 0, 2RAT = 0, PCEN = 0 )

/ MESH LOOPS

/ LOOP 1

CURVE( SELE, ID = 1 )
CURVE( SELE, ID = 9 )
CURVE( SELE, ID = 10 )
CURVE( SELE, ID = 6 )
CURVE( SELE, ID = 7 )
CURVE( SELE, ID = 8 )
MLOOP( ADD,MAP, EDG1 = 1, EDG2 = 2,EDG3 = 1, EDG4 = 2 )

/ LOOP 2

CURVE( SELE, ID = 2 )
CURVE( SELE, ID = 3 )
CURVE( SELE, ID = 4 )
CURVE( SELE, ID = 5 )
CURVE( SELE, ID = 10 )
CURVE( SELE, ID = 9 )
MLOOP( ADD,MAP, EDG1 = 1, EDG2 = 2,EDG3 = 1, EDG4 = 2 )

/ MESH FACES

/ FACE1
SURFACE( SELE, ID = 1 )
MLOOP( SELE, ID = 1 )
MFACE( ADD )

/ FACE2
SURFACE( SELE, ID = 1 )
MLOOP( SELE, ID = 2 )
MFACE( ADD )
```

Appendix B (Continued)

/ MESHING FEATURES

```
MFACE( SELE,ID = 1 )
MFACE( MESH, MAP, NOSM, ENTI = "silicon" )
MFACE( SELE,ID = 2 )
MFACE( MESH, MAP, ENTI ="water" )
```

/ MESH MAP ELEMENT ID

```
ELEMENT( SETD, EDGE, NODE = 2 )
MEDGE( SELE,ID = 3 )
MEDGE( MESH, MAP, ENTI = "inlet" )
MEDGE( SELE,ID = 5 )
MEDGE( MESH, MAP, ENTI = "outlet" )
MEDGE( SELE,ID = 4 )
MEDGE( MESH, MAP, ENTI = "top" )
MEDGE( SELE,ID )
7
8
MEDGE( MESH, MAP, ENTI = "bottom" )
MEDGE( SELE,ID = 2 )
MEDGE( MESH, MAP, ENTI = "axis" )
MEDGE( SELE,ID )
1
6
MEDGE( MESH, MAP, ENTI = "sides" )

MEDGE( SELE,ID )
9
10
MEDGE( MESH, MAP, ENTI = "interface" )
END(  )
```

/ FEM PROPERTIES OF (SOLID, LIQUID, OR GAS), ENTITY, PROBLEM TYPE AND BOUNDARY CONDITION DEFINITION

```
FIPREP(  )
```

/ CONSTANT FLUID PROPERTIES

```
DENSITY( ADD, SET = "water", CONS = 0.996 )
CONDUCTIVITY( ADD, SET = "water", CONS = 0.0014699 )
VISCOSITY( ADD, SET = "water", CONS = 0.00798 )
SPECIFICHEAT( ADD, SET = "water", CONS = 0.998137 )
SURFACETENSION( ADD, SET = "water", CONS = 73 )
```

Appendix B (Continued)

/ FLUID VARIABLE PROPERTIES

```
DENSITY (ADD, SET = "water", TYP2, CONS = 0.996, TEMP )

CONDUCTIVITY (ADD, SET = "water", CURVE = 10 )
0 37.0 43.33 48.89 54.44 65.55 76.67 87.78 104.4 115.6
0.00135277247 0.0014699 0.0015224665 0.001539197
0.0015511472 0.0015750478 0.0015965583 0.0016132887
0.0016347992 0.0016371893

VISCOSITY (ADD, SET = "water", CURVE = 10 )
0 37.0 43.33 48.89 54.44 65.55 76.67 87.78 104.4 115.6
0.017900 0.00798 0.00616 0.00562 0.00513 0.00430 0.00372
0.00327 0.00267 0.00244

SPECIFICHEAT (ADD, SET = "water", CURVE = 10 )
0 37.0 43.33 48.89 54.44 65.55 76.67 87.78 104.4 115.6
1.009799235 0.998137 0.99760994 0.99770994 0.99880497
0.99976099 1.00167304 1.003585086 1.007648184
```

/ MATERIAL PROPERTIES

```
DENSITY(ADD, SET = "silicon", CONS = 2.33 )
CONDUCTIVITY( ADD, SET = "silicon", CONS = 0.334608 )
SPECIFICHEAT( ADD, SET = "silicon", CONS = 0.17006 )
```

/ ENTITY DEFINITION

```
ENTITY(ADD, NAME = "water", FLUI, PROP = "water" )
ENTITY(ADD, NAME = "inlet", PLOT )
ENTITY(ADD, NAME = "outlet", PLOT )
ENTITY(ADD, NAME = "top", PLOT )
ENTITY(ADD, NAME = "bottom", PLOT )
ENTITY(ADD, NAME = "axis", PLOT )
ENTITY(ADD, NAME = "silicon", SOLI, PROP = "silicon" )
ENTITY(ADD, NAME = "sides", PLOT )
ENTITY(ADD, NAME = "interface", PLOT, ATTA = "water", NATT
= "silicon")
```

/ RELAXATION FACTORS (UR, UZ, Uθ, PRESSURE, TEMP, SURFACE)

```
OPTIONS (ADD, UPWI )
UPWINDING (ADD, STRE )
RELAXATION(  )
  0.6, 0.6, 0.6, 0, 0.2, 0.4
```

Appendix B (Continued)

/BOUNDARY CONDITIONS

```
BCNODE( ADD, VELO, ENTI = "top", ZERO )
BCNODE( ADD, VELO, ENTI = "bottom", ZERO )
BCNODE( ADD, URC, ENTI = "inlet", ZERO )
BCNODE( ADD, UZC, ENTI = "inlet", CONS = 100.1506  )
BCNODE( ADD, URC, ENTI = "axis", ZERO )
BCNODE( ADD, VELO, ENTI = "interface", ZERO )
BCNODE( ADD, VELO, ENTI = "sides", ZERO )
BCNODE( ADD, TEMP, ENTI = "inlet", CONS = 37 )
BCFLUX( ADD, HEAT, ENTI = "bottom", CONS = 5.971 )
```

/ SPINNING TARGET

```
BCNODE( UTHE,POLY = 1, ENTI = "silicon" )
0 13.09 0 1 0
/OR
```

/ SPINNING CONFINED WALL

```
BCNODE( UTHE,POLY = 1, ENTI = "top" )
0 13.09 0 1 0
```

/ MINIMUN TEMPERATURE

```
CLIPPING( ADD, MINI )
    0,     0,     0,     0,    37,     0
```

/ PROBLEM DESCRIPTION AND METHOD

```
PROBLEM (ADD, CYLI,INCO, STEA, LAMI, NONL, NEWT, MOME,
ENER,FIXE,SING )
DATAPRINT( ADD, CONT )
EXECUTION( ADD, NEWJ )
PRINTOUT( ADD, NONE, BOUN )
```

/ METHOD TYPE FOR VARIABLE PROPERTIES

```
SOLUTION( ADD, SEGR = 1200, VELC = 1e-4, RESC = 1e-5 )
```

/ METHOD TYPE FOR CONSTANT PROPERTIES

```
SOLUTION( ADD, S.S. = 100, VELC = 1e-4, RESC = 1e-4 )
END(  )
```

/INPUT FILE GENERATION AND RUN

```
CREATE( FISO )
RUN( FISOLV, IDEN = "EXAMPLE2", BACK, AT = "", TIME =
"NOW", COMP
```

Appendix C: CFD Partially–confined Liquid Jet Impingement

```
TITLE(  )
PARTIALLY CONFINED JET IMPINGEMENT WITH SPINNING TARGET
AND/OR SPINNING CONFINED WALL
```

/ FIGURE GENERATION SECTION

```
FI-GEN( ELEM = 1, POIN = 1, CURV = 1, SURF = 1, NODE = 0,
MEDG = 1, MLOO = 1, MFAC = 1, BEDG = 1, SPAV = 1, MSHE = 1,
MSOL = 1, COOR = 1, TOLE = 0.0001 )
```

/ POINTS

```
POINT( ADD, COOR, X = 0, Y = 0 )
POINT( ADD, COOR, X = -0.06, Y = 0 )
POINT( ADD, COOR, X = -0.18, Y = 0 )
POINT( ADD, COOR, X = -0.18, Y = 0.06 )
POINT( ADD, COOR, X = -0.18, Y = 0.36 )
POINT( ADD, COOR, X = -0.145, Y = 0.52 )
POINT( ADD, COOR, X = -0.14, Y = 0.6 )
POINT( ADD, COOR, X = -0.06, Y = 0.6 )
POINT( ADD, COOR, X = 0, Y = 0.6 )
POINT( ADD, COOR, X = 0, Y = 0.36 )
POINT( ADD, COOR, X = 0, Y = 0.06 )
POINT( ADD, COOR, X = -0.06, Y = 0.06 )
POINT( ADD, COOR, X = -0.06, Y = 0.36 )
POINT( ADD, COOR, X = -0.18, Y = 0.6 )
```

/ LINES (1,2,3,4,5,6,7)

```
POINT( SELE, ID = 1 )
POINT( SELE, ID = 2 )
CURVE( ADD, LINE )

POINT( SELE, ID = 2 )
POINT( SELE, ID = 3 )
CURVE( ADD, LINE )

POINT( SELE, ID = 3 )
POINT( SELE, ID = 4 )
CURVE( ADD, LINE )

POINT( SELE, ID = 4 )
POINT( SELE, ID = 5 )
CURVE( ADD, LINE )
```

Appendix C (Continued)

```
POINT( SELE, ID = 5 )
POINT( SELE, ID = 6 )
POINT( SELE, ID = 7 )
CURVE( ADD, ARC )

POINT( SELE, ID = 7 )
POINT( SELE, ID = 8 )
CURVE( ADD, LINE )
```

/ LINES (8,9,10,11,12,13,14)

```
POINT( SELE, ID = 8 )
POINT( SELE, ID = 9 )
CURVE( ADD, LINE )

POINT( SELE, ID = 9 )
POINT( SELE, ID = 10 )
CURVE( ADD, LINE )

POINT( SELE, ID = 10 )
POINT( SELE, ID = 11 )
CURVE( ADD, LINE )

POINT( SELE, ID = 11 )
POINT( SELE, ID = 1 )
CURVE( ADD, LINE )

POINT( SELE, ID = 2 )
POINT( SELE, ID = 12 )
CURVE( ADD, LINE )

POINT( SELE, ID = 12 )
POINT( SELE, ID = 13 )
CURVE( ADD, LINE )

POINT( SELE, ID = 13 )
POINT( SELE, ID = 8 )
CURVE( ADD, LINE )

POINT( SELE, ID = 13 )
POINT( SELE, ID = 5 )
CURVE( ADD, LINE )
```

Appendix C (Continued)

/ MODEL SURFACE BY POINTS

```
POINT( SELE, ID = 1 )
POINT( SELE, ID = 3 )
POINT( SELE, ID = 9 )
POINT( SELE, ID = 14 )
SURFACE( ADD, POIN, ROWW = 2, NOAD )
```

/ MESH EDGES

```
CURVE( SELE, ID = 1 )
MEDGE( ADD, SUCC, INTE = 12, RATI = 0, 2RAT = 0, PCEN = 0 )
CURVE( SELE, ID = 2 )
MEDGE( ADD, FRST, INTE = 16, RATI = 0.1, 2RAT = 0, PCEN =
0.5 )
CURVE( SELE, ID = 3 )
MEDGE( ADD, SUCC, INTE = 9, RATI = 0, 2RAT = 0, PCEN = 0 )
CURVE( SELE, ID = 4 )
MEDGE( ADD, SUCC, INTE = 30, RATI = 0, 2RAT = 0, PCEN = 0 )
CURVE( SELE, ID = 5 )
MEDGE( ADD, SUCC,INTE = 24, RATI = 1, 2RAT = 1.05, PCEN =
0.5 )
CURVE( SELE, ID = 6 )
MEDGE( ADD, LSTF, INTE = 16, RATI = 0.1, 2RAT = 0, PCEN =
0.5 )
CURVE( SELE, ID = 7 )
MEDGE( ADD, SUCC, INTE = 12, RATI = 0, 2RAT = 0, PCEN = 0 )
CURVE( SELE, ID = 8 )
MEDGE( ADD, SUCC, INTE = 24, RATI = 0, 2RAT = 0, PCEN = 0 )
CURVE( SELE, ID = 9 )
MEDGE( ADD, SUCC, INTE = 30, RATI = 0, 2RAT = 0, PCEN = 0 )
CURVE( SELE, ID = 10 )
MEDGE( ADD, SUCC, INTE = 9, RATI = 0, 2RAT = 0, PCEN = 0 )
CURVE( SELE, ID = 11 )
MEDGE( ADD, SUCC, INTE = 9, RATI = 0, 2RAT = 0, PCEN = 0 )
CURVE( SELE, ID = 12 )
MEDGE( ADD, SUCC, INTE = 30, RATI = 0, 2RAT = 0, PCEN = 0 )
CURVE( SELE, ID = 13 )
MEDGE( ADD, SUCC, INTE = 24, RATI = 0, 2RAT = 0, PCEN = 0 )
CURVE( SELE, ID = 14 )
MEDGE( ADD, FRST, INTE = 16, RATI = 0.1, 2RAT = 0, PCEN =
0.5 )
```

Appendix C (Continued)

/ MESH LOOPS

/ LOOP 1

```
CURVE( SELE, ID = 1 )
CURVE( SELE, ID = 11 )
CURVE( SELE, ID = 12 )
CURVE( SELE, ID = 13 )
CURVE( SELE, ID = 7 )
CURVE( SELE, ID = 8 )
CURVE( SELE, ID = 9 )
CURVE( SELE, ID = 10 )
MLOOP( ADD, MAP, VISI, NOSH, EDG1 = 1, EDG2 = 3, EDG3 = 1,
EDG4 = 3 )
```

/ LOOP 2

```
CURVE( SELE, ID = 2 )
CURVE( SELE, ID = 3 )
CURVE( SELE, ID = 4 )
CURVE( SELE, ID = 14 )
CURVE( SELE, ID = 12 )
CURVE( SELE, ID = 11 )
MLOOP( ADD, MAP, VISI, NOSH, EDG1 = 1, EDG2 = 2, EDG3 = 1,
EDG4 = 2 )
```

/ LOOP 3

```
CURVE( SELE, ID = 14 )
CURVE( SELE, ID = 5 )
CURVE( SELE, ID = 6 )
CURVE( SELE, ID = 13 )
MLOOP( ADD, MAP, VISI, NOSH, EDG1 = 1, EDG2 = 1, EDG3 = 1,
EDG4 = 1 )
```

/ MESH FACES

/ FACE1

```
SURFACE( SELE, ID = 1 )
MLOOP( SELE, ID = 1 )
MFACE( ADD )
```

Appendix C (Continued)

/ FACE 2

```
SURFACE( SELE, ID = 1 )
MLOOP( SELE, ID = 2 )
MFACE( ADD )
```

/ FACE3

```
SURFACE( SELE, ID = 1 )
MLOOP( SELE, ID = 3 )
MFACE( ADD )
```

/ MESHING FEATURES

```
MFACE( SELE, ID = 1 )
ELEMENT( SETD, QUAD, NODE = 4 )
MFACE( MESH, MAP, NOSM, ENTI = "silicon" )
MFACE( SELE, ID = 2 )
MFACE( SELE, ID = 3 )
ELEMENT( SETD, QUAD, NODE = 4 )
MFACE( MESH, MAP, ENTI = "water" )
```

/ MESH MAP ELEMENT ID

```
ELEMENT( SETD, EDGE, NODE = 2 )
MEDGE( SELE, ID )
    1
    7
MEDGE( MESH, MAP, ENTI = "sides" )
MEDGE( SELE, ID = 2 )
MEDGE( MESH, MAP, ENTI = "axis" )
MEDGE( SELE, ID = 3 )
MEDGE( MESH, MAP, ENTI = "inlet" )
MEDGE( SELE, ID = 4 )
MEDGE( MESH, MAP, ENTI = "top" )
MEDGE( SELE, ID = 5 )
MEDGE( MESH, MAP, ENTI = "surface" )
MEDGE( SELE, ID = 6 )
MEDGE( MESH, MAP, ENTI = "outlet" )
MEDGE( SELE, ID )
   8
   9
   10
MEDGE( MESH, MAP, ENTI = "bottom" )
```

Appendix C (Continued)

```
MEDGE( SELE, ID )
   11
   12
   13
MEDGE( MESH, MAP, ENTI = "interface" )
END(  )
```

/ FEM PROPERTIES OF (SOLID, LIQUID, OR GAS), ENTITY, PROBLEM TYPE AND BOUNDARY CONDITION DEFINITION

```
FIPREP(  )
```

/ FLUID VARIABLE PROPERTIES

```
DENSITY (ADD, SET = "water", TYP2, CONS = 0.996, TEMP )

CONDUCTIVITY (ADD, SET = "water", CURVE = 10 )
0 37.0 43.33 48.89 54.44 65.55 76.67 87.78 104.4 115.6
0.00135277247 0.0014699 0.0015224665 0.001539197
0.0015511472 0.0015750478 0.0015965583 0.0016132887
0.0016347992 0.0016371893

VISCOSITY (ADD, SET = "water", CURVE = 10 )
0 37.0 43.33 48.89 54.44 65.55 76.67 87.78 104.4 115.6
0.017900 0.00798 0.00616 0.00562 0.00513 0.00430 0.00372
0.00327 0.00267 0.00244

SPECIFICHEAT (ADD, SET = "water", CURVE = 10 )
0 37.0 43.33 48.89 54.44 65.55 76.67 87.78 104.4 115.6
1.009799235 0.998137 0.99760994 0.99770994 0.99880497
0.99976099 1.00167304 1.003585086 1.007648184
```

/ FLUID CONSTANT PROPERTIES

```
DENSITY( ADD, SET = "water", CONS = 0.996 )
CONDUCTIVITY( ADD, SET = "water", CONS = 0.0014699 )
VISCOSITY( ADD, SET = "water", CONS = 0.00798 )
SPECIFICHEAT( ADD, SET = "water", CONS = 0.998137 )
SURFACETENSION( ADD, SET = "water", CONS = 73 )
```

/ MATERIAL PROPERTIES

```
DENSITY( ADD, SET = "silicon", CONS = 2.33 )
CONDUCTIVITY( ADD, SET = "silicon", CONS = 0.334608 )
SPECIFICHEAT( ADD, SET = "silicon", CONS = 0.17006 )
```

Appendix C (Continued)

/ ENTITY DEFINITION

```
ENTITY( ADD, NAME = "water", FLUI, PROP = "water" )
ENTITY( ADD, NAME = "inlet", PLOT )
ENTITY( ADD, NAME = "outlet", PLOT )
ENTITY( ADD, NAME = "surface", SURF, DEPT = 17, SPIN, STRA,
ANG1 = 330,
ANG2 = 260 )
ENTITY( ADD, NAME = "bottom", PLOT )
ENTITY( ADD, NAME = "top", PLOT )
ENTITY( ADD, NAME = "axis", PLOT )
ENTITY( ADD, NAME = "silicon", SOLI, PROP = "silicon" )
ENTITY( ADD, NAME = "sides", PLOT )
ENTITY( ADD, NAME = "interface", PLOT,ATTA = "water", NATT
= "silicon")
BODYFORCE( ADD, CONS, FX = 981, FY = 0, FZ = 0 )
PRESSURE( ADD, MIXE = 1e-11, DISC )
```

/ RELAXATION FACTORS (UR, UZ, Uθ, PRESSURE, TEMP, SURFACE)

```
OPTIONS( ADD, UPWI )
UPWINDING( ADD, STRE )
RELAXATION(  )
  0.3, 0.3, 0.3, 0, 0.05, 0.25
```

/ BOUNDARY CONDITIONS

```
BCNODE( ADD, COOR, NODE = 39 )
BCNODE( ADD, SURF, NODE = 39, ZERO )
BCNODE( ADD, VELO, ENTI = "bottom", ZERO )
BCNODE( ADD, VELO, ENTI = "top", ZERO )
BCNODE( ADD, URC, ENTI = "inlet", ZERO )
BCNODE( ADD, UZC, ENTI = "inlet", CONS = 50.07531 )
BCNODE( ADD, URC, ENTI = "axis", ZERO )
BCNODE( ADD, VELO, ENTI = "interface", ZERO )
BCNODE( ADD, VELO, ENTI = "sides", ZERO )
BCNODE( ADD, UT, NODE = 39, ZERO )
BCNODE( ADD, TEMP, ENTI = "inlet", CONS = 37 )
BCFLUX( ADD, HEAT, ENTI = "bottom", CONS = 2.9855 )
```

/ SPINNING TARGET

```
BCNODE( UTHE, POLY = 1, ENTI = "silicon" )
    0, 13.09,     0,     1,     0
```

Appendix C (Continued)

```
/AND/OR

/ SPINNING CONFINED WALL

BCNODE( UTHE, POLY = 1, ENTI = "top" )
    0, 26.18,     0,     1,     0

/ MINIMUM TEMPERATURE

CLIPPING( ADD, MINI )
  0,     0,    0,     0,    37,     0

/ INITIAL CONDITIONS

ICNODE( VELO, STOKES )
ICNODE( ADD, URC, ENTI = "water", CONS = 45 )
ICNODE( ADD, UTHE, ENTI = "water", CONS = 5.333 )

/ PROBLEM DESCRIPTION AND METHOD

DATAPRINT( ADD, CONT )
EXECUTION( ADD, NEWJOB  )

/ TIMESTEP RESTART DATA BASE INPUT

EXECUTION( NEWJ, RSTEP = 220 )
PRINTOUT( ADD, NONE, BOUN )
PROBLEM(ADD, CYLI,INCO, TRAN, LAMI, NONL, NEWT, MOME, ENER,
FREE, SING)
SOLUTION( ADD, N.R. = 50, KINE = 20, VELC = 1e-4, RESC =
1e-4, SURF = 0.001 )
TIMEINTEGRATION( ADD, BACK, NSTE = 3001, TSTA = 0, DT = 1e-
05, VARI, WIND = 1, NOFI = 15 )
POSTPROCESS ( NBLOCKS = 3 )
1 601 75
601 1501 1
1501 3001 1
END(  )

/ INPUT FILE GENERATION AND RUN

CREATE( FISO )
RUN( FISOLV, IDEN = "EXAMPLE3", BACK, AT = "", TIME =
"NOW", COMP )
```

Appendix C (Continued)

/ RESTART CONDITION FROM PREVIOUS RESULTS

```
RUN( FISOLV, IDEN = "EXAMPLE4", BACK, RESTART =
"EXAMPLE3.FDPOST" )

/OR

FILES( RENAME, FROM = "EXAMPLE3.FDPOST", TO = "
EXAMPLE4.FDREST" )
FILES( RENAME, FROM = " EXAMPLE3.FDSTAT", TO = "
EXAMPLE4S.FDSTAT" )

ICNODE( VELOCITY, READ )
ICNODE( TEMP, READ )
```

Appendix D: CFD Chemical Mechanical Polishing Model

/ JOURNAL FILE FOR GAMBIT 2.3.16, DATABASE 2.3.14

/ IDENTIFIER "G04"

```
reset
solver select "FIDAP"
```

/ VERTICES

```
vertex create coordinates -0.004 -0.477 0
vertex create coordinates -0.004 -0.287 0
vertex create coordinates -0.004 -0.477 -0.19
vertex create coordinates -0.004 -0.477 0.19
vertex create coordinates -0.004 -0.667 0
vertex create coordinates -0.004 -0.382 0
vertex create coordinates -0.004 -0.477 0.095
vertex create coordinates -0.004 -0.477 -0.095
vertex create coordinates -0.004 -0.572 0
coordinate create cartesian oldsystem "c_sys.1" offset -
0.004 -0.477 0 axis1 \
  "x" angle1 0 axis2 "y" angle2 0 axis3 "z" angle3 0
rotation
```

/ EDGES

```
edge create center2points "vertex.1" "vertex.2" "vertex.3"
minarc arc
edge create center2points "vertex.1" "vertex.2" "vertex.4"
minarc arc
edge create center2points "vertex.1" "vertex.3" "vertex.5"
minarc arc
edge create center2points "vertex.1" "vertex.5" "vertex.4"
minarc arc
edge create straight "vertex.6" "vertex.7" "vertex.9"
"vertex.8"
edge create straight "vertex.8" "vertex.6"
edge create straight "vertex.6" "vertex.2"
edge create straight "vertex.8" "vertex.3"
edge create straight "vertex.9" "vertex.5"
edge create straight "vertex.7" "vertex.4"
```

Appendix D (Continued)

/ FACES

```
face create wireframe "edge.1" "edge.9" "edge.8" "edge.10"
real
face create wireframe "edge.2" "edge.12" "edge.5" "edge.9"
real
face create wireframe "edge.3" "edge.10" "edge.7" "edge.11"
real
face create wireframe "edge.4" "edge.11" "edge.6" "edge.12"
real
face create wireframe "edge.8" "edge.5" "edge.6" "edge.7"
real
```

/ VOLUMES

```
volume create translate "face.1" "face.2" "face.3" "face.4"
"face.5" vector \
  0.002 0 0
save
volume create translate "face.18" "face.23" "face.13"
"face.8" "face.27" \
  vector 0.002 0 0
save
```

/ MESH INTERVALS

```
undo begingroup
edge picklink "edge.49" "edge.35" "edge.57" "edge.27"
"edge.19" "edge.60" \ "edge.14" "edge.44" "edge.11"
"edge.12" "edge.9" "edge.10"
edge mesh "edge.44" "edge.14" "edge.10" "edge.60" "edge.19"
"edge.9" \"edge.12" "edge.27" "edge.57" "edge.11" "edge.35"
"edge.49" successive \
  ratio1 1 intervals 5
undo endgroup
undo begingroup
edge picklink "edge.69" "edge.17" "edge.62" "edge.24"
"edge.54" "edge.40" \
  "edge.47" "edge.33" "edge.8" "edge.5" "edge.6" "edge.56"
"edge.42" "edge.4" \
  "edge.64" "edge.26" "edge.2" "edge.67" "edge.15" "edge.1"
"edge.45" \"edge.31" "edge.3" "edge.7"
edge mesh "edge.7" "edge.33" "edge.47" "edge.3" "edge.31"
"edge.45" "edge.1" \
```

Appendix D (Continued)

```
  "edge.15" "edge.67" "edge.2" "edge.26" "edge.64" "edge.4"
"edge.42" \
  "edge.56" "edge.6" "edge.40" "edge.54" "edge.5" "edge.24"
"edge.62" \
  "edge.8" "edge.17" "edge.69" successive ratio1 1
intervals 8
edge picklink "edge.36" "edge.25" "edge.18" "edge.20"
"edge.28" "edge.13" \
  "edge.16" "edge.34"
edge mesh "edge.34" "edge.16" "edge.13" "edge.28" "edge.20"
"edge.18" \
  "edge.25" "edge.36" successive ratio1 1 intervals 2
undo endgroup
undo begingroup
edge picklink "edge.61" "edge.59" "edge.43" "edge.46"
"edge.58" "edge.55" \
  "edge.50" "edge.48"
edge mesh "edge.48" "edge.50" "edge.55" "edge.58" "edge.46"
"edge.43" \
  "edge.59" "edge.61" successive ratio1 1 intervals 2
undo endgroup

/ MESH VOLUME

volume mesh "volume.1" "volume.2" "volume.3" "volume.4"
"volume.5" "volume.6" \
  "volume.7" "volume.8" "volume.9" "volume.10" map size 1
physics create "water" ctype "FLUID" volume "volume.1"
"volume.2" "volume.3" \
  "volume.4" "volume.5" "volume.6" "volume.7" "volume.8"
"volume.9" \
  "volume.10"
window modify volume invisible mesh

/ ENTITIES

physics create "inlet" btype "PLOT" face "face.29"
"face.43" "face.7" \"face.17"
physics create "outlet" btype "PLOT" face "face.36"
"face.24" "face.41" \"face.14"
physics create "wafer" btype "PLOT" face "face.3" "face.1"
"face.2" "face.4" \"face.5"
physics create "pad" btype "PLOT" face "face.30" "face.44"
"face.35" \"face.40" "face.48"
```

Appendix D (Continued)

```
physics create "delta1" btype "PLOT" face "face.18"
"face.8" "face.13" \"face.23" "face.27"
physics create "outwfedge" btype "PLOT" edge "edge.4"
"edge.2"
physics create "wedge1" btype "PLOT" edge "edge.11"
"edge.6" "edge.12"
physics create "wedge2" btype "PLOT" edge "edge.12"
"edge.5" "edge.9"
physics create "inwfedge" btype "PLOT" edge "edge.3"
"edge.1"
physics create "inpadedge" btype "PLOT" edge "edge.67"
"edge.45"
physics create "outpadedge" btype "PLOT" edge "edge.56"
"edge.64"
save
export fidap "G04.FDNEUT"
```

/ IDENTIFIER “G04”

```
/ CONVERSION OF NEUTRAL FILE TO FIDAP DATABASE
/
FICONV( NEUTRAL )
INPUT( FILE="G04.FDNEUT" )
OUTPUT( DELETE )
END
```

/ GAMBIT/FiDAP 8.7.4 PREPROCESSING INPUT FILE

```
TITLE
G04
```

/ FIPREP

/ PROBLEM SETUP

```
PROBLEM (3-D, LAMINAR, NON-LINEAR, ENERGY)
EXECUTION( NEWJOB )
PRINTOUT( NONE )
DATAPRINT( CONTROL )
/
/ CONTINUUM ENTITIES
/
ENTITY ( NAME = "ALUMINA", FLUID, PROPERTY = "ALUMINA" )
/
```

Appendix D (Continued)

/ BOUNDARY ENTITIES

```
ENTITY ( NAME = "inlet", PLOT )
ENTITY ( NAME = "outlet", PLOT )
ENTITY ( NAME = "wafer", PLOT )
ENTITY ( NAME = "pad", PLOT )
ENTITY ( NAME = "delta1", PLOT )
ENTITY ( NAME = "outwfedge", PLOT )
ENTITY ( NAME = "wedge1", PLOT )
ENTITY ( NAME = "wedge2", PLOT )
ENTITY ( NAME = "inwfedge", PLOT )
ENTITY ( NAME = "inpadedge", PLOT )
ENTITY ( NAME = "outpadedge", PLOT )
```

/ LOCAL COORDINATE SYSTEMS

```
COORDINATE ( SYSTEM = 2, MATRIX,CARTESIAN )
0.000000 0.000000 0.000000 1.000000 0.000000 0.000000
0.000000 1.000000 0.000000 0.000000 0.000000 1.000000
COORDINATE ( SYSTEM = 3, MATRIX,CARTESIAN )
-0.004000 -0.477000 0.000000 1.000000 0.000000 0.000000
0.000000 1.000000 0.000000 0.000000 0.000000 1.000000
```

/ SOLUTION PARAMETERS

```
SOLUTION( SEGREGATED = 50, CR, CGS, VELCONV = .001, NCGC =
1.E-6, SCGC = 1.E-6, SCHANGE = .0 )
PRESSURE( MIXED = 1.E-8, DISCONTINUOUS )
RELAX( HYBRID )
OPTIONS( UPWINDING, , , )
SCALE( VALUE = 1 )
TIMEINTEGRATION( BACKWARD,NSTEPS = ,DT = 0,,, )
POSTPROCESS( NBLOCKS =  )
```

/ LIST OF MATERIALS PROPERTIES

```
DENSITY( SET = "ALUMINA", CONSTANT = 1 )
VISCOSITY( SET = "ALUMINA", CONSTANT = 1 )
CONDUCTIVITY( SET = "ALUMINA", CONSTANT = 1 )
SPECIFICHEAT( SET = "ALUMINA", CONSTANT = 1 )
```

Appendix D (Continued)

/ INITIAL AND BOUNDARY CONDITIONS

```
ICNODE( , CONSTANT = 0, ALL )
BCNODE( , CONSTANT = 0, ENTITY = "inlet" )
BCNODE( , CONSTANT = 0, ENTITY = "outlet" )
BCNODE( , CONSTANT = 0, ENTITY = "wafer" )
BCNODE( , CONSTANT = 0, ENTITY = "pad" )
BCNODE( , CONSTANT = 0, ENTITY = "delta1" )
BCNODE( , CONSTANT = 0, ENTITY = "outwfedge" )
BCNODE( , CONSTANT = 0, ENTITY = "wedge1" )
BCNODE( , CONSTANT = 0, ENTITY = "wedge2" )
BCNODE( , CONSTANT = 0, ENTITY = "inwfedge" )
BCNODE( , CONSTANT = 0, ENTITY = "inpadedge" )
BCNODE( , CONSTANT = 0, ENTITY = "outpadedge" )

END

CREATE( FIPREP,DELETE )
PARAMETER( LIST )
CREATE( FISOLV )
RUN( FISOLV, FOREGROUND )
```

Appendix E: MATLAB Programs for 3–D Solution Visualization

/MATLAB 7.4.0 (R2007a) Files

/CONVERSION OF NEUTRAL FILE TO MATLAB DATABASE AS AN INPUT FILE

```
function ReadFidapSolution3D
global X % X coordinate
global Y % Y coordinate
global Z % Z coordinate
global T % Temperature

folder_name = 'C:\Documents and
Settings\home\Desktop\fidap\Press\P4.5psi\';

file_name = '50SNEUT';
full_path = strcat(folder_name,'\',file_name);

[Vname,N,T,X,Y,Z] = FD2ML3D(full_path);
{file_name;Vname;N}

function [Vname,N,F,X,Y,Z] = FD2ML3D(fpneut_name)
[Vname,N] = textread(fpneut_name,'%20c %d',1);
A = zeros(4,N);
fid = fopen(fpneut_name);
fgets(fid);
A = fscanf(fid,'%*d %f %f %f %f',[4 N]);
fclose(fid);
F = A(1,:);
X = A(2,:);
Y = A(3,:);
Z = A(4,:);
```

/ DATA PREPARATION AND REARRANGE IN A MATRIX FORM

```
function OR_Plot3D_Prep

% Prepare data for 3-D plots
global X
global Y
global Z
global T
global XI
global YI
global ZI
global TI
```

Appendix E (Continued)

```
% Data limits for 3-D plots
xmin = -0.004;
xmax = 0;
ymin = -0.667;
ymax = -0.287;
zmin = -0.19;
zmax = 0.19;

% Matrices for 3-D plots

rx = xmin:0.001:xmax;
ry = ymin:0.0025:ymax;
rz = zmin:0.0025:zmax;
[XI,YI,ZI] = meshgrid(rx,ry,rz);
TI = griddata3(X,Y,Z,T,XI,YI,ZI); TI(~finite(TI))=0;
```

/OUTPUT OF FILE AS 3–D PLOTS OR FIGURES

```
function OR_Plot3D_Temperature
global XI
global YI
global ZI
global TI
figure
clf reset

%Cross-sectional Views along and across the 3-D plot

slice(XI,YI,ZI,TI,[-0.004 -0.003 -0.002 -0.001 0],-0.477,0)
shading interp;
set(gca,'CLim',[24 36])
```

Appendix F: Grid Convergence Index Analysis Sample

Table F.1 Temperature results of figure 3.13 at a dimensionless distance of $r/r_n=8$.

MESH SIZE	NUMBER OF ELEMENTS	MESH TEMP	SAFETY FACTOR
35x79	2765	323.15114	1.25
22x79	1738	323.16375	
64x76	4864	323.19566	

Grid ratio of refinement

$$r := \begin{pmatrix} \frac{h1}{h2} \\ \frac{h3}{h2} \\ \frac{h3}{h1} \end{pmatrix} \qquad r = \begin{pmatrix} 1.591 \\ 2.799 \\ 1.759 \end{pmatrix} \tag{F.1}$$

Order grid convergence (p) equations

A more direct evaluation of p can be obtained from three grid solutions using a set of grid refinement ratio, at a particular location $r/r_h=8$.

$$p1 := \frac{\ln\left(\frac{T3 - T2}{T2 - T1}\right)}{\ln(r_0)} \qquad p2 := \frac{\ln\left(\frac{T3 - T2}{T2 - T1}\right)}{\ln(r_1)} \qquad p3 := \frac{\ln\left(\frac{T3 - T2}{T2 - T1}\right)}{\ln(r_2)} \tag{F.2 a, b, c}$$

$$P := \begin{pmatrix} p1 \\ p2 \\ p3 \end{pmatrix} \qquad P = \begin{pmatrix} 2 \\ 0.902 \\ 1.644 \end{pmatrix}$$

Temperature results for zero grid spacing h=0, using Richardson's Extrapolation Method.

$$Tho := \begin{bmatrix} T1 + \frac{T1 - T2}{(r_0)^{p1} - 1} \\ T1 + \frac{T1 - T2}{(r_1)^{p2} - 1} \\ T1 + \frac{T1 - T2}{(r_2)^{p3} - 1} \end{bmatrix} \qquad Tho = \begin{pmatrix} 323.143 \\ 323.143 \\ 323.143 \end{pmatrix} \tag{F.3}$$

Appendix F (Continued)

Grid Convergence Index results

$$GCI := \begin{bmatrix} \dfrac{Fs \cdot \left|\dfrac{T2 - T1}{T1}\right|}{(r_0)^{p1} - 1} \cdot 100 \\ \dfrac{Fs \cdot \left|\dfrac{T2 - T3}{T2}\right|}{(r_1)^{p2} - 1} \cdot 100 \\ \dfrac{Fs \cdot \left|\dfrac{T3 - T1}{T3}\right|}{(r_2)^{p3} - 1} \cdot 100 \end{bmatrix} \qquad GCI = \begin{pmatrix} 3.187 \times 10^{-3} \\ 8.065 \times 10^{-3} \\ 0.011 \end{pmatrix} \qquad \text{(F.4)}$$

Asymptotic range of convergence and relative error equations of figure 3.13 results.

$$ARC := \begin{bmatrix} \left[\dfrac{\dfrac{Fs \cdot \left|\dfrac{T2 - T1}{T1}\right|}{(r_0)^{p1} - 1}}{(r_2)^{p3} \cdot \dfrac{Fs \cdot \left|\dfrac{T3 - T1}{T3}\right|}{(r_2)^{p3} - 1}} \right] \\ \left[\dfrac{\dfrac{Fs \cdot \left|\dfrac{T2 - T3}{T2}\right|}{(r_1)^{p2} - 1}}{(r_0)^{p1} \cdot \dfrac{Fs \cdot \left|\dfrac{T2 - T1}{T1}\right|}{(r_0)^{p1} - 1}} \right] \\ \left[\dfrac{\dfrac{Fs \cdot \left|\dfrac{T3 - T1}{T3}\right|}{(r_2)^{p3} - 1}}{(r_1)^{p2} \cdot \dfrac{Fs \cdot \left|\dfrac{T2 - T3}{T2}\right|}{(r_1)^{p2} - 1}} \right] \end{bmatrix} \qquad ARC = \begin{pmatrix} 0.112 \\ 1 \\ 0.551 \end{pmatrix} \qquad \text{(F.5)}$$

About the Author

Jorge C. Lallave Cortes was born in Mayaguez, Puerto Rico, on Nov. 3, 1976. The author received his Bachelor's degree in Mechanical Engineering in 1999 from University of Puerto Rico, Mayaguez Campus (RUM). At University of South Florida, Tampa, he received his Master's degree in Environmental Engineering under the supervision of Dr. Robert Carnahan in 2001. In spring of 2002 he started his PhD career in Mechanical Engineering at the University of South Florida under the supervision of Prof. Muhammad M. Rahman, PhD and Prof. Ashok Kumar, PhD in the area of fluids and heat transfer modeling of partially–confined, confined, and free liquid jet impingement over spinning boundaries and chemical mechanical polishing process. During his doctoral studies the author has coauthored more than 10 technical research articles. In addition, the author participated in the GK–12 STARS program at USF as a mentor for third, fourth and fifth graders during the last 6 years. The author is a member of the Tau Beta Pi honor society for engineers and American Society of Mechanical Engineers.